

UNCLASSIFIED

AD NUMBER
ADB277404
NEW LIMITATION CHANGE
TO Approved for public release, distribution unlimited
FROM Distribution authorized to U.S. Gov't. agencies only; Proprietary Info.; Jul 2001. Other requests shall be referred to U.S. Army Medical Research and Materiel Command, 504 Scott St., Ft. Detrick, MD 21702-5012.
AUTHORITY
USAMRMC ltr, 28 Aug 2002

THIS PAGE IS UNCLASSIFIED

AD _____

Award Number: DAMD17-98-1-8176

TITLE: Computer Simulation of Breast Cancer Screening

PRINCIPAL INVESTIGATOR: John Boone, Ph.D.

CONTRACTING ORGANIZATION: University of California, Davis
Davis, California 95616

REPORT DATE: July 2001

TYPE OF REPORT: Final

PREPARED FOR: U.S. Army Medical Research and Materiel Command
Fort Detrick, Maryland 21702-5012

DISTRIBUTION STATEMENT: Distribution authorized to U.S. Government agencies only (proprietary information, Jul 01). Other requests for this document shall be referred to U.S. Army Medical Research and Materiel Command, 504 Scott Street, Fort Detrick, Maryland 21702-5012.

The views, opinions and/or findings contained in this report are those of the author(s) and should not be construed as an official Department of the Army position, policy or decision unless so designated by other documentation.

20020329 199

NOTICE

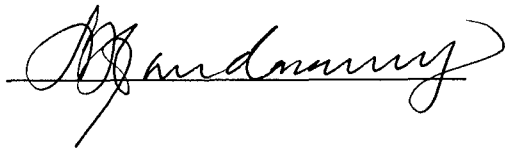
USING GOVERNMENT DRAWINGS, SPECIFICATIONS, OR OTHER DATA INCLUDED IN THIS DOCUMENT FOR ANY PURPOSE OTHER THAN GOVERNMENT PROCUREMENT DOES NOT IN ANY WAY OBLIGATE THE U.S. GOVERNMENT. THE FACT THAT THE GOVERNMENT FORMULATED OR SUPPLIED THE DRAWINGS, SPECIFICATIONS, OR OTHER DATA DOES NOT LICENSE THE HOLDER OR ANY OTHER PERSON OR CORPORATION; OR CONVEY ANY RIGHTS OR PERMISSION TO MANUFACTURE, USE, OR SELL ANY PATENTED INVENTION THAT MAY RELATE TO THEM.

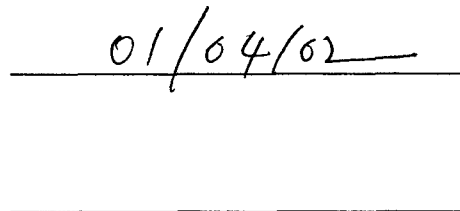
LIMITED RIGHTS LEGEND

Award Number: DAMD17-98-1-8176
Organization: University of California, Davis

Those portions of the technical data contained in this report marked as limited rights data shall not, without the written permission of the above contractor, be (a) released or disclosed outside the government, (b) used by the Government for manufacture or, in the case of computer software documentation, for preparing the same or similar computer software, or (c) used by a party other than the Government, except that the Government may release or disclose technical data to persons outside the Government, or permit the use of technical data by such persons, if (i) such release, disclosure, or use is necessary for emergency repair or overhaul or (ii) is a release or disclosure of technical data (other than detailed manufacturing or process data) to, or use of such data by, a foreign government that is in the interest of the Government and is required for evaluational or informational purposes, provided in either case that such release, disclosure or use is made subject to a prohibition that the person to whom the data is released or disclosed may not further use, release or disclose such data, and the contractor or subcontractor or subcontractor asserting the restriction is notified of such release, disclosure or use. This legend, together with the indications of the portions of this data which are subject to such limitations, shall be included on any reproduction hereof which includes any part of the portions subject to such limitations.

THIS TECHNICAL REPORT HAS BEEN REVIEWED AND IS APPROVED FOR PUBLICATION.





REPORT DOCUMENTATION PAGE			Form Approved OMB No. 074-0188	
Public reporting burden for this collection of information is estimated to average 1 hour per response, including the time for reviewing instructions, searching existing data sources, gathering and maintaining the data needed, and completing and reviewing this collection of information. Send comments regarding this burden estimate or any other aspect of this collection of information, including suggestions for reducing this burden to Washington Headquarters Services, Directorate for Information Operations and Reports, 1215 Jefferson Davis Highway, Suite 1204, Arlington, VA 22202-4302, and to the Office of Management and Budget, Paperwork Reduction Project (0704-0188), Washington, DC 20503				
1. AGENCY USE ONLY (Leave blank)	2. REPORT DATE July 2001	3. REPORT TYPE AND DATES COVERED Final (01 Jul 98 - 30 Jun 01)		
4. TITLE AND SUBTITLE Computer Simulation of Breast Cancer Screening		5. FUNDING NUMBERS DAMD17-98-1-8176		
6. AUTHOR(S) John Boone, Ph.D.				
7. PERFORMING ORGANIZATION NAME(S) AND ADDRESS(ES) University of California, Davis Davis, California 95616 E-Mail: jmboone@ucdavis.edu		8. PERFORMING ORGANIZATION REPORT NUMBER		
9. SPONSORING / MONITORING AGENCY NAME(S) AND ADDRESS(ES) U.S. Army Medical Research and Materiel Command Fort Detrick, Maryland 21702-5012		10. SPONSORING / MONITORING AGENCY REPORT NUMBER		
11. SUPPLEMENTARY NOTES				
12a. DISTRIBUTION / AVAILABILITY STATEMENT Distribution authorized to U.S. Government agencies only (proprietary information, Jul 01). Other requests for this document shall be referred to U.S. Army Medical Research and Materiel Command, 504 Scott Street, Fort Detrick, Maryland 21702-5012.			12b. DISTRIBUTION CODE	
13. Abstract (<i>Maximum 200 Words</i>) (<i>abstract should contain no proprietary or confidential information</i>) A breast cancer screening computer model was developed. Simulations of the physics of mammography detection were performed, and the detection probability of breast cancer using mammographic screening was assessed. The detection characteristics of mammographic screening were quantified as a function of breast density and tumor diameter. In addition to modeling the actual screening process, other factors that were incorporated into the screening model include the growth rate of breast cancer, the ethnic breakdown of the US female population, the age and race dependent incidence of breast cancer, and the prognosis of surviving breast cancer once it is detected (size and node status dependent). The age dependent death rate from other (non-breast cancer) causes was also included in the model. The model was capable of producing output parameters which correspond well to published data, and these parameters include the size distribution of breast cancer at detection, and the survival rates from breast cancer. The development of the model led us to consider alternate screening strategies such as breast CT techniques. We conclude that modeling the performance of breast cancer screening is an important tool which will help in the optimization of screening procedures and in reducing breast cancer mortality.				
14. SUBJECT TERMS Breast Cancer			15. NUMBER OF PAGES 148	
			16. PRICE CODE	
17. SECURITY CLASSIFICATION OF REPORT Unclassified	18. SECURITY CLASSIFICATION OF THIS PAGE Unclassified	19. SECURITY CLASSIFICATION OF ABSTRACT Unclassified	20. LIMITATION OF ABSTRACT Unlimited	

Table of Contents

Cover.....	
SF 298.....	2
Table of Contents.....	3
Introduction.....	4
Body.....	5
Key Research Accomplishments.....	10
Reportable Outcomes.....	13
Personnel.....	15
Conclusions.....	16
References.....	17
Appendices.....	18

Introduction

The notion of developing a computer model for the assessment of breast cancer screening first came to us in 1993 (ca). While other computer simulation models have been developed[1-3], the model developed in this project is a very comprehensive and flexible. Because the model developed in this project incorporates the ability to estimate the probability of cancer detection as a function of the growth of the cancer, it represents a more sophisticated and realistic simulation of breast cancer screening than previous tools reported in the literature.

While this project was focused on the development of the breast cancer screening simulator *per se*, much of the utility of the computer model will be realized after the grant period. Indeed, we predicted when writing this grant that the computer model would be useful in the comparison of breast cancer screening techniques, and that new screening techniques would become available due to the accelerated research in breast cancer has been experienced in the last eight to ten years. Certainly, interest in biomarkers for breast cancer[4;5] has been a strong focus of funding by the Department of Defense BCRP, by the NIH, and by the California BCRP. The model provides the opportunity to compare the effectiveness of biomarker techniques (and other non-imaging breast cancer screening approaches) against the conventional mammographic approaches, once sensitivity versus tumor size data becomes available (this is a necessary input to the computer model). Spurred in part by our development efforts on assessing breast cancer screening techniques, and in particular our study of mammography and its shortcomings, we have proposed an alternative breast cancer screening technology using computed tomography (CT) of the breast. The computer simulation efforts of this project spilled over into our breast CT research, and using these techniques we were able to show (manuscript is *in press* in Radiology) that breast CT can be performed at radiation dose levels that are comparable to mammography. The assessment of the feasibility of breast CT and the construction of a breast CT scanner for clinical (pilot) testing has now been funded by the NIH and California BCRP, respectively. The computer simulation model developed in this research will allow the comparison of the clinical efficacy between breast CT and digital mammography. When we predicted that the development of the computer model would be useful in comparing screening technologies, we didn't realize that we would have a perfect opportunity to use the computer simulation model in our own screening technology development.

The development of the computer simulation model is complete, and we have accomplished all the scientific aims of the proposal. Several specific aims of the proposal have led to the publication and submission of manuscripts which are relatively narrowly focused, and these are described in the Reportable Outcomes section of this report. Additional scientific manuscripts which describe this work in a more comprehensive manner (and encompass many of the data that have been reported in the 1999 and 2000 annual reports) are currently in preparation and will be submitted for peer review in the October 2001 time frame.

Body

Our efforts in the past year of research have focused on formalizing the techniques being developed, reporting the results of our research, and we have also starting to extend the *computer simulation of breast cancer screening* concept to another potential breast cancer screening tool, breast CT. There is a strong interdisciplinary nature of this research, which straddles the fields of radiology, computer modeling, and epidemiology. The principals in this investigation are from the radiology community, and we have attempted to reach across discipline boundaries for the publication of certain aspects of this research. Our activity and progress in that last year are described below, and a task by task description of the project is then detailed.

THE PROBABILITY OF BREAST CANCER DETECTION

The modeling of breast cancer screening requires that the probability of the screening procedure be known, given the characteristics of the tumor at the time of the screening examination. For mammography, the pertinent tumor characteristics are its size (which relates to it's signal to noise ratio on the image, which in turn affects detectability) and the parenchyma background (breast density) of the breast is important as well (this is discussed in the section below). The sensitivity is the probability of breast cancer detection, but it is not well known what the sensitivity of mammography is. Furthermore and very importantly, a single general value for the sensitivity of breast cancer (various numbers are reported[6-10]) is not useful for the model – For the computer model to be useful, we need to be able to accurately calculate the probability of cancer detection as a function of time, as the tumor grows and gradually becomes more visible on the mammographic image. Part of our effort in this regard is to educate the breast cancer screening scientific community (both radiologists and epidemiologists) to the fact that there is no single number which describes the probability of breast cancer screening – it is a fundamental fact of imaging physics that breast cancer will become more visible as it grows bigger – thus, its probability of detection (the sensitivity of mammographic screening) changes over time. Most articles on mammography's sensitivity in the literature report only single values, and thus reflect only a gross average sensitivity, averaged over the tumor sizes in the population studied.

Our approach to computing the absolute probability (versus tumor size) of breast cancer detection is to evaluate the receiver operating characteristic (ROC) curve, which is a plot of the sensitivity versus 1-specificity for mammographic detection. The ROC curve can be and has been measured extensively in mammography, and we have developed computer simulation techniques which determine ROC curves as a function of breast density and tumor size (see next section). The problem with an ROC curve is that it is a sliding scale which characterizes sensitivity as a function of (1-specificity), and it is not generally known where on the ROC curve an observer actually functions (the so-called *operating point* on the ROC curve). This aspect of the project is a result of the recognition that the ROC curve, combined with other bits of information that generally are known, can be used to calculate the absolute probability of breast cancer detection. Another way to say this is that other information can be used to assess the operating point on the ROC curve, and once this point is identified, the sensitivity (and absolute probability of breast cancer detection) can be computed.

Mammography is a highly studied screening procedure, and is regulated by the federal government mammography quality standards act (MQSA). As a result of such scrutiny, it is known that most screening centers have a cancer detection rate of about 3 detected breast cancers per 1000 screens. This number can vary depending on the population screened (e.g. age and screening history), but the majority of mammography clinics in the US have a CDR between 2 and 4. The positive biopsy rate, which is the fraction of patients that are sent to needle biopsy procedures who are found to actually have breast cancer (based on the histopathology analysis), is also known to be around 20-25% for most experienced radiologists. Knowing the cancer incidence (cancer detection rate) and the positive biopsy rate (essentially the positive predictive value) for mammography, coupled with the ROC curve, allows one to compute the operating point and hence the sensitivity (probability) of cancer detection.

The mathematical procedures which describe the way in which the CDR and PPV can be used to determine sensitivity are described in an accompanying appendix (Appendix A: Determining sensitivity and specificity in mammography from the positive biopsy rate, cancer incidence, and ROC curve parameters"). As reported in the July 2000 annual report, we submitted these results (in a quite different format) to the journal *Radiology*, but the manuscript was rejected as being too technical for that clinically-oriented journal. After significant revision, this manuscript was submitted for publication to *Medical Decision Making* in August 2000. We received a request for revisions on February 22, 2001, and sent a substantively revised manuscript on April 30, 2001, which is still under re-review.

THE ROLE OF BREAST DENSITY IN BREAST CANCER DETECTION

Breast density is known to affect sensitivity, however this effect has not been quantified to our knowledge. Women with dense breasts are known from clinical experience to have more difficult mammograms to interpret, due to the large amount of confounding (normal) anatomical information. Using computer simulation techniques, we have accurately quantified the relative impact that breast density has on reducing detection performance by mammography. This data was submitted as a manuscript to the *Journal of Medical Screening* on October 2, 2000. After a series of revisions, we became frustrated with this journal's lack of timeliness and the reviewer's lack of understanding of the role that physics plays in the mammography process. Therefore, we withdrew this manuscript from consideration in *JMS* (it was not rejected), substantially revised the manuscript for a different audience of readers, and submitted this to the *Journal of Women's Imaging* on or about May 15, 2001. It is still under first review. This manuscript, entitled, "The effect of breast density on cancer detection performance in mammography", is included in this report as Appendix B. We significantly modified the analysis techniques during the revision of this manuscript for *JWI*, to reduce its technical complexity and to make the results straightforward for a radiologist audience.

INCLUSION OF THE 2000 CENSUS DATA

As indicated on page 11 of the July 2000 annual report, we have completely updated the census information which drives the demographics of the breast cancer screening model. The US Census data for the 2000 census was not available until quite recently, but we felt that it was important to include this current data in our manuscripts (in preparation) which summarize the results of this work. The demographic data (specifically, the number of women in the US as a function of 1 year age groups for 5 ethnicities) was downloaded from the US Census Bureau web site on June 27, 2001. This data was incorporated into the most recent breast cancer screening model, which is capable of stochastically reproducing the parent census data. This updated model is being used presently to generate results for our pending publication.

UPDATE OF CANCER EPIDEMIOLOGY DATA

The breast cancer epidemiological data from the most recent version of DEVCAN (version 4.1, downloaded May 9, 2001) was extracted from that program. DEVCAN is a publicly available resource which is maintained by the Statistical Research and Applications Branch of the Division of Cancer Control and Population Sciences, a part of the National Cancer Institute (National Institute of Health). The breast cancer statistical data from that program, which is current as of 1998, was extracted and used to update the cancer incidence model, which is a part of the overall breast cancer screening simulation model.

STATEMENT OF WORK ACCOMPLISHMENTS

Statement of Work 1

As described in the August 2000 annual report, the computer simulation of a variety of mammography related physical properties was conducted in part to better understand the role that these properties play in breast cancer screening (and in the detection of breast cancer). The physics of x-ray detection by the detector system was studied in detail as described in Appendix C: "A Monte Carlo study of x-ray fluorescence in x-ray detectors". Appendix D ("An edge spread technique for measurement of the scatter to primary ratio in mammography") reports our efforts to develop a practical technique for the assessment of scatter in mammography, which is a significant source of contrast loss and can impact breast cancer lesion detection in a profound way. A more comprehensive Monte Carlo assessment of the influence of scatter in mammographic imaging was reported as described in Appendix E, "Scatter/primary in mammography: comprehensive results". These extensive simulations reflect the PI's background in detector physics and have increased our understanding of the mammography screening examination from a physical perspective, which is a requirement of computer modeling the process.

Statement of Work 2

The detectability of breast cancer by mammography as a function of breast cancer lesion diameter and breast density are discussed extensively in the two submitted manuscripts, Appendices A and B. In extensive discussions with Dr. Art Burgess, he has found that the detection of breast cancer in mammography is x-ray dose limited only for lesions 1 mm and

smaller[11]. Our own efforts toward understanding the role that radiation exposure plays in lesion detection in mammography (and elsewhere) was studied and resulted in the article provided as Appendix F, "A lesion detectability simulation method for digital x-ray imaging". We quantified the well known property that increasing the x-ray exposure to the detector increases the detection capabilities of breast cancer, both in terms of soft tissue lesions and microcalcifications. The detriment of increasing the exposure to the detector is realized as additional radiation dose to the glandular tissues of the breast (these are the tissues that are at risk of developing breast cancer). A study was performed to quantify the relationship between incident x-ray exposure and the average glandular dose, and this paper is provided as Appendix G, "Glandular breast dose for monoenergetic and high-energy x-ray beams: Monte Carlo assessment".

In our assessment of the role of breast density on breast cancer detection (Appendix B), we realized that tomographic methods for imaging the breast are the most straightforward way to overcome the substantial limitations that overlapping tissue anatomic noise impose on breast cancer detection. Although somewhat tangential, we studied the radiation dose levels and image quality potential of breast CT using Monte Carlo and experimental methods. These findings (Appendix G: "Dedicated breast CT: Radiation dose and image quality evaluation") are in press. In this paper, we demonstrated that the radiation dose levels of a dedicated breast CT scanner are similar to those experienced in mammography, and this has overturned two decades of dogma concerning the radiation dose in breast CT. We include a description of this effort in this report because it represents a continuum of thought with respect to studying breast cancer screening using computer simulation, and taking these results to the next logical step towards developing novel screening technology. Furthermore, the assessment of breast CT (funded projects) will definitely make use of the breast cancer screening model developed here (beyond the scope of this project).

Statement of Work 3

The breast cancer growth model was developed and reported in the Aug 1999 report, Figures 36-38. Recent breast cancer incidence data was downloaded May 9, 2001 from the DEVCAN program as discussed above. This data will be used to generate the final manuscript, which describes the comprehensive aspects of the breast cancer screening simulator which was developed in this project. These findings will be subjected to peer review with the anticipated manuscript submission in October 2001 (see Reportable Outcomes).

Statement of Work 4

The prognosis model was developed and reported in the Aug 1999 annual report, Figures 39-41. These findings will be subjected to peer review with the anticipated manuscript submission in October 2001 (see Reportable Outcomes).

Statement of Work 5

The population demographics was originally modeled based on extrapolates of the 1990 Census (e.g. Figures 1 & 2 in the Aug 1999 annual report). As described above (section titled "INCLUSION OF THE 2000 CENSUS DATA"), the results of the 2000 Census have been incorporated into the computer simulation model. The 2000 Census data was downloaded from

the US Census Bureau web site on June 27, 2001. These up-to-date input data will be used in the final evaluation and demonstration of the model performance.

Statement of Work 6

The computer simulation breast cancer screening model has been developed. This year we have split the model into two discrete components (computer programs), a cohort generator and the screening simulator. In this way, we can generate a cohort of women (e.g. in certain age groups or with various ethnic distributions mimicking various cities in the US) which is stored to disk. The screening simulation model can then evaluate the various cohorts using different screening paradigms with the intent of both understanding the underlying trends and optimizing the screening procedure for different groups of women.

Statement of Work 7

Validation efforts were described in the previous annual reports, in particular in the Aug 1999 report Figures 42, 43. These and other validations will be presented as part of the peer review manuscript that is in preparation and should be submitted for publication October 2001.

Statement of Work 8

Examples of the use of the breast cancer screening model were given in Aug 1999 Report, Figures 44 through 50. For the production of the culminating peer reviewed manuscript on this project (in preparation, to be submitted October 2001), the newly revised screening model will be used to regenerate these and other outcome data.

Key Research Accomplishments

The primary goal of this research project was to develop and validate a breast cancer screening computer model, and that goal has been realized. We predict that this tool will be useful to ourselves and potentially to other investigators into the future. We also envision that significant embellishments to the computer model will continue to be incorporated, as different modalities are developed for breast cancer screening, and as new information concerning the biology of breast cancer emerges.

One of the primary justifications for the development of a breast cancer screening model (used in writing the grant) was that such a model would be useful for the evaluation of new breast screening procedures, as they are developed. This is true for imaging-based screening technology, or for non-imaging techniques such as serum tests. The only thing that the model "needs to know" to evaluate the potential of a screening test is the probability of cancer detection as a function of the size (or age) of the tumor, and the false positive characteristics of the test. We will be adapting the breast cancer screening model developed in this project to the evaluation of what we feel will be a promising new breast cancer screening modality, breast CT. As mentioned above, the PI has been funded to study and develop a breast CT scanner for a phase II clinical trial. Once a number of breast CT images become available, we will evaluate the potential detection performance of breast CT using the methods developed in this project. Once the detection performance of Breast CT is evaluated, we will incorporate that into the model and then be able to compare the early detection capabilities of breast CT, compared to mammography. We think that the information gleaned from the breast cancer screening simulation model (which performs a clinical trial in the simulation environment) will be highly useful in designing a breast CT clinical trial with real women. Thus, many of the key research accomplishments of this project will take place after the grant period.

Additional accomplishments of this project are demonstrated in the two submitted manuscripts, provided in this report as Appendices A and B. The manuscript of Appendix A, "Determining sensitivity of mammography from the positive biopsy rate, cancer incidence, and ROC curve parameters", submitted to *Medical Decision Making*, shows that known parameters can be used to assess the operating point where mammographer's operate on their ROC curve in a clinical environment. This allows researchers to more accurately predict the sensitivity (and specificity) of mammography, when the ROC curve has been measured. We note that this overcomes a significant obstacle of the ROC methodology.

It has been known for a long time that women with dense breasts suffer from reduced utility of the mammography examination. In Appendix B, the manuscript "The effect of breast density of cancer detection performance in mammography", submitted to *The Journal of Women's Imaging*, the influence that breast density has on lesion detection performance has been quantitatively documented. The straightforward analysis of these results allows practitioners (mammographers) to fully appreciate the large influence in sensitivity that breast density has. In future analyses, the quantitative results of this work may be valuable in triaging women for screening examinations in a manner that optimizes the chance of cancer detection on a women-by-women basis. For example, women with dense breasts may be best served using breast CT or

mammographic tomosynthesis, while women with adipose breast may be best screened using traditional mammography.

Breast cancer detection in mammography was studied in depth using computer simulation techniques. Appendix C described our assessment of the impact that x-ray fluorescence has on the detection efficiency and noise. Scattered radiation is a well known source of noise in digital imaging system and is a source of contrast reduction in screen-film mammography. In this investigation, we quantified the scatter-like effect that fluorescent radiation has in mammographic and other imaging systems.

Much of the computer simulation work performed in this project involves the assessment of secondary radiation (scatter and fluorescence). In order to verify the accuracy of the simulation efforts, it was necessary to make physical measurements of scatter and compare these with the results of our computer simulations. Appendix D describes this effort, and introduces an edge spread approach towards characterizing the scatter to primary ratio in mammographic imaging.

Appendix E represents a comprehensive evaluation of the influence of scattered radiation in mammography. The parameters studied include x-ray energy, field of view, breast thickness, location in the field, the distance between the breast and the detector (the air gap), and the width of the slot for scanning slot mammography systems (Fischer's digital mammography system). Scatter has a profound effect in reducing contrast and increasing noise, and therefore our understanding of the magnitude of scatter as a function of various other parameters is important in generalizing the computer simulation of breast cancer screening.

Lesion detectability was evaluated as described in Appendix F. The influences of the x-ray exposure levels, the size of the lesion, the size of the pixel array (for digital imaging systems), and the type of lesion (soft tissue or calcific) were studied. Independent of issues of breast density (evaluated elsewhere), this investigation allowed us to assess the ROC metrics (area under the ROC curve, the so-called A_z value) for mammography in the best case scenario, where the breast parenchyma is perfectly homogeneous (like a completely adipose breast). The A_z values reported in this Appendix can be converted to probability of detection using the techniques described in Appendix A.

Radiation dose to the breast is an important issue in mammography. Our current computer simulation model does not account for radiation induced breast cancers (nor was it planned to), mostly because the information on radiogenic breast cancers is sparse to nonexistent. In terms of mammographic screening from a scientific basis (not a financial one), optimal screening frequencies will always be forced to shorter time periods (e.g. screen every day) because there is no parameter which forces the optimal screening period towards longer times (other than cost issues). However, radiation dose limitations are a scientific consideration which drive optimal screening frequencies towards longer time frames. To achieve a better understanding of the radiation dose in mammographic screening as a function of a variety of physical parameters (breast size, x-ray spectrum, etc.), the work summarized in Appendix G was performed. This article was the lead article in *Radiology* for Oct 1999.

Our work on this project in developing a screening simulation model led naturally to the notion of screening using tomographic techniques. Appendix H is a paper that has been accepted for publication in *Radiology* which describes our computer simulation of the radiation dose levels appropriate for dedicated breast CT screening. As mentioned elsewhere, the assessment of the breast CT scanner will benefit significantly from the analytical techniques that have been developed in this project.

The focus of this research has intentionally been on the scientific aspects of breast cancer screening, mostly on the computer modeling of breast cancer detection by screening and on the evaluation of screening protocols. However, the metrics that are generated by the breast cancer screening model will also allow a comprehensive approach to estimating the cost effectiveness of various screening strategies. Fiscal realities dictate screening policies at the national level, and it is our intention to extend this investigation to the evaluation of cost effective screening protocols. The evaluation of cost effectiveness was not a specific task of the grant, however may become a significant outcome of the screening simulator that was developed under the grant. By assigning costs to the screening procedures, to biopsy and therapeutic treatment, the cost (in dollars) per year of life saved can be estimated using the breast cancer screening model. Co-investigator Dr. Lindfors has performed cost effectiveness analysis in the past[12;13]. This metric (cost per year of life saved) has become a *de facto* parameter in the assessment of medical procedures, and it allows breast cancer screening to be assessed against other medical procedures such as cardiac bypass operations. The cost effectiveness analysis will be performed before the end of the year 2001, and any manuscripts produced will be forwarded to the BCRP as an addenda to this final report.

Reportable Outcomes

Outcomes from Year 1 Annual Report:

Abstract

- JM Boone and KK Lindfors, "Computer simulation of breast cancer screening efficacy", Medical Physics 26: 1065-1066 (1999)

Invited Presentation

- JM Boone and KK Lindfors, "Computer simulation of breast cancer screening efficacy", presented at the 1999 annual meeting of the American Association of Physicists in Medicine, Nashville, TN (July 26, 1999).

Outcomes from Year 2 Annual Report:

Published Papers citing this grant

- JM Boone, JA Seibert, JM Sabol, and M Tecotzky, "A Monte Carlo study of x-ray fluorescence in x-ray detectors", Medical Physics 26, 905-916 (1999)
- JM Boone, "Glandular breast dose for monoenergetic and high-energy x-ray beams: Monte Carlo assessment", Radiology 213, 23-37 (1999)
- VN Cooper, JM Boone, and JA Seibert, "A lesion detectability simulation method for digital x-ray imaging", Medical Physics 27;66-74 (2000)
- VN Cooper, JM Boone, and JA Seibert, C Pellot-Barakat, "An edge spread technique for measurement of the scatter to primary ratio in mammography", Medical Physics 27: 845-853 (2000)

Outcomes from Year 3 Final Report:

Grants Applied For

An NIH grant was written in the hopes of extending this research (R01 CA86891-01), however the grant after two submissions has not been funded. We have discussed the reasons for this with the NIH administrator, and his observation is that the grant has too much physics to be reviewed by an epidemiology study section, and too much epidemiology to be reviewed by a Radiology study section. His recommendation was to split the grant into two components, something that we are unwilling to do.

Published Papers citing this grant

- JM Boone, KK Lindfors, VN Cooper III and JA Seibert, "Scatter/primary in mammography: comprehensive results", Medical Physics 27: 2408-2416 (2000)

In Press Papers that cite this grant

- JM Boone, TR Nelson, KK Lindfors, and JA Seibert, "Dedicated breast CT: Radiation dose and image quality evaluation", Radiology 2001 (*in press*)

Manuscripts Submitted for Publication

- JM Boone, KK Lindfors, JA Seibert, "Determining sensitivity of mammography from the positive biopsy rate, cancer incidence, and ROC curve parameters", Medical Decision Making, 2001 (second revision submitted April 30, 2001)
- JM Boone and KK Lindfors, "The effect of breast density of cancer detection performance in mammography", Journal of Women's Imaging, (submitted May 15, 2001)

Manuscripts in Preparation

JM Boone and KK Lindfors, "Computer simulation of breast cancer screening", to be submitted to Radiology 2001 *Note:* This manuscript will report the comprehensive results stemming from the development of the breast cancer screening model, as described in this and the past annual reports. We have delayed the submission of the manuscript until the new 2000 Census data was available and incorporated into the model, so that the results reflect current population trends.

Future Reportable Outcomes

The completion of the research in this BCRP grant represents the end of one phase of this overall project, and the beginning of another. With the tools developed, there will be subsequent analyses which make use of these tools with the focus on optimizing digital mammography. The PI has embarked on another major research effort in the area of breast cancer screening, the development and assessment of a CT scanner for breast cancer screening. The breast CT project has been funded by the California BCRP and by the NIH. Once a number of breast CT images are acquired using the breast scanner, an extensive comparison will be made between digital mammography and breast CT using the computer simulation model developed here. The PI will submit all papers which have been spawned by the development of the breast cancer screening simulation methods as addenda to this final report, when they become available. This grant has focused on the development of the simulation techniques; however these techniques will be put to immediate (i.e. 2002-2003) usage as we explore the potential of a new modality in terms of its potential for the early detection of breast cancer.

Personnel:

Investigators who were supported by this project include:

John M. Boone, Ph.D. (principal investigator)

Karen K. Lindfors, MPH, M.D. (co-investigator)

Mary Haan, Ph.D. (co-investigator)

Virgil N. Cooper, Ph.D. (post-doctoral fellow)

Este Bailey, B.S. (medical student)

Conclusions

This three year research project has led to the development of a comprehensive computer simulation tool for studying the effectiveness of various breast cancer screening protocols. The development of this computer model differs from previous approaches because it incorporates the time-dependent behavior of breast cancer (i.e. growth). Furthermore, the computer simulation model developed in this work determines the probability of breast cancer detection based on computer observer models which are applied to actual (normal) image data sets (using simulated breast cancer lesions). This approach allows a more objective evaluation of the potential of various imaging procedures, because very large numbers of lesions and images can be studied to build up a solid statistical understanding of the sensitivity versus lesion diameter. While human observer performance data could easily be incorporated into the model, the manpower constraints of such studies limit their statistical utility and overall value. An additional benefit of this approach is that alternative imaging techniques for breast cancer detection can be studied by collection of a set of normal images. We will be studying this shortly in our evaluation of the potential of breast cancer screening using a dedicated breast CT scanner.

While the goals of the current grant have been met, we are hopeful that the breast cancer screening model developed in this project will prove useful for the assessment and comparison of breast cancer screening procedures for many years into the future.

References

- (1) Michaelson JS, Halpern E, Kopans DB. Breast cancer: computer simulation method for estimating optimal intervals for screening. *Radiology* 1999; 212:551-560.
- (2) Jansen JT, Zoetelief J. Assessment of lifetime gained as a result of mammographic breast cancer screening using a computer model. *Br J Radiol* 1997; 70:619-628.
- (3) Jansen JT, Zoetelief J. Optimisation of mammographic breast cancer screening using a computer simulation model. *Eur J Radiol* 1997; 24:137-144.
- (4) Dowsett M. Improved prognosis for biomarkers in breast cancer. *Lancet* 1998; 351:1753-1754.
- (5) Benz CC. Biomarkers for breast cancer. *West J Med* 1996; 164:164.
- (6) Kavanagh AM, Giles GG, Mitchell H, Cawson JN. The sensitivity, specificity, and positive predictive value of screening mammography and symptomatic status. *J Med Screen* 2000 ;7 (2):105 -10 2000; 7:105-110.
- (7) Warren Burhenne LJ, Wood SA, D'Orsi CJ, Feig SA, Kopans DB, O'Shaughnessy KF, Sickles EA, Tabar L, Vyborny CJ, Castellino RA. Potential contribution of computer-aided detection to the sensitivity of screening mammography. *Radiology* 2000 May ;215 (2):554 -62 2000; 215:554-562.
- (8) Duffy SW, Chen HH, Tabar L, Fagerberg G, Paci E. Sojourn time, sensitivity and positive predictive value of mammography screening for breast cancer in women aged 40-49. *Int J Epidemiol* 1996; 25:1139-1145.
- (9) Kerlikowske K, Grady D, Barclay J, Sickles EA, Ernster V. Effect of age, breast density, and family history on the sensitivity of first screening mammography [see comments]. *JAMA* 1996; 276:33-38.
- (10) Feig SA. Strategies for improving sensitivity of screening mammography for women aged 40 to 49 years [editorial; comment]. *JAMA* 1996; 276:73-74.
- (11) Burgess AE. Visual signal detection with two-component noise: low-pass spectrum effects. *J Opt Soc Am A Opt Image Sci Vis* 1999; 16:694-704.
- (12) Rosenquist CJ, Lindfors KK. Screening mammography beginning at age 40 years: a reappraisal of cost-effectiveness. *Cancer* 1998; 82:2235-2240.
- (13) Lindfors KK, Rosenquist CJ. The cost-effectiveness of mammographic screening strategies. *JAMA* 1995; 274:881-884.

Appendices

Appendix A:

JM Boone, KK Lindfors, JA Seibert, "Determining sensitivity of mammography from the positive biopsy rate, cancer incidence, and ROC curve parameters", Medical Decision Making, 2001 (second revision submitted April 30, 2001)

Appendix B:

JM Boone and KK Lindfors, "The effect of breast density of cancer detection performance in mammography", Journal of Women's Imaging, (submitted May 15, 2001)

Appendix C:

JM Boone, JA Seibert, JM Sabol, and M Tecotzky, "A Monte Carlo study of x-ray fluorescence in x-ray detectors", Medical Physics 26, 905-916 (1999)

Appendix D:

VN Cooper, JM Boone, and JA Seibert, C Pellot-Barakat, "An edge spread technique for measurement of the scatter to primary ratio in mammography", Medical Physics 27: 845-853 (2000)

Appendix E:

JM Boone, KK Lindfors, VN Cooper III and JA Seibert, "Scatter/primary in mammography: comprehensive results", Medical Physics 27: 2408-2416 (2000)

Appendix F:

VN Cooper, JM Boone, and JA Seibert, "A lesion detectability simulation method for digital x-ray imaging", Medical Physics 27;66-74 (2000)

Appendix G:

JM Boone, "Glandular breast dose for monoenergetic and high-energy x-ray beams: Monte Carlo assessment", Radiology 213, 23-37 (1999)

Appendix H:

JM Boone, TR Nelson, KK Lindfors, and JA Seibert, "Dedicated breast CT: Radiation dose and image quality evaluation", Radiology 2001 (*in press*)

DAMD17-98-18176, Final Report - August 2001

Computer Simulation of Breast Cancer Screening

PI: John M. Boone, Ph.D.

Appendix A:

JM Boone, KK Lindfors, JA Seibert, "Determining sensitivity of mammography from the positive biopsy rate, cancer incidence, and ROC curve parameters", Medical Decision Making, 2001 (second revision submitted April 30, 2001)

Determining sensitivity of mammography from the positive biopsy rate, cancer incidence, and ROC curve parameters

John M. Boone, Ph.D.
Karen K. Lindfors, M.D.
J. Anthony Seibert, Ph.D.

Department of Radiology
University of California – Davis
Sacramento, California 95817

ADDRESS FOR CORRESPONDENCE:

John M. Boone, Ph.D.
Department of Radiology
UC Davis Medical Center
4701 X Street, Research Imaging Center
Sacramento, CA 95817
(916) 734-3158 (Voice & Voice Mail)
(916) 734-0316 (FAX)
jmboone@ucdavis.edu

Manuscript: ppv_12.doc

Reference Database: PPV1

Running Title: Mammography sensitivity from the ROC curve and positive biopsy rate

This research was supported in part by grants from the US Army Breast Cancer Research Program (DAMD17-98-1-8176 and DAMD17-94-J-4424).

Abstract

Objectives: A mathematical model is presented which allows the computation of the sensitivity and specificity of breast screening based on ROC curve shape, the positive biopsy rate, and the cancer incidence, f . **Methods:** The normal and cancer populations are modeled as normal distributions with independent means and standard deviations. The distributions are normalized such that the area of the normal population is equal to $1-f$, and that of the cancer population is f . The positive biopsy rate (or positive predictive value, PPV) for breast biopsy is used to determine the operating point on the ROC curve. Knowing this leads directly to the computation of sensitivity and specificity. The derivation is general and is applicable to both symmetrical and asymmetrical ROC curves. **Results:** For symmetric ROC curves and typical values for the positive biopsy rate (30%) and cancer incidence ($f=0.003$), an A_z value of 0.95 was required to achieve 30% sensitivity, and an A_z of 0.98 was required to deliver 60% sensitivity. **Conclusions:** A model was developed which should allow researchers to deduce sensitivity and specificity for screening mammography based on ROC curve measurements. This model allows A_z values to be related to the probability of breast cancer detection.

KEY WORDS:

Breast cancer, mammography, positive predictive value, sensitivity, specificity, ROC curves, positive biopsy rates, cancer detection rates, screening.

Introduction

Mammographic screening is an essential component of breast cancer control. Despite the crucial role that mammography plays, the determination of its sensitivity and specificity is difficult[1;2]. The determination of sensitivity requires quantifying the number of true positive and false negative cases. Assessment of the number of true positive cases is relatively easy, since their outcome is determined by histopathology analysis which is considered a gold standard. False negatives, however, are not subject to independent analysis, and the number of negative cases that pass through the mammography clinic is large, making this a harder group to track[1]. Nevertheless, determining sensitivity is invaluable in the comparison of mammography with other breast cancer screening procedures[3-5].

There are a number of reports in the literature in which the receiver operating characteristic (ROC) curve has been measured for radiologists performing mammography[6-11]. ROC curve analysis is often used as an analysis tool in comparing two diagnostic techniques, and the area under the ROC curve (called A_z) is a useful parameter that is related to lesion detectability. While A_z is a useful parameter for many applications, the ROC curve itself does not allow the *probability* of detecting a lesion to be predicted. The ROC curve is a plot of sensitivity as a function of [1-specificity], however in the clinical diagnostic setting, a radiologist routinely performs near a fixed point on the ROC curve, at the so-called *operating point*. Traditional ROC analysis does not allow the determination of the operating point.

In this work, signal detection theory (which is the basis of the ROC methodology) is exploited in a manner which allows the identification of the operating point on a known ROC curve, when the positive biopsy rate and fraction of breast cancers in the screening population are known. The positive biopsy rate (or positive predictive value, PPV) in breast screening [12] is constrained by the norms of clinical practice (such that $15\% \leq \text{PPV} \leq 35\%$, approximately), and the average age-specific breast cancer incidence in the United States is well established [13], and thus the proposed method allows the estimation of the operating point for clinical mammography when the ROC curve is known. When the operating point is known for a specific ROC curve, the clinically relevant values of sensitivity and specificity can be easily determined.

The mathematical model developed here requires three input variables for symmetrical ROC curves: the area under the ROC curve (A_z), the PPV, and the cancer incidence in the screening

population. Asymmetrical ROC curves require an additional shape parameter to characterize the ROC curve asymmetry.

Methods

MATHEMATICAL PRELIMINARIES

Figure 1A illustrates two normal curves, where $C(\xi)$ corresponds to the population with cancer and $N(\xi)$ corresponds to the normal (non-cancer) population. The $N(\xi)$ distribution has a mean of \bar{N} and standard deviation σ_N , and the $C(\xi)$ distribution has a mean of \bar{C} and standard deviation σ_C . The decision parameter, ξ , is some quantifiable entity that allows the observer to make a decision concerning a diagnosis. For most radiologist-interpreted images, including mammograms, ξ corresponds to the radiologist's impression which is dependent upon a number of factors, including the assessment of the pertinent anatomy and pathology visible on the mammogram, and other patient information such as the patient's age, family history, hormone replacement status, etc. The decision parameter ξ may be considered as the radiologist's *gestalt*. There are many applications where digital mammograms are analyzed by a computer, and in these cases the value of ξ may be the numerical output of a computer aided diagnostic algorithm.

When the cancer population $C(\xi)$ and the normal population $N(\xi)$ are represented as individual normal distributions with separate means (\bar{C} and \bar{N}) and standard deviations (σ_C and σ_N), the signal to noise ratio (SNR) is given by:

$$SNR = \frac{\bar{C} - \bar{N}}{\sqrt{\sigma_N^2 + \sigma_C^2}} \quad \text{Eq. 1}$$

A decision threshold is illustrated in Figure 1A as the vertical line marked τ , and all patients with a value of ξ to the right of τ are considered by the diagnostician as having cancer, and all patients to the left of τ are considered normal. As indicated in Figure 1A, patients in $C(\xi)$ to the right of τ are correctly diagnosed and are true positives (TP: hatched area), and the cancer population to the left of τ are false negatives (FN: dark shaded area). The normal population to the left of τ are true negatives (TN), and those to the right of τ are false positives (FP). Mathematically, these terms can be defined as:

$$TN(\tau) = \int_{-\infty}^{\tau} N(\xi) d\xi \quad \text{Eq. 2}$$

$$FP(\tau) = \int_{\tau}^{\infty} N(\xi) d\xi \quad \text{Eq. 3}$$

$$FN(\tau) = \int_{-\infty}^{\tau} C(\xi) d\xi \quad \text{Eq. 4}$$

$$TP(\tau) = \int_{\tau}^{\infty} C(\xi) d\xi \quad \text{Eq. 5}$$

The sensitivity of breast cancer screening is the probability of cancer detection using that modality. The sensitivity depends on the selection of the threshold value τ :

$$\text{sensitivity}(\tau) = \frac{TP(\tau)}{TP(\tau) + FN(\tau)} \quad \text{Eq. 6}$$

The specificity of a medical test is the fraction of all normal patients who are diagnosed as such:

$$\text{specificity}(\tau) = \frac{TN(\tau)}{TN(\tau) + FP(\tau)} \quad \text{Eq. 7}$$

The receiver operating characteristic (ROC) curve is a plot of the sensitivity(τ) (or true positive fraction) as a function of (1-specificity(τ)) (or false positive fraction), as shown in Figure 1B. Each point on the ROC curve corresponds to a pair of coordinates (x, y), where $x = 1\text{-specificity}(\tau)$, and $y = \text{sensitivity}(\tau)$. Each point on the ROC curve depends on the specific value of τ , and different points on the ROC curve are produced by varying τ and plotting the pairs of points ([1-specificity],sensitivity).

It is typical in the ROC literature applied to radiology to define the individual distributions $C(\xi)$ and $N(\xi)$ such that they are each normalized to unity, however this is not a requirement of ROC analysis but rather is due to the fact that the relative areas of $C(\xi)$ and $N(\xi)$ are not necessary to the analysis. In

order to normalize the $C(\xi)$ and $N(\xi)$ distributions to take into consideration the incidence f of cancer in the study population, we define:

$$1 = \int_{-\infty}^{\infty} (C(\xi) + N(\xi)) d\xi, \quad \text{Eq. 8}$$

where:

$$f = \int_{-\infty}^{\infty} C(\xi) d\xi \quad \text{Eq. 9}$$

and thus:

$$1 - f = \int_{-\infty}^{\infty} N(\xi) d\xi \quad \text{Eq. 10}$$

BINORMAL ROC CURVES

Previous investigators[14;15] have noted that the binormal assumption (Figure 1A) for ROC curves is consistent with measured data under the vast majority of clinical conditions. ROC curves can be generated analytically when the two normal distributions $C(\xi)$ and $N(\xi)$ are exactly known. The parameters necessary to completely define these distributions are the means (\bar{C} and \bar{N}), standard deviations (σ_C and σ_N), and the fraction of cancer cases f . Since horizontal scale factors in the distributions $C(\xi)$ and $N(\xi)$ do not affect the shape of the ROC curve, we can set $\bar{N} = 0$, $\sigma_N = 1$, and define a parameter k which is the ratio of the standard deviations of the two normal distributions, such that:

$$k = \frac{\sigma_C}{\sigma_N} \quad \text{Eq. 11}$$

With this simplification, the shape of the distributions shown in Figure 1A is defined by three parameters: f , SNR and k . According to the classic work of Rose[16], if the $\text{SNR} > 5.0$ (the “*Rose Criterion*”), then an object such as a breast lesion will almost certainly be detectable, i.e. the area under

the ROC curve approaches unity. While the parameters SNR and k can be used to exactly compute an ROC curve, in general these parameters can not be derived directly from an ROC curve. However, the relationship between A_z and the SNR is independent of the value of k . Thus, the ROC curve area A_z can be used to accurately determine the SNR (Table 1). For obviously asymmetrical ROC curves, curve fitting the ROC empirical data to the analytical ROC curves (e.g. Figure 1B) to determine the most appropriate values for k would be necessary. A simple least squares fit to sensitivity for each specificity values over all pairs of points available should be sufficient to accurately model an experimentally derived ROC curve in terms of the parameters SNR and k .

BIOPSY RATES IN MAMMOGRAPHY

When a radiologist, based on screening mammograms and other ancillary information, views, or studies, (screening mammography, when combined with comprehensive subsequent tests is called *diagnostic mammography*) recommends a breast biopsy, he or she is stating that there is a reasonable chance that the patient has breast cancer. Essentially, biopsied patients are those which fall on the right side of the radiologist's threshold value (τ in Figure 1A). Biopsy results are considered the gold standard, and those patients who come back with positive biopsies represent the true positive population. Therefore, the positive biopsy rate is equal to the positive predictive value (PPV) of diagnostic mammography. Like the sensitivity and specificity defined about, the $PPV(\tau)$ is dependent upon the threshold value τ :

$$PPV(\tau) = \frac{TP(\tau)}{TP(\tau) + FP(\tau)} \quad \text{Eq. 12}$$

As mentioned previously, the PPV is *dependent* upon the fraction of disease in the total population, and therefore is dependent upon f in Eqs. 9 and 10. The cancer detection rate is a straightforward proxy for incidence, and is typically expressed in the units of *cancers detected per 1000 screens*. For breast screening, the cancer detection rate typically ranges from around 2 to upwards of 6 cancers detected per 1000 screens[12;17;18], depending upon the age group and previous screening history of the population being screened. The incidence of breast cancer in the United States is about 1.0, 2.8, 3.8, and 4.8 cancers per 1000 women for women ages 40, 50, 60, and 70, respectively[13].

Typical published values[12] for the positive biopsy rate range from approximately 15% to 35%. Mammographers are essentially obligated to operate close to this range from a medical-legal standpoint, as this range currently defines normal practice. Achieving a positive biopsy rate lower than 15% implies that the mammographer is an over-caller, while a biopsy rate greater than about 35% implies that the radiologist is an under-caller. The $PPV(\tau)$ can be computed from the parameters SNR, k , and f . For symmetric ROC curves (where $k=1$), only A_z and f are needed since the relationship between A_z and SNR is well known (Table 1). Thus, when the PPV is known or can be assumed to fall within a typical range of 20 to 25%, the value of τ can be calculated. The value of τ is solved iteratively, by varying it until the $PPV(\tau)$ (Eq. 12) is equal to the known PPV value.

ROC CURVES AND SENSITIVITY

There is an interest on the part of many [19-26] in estimating the sensitivity of mammography. While methods are available to assess the ROC curves of mammographers under mammography conditions [27-30], the ROC curve by itself cannot be used to estimate sensitivity and specificity[31]. Put differently, the ROC curve allows A_z (and k , if $\sigma_N \neq \sigma_C$) to be computed, but it is not generally straightforward to deduce the point on the ROC curve where the mammographer actually operates. The A_z performance of radiologists[7;9;10] and computer aids[6;8-11] have been reported frequently in the literature. The contribution of the present work is to introduce a technique in which the operating point on the ROC curve where the mammographer actually functions can be determined. The ROC curve is a plot of the τ -dependence of the sensitivity and specificity. Therefore, knowledge of the ROC curve (i.e. SNR and k) combined with the radiologist's operating point leads directly to the computation of sensitivity (Eq. 6) and specificity (Eq. 7).

DETAILS

The normalized distribution of patients without cancer, $N(\xi)$, is given by:

$$N(\xi) = \frac{1-f}{\sigma_N \sqrt{2\pi}} e^{-\frac{1}{2} \left(\frac{\xi - \bar{N}}{\sigma_N} \right)^2} \quad \text{Eq. 13}$$

Similarly, the cancer distribution is given by:

$$C(\xi) = \frac{f}{\sigma_C \sqrt{2\pi}} e^{-\frac{1}{2} \left(\frac{\xi - \bar{C}}{\sigma_C} \right)^2} \quad \text{Eq. 14}$$

The solution of Eqs. 2 through 4 are based on the integral of the normal distribution function with mean m and standard deviation σ [32]:

$$\frac{1}{\sigma \sqrt{2\pi}} \int_{-\infty}^x e^{-\frac{1}{2} \left(\frac{t-m}{\sigma} \right)^2} dt = \frac{1}{2} \left(1 + \text{ERF} \left[\frac{x-m}{\sigma \sqrt{2}} \right] \right) \quad \text{Eq. 15}$$

Setting $\bar{N} = 0$ and $\sigma_N = 1$ as before, coupled with equation 11, yields:

$$\bar{C} = \text{SNR} \sqrt{1 + k^2} \quad \text{Eq. 16a}$$

and

$$\sigma_C = k \quad \text{Eq. 16b}$$

Given Eqs. 13, 15, and 16, the solution to Equation 2 is:

$$TN(\tau) = \left(\frac{1-f}{2} \right) \left(1 + \text{ERF}(\alpha) \right) \quad \text{Eq. 17}$$

and since $TN + FP = (1-f)$, Eq. 3 becomes:

$$FP(\tau) = \left(\frac{1-f}{2} \right) (1 - ERF(\alpha)) \quad \text{Eq. 18}$$

where $\alpha = \frac{\tau}{\sqrt{2}}$.

The solutions to Eqs. 4 and 5 are:

$$FN(\tau) = \left(\frac{f}{2} \right) (1 + ERF(\beta)), \quad \text{Eq. 19}$$

and

$$TP(\tau) = \left(\frac{f}{2} \right) (1 - ERF(\beta)), \quad \text{Eq. 20}$$

respectively, where $\beta = \frac{\tau - SNR\sqrt{1 + k^2}}{k\sqrt{2}}$.

With the values of TP, TN, FP, and FN defined in Eqs. 17-20, the sensitivity from Eq. 6 can be expressed as:

$$sensitivity(\tau) = \frac{1 - ERF(\beta)}{2}. \quad \text{Eq. 21}$$

The specificity from Eq. 7 can be rewritten as:

$$specificity(\tau) = \frac{1 + ERF(\alpha)}{2}. \quad \text{Eq. 22}$$

It is noted that the dependency on f drops out of Eqs. 21 and 22, giving mathematical verification that sensitivity and specificity (and ROC curves which are a function of these two parameters) are independent of incidence.

The positive predictive value (Eq. 12) becomes:

$$PPV(\tau) = \frac{f (1 - ERF(\beta))}{1 + (1-f) ERF(\alpha) - f ERF(\beta)} \quad \text{Eq. 23}$$

The incidence f cannot be eliminated from Eq. 23, and thus the PPV is dependent upon the incidence of the disease of interest.

The steps necessary to identify the operating point on an ROC curve (and thus sensitivity and specificity) are enumerated below:

- (1) An ROC curve for breast screening is identified or measured, and is used to determine the parameters SNR and k . The area of the ROC curve (A_z) should be calculated. The A_z versus SNR values given in Table 1 can be used to identify the SNR, and these values are independent of k . If the ROC is symmetric along the upper left to lower right axis, as most are, then $k=1$. If it is asymmetric, then the known ROC curve can be fit using least squares techniques using Equations 21 and 22 to determine the parameter k .
- (2) Appropriate values for the PPV and cancer detection rate f should be identified. We have discussed typical values for these parameters elsewhere in this work, but if specific values are known for a given screening population, then those values could be used.
- (3) Equation 23 relates PPV, f , SNR, k and τ . Step 1 was used to define SNR and k , and step 2 was used to define PPV and f . Iterative solution techniques can then be used to solve for τ in Eq. 23 (which appears in the α and β terms).
- (4) Once τ is defined in Step 3, the sensitivity can be computed using Eq. 21 and the specificity can be calculated using Eq. 22 using the determined value of τ . This pair of coordinates defines the sensitivity and (1-specificity) point on the ROC curve, corresponding to the operating point.

The above equations were evaluated using programs written in C using the Microsoft C/C++ 5.0 compiler, and additional evaluations were performed using Microsoft Excel (Microsoft Corporation, Redmond, WA). A personal computer incorporating a 1.1 GHz Athlon CPU chip was used with the Microsoft Windows 2000 operating system for the computer workstation.

Results

Figure 2A illustrates the trend in sensitivity as a function of A_z value, for symmetrical ROC curves ($k=1$) and a typical PPV for breast biopsy of 30%. A family of curves is shown, corresponding to different cancer incidence f in the screening population. The value of f ranges in the figure from $f=0.001$ to $f=0.009$, which spans the cancer detection rate in most screening populations in the United States. It is seen that higher cancer incidence in the screening population leads to better sensitivity at a given A_z .

Figure 2B illustrates sensitivity versus A_z for symmetrical ROC curves ($k=1$) and a cancer incidence of $f=0.003$ (3 cancers detected per 1000 screens). A family of curves illustrates the effect of the PPV on sensitivity: Decreasing the PPV increases sensitivity, which is to be expected because a reduced PPV implies a more aggressive diagnostician. A PPV of 0.10 implies that for every ten women biopsied, only one has cancer. PPV values up to 0.5 are shown.

Table 1 gives the relationship between SNR and A_z for ROC curves. This relationship is independent of the value of k . The table was generated using Eqs. 13 through 22, and can be used to relate A_z to the SNR.

Discussion

Reported values for radiologist A_z performance in screening mammography vary widely, with reports of A_z values of 0.61[10], $A_z = 0.81$ [8], $A_z = 0.83$ [9] to $A_z = 0.94$ [7]. The variability is likely due to differences in radiologist performance[25] and variation in the degree of diagnostic difficulty of the databases used for testing[33]. Even the best A_z value mentioned above, however, corresponds to abysmally low sensitivity as seen on Figure 2A. For $A_z = 0.94$, with $f = 0.003$ and $PPV = 0.30$, the sensitivity is $\sim 23\%$. There are two considerations which contribute to this artifactually low sensitivity: case mix and cancer case enrichment.

Case Mix: If ROC curves measured in the research setting are intended to be used to measure clinical sensitivity, then the case mix used needs to reflect that of the clinical environment. ROC studies are usually used to study the difference between two diagnostic methods, and this can be best performed by selecting substantially more difficult cases. This is because differences in A_z are more readily seen when $SNR \approx 1$, than when $SNR \geq 3$, and thus a more difficult case set will provide more discrimination between the two techniques compared. Consequently, most ROC studies make use of data sets comprised solely of difficult cases, and thus the A_z values are substantially lower than that which would be typical of the clinical environment. The A_z values and resulting calculated sensitivities determined in ROC studies should therefore define the lower bounds of screening sensitivity that would be achieved using a clinical case mix.

Cancer Case Enrichment: The other factor which reduces the validity of extrapolation of ROC study results to the clinical mammography environment is that ROC studies almost always make use of so-called *enriched* data sets, where the cancer incidence is far greater than that seen clinically. For example, many ROC data sets are comprised of 50% cancers cases as opposed to the $\sim 0.3\%$ seen clinically. The theoretical basis for extrapolating ROC results measured at one incidence to a substantially different incidence is uncertain. Although sensitivity and specificity are independent of incidence (f does not occur in Eqs. 21 or 22), the highly enriched data bases used in ROC studies will likely distort the threshold value τ used by the radiologist, and sensitivity and specificity both depend on τ . A straightforward approach for adjusting for the amplified cancer incidence in ROC studies using the methods discussed here is to use the cancer incidence (f) of the ROC data set to determine sensitivity. For example, for $PPV = 0.30$ and $A_z = 0.94$, incidences of 1%, 5%, and 10% yield sensitivities of 47%,

82%, and 93%, respectively. This observation is made to simulate discussion on the issue of how the enrichment factor affects ROC results.

Typically, about one in three biopsies ($PPV = 0.33$) to one in five biopsies ($PPV = 0.20$) yields an actual breast cancer. The low positive biopsy rate resulting from breast cancer screening using mammography is often cited as a weakness of mammographic screening. As evident in Figure 2B, however, low positive biopsy rates are *theoretically necessary* for achieving higher levels of sensitivity, *given the overlap in appearance between normal and cancer-containing mammograms*. The biopsy of women who do not have breast cancer, in effect, leads to better detection rates for women who do. This can be referred to as the *biopsy conundrum*. The low positive predictive value of mammography is necessary to achieve adequate detection of breast cancer at its earliest stage. This conundrum can be mitigated by the development of a diagnostic test which has a higher SNR for breast cancer than mammography, a goal many are striving for. Alternately, if a diagnostic test intermediate between mammography and breast biopsy were developed which had better sensitivity with high specificity, low morbidity, and low cost compared to current tests (e.g. magnification mammography, ultrasound, spot compression, etc.), it may play a role in alleviating the biopsy conundrum.

Radiologists substantially alter their operating point when participating in ROC studies. The discrete and continuous scales[34-39] associated with ROC analysis explicitly require the radiologist to adjust his or her operating point – this is necessary to determine the several points (1-specificity, sensitivity) that are used to estimate the ROC curve. In clinical practice, a radiologist either refers the patient for biopsy or does not, and the decision threshold applied to make this decision corresponds to only one point on the ROC curve, the operating point. Measuring a radiologist's ROC curve therefore does not identify the operating point.

Clinical mammography is not practiced as a research study, and the absence of painstaking follow-up procedures to determine "truth" means that radiologists do not receive direct feedback in terms of their sensitivity or specificity performance. Indeed, for missed cancers (false negatives), time is needed for the tumor to grow large enough to be noticed on the subsequent film, thereby allowing retrospective realization that a cancer was present (this is the only practical way of determining false negatives in a research study of screening mammography). In the absence of feedback concerning sensitivity and specificity, the positive biopsy rate (i.e. the PPV) can be used as an alternative measure of the operating point at which the radiologist operates. Indeed, each radiologist is required to monitor their positive biopsy rate by MQSA. The monitoring of positive biopsy rates in mammography provides

feedback and imposes a degree of self-normalization on mammographers, which likely helps to maintain a more uniform decision threshold (operating point on the ROC curve) between radiologists.

Since the sensitivity of mammography improves as a function of lesion diameter (in general), the determination of sensitivity for mammography is dependent upon the screening history of the study population. Thus, the mean sensitivity is averaged over the range of lesion diameters that are experienced in a specific screening population. An effective cancer screening program acts to drive sensitivity down over time, since the lesion diameters discovered are smaller (reducing sensitivity in mammography) in a previously screened population.

ROC studies usually employ only screening mammograms. In clinical screening, however, when an abnormality is seen on an image, subsequent diagnostic tests (e.g. additional mammographic views, spot compression, ultrasound) are often utilized to increase diagnostic confidence. These additional tests undoubtedly improve the diagnostic performance of a given radiologist, typically by reducing false positives. Most ROC experiments are not designed to assess this.

Despite the above mentioned limitations, ROC curve performance metrics can be useful for estimating sensitivity in breast cancer diagnosis, based on reasonably sound assumption of the PPV and cancer incidence. The techniques discussed here are equally valid for determining specificity. The estimation of sensitivity and specificity is useful for a variety of scientific evaluations, including the comparison of screening techniques, analyses of cost effectiveness, and computer modeling of breast cancer screening[40].

Acknowledgements

This research was supported in part by grants from the US Army Breast Cancer Research Program (DAMD17-98-1-8176 and DAMD17-94-J-4424).

REFERENCES

- (1) Walter SD. Estimation of test sensitivity and specificity when disease confirmation is limited to positive results. *Epidemiology* 1999; 10:67-72.
- (2) Duffy SW, Chen HH, Tabar L, Fagerberg G, Paci E. Sojourn time, sensitivity and positive predictive value of mammography screening for breast cancer in women aged 40-49. *Int J Epidemiol* 1996; 25:1139-1145.
- (3) Thurfjell EL, Holmberg LH, Persson IR. Screening mammography: sensitivity and specificity in relation to hormone replacement therapy [see comments]. *Radiology* 1997; 203:339-341.
- (4) Duijm LE, Guit GL, Zaat JO, Koomen AR, Willebrand D. Sensitivity, specificity and predictive values of breast imaging in the detection of cancer. *Br J Cancer* 1997; 76:377-381.
- (5) Davis PL, McCarty KS, Jr. Sensitivity of enhanced MRI for the detection of breast cancer: new, multicentric, residual, and recurrent. *Eur Radiol* 1997; 7 Suppl 5:289-298.
- (6) Gilhuijs KG, Giger ML, Bick U. Computerized analysis of breast lesions in three dimensions using dynamic magnetic-resonance imaging. *Med Phys* 1998; 25:1647-1654.
- (7) Sahiner B, Chan HP, Petrick N, Helvie MA, Goodsitt MM. Computerized characterization of masses on mammograms: the rubber band straightening transform and texture analysis. *Med Phys* 1998; 25:516-526.
- (8) Kacel GM, Liu P, Debatin JF, Garzoli E, Caduff RF, Krestin GP. Detection of breast cancer with conventional mammography and contrast-enhanced MR imaging. *Eur Radiol* 1998; 8:194-200.
- (9) Lin JS, Hasegawa A, Freedman MT, Mun SK. Differentiation between nodules and end-on vessels using a convolution neural network architecture. *J Digit Imaging* 1995; 8:132-141.
- (10) Jiang Y, Nishikawa RM, Schmidt RA, Metz CE, Giger ML, Doi K. Improving breast cancer diagnosis with computer-aided diagnosis. *Acad Radiol* 1999; 6:22-33.
- (11) Lo JY, Baker JA, Kornguth PJ, Iglehart JD, Floyd CE, Jr. Predicting breast cancer invasion with artificial neural networks on the basis of mammographic features. *Radiology* 1997; 203:159-163.

- (12) Arnesson LG, Vitak B, Manson JC, Fagerberg G, Smeds S. Diagnostic outcome of repeated mammography screening. *World J Surg* 1995; 19:372-377.
- (13) SEER Cancer Statistics Review, 1973-1991: Tables and graphs. Bethesda, MD: National Cancer Institute, MIN PUb. No. 94-2789, 1994.
- (14) Swets JA. Form of empirical ROCs in discrimination and diagnostic tasks: implications for theory and measurement of performance. *Psychological Bulletin* 1986; 99:181-189.
- (15) Hanley JA. The robustness of the binormal assumptions used in fitting ROC curves. *Medical Decision Making* 1988; 8:197-205.
- (16) Rose A. *Vision, Human and Electronic*. New York: Plenum Press, 1974.
- (17) Akker-van Marle ME, Reep-van den Bergh CM, Boer R, Del Moral A, Ascunce N, de Koning HJ. Breast cancer screening in Navarra: interpretation of a high detection rate at the first screening round and a low rate at the second round. *Int J Cancer* 1997; 73:464-469.
- (18) Kopans DB, Moore RH, McCarthy KA, Hall DA, Hulka CA, Whitman GJ, Slanetz PJ, Halpern EF. Positive predictive value of breast biopsy performed as a result of mammography: there is no abrupt change at age 50 years. *Radiology* 1996; 200:357-360.
- (19) Mushlin AI, Kouides RW, Shapiro DE. Estimating the accuracy of screening mammography: A meta-analysis. *Am J Prev Med* 1998; 14:143-153.
- (20) Nawano S, Murakami K, Moriyama N, Kobatake H, Takeo H, Shimura K. Computer-aided diagnosis in full digital mammography. *Invest Radiol* 1999; 34:310-316.
- (21) Avril N, Dose J, Janicke F, Bense S, Ziegler S, Laubenbacher C, Romer W, Pache H, Herz M, Allgayer B, Nathrath W, Graeff H, Schwaiger M. Metabolic characterization of breast tumors with positron emission tomography using F-18 fluorodeoxyglucose. *J Clin Oncol* 1996; 14:1848-1857.
- (22) Leichter I, Lederman R, Bamberger P, Novak B, Fields S, Buchbinder SS. The use of an interactive software program for quantitative characterization of microcalcifications on digitized film-screen mammograms. *Invest Radiol* 1999; 34:394-400.

- (23) Cooper GS, Yuan Z, Stange KC, Dennis LK, Amini SB, Rimm AA. The sensitivity of Medicare claims data for case ascertainment of six common cancers [see comments]. *Med Care* 1999; 37:436-444.
- (24) Ciatto S, Del Turco MR, Morrone D, Catarzi S, Ambrogetti D, Cariddi A, Zappa M. Independent double reading of screening mammograms. *J Med Screen* 1995; 2:99-101.
- (25) Beam CA, Layde PM, Sullivan DC. Variability in the interpretation of screening mammograms by US radiologists. *Archives of Internal Medicine* 1996; 156:209-213.
- (26) Pep MS, Urban N, Rutter C, Longton G. Design of a study to improve accuracy in reading mammograms. *Journal of Clinical Epidemiology* 1997; 50:1327-1338.
- (27) Dorfman DD, Berbaum KS, Metz CE. Receiver operating characteristic rating analysis. Generalization to the population of readers and patients with the jackknife method. *Invest Radiol* 1992; 27:723-731.
- (28) Rockette HE, Gur D, Metz CE. The use of continuous and discrete confidence judgments in receiver operating characteristic studies of diagnostic imaging techniques. *Invest Radiol* 1992; 27:169-172.
- (29) Gur D, Rockette HE, Good WF, Slasky BS, Cooperstein LA, Straub WH, Obuchowski NA, Metz CE. Effect of observer instruction on ROC study of chest images. *Invest Radiol* 1990; 25:230-234.
- (30) Metz CE, Shen JH. Gains in accuracy from replicated readings of diagnostic images: prediction and assessment in terms of ROC analysis. *Med Decis Making* 1992; 12:60-75.
- (31) Jiang Y, Metz CE, Nishikawa RM. A receiver operating characteristic partial area index for highly sensitive diagnostic tests [see comments]. *Radiology* 1996; 201:745-750.
- (32) Abramowitz M, Stegun IA. *Handbook of Mathematical Functions*. New York: Dover Publications, Inc., 1972.
- (33) Nishikawa RM, Giger ML, Doi K, Metz CE, Yin FF, Vyborny CJ, Schmidt RA. Effect of case selection on the performance of computer-aided detection schemes. *Med Phys* 1994; 21:265-269.

- (34) Song HH. Analysis of correlated ROC areas in diagnostic testing. *Biometrics* 1997; 53:370-382.
- (35) Rockette HE, Gur D, Kurs-Lasky M, King JL. On the generalization of the receiver operating characteristic analysis to the population of readers and cases with the jackknife method: an assessment. *Acad Radiol* 1995; 2:66-69.
- (36) Dorfman DD, Berbaum KS, Lenth RV, Chen YF, Donaghy BA. Monte Carlo validation of a multireader method for receiver operating characteristic discrete rating data: factorial experimental design. *Acad Radiol* 1998; 5:591-602.
- (37) Dorfman DD, Berbaum KS. Degeneracy and discrete receiver operating characteristic rating data. *Acad Radiol* 1995; 2:907-915.
- (38) Zou KH, Tempany CM, Fielding JR, Silverman SG. Original smooth receiver operating characteristic curve estimation from continuous data: statistical methods for analyzing the predictive value of spiral CT of ureteral stones. *Acad Radiol* 1998; 5:680-687.
- (39) Pepe MS. Three approaches to regression analysis of receiver operating characteristic curves for continuous test results. *Biometrics* 1998; 54:124-135.
- (40) Boone JM, Lindfors KL. Computer simulation of breast cancer screening efficacy. *Med.Phys.* 26, 1065-1066. 1999. (Abstract)

Table 1: A_z as a function of SNR, for any value of k .

SNR	A_z	SNR	A_z
0.0	0.5000		
0.2	0.5792	2.2	0.9861
0.4	0.6554	2.4	0.9918
0.6	0.7257	2.5	0.9938
0.8	0.7881	2.6	0.9953
1.0	0.8413	2.8	0.9973
1.2	0.8849	3.0	0.9985
1.4	0.9192	3.5	0.9996
1.6	0.9452	4.0	0.9998
1.8	0.9640	4.5	0.9999
2.0	0.9772	5.0	0.9999

Figure Captions

FIGURE 1A:

The basic assumptions of signal detection theory are illustrated. A screening test is designed to differentiate between two populations, the normal population $N(\xi)$ and those patients with cancer $C(\xi)$. These populations are assumed to be normally distributed, with means of \bar{N} and \bar{C} , and standard deviations σ_N and σ_C . The area of the distribution $N(\xi)$ is normalized to $1 - f$, and the area of $C(\xi)$ is normalized to f , where f is the fraction of cancers observed in the screening population. A decision parameter ξ is used as the basis of the diagnosis, and a threshold value τ (solid vertical line) is chosen by the diagnostician (a radiologist or other decision maker). In selecting τ , all cases of ξ to the right of the threshold ($\xi > \tau$) are considered by that diagnostician as having cancer, and all cases to the left of τ ($\xi < \tau$) are considered normal. For simplicity and to reduce the parameter count, the simplifications of $\bar{N} = 0$ and $\sigma_N = 1$ are made. The decision axis is then easily defined in units of σ_N .

FIGURE 1B:

ROC curves are illustrated for $\text{SNR} = 1$. A symmetrical ROC curve (symmetrical about the negative diagonal axis running from the upper left to the lower right) results when the standard deviations of the normal and cancer distributions are equal (i.e. when $k = 1.0$). Asymmetrical ROC curves result for non-unity values of k . The area under each ROC curve, A_z , at fixed SNR is seen to vary as a function of k .

FIGURE 2A:

The sensitivity is plotted as a function of the A_z is illustrated for symmetrical ROC curves (where $k=1$) and for a positive biopsy rate (PPV) of 20%, which is typical. The cancer incidence in the screening population, f , affects sensitivity and curves corresponding to values of f ranging from $f = 0.001$ to $f = 0.010$ (in intervals of 0.001) are shown. The typical cancer detection rate (a surrogate for incidence) in the United States is about 3 cancers per 1000 screens, or $f = 0.003$. At a given degree of diagnostic performance (A_z level), clearly sensitivity increases as the number of cancers in the screened population increases.

FIGURE 2B:

The sensitivity is plotted as a function of A_z , for a range of positive predictive values (PPV) as indicated. The value of PPV essentially determines the radiologist's operating point on his or her personal ROC curve. A reduction in the positive biopsy rate (PPV), which corresponds to a reduced threshold and a more aggressive diagnosis, results in better sensitivity (and worse specificity). A PPV of 20% (1 cancer per 5 biopsies) is fairly typical.

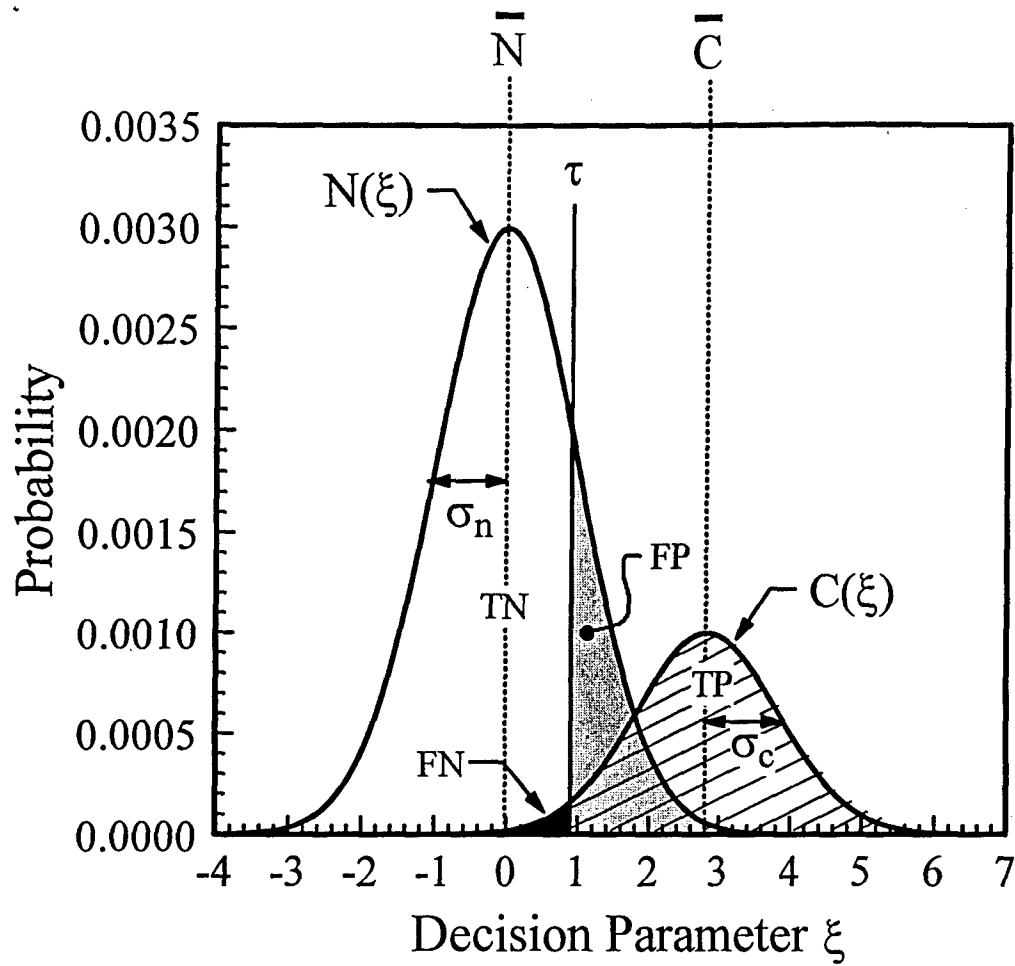


Figure 1A

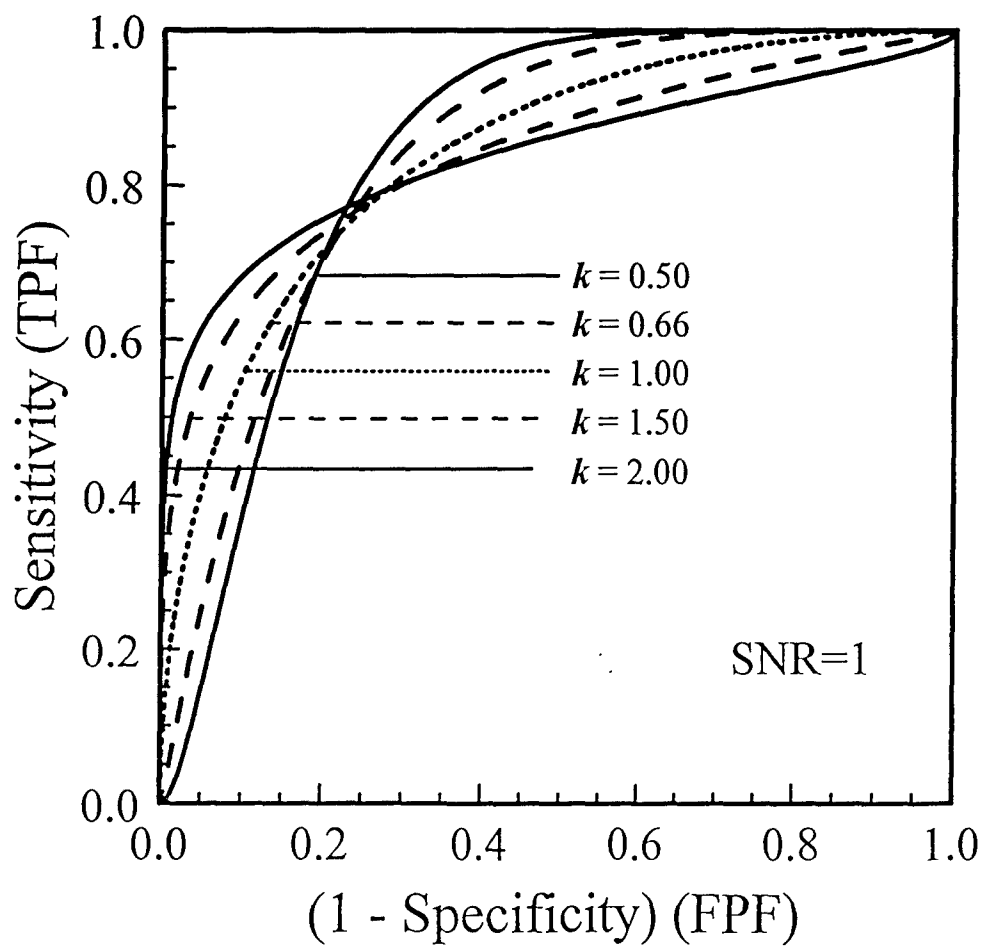


Figure 1B

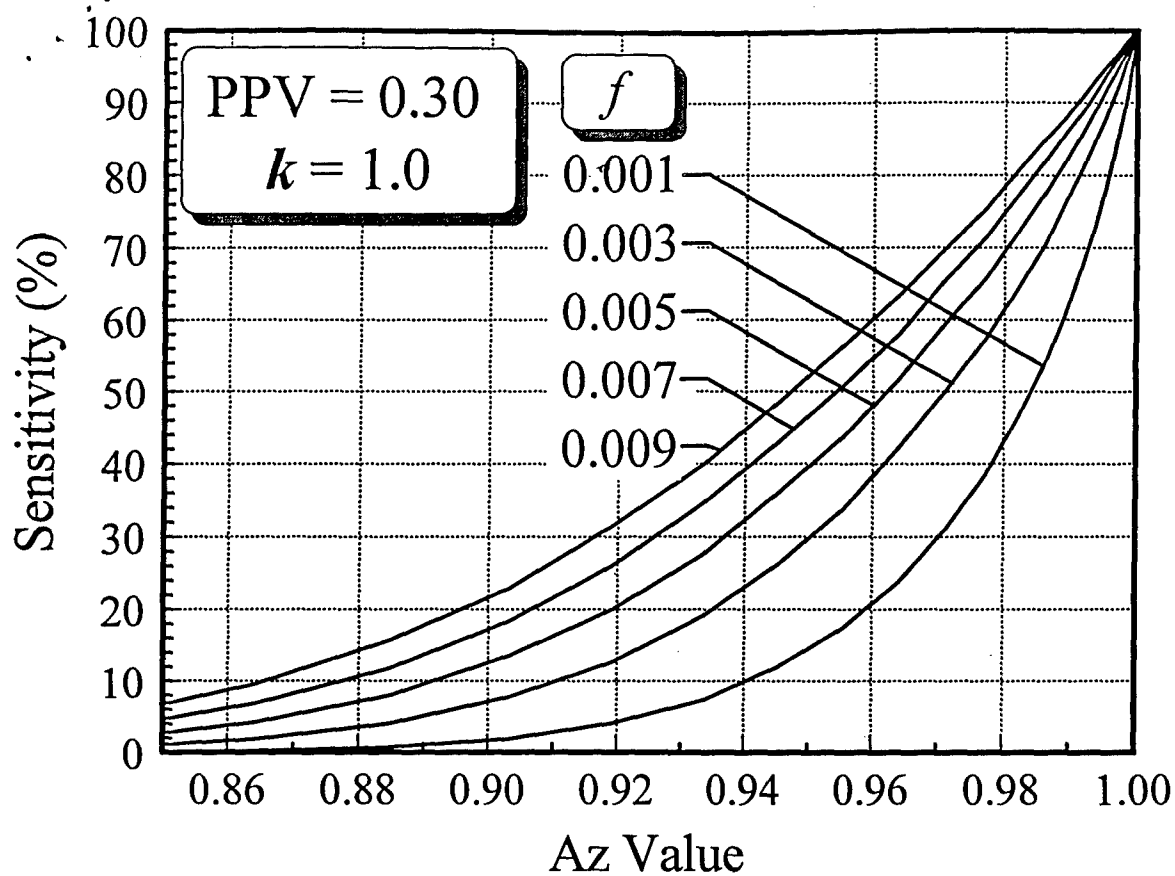


Figure 2A

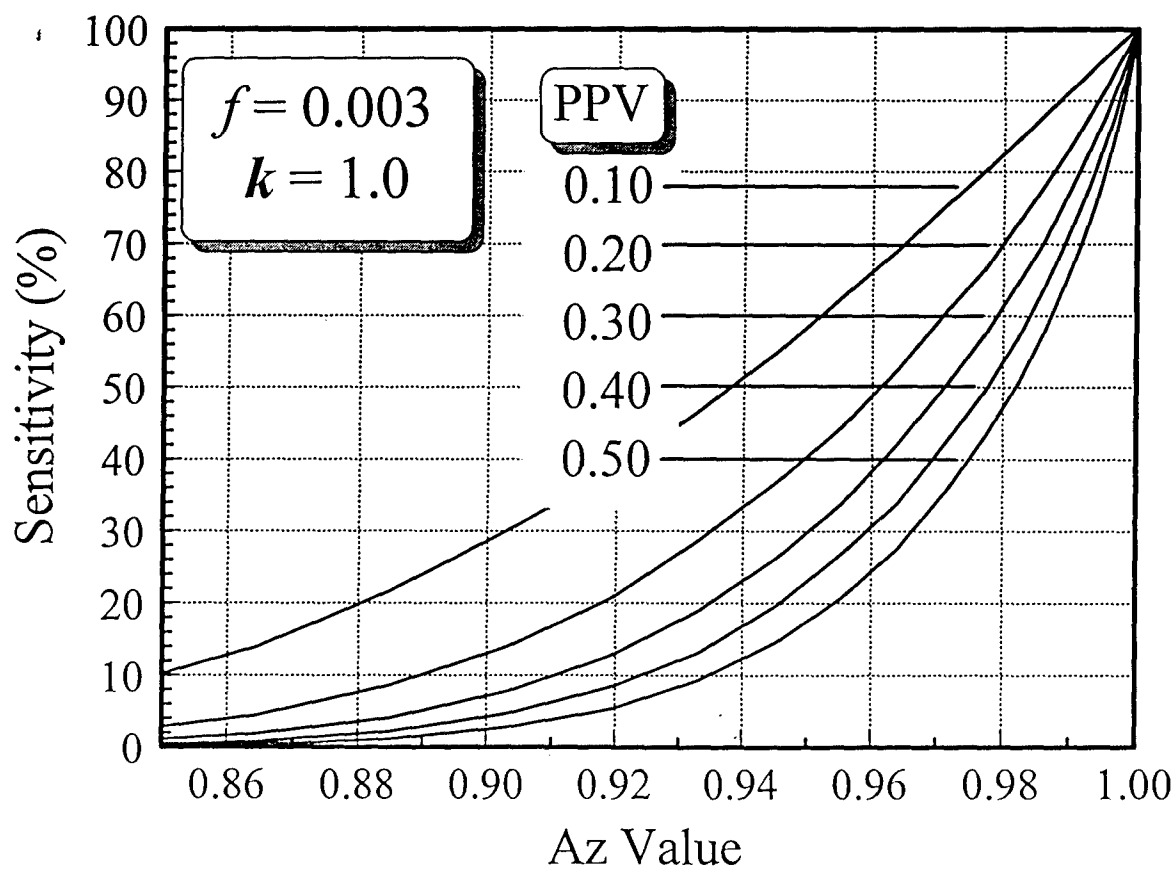


Figure 2B

DAMD17-98-18176, Final Report - August 2001

Computer Simulation of Breast Cancer Screening

PI: John M. Boone, Ph.D.

Appendix B:

JM Boone and KK Lindfors, "The effect of breast density of cancer detection performance in mammography", Journal of Women's Imaging, (submitted May 15, 2001)

THE EFFECT OF BREAST DENSITY ON CANCER DETECTION PERFORMANCE IN MAMMOGRAPHY

John M. Boone, Ph.D.

Karen K. Lindfors, M.D.

Department of Radiology
University of California, Davis

ADDRESS FOR CORRESPONDENCE:

John M. Boone, Ph.D.
Department of Radiology
UC Davis Medical Center
4701 X Street, X-ray Imaging Laboratory
Sacramento, CA 95817
United States of America

(916) 734-3158
(916) 734-0316 (FAX)
jmboone@ucdavis.edu

ACKNOWLEDGEMENT: This research was performed with support from the United States Department of Defense Breast Cancer Research Program (DAMD17-98-1-8176).

RUNNING TITLE: The Effect of Breast Density on Cancer Detection

REFERENCE DATABASE: BDI

DATE: May 10, 2001

Abstract

Objectives: The purpose of this study was to quantify the effect that breast density has on the detection performance of mammography, as measured by the area under the ROC curve (A_z).

Methods: Each of 998 digitized normal mammograms were classified into 5 categories based on a radiologist-determined breast density scale (BDI). Computer-generated spherical soft-tissue cancer lesions (2 mm to 40 mm in diameter) were randomly positioned on each image using mathematics which accurately reflect the physics of mammography imaging. Computer simulations using a computer-based matched template ideal observer were used to determine A_z for each image and lesion size. **Results:** The results demonstrated that increased breast density resulted in significantly reduced detection performance between each of the 5 pentiles. Using the BDI classifier, women in the most dense pentile demonstrated a 22.2% reduction in absolute detection performance compared to women in the least dense pentile. For a 10 mm soft-tissue lesion, the estimated sensitivity (at 90% specificity) decreased from 74% for an average adipose breast to 47% for a breast in the high breast density pentile. **Conclusions:** It was estimated that a 1.3 year delay in detection occurs for women in the densest category, compared to the least dense category. Over lesion diameters from 6 to 20 mm, a reduction of sensitivity of 8% was realized for each pentile as breast density increased. These results were computed for soft tissue lesions, and cancers which present with microcalcifications would likely have higher sensitivities associated with them.

KEYWORDS:

Mammography, Ideal Observer, Breast density, Receiver Operating Characteristic (ROC), Computer Simulation

Introduction

Mammography is the primary screening tool used for the early detection of breast cancer. Despite this important role[1;2], it is widely suspected that screen-film mammography is less sensitive in the dense breast[3-5]. While some studies have equivocal findings with respect to breast density alone[6;7], other recent clinical studies have demonstrated a reduction in sensitivity attributed to breast density[8-10]. This dilemma of reduced screening sensitivity in the dense breast is compounded by the fact that women with dense breasts are at higher risk for breast cancer[11-14], with odds ratios thought to range from 4 to 6 compared to women with adipose breasts. The development of digital mammography[15] and other techniques[16-18] are, in part, predicated on improved imaging of the dense breast.

To our knowledge, a systematic approach for quantifying the reduction in detectability of soft tissue lesions caused by breast density has not been reported. Whereas some clinical studies have demonstrated correlation between high breast density and low sensitivity, this study was designed to demonstrate causality, since mechanisms associated with breast cancer detection were simulated. The detectability of simulated breast cancer lesions was studied using a data base of 998 digitized screen-film mammograms. While human performance studies remain the gold standard, expert human observers have limited available time and varying degrees of concentration for the highly repetitive tasks required in this work. Consequently, an ideal computer-based observer was used to evaluate the 8 million potential lesion sites required for this study. Human observers are thought to perform comparably to an ideal computer observer, differing only by an efficiency term[19]. Since relative performance was evaluated here, the efficiency term is not important to the results.

Methods

Case Selection

A series of 1053 normal craniocaudal (CC) mammograms from the breast screening service at our institution was digitized using a laser digitizer capable of $50\text{ }\mu\text{m} \times 50\text{ }\mu\text{m} \times 12\text{ bit}$ resolution (Lumysis 150, Lumysis Corporation, Sunnyvale, CA), operating in varying resolution modes, depending on film size (both $18 \times 24\text{ cm}$ and $24 \times 30\text{ cm}$ film images were digitized). Normal mammography cases were selected randomly and serially (with some gaps due to absence of the individual doing this), over a 2 month time period. A few of the digitized images were lost to file corruption, and others were inadvertently overlooked during radiologist classification, eliminating 55 of the cases, and thus 998 cases were available for this investigation. The matrix size of the digitized images used for this study was reduced by averaging to approximately $0.275 \times 0.275\text{ mm}$ pixels. Reducing the matrix size of the images was necessary for display on a 1280×1024 pixel monitor, and for rapid handling of the images. The digitized images were used for ideal observer performance evaluations, using simulated soft tissue lesions spanning diameters from 2 mm to 40 mm. The 275 μm pixel dimension resulted in a 2 mm diameter lesion occupying about 41 pixels, and a 40 mm diameter lesion occupying ~16,000 pixels. The pixel size was therefore considered adequate to conduct simulated lesion studies of the size range $\geq 2\text{ mm}$.

Only CC mammograms were used in this study, whereas two view mammography is the more common practice for screening mammography in the United States. However, the focus of this investigation is not on precisely quantifying the detection capabilities of screening mammography *per se*, but rather to assess the role that breast density plays in modulating detectability. In a previous study[20], breast density in the CC view was shown to be highly

correlated to that in the mediolateral oblique (MLO) view. Thus, the focus here on the effects of breast density detection in the CC view should apply to the MLO projection as well.

Breast Density Assessment

A board-certified MQSA-qualified radiologist with 15 years of mammography experience (KKL) evaluated the breast density of each image. Each digital image was displayed on a monitor, and a density rating from 1 (being least dense) to 100 (most dense) was entered by the mammographer. These values have been dubbed the breast density index (BDI). It has been previously shown[20] that the radiologist's subjective density rating was quite reproducible. The breast density scores were rank-ordered and the rank was used to assign the 998 images to 5 different categories (pentiles), with 200 images in each of the categories 1 to 4, and 198 images in category 5. Pentile 1 corresponded to low density (mostly adipose) breasts, and pentile 5 contained the most dense (glandular) breasts.

Mammography Physics of Image Contrast

The presence of spherical breast cancer lesions was computer simulated. Lesion diameters ranging from 2 mm to 40 mm with 2 mm intervals were studied. For each digitized mammogram and each lesion diameter under study, 400 possible lesion locations were evaluated. The placement of computer simulated lesions was necessary to quantify true positives and false negatives, and identical analyses were conducted on areas of the image where no lesion was placed, to quantify true negative and false positive events (the latter regions are referred to here as "non-lesion" areas). For each image, 200 lesions and 200 non-lesions were studied.

The contrast of each simulated lesion was computed based on the physical properties of breast cancer and soft tissue, and realistic assumptions concerning the x-ray spectrum. A detailed description of the techniques used to place lesion contrast on the digitized mammographic images is given in the appendix. These techniques made use of the detailed but well known physical properties involved in the acquisition of mammographic images.

Ideal Observer Methodology

Mammograms consist of the radiographic image of the breast, surrounded by the film exposed to unattenuated radiation beyond the edge of the breast. In preparation for the ideal observer study, the breast border was outlined by hand on all images, using mouse-and-cursor software written for this purpose, and the edge coordinates of the breast were recorded. The placement of each synthetic lesion was selected using randomly generated coordinates of the lesion center. All lesions were positioned such that they fell completely within the breast boundaries.

The detectability of the computer-generated spherical breast lesions was evaluated using ideal computer observer methods[19;21], combined with receiver operator characteristic (ROC) curve analysis[22-27]. The so-called *ideal observer* is an analytical device which is thought to emulate human performance in terms of lesion detection[26;28-30]. In many instances involving simple, well-defined tasks, ideal observers, which are computer algorithms, can outperform human observers. The essential property of ideal observer techniques pertinent to this study is not that ideal observers exactly mimic radiologist performance, but that the ideal observer's performance will be influenced by breast density with the same trends as those of human detection performance.

ROC methods require that the observer being tested be shown areas containing both abnormalities (lesions) and normal areas (non-lesions). For each simulated lesion diameter, 200 lesions and 200 non-lesions were randomly placed on each of the 998 mammograms. Because the computer explicitly determines whether a lesion is present or not, "truth" concerning the presence and position of the lesion is known with complete certainty. ROC analysis using a computer observer is not dependent upon the ratio of lesions to non-lesions used in the analysis, because both sensitivity and specificity are independent of incidence. Whereas human observers may alter their decision thresholds based on disease incidence, computers are unwavering in this regard.

Because a variety of parenchyma patterns were the focus of this investigation, the ideal observer method employed here used non-pre-whitening techniques, where the correlated noise of the anatomical background was not corrected for. For the image patterns which correspond to the light striking the radiologist's eyes, a matched filter was applied. A matched filter is one in which the detection algorithm is tailored mathematically to suit the known shape of the suspected lesion. Each pixel inside the boundaries of the suspected lesion was multiplied by a filter coefficient corresponding to the projected thickness of the spherical lesion at that location. The filter values over the area of the projected sphere (corresponding to the known location of the suspected lesion) were normalized to unity. The sum of the weighted signal, ΣL_{lesion} , was computed. An annular background template equal in area to the lesion area was placed just outside the lesion boundary, and was used to filter the background region. The filter coefficients were constant, and equal to $1/n$, where n was the number of pixels in the background region. The sum of the weighted background region was computed as ΣL_{bg} . A detection parameter d was computed as $d = \Sigma L_{\text{lesion}} / \Sigma L_{\text{bg}}$, for each lesion and non-lesion. The 400 values of d

computed on each image (200 lesions and 200 non-lesions) for each lesion diameter (and the knowledge of "truth" associated with each value) provided the data set necessary to compute an ROC curve for each image and each lesion diameter. The area under the ROC curve, A_z , was then calculated using numerical integration. A 333 MHz Pentium workstation was used for this study, using C code written by one of the authors (Microsoft C/C++ 5.0, Redmond, WA).

Sensitivity Analysis

For symmetric ROC curves, the A_z value defines the shape of the curve when the underlying distributions are normal with independent means and standard deviations. Using this assumption, the sensitivity values were computed for fixed values of specificity. To "map" A_z values to sensitivity, the sensitivity was computed (at fixed specificity) using analytically generated ROC curves with A_z values ranging from 0.50 to 1.00 by intervals of 0.01. The resulting data was computer-fit using commercial software (TableCurve 2D, Jandel Scientific, Corte Madera, CA), and this function was used to convert A_z to sensitivity.

Overall Analysis

For each of the five categories of breast density, the mean A_z value and standard deviation was computed over the 200 images in each category (198 images in pentile 5). Differences between the mean A_z values of adjacent pentiles were evaluated for significance using the unpaired t-test. Differences between the means were determined to be significant if $p < 0.001$. The statistical analysis was performed using spreadsheet software (Microsoft Excel, Redmond, WA), running on a 1.1 GHz Athlon-based workstation.

Results

Figure 1 illustrates the mean A_z (expressed as a percentage) for each density pentile as a function of lesion diameter. An A_z value of 100% is indicative of ideal detection performance, and an A_z of 50% corresponds to pure guessing. The difference between adjacent categories is significant ($p < 0.001$) for lesions diameters from 2 mm to 30 mm (pentiles 1-2, 2-3, and 3-4), and for lesion diameters 2 mm to 16 mm for the pentile 4-5 comparisons. There is reduced detection performance (lower A_z) as breast density increases. For example, for a 10 mm diameter lesion, $A_z = 91.4\%$ for the mean of the least dense category (pentile 1) and $A_z = 80.3\%$ for the most dense breasts (pentile 5). The difference in absolute detection performance between pentiles 5 and 1 is 11.1%, however given that the A_z scale runs between 50% and 100%, the difference expressed as a fraction of the entire scale (*relative difference*) is 22.2% (i.e. $[91.4 - 80.3] \times 2$). For the clinically relevant lesion diameters from 6 mm to 20 mm (inclusive), the average relative difference in detection performance between adjacent breast density pentiles was 5.3% ($\sigma = 1.4\%$).

Another way to look at Figure 1 is to assess the difference in lesion diameter for a fixed detection performance level. For example, assume that a threshold of $A_z \geq 90\%$ is required for lesion detection. Women in pentile 1 (least dense) will have cancers detected at a diameter of 7 mm, whereas women in pentile 5 (most dense) will have their cancers detected at 21 mm in diameter. A 7 mm diameter lesion contains less than 4% ($[7/21]^3$) of the cancer cells as does a 21 mm lesion. Assuming a cell doubling time of 100 days[31], women in the most dense breast category will have their cancers detected 1.3 years (4.75 doublings) later than women in the least dense breast category.

ROC curves are plots of sensitivity versus (1-specificity), and by setting a fixed value for the specificity, the sensitivity can be calculated from A_z , for symmetric curves which are most common[32;33]. Figure 2 illustrates 5 ROC curves with different A_z values (indicated in figure). At 95% sensitivity, corresponding to the vertical dotted line in Figure 2, the intersection of this dotted line and each ROC curve yields the sensitivity at 95% specificity.

Linver et al suggest that the specificity of mammography should be better than 90%[34]. Figure 3A and 3B illustrate the sensitivity as a function of lesion diameter, for two different specificity levels. Figure 3A corresponds to a specificity of 95%, and Figure 3B corresponds to a specificity of 90%. Of course sensitivity drops as specificity increases, and so the curves in Figure 3A (95% specificity) are lower than the corresponding curves in Figure 3B (90% specificity). At 95% specificity, in the clinically important lesion diameter region from 6 mm to 20 mm (inclusive), the sensitivity decreases on average by 7.9% ($\sigma=2.6\%$) between each pentile as the breast density increases. The difference in sensitivity for a 10 mm lesion between the most (pentile 5) and least (pentile 1) dense categories was 28.2%, and the difference for a 20 mm lesion was 36.8%.

Discussion

Breast density has a profound influence on the detectability of breast cancer, and this has been known for several decades. In this study, the drop in sensitivity due to breast density was quantified and found to be about 8% per breast density pentile in the clinically relevant range from 6 mm to 20 mm diameter lesions. Microcalcifications on a mammogram represent a high contrast, high spatial frequency (small) signature that is uniquely different than the background pattern of the normal anatomy of the breast. Cancers which manifest with microcalcifications are usually more detectable than cancers which are soft tissue in nature only. The positive predictive value of microcalcifications is intermediate (45%) between well-defined masses (4%) and spiculated ones (94%)[35]. Tabar[36] has shown that microcalcifications are crucial to the diagnosis in about 19% of breast cancers. The presence of microcalcifications was not simulated in this research, but it is likely that their presence would increase the detection performance. Thus, the sensitivity values reported here (Figures 3A and 3B) apply only to breast cancer detection in the absence of microcalcifications. In the presence of microcalcifications, sensitivity will be higher. The detection of breast cancer was simulated in this study using only one view, whereas two views are acquired and interpreted for mammography as practiced in the United States. The evaluation of two views will slightly increase the detection sensitivity for soft tissue lesions.

The results of this study were achieved using computer simulation. While the simulation methods were rigorous and thorough, it is important to keep in mind that there are limitations on the ability of simulated data to mimic reality. Therefore, rather than emphasizing the importance of the specific values for A_z or sensitivity, it is the trends observed in this study that are most important. The ideal observer techniques used in this study are far less sophisticated than the

image processing performed by an actual human observer. However, just under 8 million potential lesion locations were evaluated in this study in order to extract subtle but statistically significant differences in detection performance. Clearly, a study of this scale using human observers would not be possible.

The results of this study provide mechanistic and quantitative evidence concerning the disparity in detection performance that breast density imposes on breast cancer screening using mammography. Women in the most dense pentile were shown in this computer simulation to suffer delayed breast cancer diagnosis by about 1.3 years, on average. In an annual screening program, this means that women in the highest breast density pentile will have their cancers detected one or two screens after women in the lowest breast density pentile.

Appendix

The contrast of each simulated breast lesion was placed onto each image using methods consistent with the physics of mammography. The characteristic curve (optical density versus x-ray exposure) of the mammography film used in our clinic was measured, and it was mathematically characterized using commercially-available curve fitting software (Table Curve 2D, Jandell Scientific, Corte Madera, CA). Its inverse function was characterized as well. The characteristic curve (gray scale [GS] versus optical density [OD]) of the laser digitizer was also measured, and was found to be linear with $r^2=0.999$. The linear relationship and its inverse were used to convert between OD and GS units.

The x-ray attenuation of a lesion of thickness t and linear attenuation coefficient μ is computed as $e^{-\mu t}$. When the lesion is present in the breast, a change in thickness of the breast does not occur, but rather a slight change in the linear attenuation coefficient results. If μ' corresponds to the linear attenuation of the breast cancer lesion, and μ is the linear attenuation coefficient of the surrounding normal breast tissue, then the additional attenuation of the lesion is given by $e^{-(\mu'-\mu)t}$. Letting $\Delta\mu = (\mu' - \mu)$, the differential attenuation becomes $e^{-\Delta\mu t}$. In clinical mammography, the attenuation coefficients are dependent on the x-ray energies used to produce the image. While the compressed thickness and glandularity of the 998 breasts used in the mammography database varied, the most common x-ray technique used at our institution was a 26 kVp molybdenum anode-molybdenum filter (Mo-Mo) spectrum. A 26 kVp Mo-Mo x-ray spectrum, $\Phi(E)$, was simulated using a spectral model[37], and the $\Delta\mu$ value was computed using the linear attenuation coefficients of breast cancer[38], $\mu'(E)$, and that of normal 50% glandular-

50% adipose breast tissue, $\mu(E)$. Because of beam hardening[39], the value of $\Delta\mu$ is dependent both on the overall thickness of the breast T and the thickness of the lesion t :

$$\Delta\mu = \frac{1}{-t} \ln \left[\frac{\int_{E=0}^{E_{\max}} \Phi(E) e^{-\mu(E)T} e^{-[\mu'(E)-\mu(E)]t} dE}{\int_{E=0}^{E_{\max}} \Phi(E) e^{-\mu(E)T} dE} \right] \quad \text{Eq. 1}$$

The values of $\Delta\mu$ were computed over breast thicknesses (T) ranging from 1 cm to 8 cm, for lesion thicknesses (t) from 1 mm to 10 mm. While strong thickness-related dependencies in $\Delta\mu$ were observed for breast thicknesses less than 2 cm, for the 90% range of breast thicknesses undergoing mammography at our institution[40] (2.8 to 7.1 cm), the mean $\Delta\mu$ calculated over this range was found to be 0.150 cm^{-1} ($\sigma = 0.0123 \text{ cm}^{-1}$). Due to this small variation in $\Delta\mu$, and in order to simplify the calculations, $\Delta\mu$ was set to 0.150 cm^{-1} for all simulated lesions. Non-lesion areas were generated using the same techniques described here, but where $\Delta\mu = 0$.

Spherical breast cancer lesions were mathematically overlaid onto the digital images using the following procedure: (1) gray scale images were converted to optical density and then to relative x-ray exposure using the characteristic curve, (2) the projected thickness t of a spherical lesion of the desired diameter was calculated for each pixel in which the lesion overlays, (3) the perturbation (reduction) in x-ray exposure due to the lesion was calculated at each pixel using $e^{-\Delta\mu t}$, (4) the modified exposure distribution was converted back to optical density (OD) using the characteristic curve of the film, and (5) the relative image luminance, L , corresponding to the OD at each pixel, where $L = 10^{-\text{OD}}$, was computed. The resulting image, $L(x,y)$, was representative of the spatial distribution of image luminance striking the radiologist's eyes when viewing mammograms on a lightbox.

Acknowledgements

This research was performed with support from the United States Department of Defense Breast Cancer Research Program (DAMD17-98-1-8176).

Figure Captions

Figure 1:

The area under the ROC curve, A_z , is shown as a function of simulated breast cancer lesion diameter, for five breast density categories. The breast density index (a subjective rating performed by an experienced mammographer) was used to classify images into the five categories shown. Data between adjacent categories are significant ($p < 0.001$) for lesion diameters to the left of the vertical lines shown in the figure.

Figure 2:

A series of 5 receiver operating characteristic (ROC) curves are shown, each with a different area under it (A_z). Since ROC curves are a plot of sensitivity versus 1-specificity, sensitivity can be computed from the curve (i.e. from A_z) when the specificity value is set. The vertical dotted line illustrates a fixed specificity of 95%, and the vertical location where this line interests the 5 ROC curves corresponds to the sensitivity. This approach was used to calculate sensitivity from the A_z value measured in this study.

Figure 3A:

The sensitivity is shown as a function of lesion diameter for 5 breast density categories. The sensitivity was fixed at 95% for these data.

Figure 3B:

The sensitivity was fixed at 90% for these data.

References

- (1) Tabar L, Chen HH, Fagerberg G, Duffy SW, Smith TC. Recent results from the Swedish Two-County Trial: the effects of age, histologic type, and mode of detection on the efficacy of breast cancer screening. *J Natl Cancer Inst Monogr* 1997;43-47.
- (2) Larsson LG, Nystrom L, Wall S, Rutqvist L, Andersson I, Bjurstam N, Fagerberg G, Frisell J, Tabar L. The Swedish randomised mammography screening trials: analysis of their effect on the breast cancer related excess mortality. *J Med Screen* 1996; 3:129-132.
- (3) Jackson VP, Hendrick RE, Feig SA, Kopans DB. Imaging of the radiographically dense breast. *Radiology* 1993; 188:297-301.
- (4) Jackson VP. What is the role of sonographic breast imaging for detecting occult cancer in a patient with a strong family history of breast cancer and mammographically dense breasts without obvious masses? *AJR Am J Roentgenol* 1995; 165:1004.
- (5) Page DL, Winfield AC. The dense mammogram [editorial]. *AJR Am J Roentgenol* 1986; 147:487-489.
- (6) Hackshaw AK, Wald NJ, Michell MJ, Field S, Wilson AR. An investigation into why two-view mammography is better than one-view in breast cancer screening. *Clin Radiol* 2000 Jun ;55 (6):454 -8 2000; 55:454-458.
- (7) Rosenberg RD, Hunt WC, Williamson MR, Gilliland FD, Wiest PW, Kelsey CA, Key CR, Linver MN. Effects of age, breast density, ethnicity, and estrogen replacement therapy on screening mammographic sensitivity and cancer stage at diagnosis: review of

- 183,134 screening mammograms in Albuquerque, New Mexico. *Radiology* 1998; 209:511-518.
- (8) Mandelson MT, Oestreicher N, Porter PL, White D, Finder CA, Taplin SH, White E. Breast density as a predictor of mammographic detection: comparison of interval- and screen-detected cancers. *J Natl Cancer Inst* 2000; 92:1081-1087.
- (9) Kotre CJ. The effect of background structure on the detection of low contrast objects in mammography. *Br J Radiol* 1998; 71:1162-1167.
- (10) van Gils CH, Otten JD, Verbeek AL, Hendriks JH, Holland R. Effect of mammographic breast density on breast cancer screening performance: a study in Nijmegen, The Netherlands. *J Epidemiol Community Health* 1998; 52:267-271.
- (11) Wolfe JN, Albert S, Belle S, Salane M. Breast parenchymal patterns and their relationship to risk for having or developing carcinoma. *Radiol Clin North Am* 1983; 21:127-136.
- (12) Wolfe JN. Breast patterns as an index of risk for developing breast cancer. *Am J Roentgenol* 1976; 126:1130-1137.
- (13) Byrne C, Schairer C, Wolfe J, Parekh N, Salane M, Brinton LA, Hoover R, Haile R. Mammographic features and breast cancer risk: effects with time, age, and menopause status. *J Natl Cancer Inst* 1995; 87:1622-1629.
- (14) Boyd NF, Jensen HM, Cooke G, Han HL. Relationship between mammographic and histological risk factors for breast cancer. *J Natl Cancer Inst* 1992; 84:1170-1179.

- (15) Yaffe MJ. Direct digital mammography using a scanned-slot CCD imaging system. *Med Prog Technol* 1993; 19:13-21.
- (16) Sabol JM, Soutar IC, Plewes DB. A method for practical equalization mammography of the radiographically dense breast. *Radiographics* 1995; 15:1191-1202.
- (17) Suryanarayanan S, Karellas A, Vedantham S, Glick SJ, D'Orsi CJ, Baker SP, Webber RL. Comparison of tomosynthesis methods used with digital mammography. *Acad Radiol* 2000; 7:1085-1097.
- (18) Niklason LT, Christian BT, Niklason LE, Kopans DB, Castleberry DE, Opsahl-Ong BH, Landberg CE, Slanetz PJ, Giardino AA, Moore R, Albagli D, DeJule MC, Fitzgerald PF, Fobare DF, Giambattista BW, Kwasnick RF, Liu J, Lubowski SJ, Possin GE, Richotte JF, Wei CY, Wirth RF. Digital tomosynthesis in breast imaging. *Radiology* 1997; 205:399-406.
- (19) Burgess AE, Wagner RF, Jennings RJ, Barlow HB. Efficiency of human visual signal discrimination. *Science* 1981; 214:93-94.
- (20) Boone JM, Lindfors KK, Beatty CS, Seibert JA. A breast density index for digital mammograms based on radiologists' ranking. *J Digit Imaging* 1998; 11:101-115.
- (21) Burgess AE. The Rose model, revisited. *J Opt Soc Am A Opt Image Sci Vis* 1999; 16:633-646.

- (22) Metz CE, Herman BA, Shen JH. Maximum likelihood estimation of receiver operating characteristic (ROC) curves from continuously-distributed data. *Stat Med* 1998; 17:1033-1053.
- (23) Roe CA, Metz CE. Variance-component modeling in the analysis of receiver operating characteristic index estimates. *Acad Radiol* 1997; 4:587-600.
- (24) Pan X, Metz CE. The "proper" binormal model: parametric receiver operating characteristic curve estimation with degenerate data. *Acad Radiol* 1997; 4:380-389.
- (25) Roe CA, Metz CE. Dorfman-Berbaum-Metz method for statistical analysis of multireader, multimodality receiver operating characteristic data: validation with computer simulation. *Acad Radiol* 1997; 4:298-303.
- (26) Barrett HH, Abbey CK, Clarkson E. Objective assessment of image quality. III. ROC metrics, ideal observers, and likelihood-generating functions. *J Opt Soc Am A Opt Image Sci Vis* 1998; 15:1520-1535.
- (27) Burgess AE. Comparison of receiver operating characteristic and forced choice observer performance measurement methods. *Med Phys* 1995; 22:643-655.
- (28) Swensson RG, Judy PF. Measuring performance efficiency and consistency in visual discriminations with noisy images. *J Exp Psychol Hum Percept Perform* 1996; 22:1393-1415.
- (29) Burgess A. Image quality, the ideal observer, and human performance of radiologic decision tasks. *Acad Radiol* 1995; 2:522-526.

- (30) Liu Z, Knill DC, Kersten D. Object classification for human and ideal observers. *Vision Res* 1995; 35:549-568.
- (31) Spratt JS, Greenberg RA, Heuser LS. Geometry, growth rates, and duration of cancer and carcinoma in situ of the breast before detection by screening. *Cancer Res* 1986; 46:970-974.
- (32) Hanley JA. The robustness of the binormal assumptions used in fitting ROC curves. *Medical Decision Making* 1988; 8:197-205.
- (33) Swets JA. Form of empirical ROCs in discrimination and diagnostic tasks: implications for theory and measurement of performance. *Psychological Bulletin* 1986; 99:181-189.
- (34) Linver MN, Osuch JR, Brenner RJ, Smith RA. The mammography audit: a primer for the mammography quality standards act (MQSA). *AJR Am J Roentgenol* 1995; 165:19-25.
- (35) Burrell HC, Pinder SE, Wilson AR, Evans AJ, Yeoman LJ, Elston CW, Ellis IO. The positive predictive value of mammographic signs: a review of 425 non-palpable breast lesions. *Clin Radiol* 1996; 51:277-281.
- (36) Tabar L. Radiology of the minimal breast cancer. *Radiology* 217(P), 54. 11-1-2000.
(Abstract)
- (37) Boone JM, Fewell TR, Jennings RJ. Molybdenum, rhodium, and tungsten anode spectral models using interpolating polynomials with application to mammography. *Med Phys* 1997; 24:1863-1874.

- (38) Hammerstein GR, Miller DW, White DR, Masterson ME, Woodard HQ, Laughlin JS. Absorbed radiation dose in mammography. Radiology 1979; 130:485-491.
- (39) Bushberg JT, Seibert JA, Leidholdt EM, Boone JM. The Essential Physics of Medical Imaging. Baltimore: Williams and Wilkins, 1994.
- (40) Boone JM, Lindfors KK, Cooper VN, Seibert JA. Scatter/Primary in mammography: Comprehensive results. Med Phys 2000; 27:1-9.

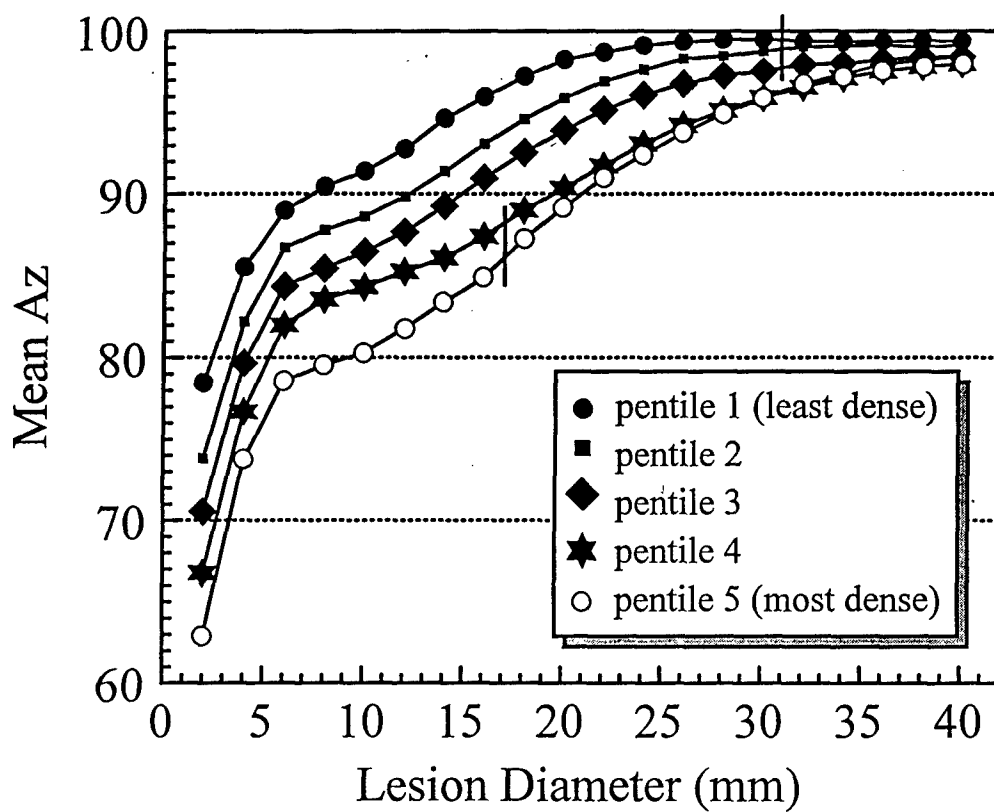


Figure 1

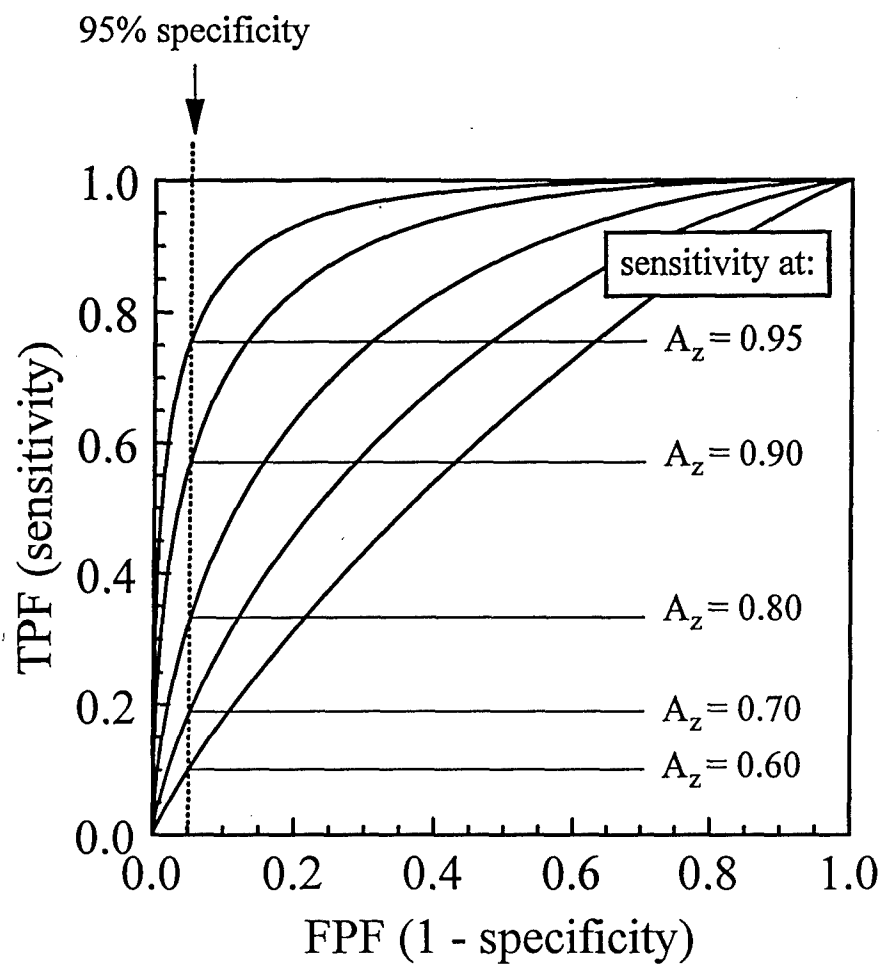


Figure 2

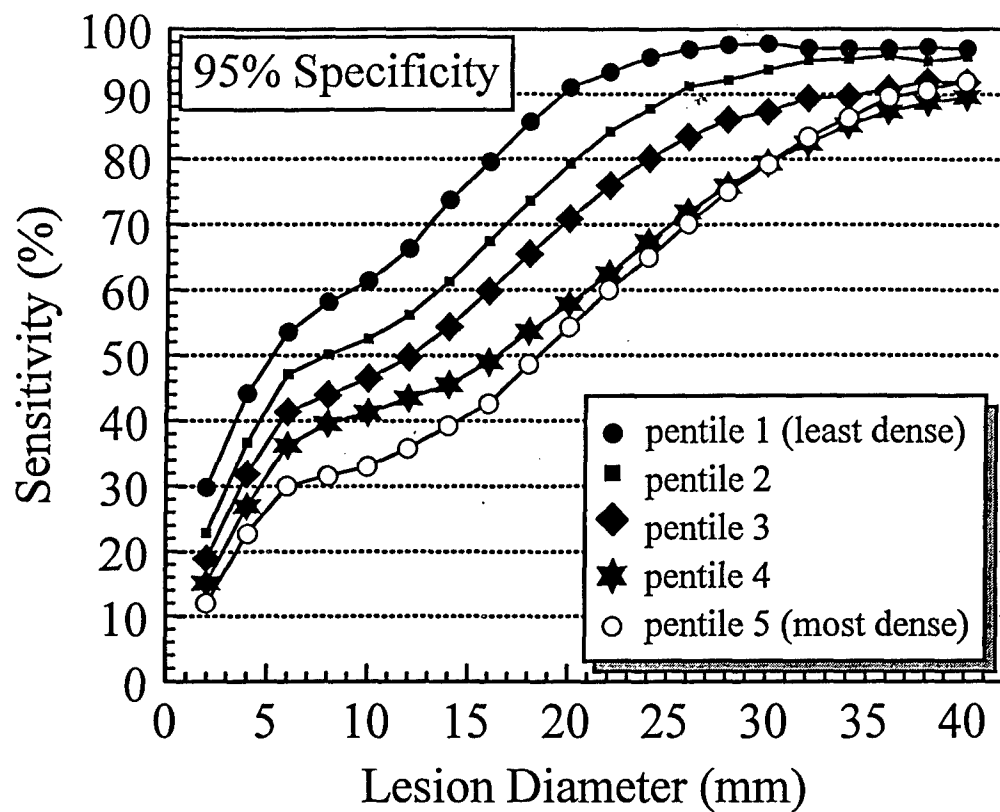


Figure 3A

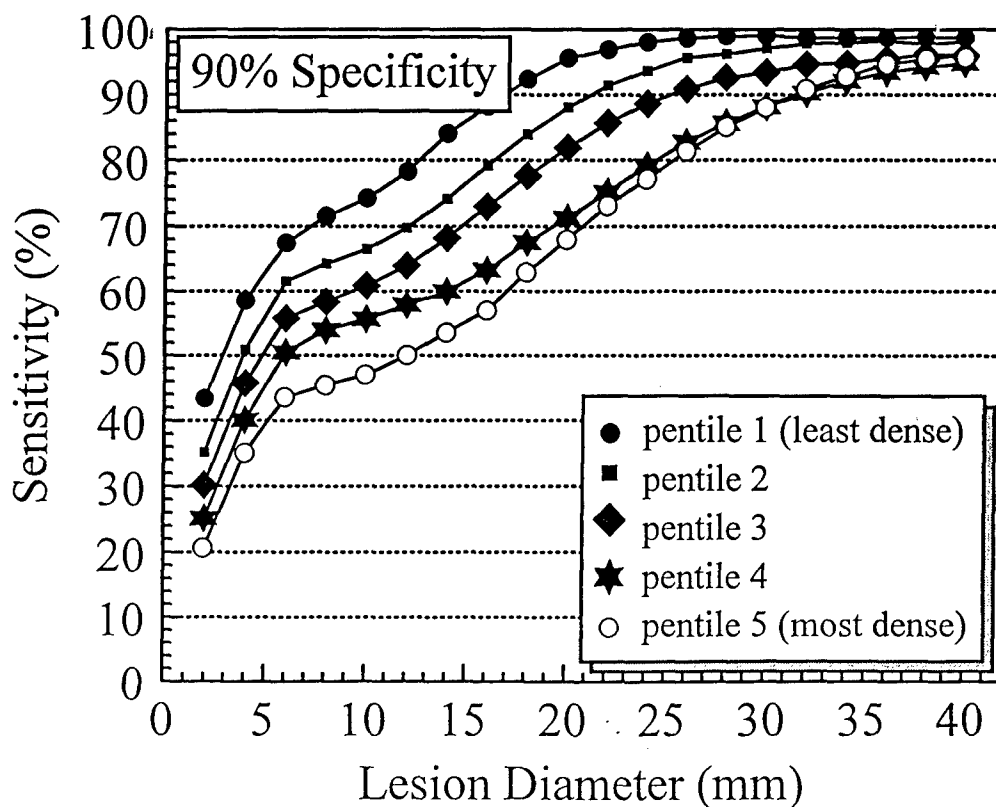


Figure 3B

DAMD17-98-18176, Final Report - August 2001

Computer Simulation of Breast Cancer Screening

PI: John M. Boone, Ph.D.

Appendix C:

JM Boone, JA Seibert, JM Sabol, and M Tecotzky, "A Monte Carlo study of x-ray fluorescence in x-ray detectors", Medical Physics 26, 905-916 (1999)

A Monte Carlo study of x-ray fluorescence in x-ray detectors

John M. Boone^{a)} and J. Anthony Seibert

Department of Radiology, University of California, Davis, UC Davis Medical Center, Sacramento, California 95817

John M. Sabol

Sterling Diagnostic Imaging, Brevard, North Carolina 28712

Melvin Tecotzky

Department of Radiology, Thomas Jefferson University, Philadelphia, Pennsylvania 19107

(Received 5 November 1998; accepted for publication 25 March 1999)

Advances in digital x-ray detector systems have led to a renewed interest in the performance of x-ray phosphors and other detector materials. Indirect flat panel x-ray detector and charged coupled device (CCD) systems require a more technologically challenging geometry, whereby the x-ray beam is incident on the front side of the scintillator, and the light produced must diffuse to the back surface of the screen to reach the photoreceptor. Direct detector systems based on selenium have also enjoyed a growing interest, both commercially and academically. Monte Carlo simulation techniques were used to study the x-ray scattering (Rayleigh and Compton) and the more prevalent x-ray fluorescence properties of seven different x-ray detector materials, $\text{Gd}_2\text{O}_2\text{S}$, CsI, Se, BaFBr, YTaO_4 , CaWO_4 , and ThO_2 . The redistribution of x-ray energy, back towards the x-ray source, in a forward direction through the detector, and lateral reabsorption in the detector was computed under monoenergetic conditions (1 keV to 130 keV by 1 keV intervals) with five detector thicknesses, 30, 60, 90, 120, and 150 mg/cm^2 (Se was studied from 30 to 1000 mg/cm^2). The radial distribution (related to the point spread function) of reabsorbed x-ray energy was also determined. Representative results are as follows: At 55 keV, more (31.3%) of the incident x-ray energy escaped from a 90 mg/cm^2 $\text{Gd}_2\text{O}_2\text{S}$ detector than was absorbed (27.9%). Approximately 1% of the total absorbed energy was reabsorbed greater than 0.5 mm from the primary interaction, for 90 mg/cm^2 CsI exposed at 100 kVp. The ratio of reabsorbed secondary (fluorescence+scatter) radiation to the primary radiation absorbed in the detectors (90 mg/cm^2) (S/P) was determined as 10%, 16%, 2%, 12%, 3%, 3%, and 0.3% for a 100 kVp tungsten anode x-ray spectrum, for the $\text{Gd}_2\text{O}_2\text{S}$, CsI, Se, BaFBr, YTaO_4 , CaWO_4 , and ThO_2 detectors, respectively. The results indicate significant x-ray fluorescent escape and reabsorption in common x-ray detectors. These findings suggest that x-ray fluorescent radiation redistribution should be considered in the design of digital x-ray imaging systems. © 1999 American Association of Physicists in Medicine. [S0094-2405(99)01006-8]

Key words: X-ray fluorescence, K -edge, Monte Carlo, digital image detectors, imaging science

I. INTRODUCTION

For general diagnostic radiology, screen film systems employ dual-emulsion, dual-screen cassettes. In this design, the x-ray phosphor is essentially sliced into two halves, with the photoreceptor (the dual-emulsion film) sandwiched between the two x-ray phosphor screens. This is possible because x rays pass efficiently through the film base and emulsion. Positioning the photoreceptor in the middle of the intensifying screen layers reduces the distance in the screen that light must diffuse through to reach the film emulsion, improving spatial resolution. With digital radiographic systems based on amorphous silicon thin film transistor technology (α -Si TFT),^{1,2} charge coupled devices (CCDs),^{3,4} or complementary metal oxide semiconductors (CMOS),⁵ however, only a single x-ray screen can be used because these photodetectors are radio-opaque. With such systems, the x rays are incident upon the x-ray phosphor from the front, while the photoreceptor collects the light behind the screen. Thus the light emitted by the screen, which is produced preferentially near

the front of the screen, must diffuse through the thickness of the intensifying screen in this geometry. Because of this important difference in x-ray detection geometry, the search for x-ray phosphors for digital systems has led to more exotic detector materials for the digital radiographic application. Because of differences in applications between digital x-ray detectors and screen/film cassettes, the constraints of cost, durability, and high-end spatial resolution are quite different, and this has also fueled a renewed investigation of x-ray detectors for digital imaging.

The K -edge of an x-ray detector material is an important consideration in the detector performance for a given diagnostic imaging task. While it is widely assumed that it is desirable to have the majority of the x-ray photons incident upon the detector with energies above the K -edge, to improve quantum detection efficiency, the re-emission of characteristic radiation (x-ray fluorescence) will reduce the overall absorption efficiency. Worse, when x-ray fluorescence is reabsorbed by the detector adjacent to the primary x-ray in-

teraction, a loss of spatial resolution and an increase in image noise may occur. X-ray fluorescence and related energy absorption phenomena occurring in imaging detectors has been investigated by others.⁶⁻⁹ Previous studies primarily focused on screen-film radiography. In this study, Monte Carlo procedures were used in an analysis of several different possible candidates for x-ray detectors: $\text{Gd}_2\text{O}_2\text{S}$, CsI, Se, YTaO_4 , CaWO_4 , and ThO_2 .

This study focused solely on the Monte Carlo transport of x-ray photons, however, the transport of optical photons in an x-ray scintillation detector (intensifying screen) is also an important consideration and certainly plays the predominant role in broadening the point spread function of the screen. Whereas x-ray intensifying screens are indirect detectors in which optical energy ultimately stimulates the photoreceptor, direct detectors such as Se do not make use of intermediary optical photons. Rather, the detector reads out the charge (electrons) liberated in the detector by direct x-ray interaction. This study was designed in part to compare the x-ray scatter and photoelectric reabsorption contribution to the point spread function in both direct (selenium) and indirect x-ray detectors.

II. METHODS AND MATERIALS

Monte Carlo simulations were employed to study the x-ray absorption, scatter, and x-ray fluorescent reabsorption in a direct x-ray detector material (selenium), a photostimulable phosphor (BaFBr) used in "computed radiography" (CR), and in various x-ray scintillators. The conventional x-ray phosphors studied were $\text{Gd}_2\text{O}_2\text{S}$, YTaO_4 , and CaWO_4 . We have an interest in the potential of ThO_2 as an x-ray phosphor, and therefore included it in this study. Many prototype α -Si TFT systems currently make use of CsI as a scintillator, and hence it is included here as well.

The TART 98 Monte Carlo simulation package was used to study the x-ray transport dynamics in this study. TART is a completely verified Monte Carlo set of programs which has a development history spanning several decades. The current generation of this code was developed at Lawrence Livermore National Laboratory,¹⁰ and distributed on CD ROM by Oakridge National Laboratory.¹¹ The Monte Carlo code uses a script language which allows the user to define relatively complex geometries, and to specify x-ray source properties, emission characteristics, and arbitrary detector chemical compositions and densities. The newest version of TART, TART 98-2, was provided by its developer¹² and was used for the Monte Carlo studies reported here.

The detector under study was partitioned into a series of annuli of increasing radius encompassing a center circle [Fig. 1(A)]. X-ray photons were normally incident upon the center of the circle at a point. The spacing of the concentric annuli was 0.100 mm extending out to 4.5 mm. For each detector composition and thickness, 10^6 x-ray photons were input to the detector at each x-ray energy. X-ray energies ranging from 1 keV to 130 keV by 1 keV increments were studied. For each composition, phosphor thickness, and x-ray energy, two Monte Carlo runs were initiated each with 10^6 photons.

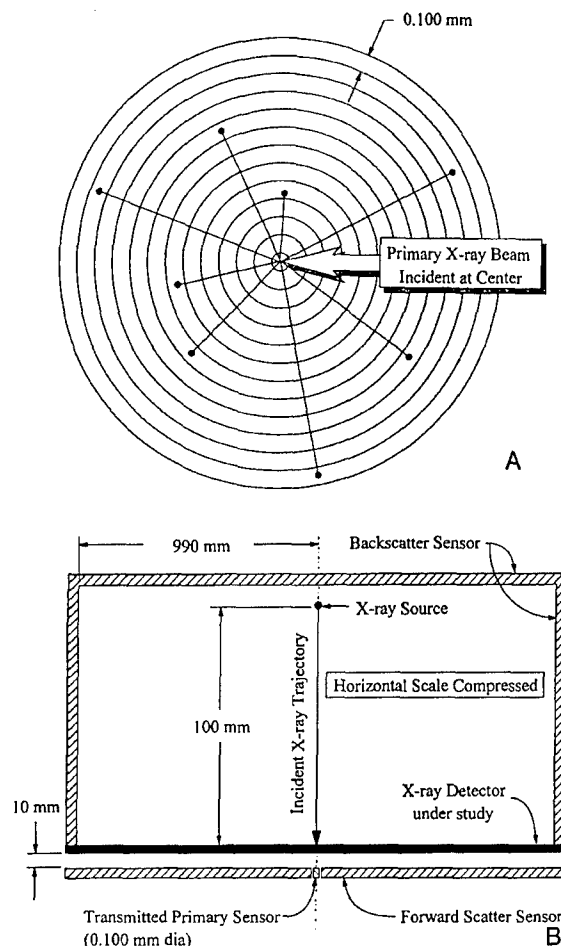


FIG. 1. (A) The geometry of the Monte Carlo simulation is illustrated. The x-ray beam was normally incident upon the x-ray detector under study. For the purposes of the Monte Carlo evaluation, "sensors" were positioned as illustrated in order to measure the backscattered energy, the transmitted primary radiation, and the forward scatter generated in the x-ray detector. (B) The x-ray detector was subdivided into a series of annular regions, each differing in radius by 0.100 mm. The energy absorbed in the center circle and in each annulus was tallied independently in the Monte Carlo simulations.

The first Monte Carlo run ("tracking ON mode") tracked all scattering (Rayleigh and Compton) and x-ray characteristic photons through the detector matrix and the surround. A second Monte Carlo run ("tracking OFF mode") tracked all scatter interactions, however, with this mode the energy resulting from x-ray fluorescence was considered completely deposited at the spatial coordinates of the photoelectric interaction. The results of these two Monte Carlo runs were compared to better understand the relative contributions of scatter (Rayleigh and Compton) compared to x-ray fluorescence.

Densities used for each phosphor composition are given in Table I. With the exception of the amorphous Se and CsI, all the other scintillators were considered to be combined with a 5% weight fraction of binder. The elemental composition (C, H, and O) of Carboset 526 (BF Goodrich, Cleveland, OH) was utilized as the binder, and was added to the various intensifying screen compositions. The physical den-

TABLE I. Physical characteristics of the x-ray detector materials studied.

Detector	Density ^a (g/cm ³)	Element 1 ^b	Element 2 ^b	Binder?
Gd ₂ O ₂ S	7.34	Gd: Z=64, K=50.3 keV	...	✓
CsI	4.51	Cs: Z=55, K=36.0 keV	I: Z=53, K=33.2 keV	
Se	4.79	Se: Z=34, K=12.6 keV	...	
BaFBr	4.56	Ba: Z=56, K=37.5 keV	Br: Z=35, K=13.4 keV	✓
YTaO ₄	7.57	Y: Z=39, K=17.0 keV	Ta: Z=73, K=67.6 keV	✓
CaWO ₄	6.12	W: Z=74, K=69.7 keV	...	✓
ThO ₂	9.86	Th: Z=90, K=110.1 keV	...	✓

^aDensities vary depending on the source. The densities used here were developed by consensus from industrial contacts.

^bOnly the K-edges or atomic numbers of the principal x-ray absorbing elements in the detector material are reported.

sities indicated in Table I were used to adjust the physical thickness of the various x-ray phosphors appropriately. A series of different mass thicknesses (mg/cm²) was studied, ranging from 30 mg/cm² to 150 mg/cm² by 30 mg/cm² intervals. The mass thicknesses reported here do not include the contribution of the Carboset binder, as this is the convention used in the x-ray screen industry.

The x-ray source for each Monte Carlo run consisted of monoenergetic photons normally incident on the x-ray screen [Fig. 1(B)]. The source to detector distance was 100 mm, and a parallel pencil x-ray beam was simulated using a cone with an extremely small cone angle (0.001 deg or 17.5 μ rad). In addition to the source and x-ray detector, a series of x-ray monitors referred to here [and on Fig. 1(B)] as "sensors" were used to monitor the x-ray energy redistribution away from the detector itself. Two sensors forming a closed cylinder on top of the detector were positioned above and around the x-ray source. Together these sensors effectively measured the x-ray fluorescent re-emission and x-ray scatter emanating from the front surface of the x-ray detector [labeled "backscatter sensor" in Fig. 1(B)]. Another sensor, 0.100 mm in diameter, was placed behind the x-ray detector (separated from the bottom of the detector plane by 10 mm) to measure the transmitted primary radiation. A sensor was also placed parallel to and just outside the transmitted primary sensor, and was used to measure the x-ray energy from x-ray fluorescence and scatter mechanisms that were forward-directed. The sensors referred to here and shown in Fig. 1(B) are a fabrication of computer simulation, and in effect are ideal detector systems; they simply measure all the radiation energy striking them, and no scattering, x-ray fluorescence, or transmission occurs at these sensors.

The Monte Carlo experiments led to the generation of a lot of detailed information, however an attempt was made to make the reported results concise. While the Monte Carlo runs themselves were performed using monoenergetic x-ray beams, such beams are not available in radiology departments in general. Therefore, the monoenergetic results were spectrally weighted in some situations using typical polychromatic tungsten-anode spectra in the 40–130 kVp range.¹³

Validation of Monte Carlo studies is essential towards an understanding of the limitations and accuracy of the method. The TART 98 code package is a fully validated Monte Carlo

transport code for photons and neutrons, and is used at national weapons laboratories for simulating energy transport. Additionally, the authors have recently performed extensive comparisons between the TART 98 code and other sources of medical physics related data, derived both experimentally and by the Monte Carlo methods of others. While the comparison work is still in progress, comparisons pertinent to radiation dose levels in mammography have been published¹⁴ and demonstrate excellent agreement with two other sources of data.

The Monte Carlo simulations were performed on 333 MHz and 400 MHz Pentium-based computers running NT 4.0 (Microsoft Corporation, Redmond, WA). A significant amount of custom software (Visual C/C++ 5.0, Microsoft Corporation, Redmond, WA) was used for the generation of the input script files and subsequent analysis of the output results of the TART 98 Monte Carlo package. Some of the data presented in this study were produced by straightforward numerical calculations utilizing the mass attenuation coefficients.¹⁵

III. RESULTS WITH DISCUSSION

A. Stopping power comparisons

In any comparison between various x-ray detectors, it is useful to explore the relative stopping power of different x-ray detector materials. Figure 2 illustrates both the 50% stopping power [Fig. 2(A)] and the 90% stopping power [Fig. 2(B)] for the seven detector materials under study. The photon thickness required to attenuate a given fraction (0.5 or 0.9) of the incident x-ray photons is shown for each detector material as a function of x-ray energy. In general, detector materials with greater density and higher atomic number attenuate efficiently. Selenium, with Z=34 and a relatively low density is the poorest x-ray absorber (Fig. 2), implying that selenium detectors need to be much thicker. In conventional intensifying screens, increasing thickness is usually accompanied by a loss of spatial resolution due to the spread of optical light photons. Selenium detectors, on the other hand, are used to directly detect the charges released in the detector by x-ray ionization. Selenium detector systems currently being studied^{16,17} employ an electric field across the detector surface, which acts to limit (and almost elimi-

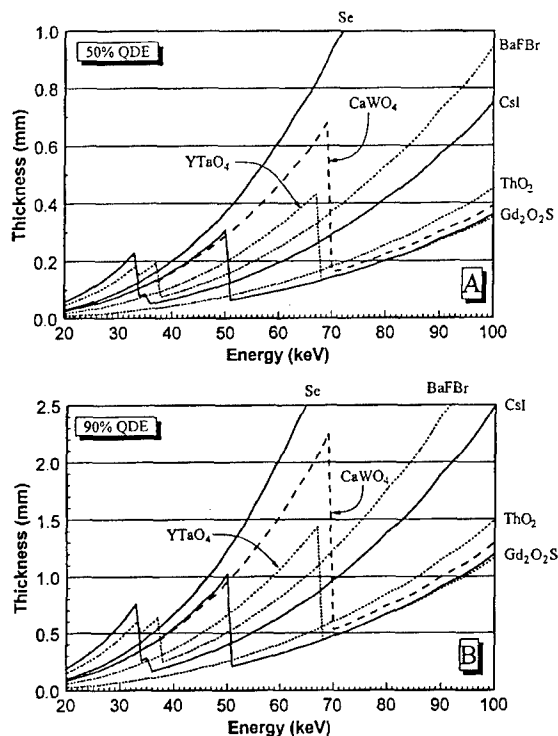


FIG. 2. (A) The thickness of various x-ray detector materials needed to attenuate 50% of the incident x-ray photons is illustrated. (B) The thickness of the detector materials required to achieve 90% quantum detection efficiency, illustrated.

nate) lateral charge diffusion, meaning that the Se thickness can be increased substantially without a loss in spatial resolution. Because of this, the thicknesses of Se studied was extended beyond the thickness range used for the other detector materials, from 30 to 1000 mg/cm². While light spread blurring is not a consideration with Se detectors, extremely thick flat detectors may suffer from parallax problems at the periphery of the field of view and this effect is not considered here.

The detector materials with better absorption properties are the ones with curves near the bottom of Figs. 2(A) and 2(B), indicating a smaller thickness of material is needed to detect the same fraction of incident photons. The BaFBr phosphor, the most common component of CR systems, is seen in Fig. 2 to possess a fairly low x-ray detection efficiency, compared to the other intensifying screen materials illustrated. The advantage that Gd₂O₂S has over CaWO₄ in terms of detection efficiency, and one of the several reasons why this "rare earth" phosphor became dominant in the intensifying screen business in the 1970s, is apparent from Figs. 2(A) and 2(B). These two phosphors are roughly equivalent up to 50 keV, although Gd₂O₂S clearly outperforms CaWO₄ between the Gd *K*-edge at 50.3 keV and the W *K*-edge at 69.7 keV.

Thorium oxide (ThO₂) is a phosphor that the authors have been interested in for some time.^{18,19} It is a known scintillator,¹⁹ with a conversion efficiency of approximately 5%–8%. However, ThO₂ has a radioactive aspect to it that

has precluded its use in screen–film radiography. Since film may in some cases sit next to the intensifying screen in the cassette for hours or even weeks, depending on the cassette usage, radiation-induced artifacts (black spots) would be a serious problem. For use in digital radiography, however, where the total integration time of the photoreceptor signal is very short (comparable to the x-ray exposure time, typically $\ll 1.0$ s), the radioactivity of ThO₂ becomes much less of an issue. As seen from Figs. 2(A) and 2(B), based on its x-ray energy absorption properties, ThO₂ has excellent potential as a radiographic detector. There are advantages of having the *K*-edge of the detector above (110 keV) and the *L*-edge below (20 keV) the x-ray energies used most commonly for general radiography, since this eliminates x-ray characteristic emission.

B. The relative magnitude of energy redistribution

Figure 3 illustrates the way in which incident x-ray energy is distributed phenomenologically for the seven x-ray detector materials studied. Monte Carlo experiments were performed at thicknesses ranging from 30 to 150 mg/cm²; however only the 90 mg/cm² thickness data are presented in Fig. 3 for brevity. The 90 mg/cm² thickness is probably close to the practical thickness used clinically for single-screen, general purpose digital radiography. In Fig. 3, the ordinate axis is logarithmic in order to better present the wide range of the results. For Fig. 3(A) (Gd₂O₂S), at 55 keV (a little above the Gd *K*-edge), the amount of x-ray energy redirected back towards the x-ray tube by backscattering and x-ray fluorescence was 16.5% [as measured by the "backscatter sensor" in Fig. 1(B)] whereas 14.8% of the x-ray energy incident on the detector was directed forward through the detector as secondary emissions [and measured by the "forward scatter sensor" in Fig. 1(B)]. Another 7.6% of the incident energy was redistributed in the x-ray detector itself [Fig. 1(A)] as reabsorbed scatter and fluorescence. At 55 keV, therefore, a total of 38.9% of the incident x-ray energy is redistributed by scattering or x-ray fluorescent events, while only 27.9% of the energy is absorbed as primary. Figure 3(A) demonstrates clearly that the backscatter fraction, forward scatter fraction, and secondary radiation reabsorbed in the screen each experience a dramatic increase at the *K*-edge, implying that the principal component of this redistributed secondary radiation is actually photoelectric re-emission (x-ray fluorescence). There is also a small peak (~3%) in backscatter at 8 keV, corresponding to the *L*-edge fluorescence of gadolinium.

Figures 3(A)–3(G) illustrate the absorbed primary and transmitted primary energy distributions. These curves can be calculated fairly accurately using simple Lambert–Beers Law relationships, but were determined from the Monte Carlo simulations. They are included in Figs. 3(A)–3(G) for reference. The other three curves on each graph were pro-

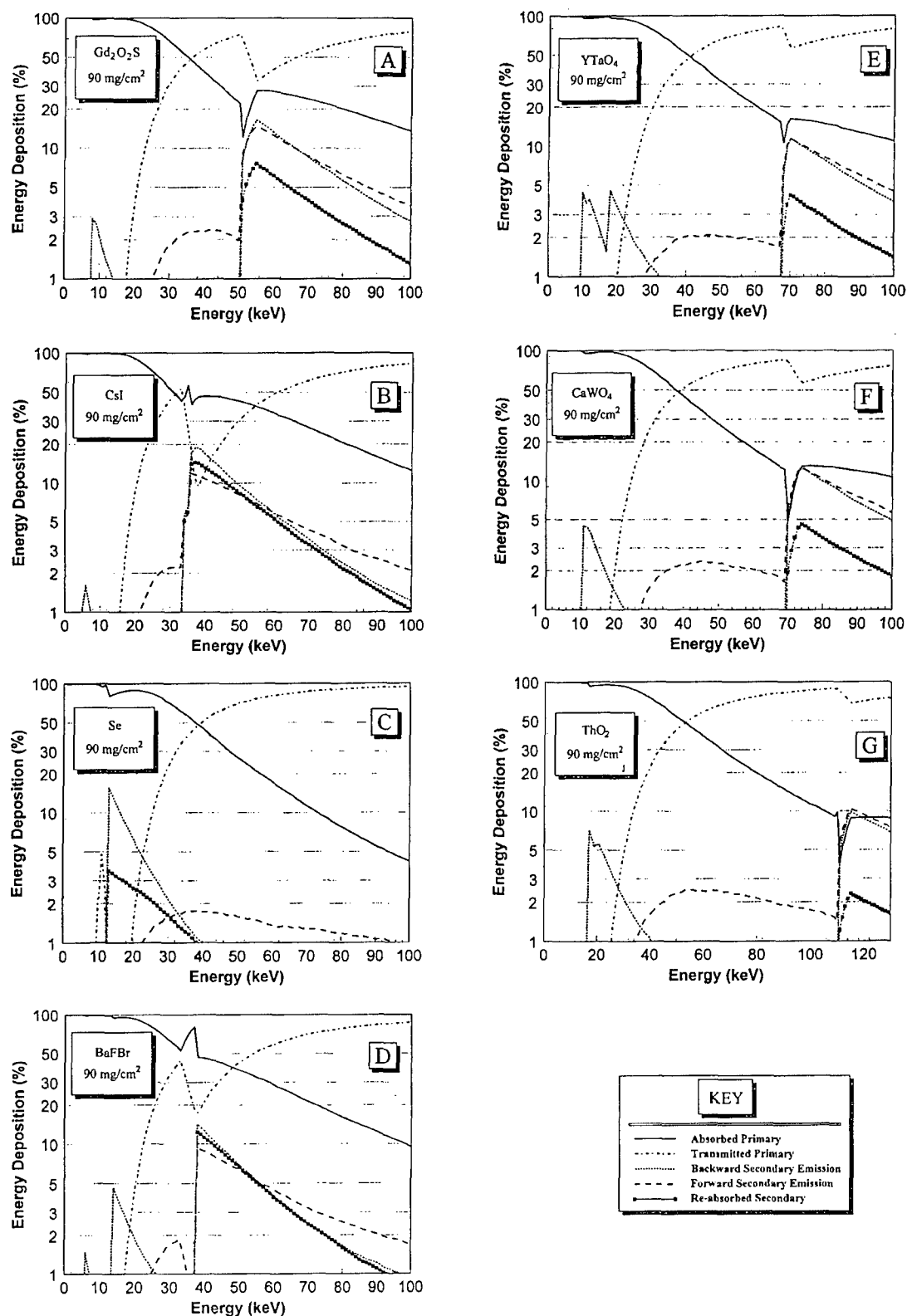


FIG. 3. The energy deposition for seven different x-ray detector materials is illustrated as a function of energy. For all seven figures (A–G), a detector thickness of 90 mg cm^{-2} was simulated. The key indicates the deposition type of each of the five lines illustrated in each graph. The graphs correspond to (A) Gd_2O_2S , (B) CsI , (C) Se , (D) $BaFBr$, (E) $YTaO_4$, (F) $CaWO_4$, and (G) ThO_2 . Notice that the ordinate axis is a logarithmic scale.

duced using Monte Carlo techniques. For the seven detector materials in Fig. 3 (A:Gd₂O₂S, B:CsI, C:Se, D:BaFBr, E:YTaO₄, F:CaWO₄, and G:ThO₂) the graphs illustrate, more or less, the effects discussed in the last paragraph concerning Gd₂O₂S. At the *K*-edge of the detector materials (and to a lesser extent at the *L*-edges), there is a precipitous jump in backward, forward, and lateral (reabsorbed) secondary emissions. On all seven of the detector materials, just above the *K*-edge where x-ray fluorescence is the overwhelming majority of the secondary radiation, it can be seen that the forward scatter and the backscatter are approximately the same. For relatively thin detectors such as those represented in Fig. 3 (90 mg/cm²), since x-ray fluorescence is isotropic, there is an approximately equal chance of forward or backward emission at the photoelectric interaction site. However, because x-ray interactions occur predominantly near the front surface of the detector, x-ray fluorescent photons which are forwardly directed may be absorbed in the detector thickness. For detector materials with lower *K*-edges, such as CsI [Fig. 3(B)] and BaFBr [Fig. 3(D)], this effect is amplified because the low energy of the x-ray fluorescent photons reduce their probability of penetrating the thickness of the detector.

Figure 4 illustrates the redistributed energy curves (as shown in Fig. 3) for Gd₂O₂S, which is illustrative of the other detector materials. Figure 4(A) shows backward emissions from the detector, Fig. 4(B) illustrates the forward emissions, and Fig. 4(C) shows the secondary radiation reabsorbed laterally in the detector. These data are shown on a linear axis, and the curves for all five detector thicknesses are illustrated to convey the trends of secondary re-emission that are detector-thickness related. First of all, an abrupt jump occurs in all curves [Figs. 4(A), 4(B), and 4(C)] at 51 keV, just above the 50.3 keV *K*-edge of Gd. Since Rayleigh and Compton scattering cross sections do not experience dramatic changes in cross section, whereas the photoelectric interaction does, clearly most of the secondary energy redistribution is due to x-ray fluorescence and very little is due to Rayleigh or Compton scattering. For the case in which x-ray fluorescence is re-emitted back towards the x-ray source [Fig. 4(A)], there is an increase in the percentage of energy being "backscattered" as the detector thickness increases. In fact, there is no mechanism to suggest that this trend reverses, and one would therefore anticipate that with increasing detector thickness (beyond 150 mg/cm²), the curves would continue to increase in height, albeit slowly, and at some point no change would be observed with increasing thickness.

How does the re-emission of x-ray fluorescence back towards the x-ray tube affect the imaging performance in digital radiography? First, radiation that "bounces off" the front surface of the x-ray detector is headed back (through the antiscatter grid, if present) toward the patient, and much of this energy will be absorbed in the patient as radiation dose. In detector optimization scenarios where patient dose is considered,^{20,21} the dose contribution due to x-ray fluorescence may be significant and should be considered in optimization calculations. However, it is expected from geo-

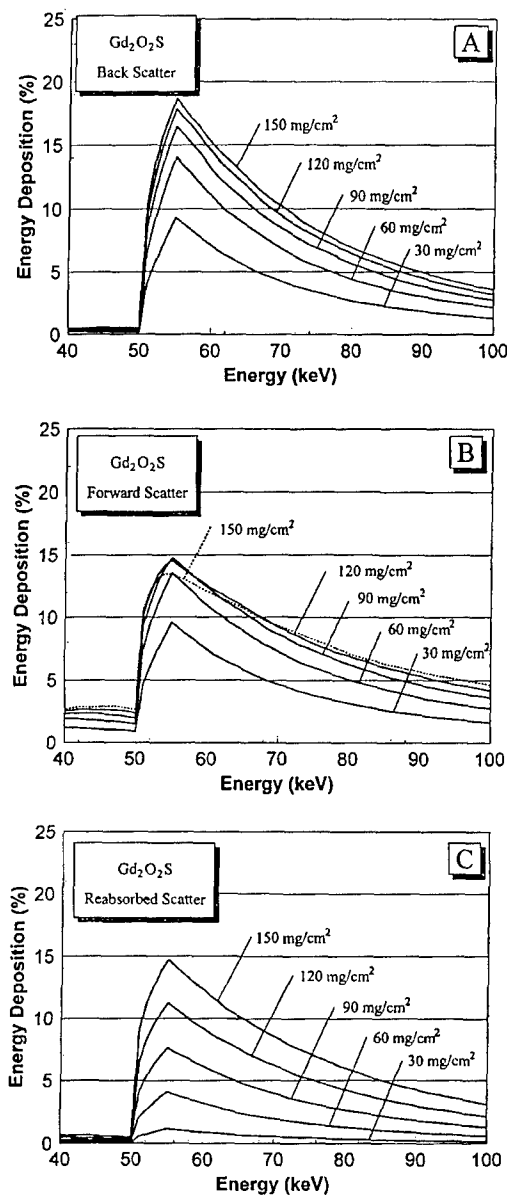


FIG. 4. The energy deposition near the *K*-edge of Gd₂O₂S is illustrated for the five detector thickness indicated. In (A), the "backscatter" is illustrated, in (B) the energy escaping the x-ray detector in the forward direction (opposite the x-ray source) is indicated, and in (C) the fraction of reabsorbed scatter is illustrated. In this figure, the term "scatter" refers to both photoelectric readmission as well as Rayleigh and Compton scatter.

metrical considerations that the presence of an antiscatter grid between patient and detector would substantially reduce patient exposure, although above 88 keV, the backwards-directed x-ray fluorescence of the lead in the grid slats would become a concern. Second, x-ray detector systems perform best when each x-ray quantum absorbed in the detector contributes the same size signal in the detector electronics. Take the example of a 70 keV incident x-ray interacting by the photoelectric effect in a Gd₂O₂S detector. In those interactions where the x-ray fluorescent energy is reabsorbed in the detector, the signal generated corresponds to the deposition

of 70 keV. However, when K escape occurs, the energy deposited in the detector is $70 - 50 = 20$ keV, generating a signal just 29% of the previous example. Therefore, the escape or lateral reabsorption of x-ray fluorescence results in a broadening of the signal variance per incident x-ray photon, and this acts to reduce the detective quantum efficiency (DQE) of the detector system.^{2,22-26}

In Fig. 4(B), the curve corresponding to the thickest detector (150 mg/cm^2) "bends over," that is, the curves (in the 50–70 keV range, at least) appear to have reached a maximum somewhere near the 120 mg/cm^2 thickness, and the fractional energy allocation to forward scattering decreases with increasing thickness past this point. The mechanisms were alluded to previously, where most x-ray interactions occur at the entrant surface of the detector. Fluorescent x-ray photons emitted with a forward scatter trajectory tend to be attenuated by increasing detector thickness. Indeed, in the limit of infinite screen thickness, the amount of secondary energy passing through the screen in the forward direction would drop to zero. This investigation is focused on evaluating properties of x-ray detectors for digital radiography systems. For indirect systems such as a -Si TFTs, CCDs, or CMOS systems, the amount of x-ray radiation reaching the silicon electronics is a source of concern. X-rays reaching and interacting with the silicon electronics can cause the appearance of "snow" on the image, and over prolonged periods may cause radiation damage.²⁷ Standard Lambert Beers calculations will underestimate the fraction of x-ray energy reaching the photoreceptor. At the energies just above the detector K -edges, a significant fraction (e.g., $\sim 10\%$ – 15% in the 50–70 keV energy region for $\text{Gd}_2\text{O}_3\text{S}$) of the incident x-ray energy is seen to be re-emitted as fluorescence directed towards the photoreceptor.

Figure 4(C) demonstrates that the fraction of energy reabsorbed in the detector (laterally) increases with detector thickness. This component of x-ray energy deposition is the integrated energy deposited in all the concentric annuli except for the innermost circle [see Fig. 1(A)].

Figures 2–4 illustrate energy allocation trends as a function of monoenergetic x-ray energy, as opposed to "real world" polyenergetic x-ray sources. While x-ray fluorescent energy that escapes the detector in either direction has some subtle adverse effects as discussed above, x-ray fluorescence that is reabsorbed in the detector may cause either a reduction in the spatial resolution, an increase in noise, or both. Figure 5 illustrates the secondary radiation/primary radiation fraction (S/P) absorbed in the detector, as a function of polyenergetic x-ray beams ranging from 40 kVp to 130 kVp. The x-ray spectra were generated²⁸ assuming a standard tungsten anode x-ray system with 2.0 mm of added Al filtration and were calculated at 5 kVp intervals. The five detector thicknesses ranging from 30 mg/cm^2 to 150 mg/cm^2 are shown (200 – 1000 mg/cm^2 for Se). The thickness labels are omitted in Figs. 5(B) and 5(D), 5(G) for clarity.

In Fig. 5(A), the S/P ratio increases rapidly as the kVp exceeds the 50 keV K -edge of the Gd-based detector. In Fig. 5(B), the curves rapidly increase from the 33 to 35 keV K -edges of cesium and iodine; however, the graph is limited

to 40 kV and above since x-ray spectra generated below 40 kVp are rarely used in general radiography settings. The S/P ratios for CsI [Fig. 5(B)] are quite high, reaching $\sim 17\%$ for the 90 mg/cm^2 detector in the 65–90 kVp region. The S/P ratios for selenium [Fig. 5(C)] are quite low, in part due to the low K -edge of selenium (12.6 keV). BaFBr demonstrates a S/P ratio of $\sim 12\%$ above 70 kVp [Fig. 5(D)] for the 90 mg/cm^2 detector. The detectors comprised of YTaO_4 [Fig. 5(E)] and CaWO_4 [Fig. 5(F)] show marked increases in the S/P ratio above their respective K -edges of 67.6 keV and 69.7 keV, respectively; however, the overall S/P ratio is lower with these detectors compared to $\text{Gd}_2\text{O}_3\text{S}$ and CsI. The ThO_2 detector, with S/P results shown in Fig. 5(G) shows very low S/P values ($<1\%$) across the usable energy region. The secondary component (the numerator of S/P) is primarily x-ray fluorescence, and with a K -edge of 110 keV, fluorescence is not produced with most clinical x-ray spectra. There is another source of "secondary" radiation in a thorium-based detector, that from radioactive emissions in the screen itself (thorium is a 4 MeV α^{++} emitter with a 1.4×10^{10} year half-life). This consideration is beyond the scope of this study.

C. Lateral reabsorption of scattered and fluorescent energy

The geometry of the Monte Carlo studies [Figs. 1(A) and 1(B)] was designed to allow the assessment of the lateral (radial) distribution of energy, away from the point where the incident x-ray beam was incident upon the detector. Figure 6 illustrates the radial distribution of energy for the 90 mg/cm^2 $\text{Gd}_2\text{O}_3\text{S}$ detector under various simulation conditions. This figure is provided to directly illustrate the role of x-ray fluorescence relative to Rayleigh and Compton scattering. The results of three different Monte Carlo runs are illustrated, as indicated in the figure. The Monte Carlo routine provides the option to turn on or off the tracking of characteristic x-ray emissions, and if routine was run in the "tracking OFF" mode, the energy of the characteristic x-ray was deposited at the site of the photoelectric interaction. Two curves are shown in Fig. 6 at 51 keV, just above the K -edge of Gd; and the 51 keV "tracking ON" curve shows a radial distribution profile with much greater amplitude than the 51 keV "tracking OFF" curve. The 51 keV "tracking OFF" curve shows the radial distribution of energy due to Rayleigh and Compton scattering only, while the 51 keV "tracking ON" curve also includes the effect of fluorescence. To further illustrate the role of fluorescence, the results from a 50 keV "tracking ON" run are shown. While x-ray fluorescence was tracked, the 50 keV simulation was just below the 50.3 keV K -edge of Gd, and therefore K -shell fluorescence was not produced. Consequently, the 50 keV "Tracking ON" curve is comparable to the 51 keV "Tracking OFF" curve, with differences being due to L -edge fluorescence and stochastic effects. The exponential tails of the 51 keV "Tracking ON" and "Tracking OFF" curves were computer fit ($r \geq 0.98$) over the radial distances between 0.10 mm and 1.0 mm. The y -intercept ratio was calculated as

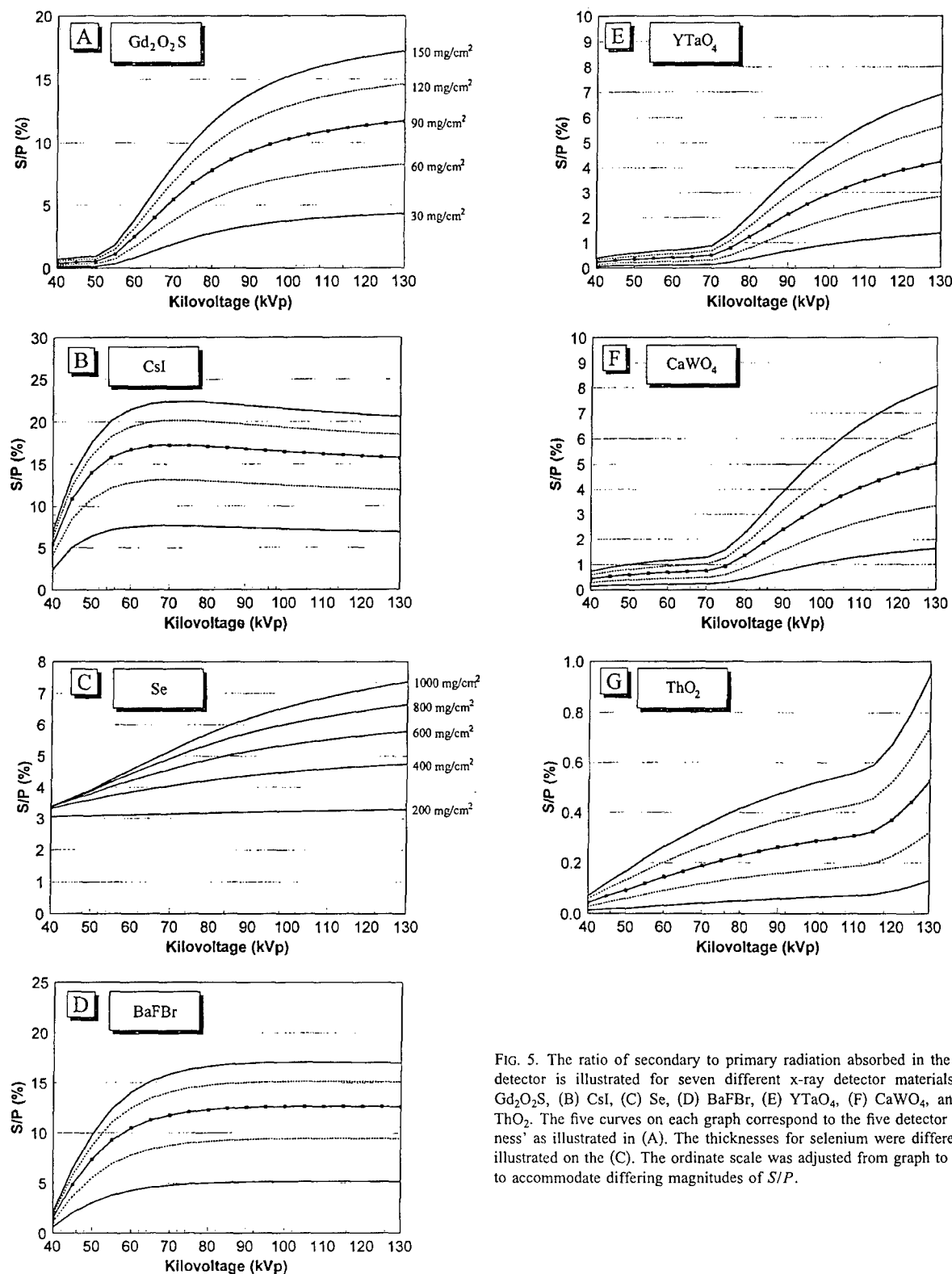


FIG. 5. The ratio of secondary to primary radiation absorbed in the x-ray detector is illustrated for seven different x-ray detector materials; (A) Gd_2O_2S , (B) CsI, (C) Se, (D) BaFBr, (E) $YTaO_4$, (F) $CaWO_4$, and (G) ThO_2 . The five curves on each graph correspond to the five detector thicknesses as illustrated in (A). The thicknesses for selenium were different, as illustrated on the (C). The ordinate scale was adjusted from graph to graph to accommodate differing magnitudes of S/P .

18.2, suggesting that the difference in amplitude between fluorescence+scatter vs scatter alone is approximately a factor of 20. Clearly, x-ray fluorescence is the predominant contributor toward the lateral spread of energy in the detector.

Figure 7 shows the effect of detector thickness for the Gd_2O_2S detector at 51 keV. The curves shown in Fig. 7 illustrate the radial distribution of energy due (primarily) to x-ray fluorescence. Energy deposition was calculated by

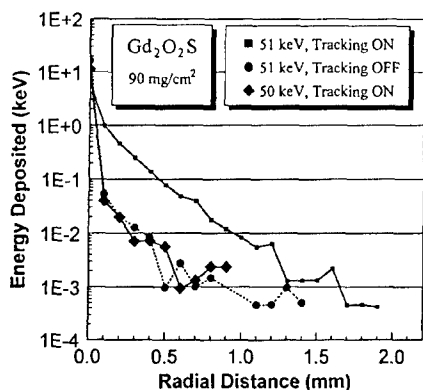


FIG. 6. The radial distribution of the energy deposition as determined in the Monte Carlo simulations is shown for various Monte Carlo runs. The results for a 90 mg/cm² thick Gd₂O₂S intensifying screen are shown. The two "tracking ON" curves straddled the K-edge of Gd, and the difference between the curves illustrates the influence of x-ray fluorescence. The two 51 keV curves, one which followed x-ray fluorescence and one which did not, also demonstrate that the influence of x-ray fluorescence is greater than an order of magnitude greater than the combined influence of Rayleigh and Compton scattering.

summing the energy over all radial distances. As shown in Fig. 4(C), the magnitude of energy reabsorbed in the detector increases with detector thickness. Figure 7 also shows this trend, with the thicker detectors experiencing markedly more energy deposited at a given distance than the thinner detectors. For example, at a radial distance of 0.50 mm, the ratio of energies deposited in 150 and 30 mg/cm² thick detectors is 28.

The radial distribution of fractional energy deposition is illustrated in Figs. 8(A)–8(G). Curves are shown for each detector thickness studied, with the 30 mg/cm² curve consistently being the lowest and the 150 mg/cm² being the uppermost [the Se thicknesses were different, and are indicated in Fig. 8(C)], with monotonic progression of curves between thicknesses. Each curve was produced by weighting 100 monoenergetic curves (1 keV–100 keV) by a 100 kVp x-ray spectrum, as described previously. The curves shown in Fig. 8 must be interpreted carefully. These are not "cuts"

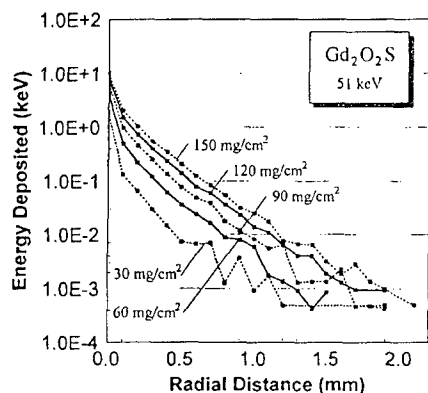


FIG. 7. This figure illustrates the influence of detector thickness on the radial distribution. Not surprisingly, the thicker detectors result in a broadened radial distribution.

through the point spread function (PSF) of the detector, because the energy at each radial distance Γ is integrated around the annulus of radius Γ [Fig. 1(E)]. Therefore, the curves illustrated in Fig. 8 must be multiplied by $1/\Gamma$ to yield the PSF. Such a procedure would attenuate the profiles shown to even lower levels.

The curves in Fig. 8 are shown on semilogarithmic axes, and certainly the amount of x-ray energy distributed radially at some distance Γ (as shown on the figures) appears very small. However, to compute the total amount of energy redistributed radially, one has to integrate the individual curves. This was computed, and the results are shown in Fig. 9 for the three most practical thicknesses for radiographic applications. For example, in Fig. 9(A), the CsI curve (open circles) at a radial distance of 0.50 mm has an ordinate value of 0.80%. This means that 0.80% of the absorbed energy for the 60 mg/cm² CsI detector was deposited *outside* a circle 0.5 mm in radius, and conversely 99.20% of the absorbed energy was deposited *within* a circle 1.0 mm in diameter.

IV. FURTHER DISCUSSION

The redistribution of x-ray energy in an x-ray detector was the focus of this investigation. Other factors are also responsible for the redistribution of signal intensity in an image receptor. For example, the full-width at half-maximum (FWHM) of the line spread function for a Lanex screen (120 mg/cm² Gd₂O₂S) is approximately 1.9 mm, and the radial distribution profiles calculated here (Fig. 8) imply that the FWHM of the line spread or point spread function due to x-ray fluorescence and x-ray scattering is much narrower, on the order of 0.10 mm. Under most conditions, therefore, the spread function owing to the lateral diffusion of optical photons in an intensifying screen will completely dominate the point spread function of the system. In the case of a direct detector, however, where an electric field across the plane of the detector effectively eliminates the lateral diffusion of electronic charge liberated in the detector, x-ray fluorescence could degrade spatial resolution (i.e., broaden the point spread function).

Does x-ray fluorescence contribute to a loss of spatial resolution by broadening the PSF, or does it contribute to noise? The short answer is probably both. Take as an example an imaginary x-ray intensifying screen that experiences no lateral diffusion of the light photons emitted; and therefore has a near-perfect PSF. X-ray fluorescent photons which are emitted at a point P and then are reabsorbed in the screen a distance Γ away from that point, will be resolved as separate points. The signal generated by the reabsorbed fluorescent x-ray will contribute to the noise in the detector. Because the distance between the site of initial photoelectric interaction and the site of the fluorescent photons interaction is nonrandom (and has a well-defined probability density function as shown in Fig. 8), the noise due to fluorescent reabsorption will be correlated.²⁵ Continuing with the example, let the width of the optical diffusion PSF component of the intensifying screen be increased. Now when the fluorescent x-ray photon is reabsorbed a distance Γ away from

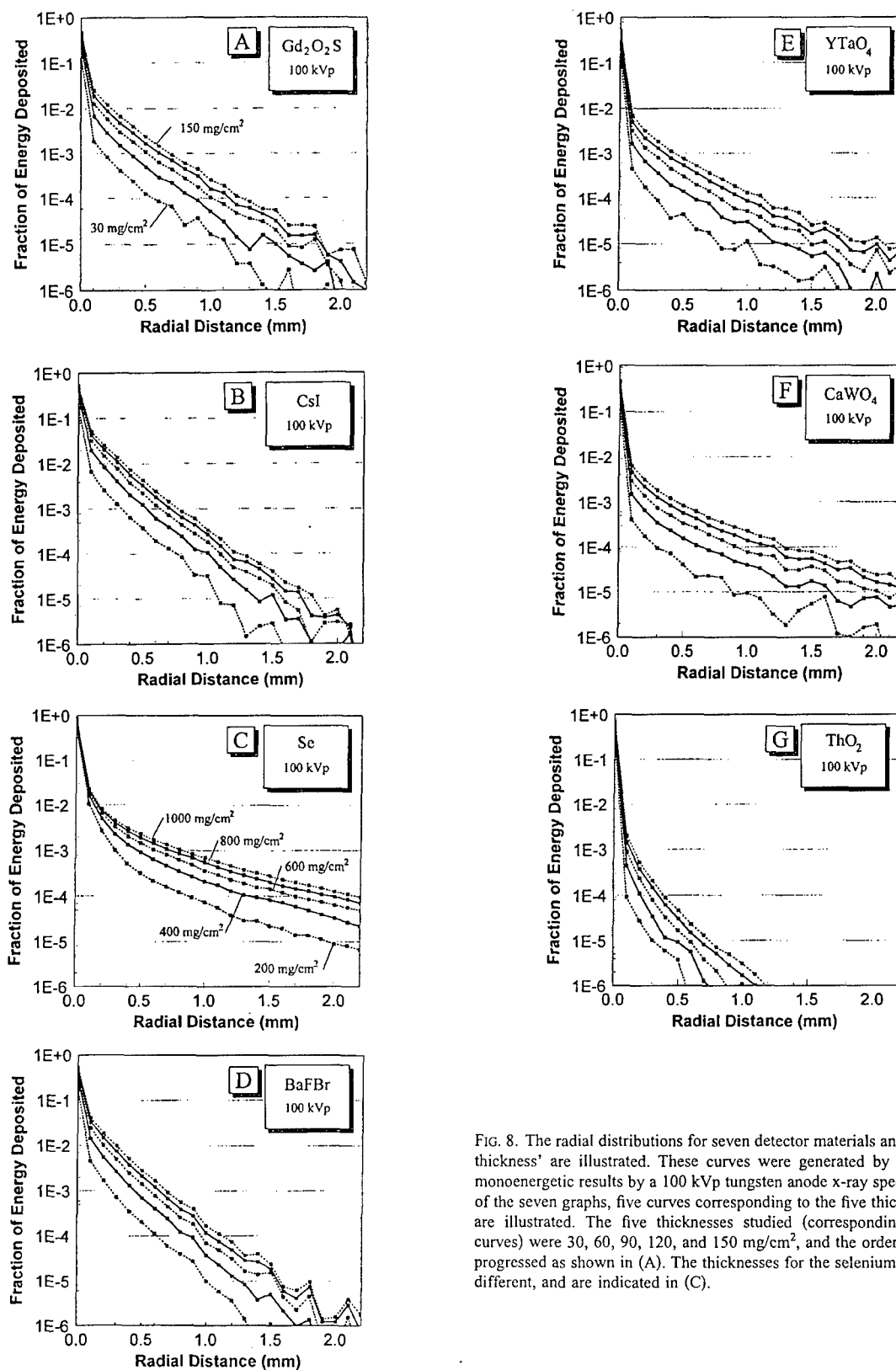


FIG. 8. The radial distributions for seven detector materials and five detector thicknesses are illustrated. These curves were generated by weighting the monoenergetic results by a 100 kVp tungsten anode x-ray spectrum. In each of the seven graphs, five curves corresponding to the five thicknesses studied are illustrated. The five thicknesses studied (corresponding to the five curves) were 30, 60, 90, 120, and 150 mg/cm^2 , and the order of the curves progressed as shown in (A). The thicknesses for the selenium detector were different, and are indicated in (C).

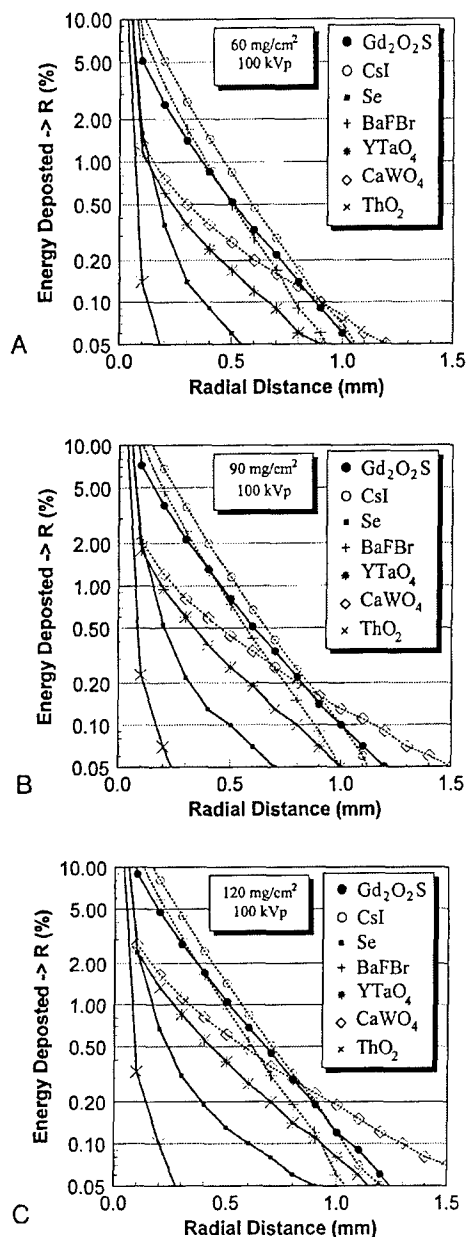


FIG. 9. The curves illustrate the fraction (in %) of absorbed x-ray energy that is deposited outside a given radial distance. The figures are for (A) 60 mg/cm² detector thicknesses, (B) for 90 mg/cm² detector thicknesses, and (C) for 120 mg/cm² detector thicknesses. For example, in (B) 0.50% of the energy absorbed in the Gd₂O₃S detector was reabsorbed greater than 0.60 mm away from the position of the incident primary x-ray beam.

the primary interaction point *P*, the optical signals generated in the two interactions are blurred together such that they both contribute to the signal under the point spread "cone." In this case, because the fluorescent photon is not resolved spatially, it no longer is a source of noise but rather becomes part of the signal. Furthermore, by combining the signals generated by the photoelectric interaction and the reabsorbed fluorescent x-ray under the same signal cone, the signal to noise ratio would slightly increase, although this is a rela-

tively small contribution.^{24,25} So, while optical photon broadening of the PSF of an intensifying screen obviously reduces the spatial resolution of that detector, it also increases the SNR somewhat.

In a real x-ray intensifying screen with optical photon induced PSF widths in millimeters, it is likely given the very short range of radial redistribution (Fig. 8) for x-ray fluorescence (and scatter), that the majority of fluorescent interactions occur within the point spread cone. Some small fraction will occur outside the signal cone, and these will contribute a source of a correlated noise to the image. To give real numbers to this example, for 90 mg/cm² Cs I exposed at 100 kV [Fig. 9(B)], 2% of the absorbed energy is deposited outside a circle of diameter of 0.80 mm, and 0.5% of the absorbed energy is deposited outside a circle 1.3 mm in diameter. In a pixelated digital detector system designed for general radiography, which pixel dimensions in the 100–200 μm range, some small but not negligible redistribution effects due to x-ray fluorescence will be realized.

V. SUMMARY

The *K*-edge(s) of a detector material are traditionally thought of as an opportunity to improve the energy absorption of the detector; however the results of this study indicate that this opportunity is fraught with compromise. The emission of characteristic x-rays after photoelectric interactions in the detector results in a substantial loss in energy absorption at the interaction site, and this transiently absorbed x-ray energy is then dispersed backward, forward, and laterally in the detector. The radial distribution of x-ray fluorescence will have little consequence on the point spread function of scintillation detectors studied. In selenium direct detectors with their near-perfect point spread functions, however, reabsorbed x-ray fluorescence may be more of a concern. Finally, the properties of a little studied phosphor, ThO₂, appear promising in the context of energy absorption.

ACKNOWLEDGMENTS

This research was supported in part from grants from the United States Army Breast Cancer Research Program (DAMD 17-94-J-4424 and DAMD 17-98-1-8176), the California Breast Cancer Research Program (1RB-0192), and the National Cancer Institute (R21 CA82077-01). We are grateful to Dr. Red Cullen for providing the TART 98-2 update to the authors for its use in this study.

^{a)}Address for correspondence: John M. Boone, Ph.D., Department of Radiology, UC Davis Medical Center, 4701 X Street, Sacramento, CA 95817. Phone: (916) 734-3158; FAX: (916) 734-0316; electronic mail: jmbone@ucdavis.edu

¹L. E. Antonuk, Y. el-Mohri, J. H. Siewerdsen, J. Yorkston, W. Huang, V. E. Scarpine, and R. A. Street, "Empirical investigation of the signal performance of a high-resolution, indirect detection, active matrix flat-panel imager (AMFPI) for fluoroscopic and radiographic operation," *Med. Phys.* **24**, 51–70 (1997).

²J. H. Siewerdsen, L. E. Antonuk, Y. el-Mohri, J. Yorkston, W. Huang, and I. A. Cunningham, "Signal, noise power spectrum, and detective quantum efficiency of indirect-detection flat-panel imagers for diagnostic radiology," *Med. Phys.* **25**, 614–628 (1998).

- ³T. T. Farman and A. G. Farman, "Clinical trial of panoramic dental radiography using a CCD receptor," *J. Digit. Imaging* **11**, 169–171 (1998).
- ⁴S. Hejazi and D. P. Trauernicht, "System considerations in CCD-based x-ray imaging for digital chest radiography and digital mammography," *Med. Phys.* **24**, 287–297 (1997).
- ⁵T. Yu, J. M. Sabol, J. A. Seibert, and J. M. Boone, "Scintillating fiber optic screens: A comparison of MTF light conversion efficiency, and emission angle with $Gd_2O_2S: Tb$ screens," *Med. Phys.* **24**, 279–285 (1997).
- ⁶H. P. Chan and K. Doi, "Energy and angular dependence of x-ray absorption and its effect on radiographic response in screen–film systems," *Phys. Med. Biol.* **28**, 565–579 (1983).
- ⁷H. P. Chan and K. Doi, "Studies of x-ray energy absorption and quantum noise properties of x-ray screens by use of Monte Carlo simulation," *Med. Phys.* **11**, 37–46 (1984).
- ⁸C. S. Chen, K. Doi, C. Vyborny, H. P. Chan, and G. Holje, "Monte Carlo simulation studies of detectors used in the measurement of diagnostic x-ray spectra," *Med. Phys.* **7**, 627–635 (1980).
- ⁹Y. Kodera, K. Doi, and H. P. Chan, "Absolute speeds of screen–film systems and their absorbed-energy constants," *Radiology* **151**, 229–236 (1984).
- ¹⁰D. E. Cullen, "A coupled neutron–photon 3D combinatorial geometry Monte Carlo transport code," UCRL-ID 126455, 1997.
- ¹¹The Monte Carlo code was distributed through the Oak Ridge National Laboratory Radiation Safety Information Computational Center: <http://www.rsicc.ornl.gov/codes.ccc.ccc6.ccc-638.html>.
- ¹²Dr. Red Cullen at Lawrence Livermore National Laboratory provided the TART 98-2 update to the authors (see acknowledgments).
- ¹³J. M. Boone and J. A. Seibert, "An accurate method for computer-generating tungsten anode x-ray spectra from 30 to 140 kV," *Med. Phys.* **24**, 1661–1670 (1997).
- ¹⁴J. M. Boone, "Monte Carlo assessment of glandular breast dose for monoenergetic and high-energy polyenergetic x-ray beams," *Radiology* (in press).
- ¹⁵J. M. Boone and A. E. Chavez, "Comparison of x-ray cross sections for diagnostic and therapeutic medical physics," *Med. Phys.* **23**, 1997–2005 (1996).
- ¹⁶D. L. Lee, L. K. Cheung, B. G. Rodricks, and G. F. Powell, "Improved imaging performance of a 14×17 in direct radiography system using a Se/TFT detector," *SPIE* **3336**, 14–23 (1998).
- ¹⁷U. Neitzel, I. Maack, and S. Gunther-Kohfahl, "Image quality of a digital chest radiography system based on a selenium detector," *Med. Phys.* **21**, 509–516 (1994).
- ¹⁸T. Moeller and M. Tecotzky, "Observations on the rare earths. Napht-hazarin complexes of certain rare earth metal ions," *J. Am. Chem. Soc.* **77**, 2649–2650 (1955).
- ¹⁹J. Hubert and P. Thouvenot, "Luminescence properties of Eu^{3+} and Am^{3+} in thorium oxide," *J. Alloys Compd.* **80**, 193–200 (1992).
- ²⁰J. M. Boone and J. A. Seibert, "A comparison of mono- and polyenergetic x-ray beam performance for radiographic and fluoroscopic imaging," *Med. Phys.* **21**, 1853–1863 (1994).
- ²¹J. M. Boone, G. S. Shaber, and M. Tecotzky, "Dual-energy mammography: A detector analysis," *Med. Phys.* **17**, 665–675 (1990).
- ²²J. T. Dobbins, D. L. Ergun, L. Rutz, D. A. Hinshaw, H. Blume, and D. C. Clark, "DQE(f) of four generations of computed radiography acquisition devices," *Med. Phys.* **22**, 1581–1593 (1995).
- ²³J. P. Bissonnette, I. A. Cunningham, D. A. Jaffray, A. Fenster, and P. Munro, "A quantum accounting and detective quantum efficiency analysis for video-based portal imaging," *Med. Phys.* **24**, 815–826 (1997).
- ²⁴I. A. Cunningham, M. S. Westmore, and A. Fenster, "A spatial-frequency dependent quantum accounting diagram and detective quantum efficiency model of signal and noise propagation in cascaded imaging systems," *Med. Phys.* **21**, 417–427 (1994).
- ²⁵I. A. Cunningham, "Linear systems modeling of parallel cascaded stochastic processes: The NPS of radiographic screens with reabsorption of characteristic x radiation," *SPIE* **3336**, 220–230 (1998).
- ²⁶J. H. Siewerdsen, L. E. Antonuk, Y. el-Mohri, J. Yorkston, W. Huang, J. M. Boudry, and I. A. Cunningham, "Empirical and theoretical investigation of the noise performance of indirect detection, active matrix flat-panel imagers (AMFPIs) for diagnostic radiology," *Med. Phys.* **24**, 71–89 (1997).
- ²⁷J. M. Boudry and L. E. Antonuk, "Radiation damage of amorphous silicon, thin-film, field-effect transistors," *Med. Phys.* **23**, 743–754 (1996).
- ²⁸J. M. Boone, T. R. Fewell, and R. J. Jennings, "Molybdenum, rhodium, and tungsten anode spectral models using interpolating polynomials with application to mammography," *Med. Phys.* **24**, 1863–1874 (1997).

DAMD17-98-18176, Final Report - August 2001

Computer Simulation of Breast Cancer Screening

PI: John M. Boone, Ph.D.

Appendix D:

VN Cooper, JM Boone, and JA Seibert, C Pellot-Barakat, "An edge spread technique for measurement of the scatter to primary ratio in mammography", Medical Physics 27: 845-853 (2000)

An edge spread technique for measurement of the scatter-to-primary ratio in mammography

Virgil N. Cooper III,^{a)} John M. Boone,^{b)} J. Anthony Seibert, and Claire J. Pellot-Barakat
University of California, Davis, Department of Radiology, 4701 X Street, Sacramento, California 95817

(Received 13 September 1999; accepted for publication 1 March 2000)

An experimental measurement technique that directly measures the magnitude and spatial distribution of scatter in relation to primary radiation is presented in this work. The technique involves the acquisition of magnified edge spread function (ESF) images with and without scattering material present. The ESFs are normalized and subtracted to yield scatter-to-primary ratios (SPRs), along with the spatial distributions of scatter and primary radiation. Mammography is used as the modality to demonstrate the ESF method, which is applicable to all radiographic environments. Sets of three images were acquired with a modified clinical mammography system employing a flat panel detector for 2, 4, 6, and 8 cm thick breast tissue equivalent material phantoms composed of 0%, 43%, and 100% glandular tissue at four different kV settings. Beam stop measurements of scatter were used to validate the ESF methodology. There was good agreement of the mean SPRs between the beam stop and ESF methods. There was good precision in the ESF-determined SPRs with a coefficient of variation on the order of 5%. SPRs ranged from 0.2 to 2.0 and were effectively independent of energy for clinically realistic kVps. The measured SPRs for 2, 4, and 6 cm 0% glandular phantoms imaged at 28 kV were 0.21 ± 0.01 , 0.39 ± 0.01 , and 0.57 ± 0.02 , respectively. The measured SPRs for 2, 4, and 6 cm 43% glandular phantoms imaged at 28 kV were 0.20 ± 0.01 , 0.35 ± 0.02 , and 0.53 ± 0.02 , respectively. The measured SPRs for 2, 4, and 6 cm 100% glandular phantoms imaged at 28 kV were 0.22 ± 0.02 , 0.42 ± 0.03 , and 0.88 ± 0.08 , respectively. © 2000 American Association of Physicists in Medicine. [S0094-2405(00)02705-X]

Key words: scatter, scatter-to-primary ratio (SPR), measurement technique, edge spread function (ESF), mammography

I. INTRODUCTION

It is well known that scattered x-rays reduce image contrast and therefore lower lesion conspicuity, especially for low contrast lesions.¹⁻⁵ This has important implications for breast imaging since, other than those containing microcalcifications, lesions are generally of similar composition and density to surrounding breast tissue. Hence, degradation of inherently low lesion contrast has important clinical repercussions. As a result, scatter in mammography and methods of reducing its effects have been studied by several authors.^{4,6-19}

The first step in reducing the effects of scatter is to understand the nature of scatter and its resulting image signal. Heretofore, the classic beam stop technique was used to quantify the magnitude of scatter relative to primary radiation, and various theoretical and semi-empirical methods were used to separate the distribution of scatter and primary radiation signals.^{8,20-23} In this work, an experimental technique that quantifies both the magnitude and spatial distribution of scatter is demonstrated. The technique involves the acquisition of spatially registered primary and primary-plus-scatter radiation edge spread images. The resulting edge spread functions (ESFs) are normalized and subtracted resulting in separate measurements of scatter and primary ra-

diation. The principal advantages of this technique are that the magnitude and spatial distribution of the scatter signal are measured directly and extrapolation techniques are not required as they are in using the beam stop method. The latter is important because the shape of the extrapolation function requires an assumption concerning the shape of the scatter point spread function (PSF) and is a source of ambiguity. This ambiguous extrapolation function can have a strong influence on the results.

As a vehicle to demonstrate the experimental ESF methodology, experimental measurement of scatter in the mammography setting is revisited 20 years after the early work of Barnes and Brezovich.⁷ Many improvements in mammography have occurred since then, including the development of dedicated mammography systems employing molybdenum and rhodium targets, digital detectors, and x-ray generators with low kV ripple. The current availability of breast-mimicking phantoms allows scatter assessment in tissue equivalent phantoms. Scatter is studied for a range of breast compositions and thicknesses imaged over a range of beam qualities. Breast equivalent material slabs were used as the scattering media and a flat panel digital radiographic imaging system (Varian Imaging Products, Palo Alto, CA) was used for image acquisition.

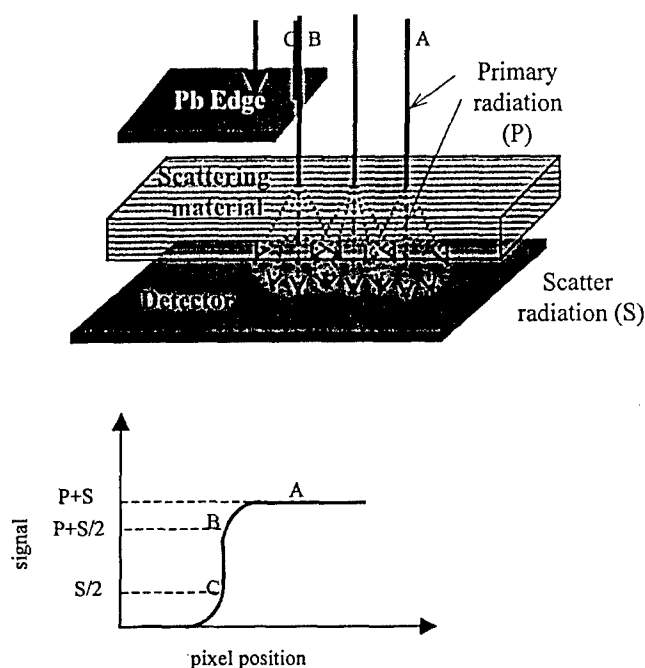


FIG. 1. The basic acquisition geometry: X-rays incident on a Pb edge placed on a scattering phantom. The edge is oriented parallel to the anode-cathode axis and bisects the x-ray field. A digital detector resides beneath the scattering medium. Below: the resulting signal profile.

II. MATERIALS AND METHODS

A. Theory

An experimental technique using edge spread functions, (ESFs) to quantify the detected scattered radiation in relation to primary radiation is described in this section. This technique also gives a direct measurement of the spatial distribution of scatter, differentiating it from the beam stop technique. The direct measurement of the spatial distribution of scatter may be useful for the development of scatter correction algorithms pertinent to quantitative digital mammography (e.g., dual energy mammography or breast density analysis).

A parallel beam of x-rays incident on an elevated thick Pb sheet with the Pb edge oriented parallel to the anode-cathode axis is illustrated in Fig. 1. A digital detector is positioned beneath the Pb sheet and intercepts the entire field. A slab of scattering material resides between the sheet and detector. Labels "A," "B," and "C," refer to the points centrally located in the open field, located adjacent to the edge in the open field, and located adjacent to the edge in the closed field, respectively. The resulting image profile or edge spread function (ESF) is also depicted in Fig. 1.

If the edge were re-oriented 180 degrees from its original position, a mirror image profile would result. Figure 2 shows the resulting profiles, denoted by ESF_L and ESF_R, and their sum. Qualitatively, the addition of those two profiles results in a flat profile across the field (ignoring field edge effects) and this profile is equivalent to a profile measured for a fully open field. Since the ESF profiles are mirror images of one another, the toe of one ESF curve compensates for the shoulder of the other curve. Physically, the toe of the

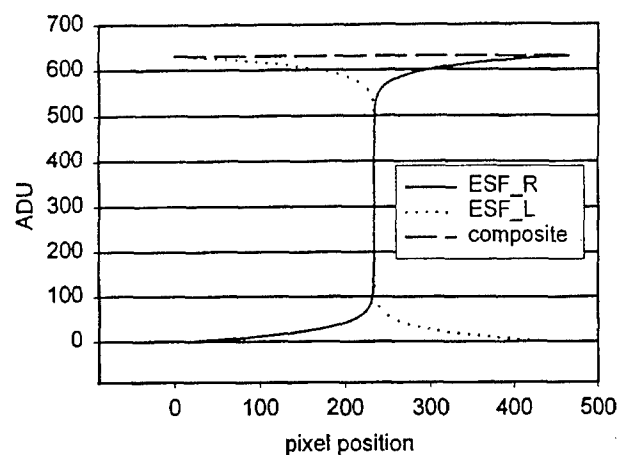


FIG. 2. This schematic illustration shows that for an effectively infinite field, primary plus scatter ESF profiles acquired 180 degrees from one another sum to the profile for a totally open field.

profile is composed of scattered radiation signal and the plateau of the curve is composed of scatter and primary radiation signals. The shoulder is also composed of scatter and primary radiation signal. The presence of this shoulder is a manifestation of scattered radiation signal that "leaks" across the discontinuity of the edge and forms the toe. Therefore, it follows that, by subtracting the different parts of the edge profile, scatter and primary radiation may be separated in a single edge profile.

The signals arising from scatter and primary radiation may be separated by the following argument. Referring to Fig. 3, if the length, L , and width, W , of the open field are

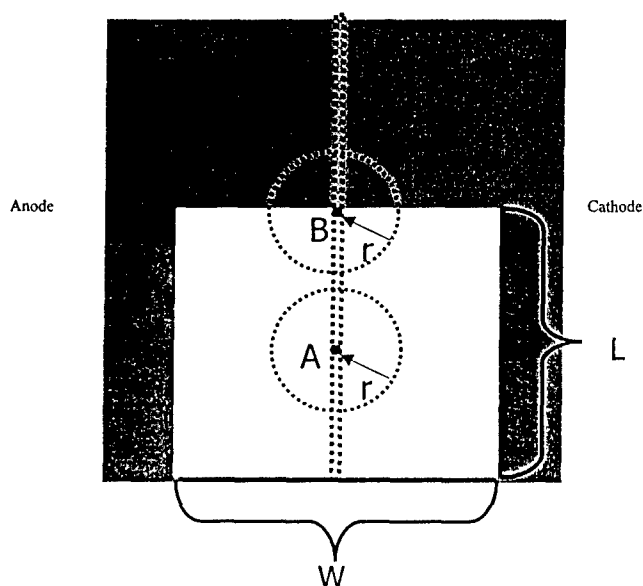


FIG. 3. This schematic illustration shows that an effectively infinite open field in this work, is one that is at least twice as wide (width denoted by W) as the radial range of scatter, r , and at least twice as long (length denoted by L). In this case point B (adjacent to the edge but in the open field) will receive one-half the scatter that point A (centrally located in the open field) receives. The dotted line denotes a 10 pixel wide region of interest (ROI) perpendicular to the anode-cathode axis from which the edge spread function (ESF) is derived.

each greater than twice the effective radial range of scatter, r (found to be between 4 and 6 cm in this work), then the scatter component of the signal at point B is one-half the scatter component at point A. This is because point A receives scatter from the scattering medium over 2π geometry, while point B receives scatter from the scattering medium over π geometry since π radians adjacent to point B are covered by the Pb sheet and therefore do not generate first order scatter. Points A and B receive essentially the same amount of primary radiation. Hence, the scatter-to-primary ratio (SPR) at point B is one-half the SPR at point A.

Given the composition of the signals at pixel positions A and B, the scatter-to-primary ratio may be calculated. The signals at A and B may be, respectively, written as

$$ESF_A = P + S, \quad (1)$$

$$ESF_B = P + S/2, \quad (2)$$

where P is the signal due to primary radiation and S is the maximum signal due to scatter radiation (corresponding to the center of the open field, point A) and ESF_m is the signal value at the m th pixel position due to scatter and primary radiation. Therefore, scatter, primary, and the scatter-to-primary ratio at point A (SPR) may be computed from the digital signal values (among other ways) as:

$$S = 2 \times (ESF_A - ESF_B), \quad (3)$$

$$P = ESF_A - S, \quad (4)$$

$$SPR = S/P. \quad (5)$$

Since the imaging system under consideration does not exhibit perfect resolution, nor does it use parallel rays, these effects must be considered. If the scattering material in the experimental setup is removed without disturbing the rest of the system, then image acquisition results in a primary profile that is spatially aligned with the primary-plus-scatter (P+S) profile. However, with the removal of the scattering material, the shape of the primary profile will be slightly different than that with the scattering material present because the primary photons traveling at different angles will traverse different pathlengths through the phantom. For the field sizes, source-to-object distance, energies, and scattering materials involved, the maximum parallax error was found to be on the order of 0.5%, and therefore was considered negligible.

In the acquisition of the primary-only image, the x-ray intensity may be normalized such that the maximum open field signal matches the open field signal acquired with the scattering material present. Figure 4(a) shows the matched primary and primary plus scatter (P+S) profiles. The non-zero signal of the P+S profile under the radiopaque sheet arises from the detection of scatter originating from x-ray interactions with the phantom in the open field. The presence of the shoulder in the P+S profile, positioned near the edge of the open field, is due to the scatter lost to the covered field region.

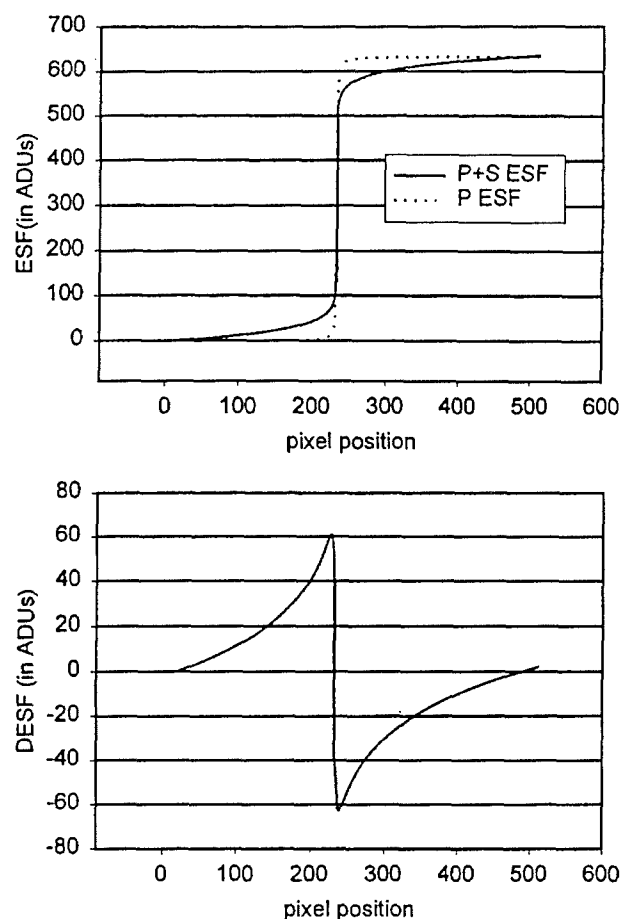


FIG. 4. (a) Matched primary-only and primary plus scatter ESFs and (b) the resulting profile if the primary ESF is subtracted from the primary plus scatter ESF. The magnitude of the discontinuity in this profile is equal to the scatter signal at the center of the open field (previously denoted by point A).

While there are several ways of quantifying the maximum scatter signal, a difference profile may be computed from Fig. 4(a) as

$$DESF_m = ESF_m - PESF_m, \quad (6)$$

where $DESF_m$ is the signal difference at the m th pixel position, ESF_m is the signal value at the m th pixel position due to scatter and primary radiation, and $PESF_m$ is the signal value at the m th pixel position due to primary radiation.

Figure 4(b) shows the resultant $DESF$. The positive and negative peaks, respectively, correspond to the maximum scatter gain in the covered field and maximum scatter loss in the open field. Thus, the signal due to scatter at the center of the open field in Eq. (3) may be rewritten as:

$$S = 2 \times |DESF_B|, \quad (7)$$

where $DESF_B$ corresponds to the difference profile value at point B in Fig. 1. Since there is symmetry in the scatter losses from the open field and scatter gains in the covered field about the discontinuity of the edge, scatter signal may also be calculated as

$$S = DESF_C + |DESF_B|, \quad (8)$$

where $DESFC$ corresponds to the difference profile value at point C in Fig. 1. Since the scatter signal at the center of the open field, point A, is isolated by Eq. (8), the primary signal component and the SPR may be calculated, respectively, from Eqs. (4) and (5).

Since the primary signal at point A, given by P , and the functional form of primary signal are known, the primary-only ESF may be renormalized such that the value at point A is equivalent to P . Thus the entire primary ESF would be correctly scaled and give the signal due to primary radiation along the center of the field. Given the renormalized primary ESF, the scatter ESF, $SESF$, is computed by subtracting the renormalized primary ESF, $NPESF$, from the total signal profile and is given as:

$$SESF_m = ESF_m - NPESF_m. \quad (9)$$

$SESF$ is then differentiated to yield the scatter line spread function.

B. Experimental conditions

Breast equivalent material phantoms representing 0%, 43%, and 100% glandular tissue (Computerized Imaging Reference Systems, Inc., Norfolk, VA) were imaged with a clinical mammography system employing a molybdenum target and 30 μm thick molybdenum filter (Senographe 600T Senix H.F., General Electric Medical Systems). The images were acquired with a flat panel imaging system employing thin film transistor circuitry, 127 μm pixels, and a 60 mg/cm^2 $\text{Gd}_2\text{O}_2\text{S}$ intensifying screen (Varian Imaging Products, Palo Alto, CA). As calculated by simple attenuation methods, the detection system represented greater than 90% interaction efficiency for all spectra employed. The flat panel detector resided under a custom fabricated stand which allowed placement of the breast equivalent material with a 1.5 cm air gap on the incident surface of the detector and beneath the top surface of the stand. The focal spot to image receptor distance was 122 cm. The top surface of the stand was located 111 cm from the focal spot and was covered by lead except for a square cutout representing a projected 10 $\text{cm} \times 10$ cm "open" field of view. Lead (1.5 mm thick) with finely cut straight edges was used to confine this field. An edge was oriented parallel to the anode-cathode axis and bisecting the x-ray field and was used for computing the ESFs. Since scatter is a known low-frequency phenomenon and occurs well below the Nyquist frequency of the flat panel imaging system, there was no need to angle the edge for oversampling. Phantoms ranging from 2 to 8 cm in thickness in 2 cm increments were imaged from 24 to 36 kVp in 4 kVp increments. Each data set was acquired three times for repeated measures estimation of error. Table I lists the half-value layers for the incident spectra used in this study.

The breast equivalent phantoms were imaged at very similar radiation exposures incident to the detector. The resultant signal data due to scattered and primary radiation measured in the open field were consequently very similar in amplitude. After imaging the breast phantoms, they were carefully removed so as not to disturb the setup. Images were

TABLE I. Beam quality parameters.

kVp	HVL (mm Al)
24	0.30
28	0.32
32	0.37
36	0.38

again acquired, representing primary-only images. It was found that there was no appreciable difference in the spatial distribution of the primary-only images of the edge as a function of kVp.

C. Image correction

All images were gain and offset-corrected using gain and offset maps constructed from five image acquisitions each of white (x-rays on) and dark (x-rays off) fields. The gain map was constructed such that the radiation exposure levels to the incident surface of the detector were very similar to those exposure levels during the ESF acquisitions.

Careful examination of the images showed a non-negligible amount of low-frequency signal in the images similar to that that would be expected from veiling glare. (This low-frequency signal variation is hereafter referred to as "glare" in this manuscript.) Lead beam stop experiments (with no phantom present) were subsequently performed to quantify this glare using the methodology of Seibert *et al.*²⁴ The glare point spread function, $h(r)$, was found to have the form given by:

$$h(r) = (1 - \rho) \times \frac{\delta(r)}{r} + \frac{\rho}{2kr} \times e^{-r/k}, \quad (10)$$

where r is radial distance, $\delta(r)$ is the Dirac delta function, ρ is the fraction of strongly scattered light, and k is the mean propagation distance of that light. For the detector used in this work, ρ and k were found to have values of 0.069 and 7.33 mm, respectively.

The images were cropped to 1024×1024 and deconvolved²⁵ with the inverse filter given by

$$H(f)^{-1} = \frac{\sqrt{1 + (2\pi kf)^2}}{\rho + (1 - \rho) \times \sqrt{1 + (2\pi kf)^2}}, \quad (11)$$

where f is the spatial frequency. For the two dimensional images, f was taken to be given by

$$f = \sqrt{u^2 + v^2}, \quad (12)$$

where u and v are the spatial frequencies across rows and columns.

D. ESF calculations

After the images were deconvolved for glare, a rectangular region of interest (ROI) was positioned on the images and an ESF was calculated for each image. The ROI was chosen such that it was sufficiently wide to allow reasonable averaging (10 pixels or 1.27 mm), while narrow enough such that there was no appreciable difference between the profiles of

the lateralmost extents of the ROI (i.e., no rotation). The length of the ROI was 600 pixels (76 mm), sufficiently long to encompass the ESF from the center of the field of view to well beyond the collimated edge of the field. The ESF was calculated as:

$$ESF_m = \frac{1}{N} \times \sum_{n=1}^N ADU_{m,n}, \quad (13)$$

where n is the column index, N is the number of columns in the ROI, and the summation is along the anode-cathode axis (i.e., across the short-axis dimension of the ROI). $ADU_{m,n}$ is the digital signal value at the m th by n th pixel. The same ROI/averaging protocol was done for the primary-only ESF as well. The magnitudes of scatter signal, primary signal, and their spatial distributions were calculated from the measured data using Eqs. (4)–(6), (8), and (9).

The resulting scatter ESFs were functionally fitted using commercially available software (Table Curve 2D, Jandel Scientific, Corta Madera, CA) and numerically differentiated to yield line spread functions (LSFs). These LSFs were subsequently Fourier transformed and normalized to yield scatter MTFs.

E. Beam stop measurements

To validate the ESF methodology, images were acquired and SPRs were calculated using the conventional beam stop method. A linear extrapolation function,²⁶ and six beam stops having 0.3, 0.4, 0.5, 1.0, 2.0, and 3.0 cm diameters, were used in the beam stop experiments. The same field size and *a priori* selected exposure scenarios covering the entire range of realistic clinical conditions were utilized. As with the ESF measurements, all images were acquired for each beam stop in sets of three for repeated-measures estimation of error. The ROIs used in the centers of the beam stop shadows were 3-pixel-wide squares. Each image was deconvolved for glare using the same inverse filter as in the ESF methodology. Linear regression analysis was performed on the mean SPRs measured with both methodologies.

III. RESULTS AND DISCUSSION

Figure 5(a) and (b) shows the comparison of the mean SPRs calculated via the ESF and beam stop methods. There is good agreement ($r^2=0.97$, slope=0.98, intercept=0.02) between the beam stop method and ESF method.

Figure 6(a)–(c) gives the resultant SPR plots as functions of kVp for each thickness under consideration. Figure 6(d) shows the SPRs as a function of thickness and glandularity at 28 kVp. Table II lists the SPRs in tabular form. The SPRs for the different compositions and thicknesses are effectively energy independent above certain energy thresholds. At the lower energies for the thicker breast phantoms the SPRs were markedly elevated (e.g., the 6 cm, 43% glandular phantom imaged at 24 kVp, the 8 cm, 43% glandular phantom imaged at 28 kVp, the 6 cm, 100% glandular breasts imaged at 28 kVp, etc.). This phenomenon could represent inadequate penetration of the phantoms due to generator power

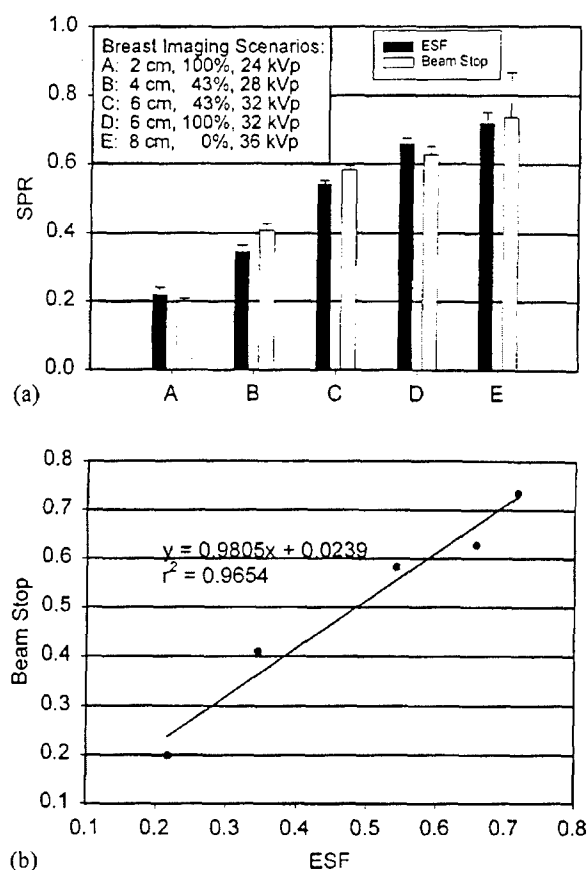


FIG. 5. Comparison of the edge spread and beam stop methods. There is good agreement between the two methods.

constraints and limited detector dynamic range. Therefore these SPRs are artificially elevated and should be looked upon with great suspicion. Furthermore, the imaging scenarios (kVp, thickness, and glandularity) that produced these SPRs are probably clinically unrealistic. Nevertheless, they are included for completeness.

It is difficult to compare this work with the work of Barnes and Brezovich, as they used a tungsten target and (presumably) a single-phase generator, a 0 cm air gap, and markedly different kVps. In addition, Lucite was used as the scattering phantom in the Barnes and Brezovich research. Lucite has a higher density (1.19 g/cm^3) and different elemental composition than breast tissue, and is not consistent with the scattering media used in this work. For the purposes of comparison, however, SPRs for the exposure scenarios most closely resembling those used by Barnes and Brezovich are presented in Table III(a). Poor agreement between the two data sets is observed.

Table III(b) presents a comparison with the work of Dance and Day. The SPRs listed do not include the extraneous sources of scatter as described in their work. Since they simulated a 50% glandular breast at monochromatic energies and since the effective energies of the beams used in this work ranged between 14.22 and 15.24 keV, the SPRs contained in this work for the 43% glandular breast were averaged across energy and are presented for comparison. The SPR listed in Table III(b) for the 6 cm breast does not in-

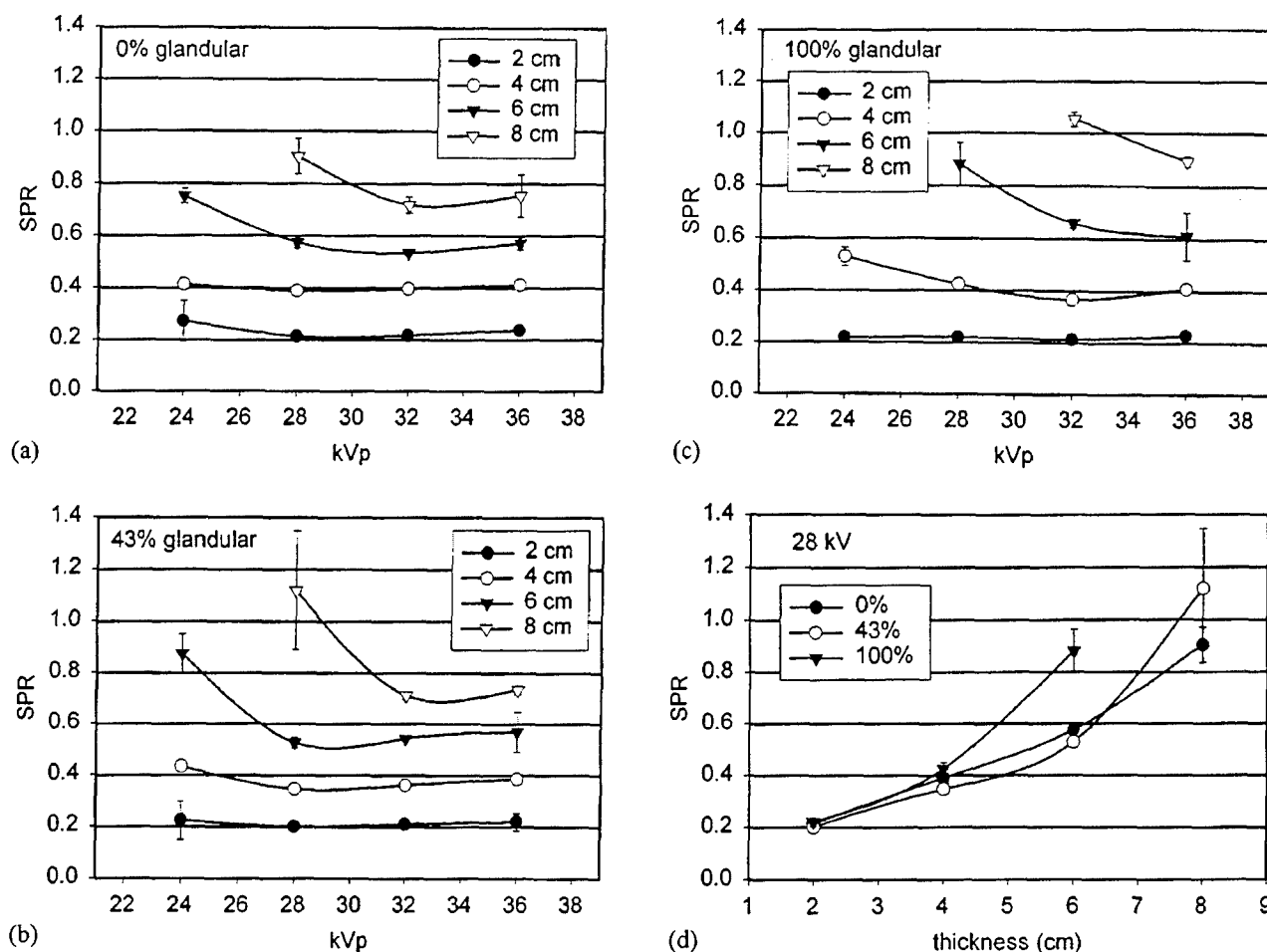


FIG. 6. Scatter-to-primary ratios (SPRs) for (a) 0% glandular breast phantoms, (b) 43% glandular breast, (c) 100% glandular breast phantoms, and (d) 0%, 43%, and 100% glandular breast phantoms imaged at 28 kVp.

clude the 24 kVp data point due to inadequate penetration/limited detector dynamic range. Inclusion of this point elevates the SPR to 0.63. The SPR shown for the 8 cm breast for the work of Dance and Day is for an energy of 25 keV. Overall, there is very good agreement (within 7%) between the two data sets ($r^2=0.991$, slope= 1.066 ± 0.020).

Scatter MTFs for selected exposure scenarios were measured. Figure 7(a) illustrates a representative example of the fit ESFs ($r^2>0.992$ for all fits) (2 cm, 100% glandularity, 24 kVp). Figure 7(b) illustrates a representative LSF (2 cm, 100% glandularity, 24 kVp). Figure 8(a)–(c) shows representative scatter-only MTFs as functions of thickness, kVp, and glandularity, respectively. The spatial distribution of scatter was not strongly influenced by kVp or glandularity based on these data. However, there was a clear trend with thickness. The overall scatter MTF decreased for increasing breast thickness between 2 and 6 cm, after which there was essentially no effect, as witnessed by the 6 and 8 cm breast data plotted in Fig. 8(a). This effect is consistent with the effective range of the scatter being between 4 and 6 cm. The scatter generated in the incident 2 cm of the 8 cm breast probably did not reach the detector plane in any detectable quantity. If it did, it would have widened the scatter PSF purely due to geometry. Although the geometry differs by 90

degrees, this finding is also consistent with the work of Barnes and Brezovich, as there was little change in their reported SPRs for circular field sizes with radii greater than 5 cm.

For breast thicknesses less than the effective range of scatter, increasing thickness yields widening scatter spatial distributions. For thinner phantoms, scatter originating from the entrance layers (sub-volumes) of the scattering medium has the penetrability and geometry to reach the detector and be recorded. Increasing the thickness beyond some effective range of scatter results in self-attenuation of the scatter originating near the entrance surface of the phantom. After this point, increasing thickness has little effect on the scatter distribution. Theoretically, with *a priori* knowledge of the above MTFs, inverse filters could be constructed to counteract the effects of scatter degradation of low contrast detectability.

IV. FURTHER DISCUSSION

There are several advantages to the ESF methodology. The ESF method directly gives the spatial distribution of scatter, including small angle scatter effects. Although the spatial distribution of scatter may be inferred from the

TABLE II. SPRs for a 10 cm×10 cm field size.

		2		4		6		8	
kVp		SPR	st. dev.	SPR	st. dev.	SPR	st. dev.	SPR	st. dev.
Thickness (cm) (0% glandular)									
(a)	24	0.27±0.08		0.41±0.01		0.75±0.03		1.93±0.17	
	28	0.21±0.01		0.39±0.01		0.57±0.02		0.90±0.07	
	32	0.22±0.01		0.40±0.01		0.53±0.01		0.72±0.03	
	36	0.24±0.00		0.41±0.01		0.57±0.02		0.75±0.08	
Thickness (cm) (43% glandular)									
(b)	24	0.22±0.07		0.43±0.01		0.87±0.08		—±—	
	28	0.20±0.01		0.35±0.02		0.53±0.02		—±—	
	32	0.21±0.01		0.36±0.00		0.54±0.01		0.71±0.01	
	36	0.22±0.03		0.38±0.01		0.57±0.08		0.73±0.02	
Thickness (cm) (100% glandular)									
(c)	24	0.22±0.02		0.53±0.03		—±—		—±—	
	28	0.22±0.02		0.42±0.03		0.88±0.08		—±—	
	32	0.21±0.01		0.37±0.01		0.66±0.02		1.05±0.03	
	36	0.23±0.01		0.41±0.01		0.61±0.09		0.89±0.02	

method of Seibert *et al.* using the beam stop method, this is not a direct measurement²⁶ as an assumption about the functional form of the scatter spatial distribution is required. Furthermore, the ESF method does not require extrapolation in order to quantify SPR. The beam stop method does, and the extrapolation function, which is generally not well known, can have a significant impact on the calculated SPR. The ESF method has another advantage in that only two image acquisitions are needed for each SPR measurement. The beam stop method requires multiple acquisitions so that an adequate regression/extrapolation may be performed.

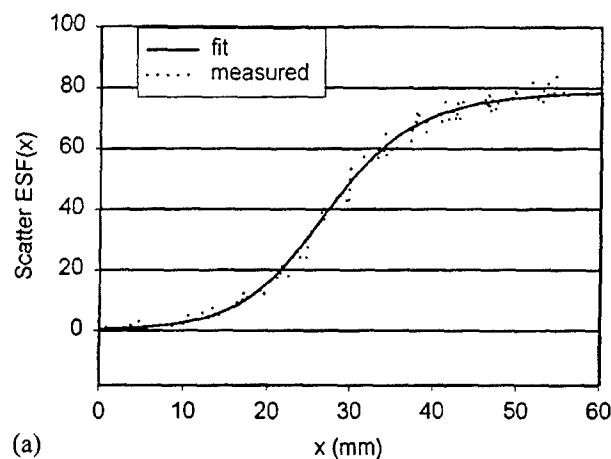
There are some disadvantages to the ESF method compared to the beam stop method. The ESF method requires that the resolution and primary plus scatter images be acquired under identical conditions with respect to the location and alignment of the edge. This is easily achieved, however, with a simple stand that allows immobilization of the edge with easy removal of the scattering material. The ESF method assumes the use of a spatially uniform scattering medium and in its current form does not allow for measure-

ment of SPRs for scattering media involving image structure (e.g., a bone embedded in soft tissue, breasts with "lumpy image texture," etc.). However, the SPRs and scatter spatial distributions did not vary widely for the studied 0%, 43%, and 100% glandular tissues when imaged under clinically realistic conditions. This suggests that regardless of the texture of the breast (i.e., lumpy, dense, fatty, etc.) the tissues contained therein may be thought of as a single homogeneous scattering medium.

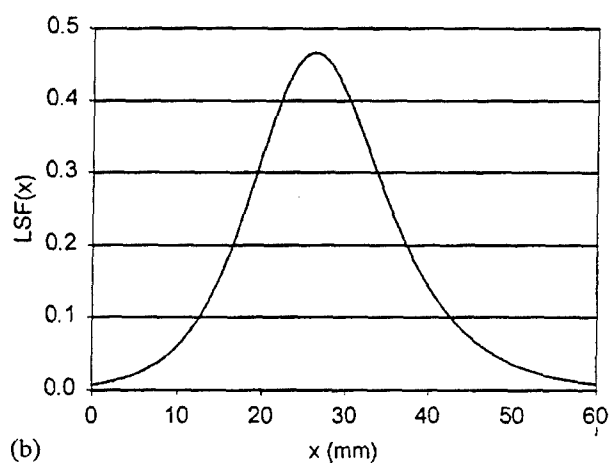
Finally, the ESF method of measuring scatter radiation and its distribution has a potential clinical use in digital mammography. One of the advantages of digital mammography is the ability to process the digital image data such that the displayed images coincide with a specific visual perception task. In this scenario, the direct measurement of the spatial distribution of detected scatter resulting from the use of edge spread functions promotes the construction of filters that would enhance low frequencies thereby increasing image contrast and hence, increasing low-contrast detectability. Moreover, quantitative techniques such as dual energy mam-

TABLE III. SPR comparison with Barnes and Brezovich (a) and Dance and Day (b).

		Barnes and Brezovich		This work		
		Lucite thickness (cm)		100% glandular thickness		
(a)	Field size (cm)	3	6	2	4	6
	10.0	0.39	0.80	—	—	—
	10.0 square	—	—	0.21±0.01	0.37±0.01	0.66±0.02
	14.0	0.40	0.86	—	—	—
(b)	Thickness (cm)	Dance and Day		This work		
	2	0.25		0.21		
	4	0.42		0.38		
	6	0.59		0.55		
	8	0.75		0.72		



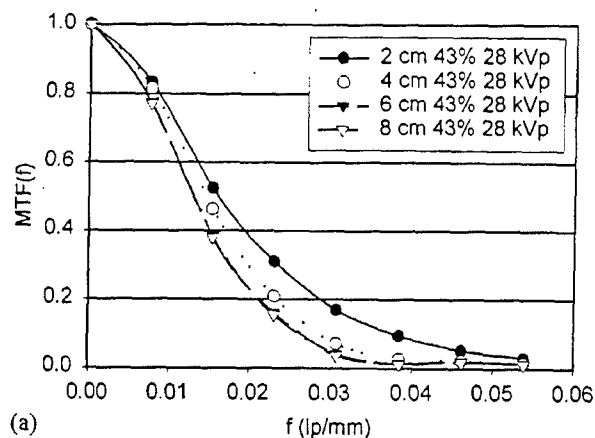
(a)



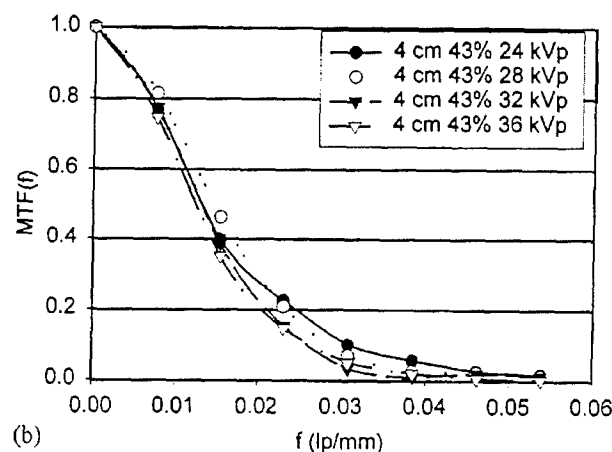
(b)

FIG. 7. (a) Measured and fit ($r^2=0.993$) scatter ESFs for a 2 cm 100% glandular breast phantom, 24 kVp, and (b) the resulting scatter LSF calculated by numerically differentiating the fit scatter ESF.

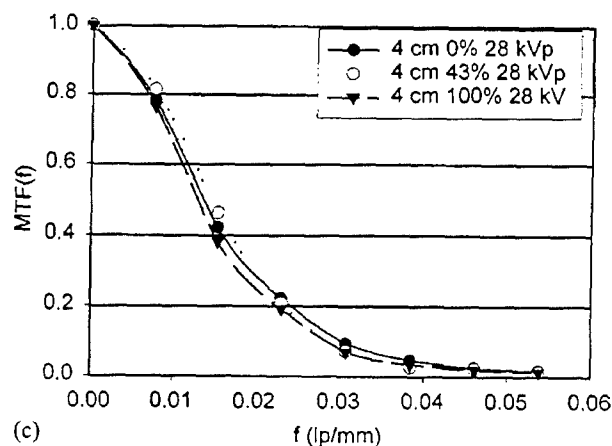
mography may be improved if the low-frequency bias from scatter is removed. Since lesions of the breast are inherently low contrast in nature, this has substantial clinical implications. Furthermore, the data suggest a weak kVp dependence and a weak glandularity dependence for scatter, thus a family of filters constructed for different breast thicknesses should be reasonably robust for a range of clinical conditions. This family of filters could be derived from measurements such as these described in this manuscript. The field size and shape dependence of the filter could be readily solved numerically by way of convolving the measured scatter point spread function (measured all the way to 0 in the tails) with the breast image. In this scenario, one could use the image to estimate the object and hence, the SPR and spatial distribution of scatter, similar to that estimation used where the image power spectrum is used to estimate the object power spectrum for other filtering techniques such as Wiener filtering. The inverse filter that would be derived from this approach could then be applied to the image. Whether this approach is feasible or not is a subject that may require future research.



(a)



(b)



(c)

FIG. 8. Scatter MTFs demonstrating (a) thickness dependence, (b) kVp dependence, and (c) glandularity dependence.

V. CONCLUSIONS

An experimental method of directly measuring the magnitude and spatial distribution of scattered radiation in relation to primary radiation has been presented. The method involves subtracting spatially aligned primary radiation and primary-plus-scatter radiation edge spread functions. The method shows good agreement with the more conventional beam stop technique of measuring scatter in relation to primary radiation. Demonstration of the method in measuring scatter-to-primary ratios under the conditions using current

image acquisition spectra and breast-mimicking phantoms suggest that SPRs in mammography may be lower than those reported in the early work of Barnes and Brezovich.

ACKNOWLEDGMENTS

This research was supported in part by grants from the US Department of Defense Breast Cancer Research Program (DAMD17-94-4424 and DAMD17-98-8176), the California Breast Cancer Research Program (1RB-0912 and 2RB-0071), and the National Cancer Institute (R21-CA82077). The authors are grateful to Varian Imaging Products for the use of the flat panel imager used in this study.

^aAddress for correspondence: Virgil N. Cooper III, 4701 X Street, Sacramento, CA 95817, electronic mail: vncooper@ucdavis.edu

^bAddress for reprint requests: John M. Boone, 4701 X Street, Sacramento, CA 95817, electronic mail: jmboone@ucdavis.edu

¹G. T. Barnes, "Contrast and scatter in x-ray imaging," *Radiographics* **11**, 307-323 (1991).

²R. H. Miettinen and O. A. Korhola, "The effect of scatter reduction on the signal-to-noise ratio in computed radiography," *Eur. J. Radiol.* **12**, 167-170 (1991).

³J. W. Motz and C. E. Dick, "X-ray scatter background signals in transmission radiography," *Med. Phys.* **2**, 259-267 (1975).

⁴B. Nielsen and G. Fagerberg, "Image quality in mammography with special reference to anti-scatter grids and the magnification technique," *Acta Radiol.: Diagn.* **27**, 467-479 (1986).

⁵D. M. Tucker, M. Souto, and G. T. Barnes, "Scatter in computed radiography," *Radiology* **188**, 271-274 (1993).

⁶M. J. Yaffe, "Direct digital mammography using a scanned-slot CCD imaging system," *Med. Prog. Technol.* **19**, 13-21 (1993).

⁷G. T. Barnes and I. A. Brezovich, "The intensity of scattered radiation in mammography," *Radiology* **126**, 243-247 (1978).

⁸D. R. Dance and G. J. Day, "The computation of scatter in mammography by Monte Carlo methods," *Phys. Med. Biol.* **29**, 237-247 (1984).

⁹R. L. Egan, M. B. McSweeney, and P. Sprawls, "Grids in mammography," *Radiology* **146**, 359-362 (1983).

¹⁰R. Fahrig, J. G. Mainprize, N. Robert, A. Rogers, and M. J. Yaffe, "Performance of glass fiber antiscatter devices at mammographic energies," *Med. Phys.* **21**, 1277-1282 (1994).

¹¹S. L. Fritz, C. H. J. Chang, and W. H. Livingston, "Scatter/primary ratios for x-ray spectra modified to enhance iodine contrast in screen-film mammography," *Med. Phys.* **10**, 866-870 (1983).

¹²Z. Jing, W. Huda, and J. K. Walker, "Scattered radiation in scanning slot mammography," *Med. Phys.* **25**, 1111-1117 (1998).

¹³E. P. Muntz, "Analysis of the significance of scattered radiation in reduced dose mammography, including magnification effects, scatter suppression, and focal spot and detector blurring," *Med. Phys.* **6**, 110-117 (1979).

¹⁴K. H. Ng, R. J. Aus, L. A. DeWerd, and J. R. Vetter, "Entrance skin exposure and mean glandular dose: Effect of scatter and field gradient at mammography," *Radiology* **205**, 395-398 (1997).

¹⁵P. S. Rezentes, A. de Almeida, and G. T. Barnes, "Mammography grid performance," *Radiology* **210**, 227-232 (1999).

¹⁶G. T. Barnes, X. Wu, and A. J. Wagner, "Scanning slit mammography," *Med. Prog. Technol.* **19**, 7-12 (1993).

¹⁷A. Krol, D. A. Bassano, C. C. Chamberlain, and S. C. Prasad, "Scatter reduction in mammography with air gap," *Med. Phys.* **23**, 1263-1270 (1996).

¹⁸E. P. Muntz and W. W. Logan, "Focal spot size and scatter suppression in magnification mammography," *Am. J. Roentgenol.* **133**, 453-459 (1979).

¹⁹M. V. Yester, G. T. Barnes, and M. A. King, "Experimental measurements of the scatter reduction obtained in mammography with a scanning multiple slit assembly," *Med. Phys.* **8**, 158-162 (1981).

²⁰H. Bernstein and E. P. Muntz, "Experimental verification of a technique for predicting scattered radiation transfer: Application to low photon energies," *Med. Phys.* **13**, 836-842 (1986).

²¹C. E. Floyd, Jr., J. Y. Lo, H. G. Chotas, and C. E. Ravin, "Quantitative scatter measurement in digital radiography using a photostimulable phosphor imaging system," *Med. Phys.* **18**, 408-413 (1991).

²²C. E. Floyd, Jr., J. A. Baker, J. Y. Lo, and C. E. Ravin, "Posterior beam-stop method for scatter fraction measurement in digital radiography," *Invest. Radiol.* **27**, 119-123 (1992).

²³D. J. Klein, H.-P. Chan, E. P. Muntz, K. Doi, K. Lee, P. Chopelas, H. Bernstein, and J. Lee, "Experimental and theoretical energy and angular dependencies of scattered radiation in the mammography energy range," *Med. Phys.* **10**, 664-668 (1983).

²⁴J. A. Seibert, O. Nalcioglu, and W. W. Roeck, "Characterization of the veiling glare PSF in x-ray image intensified fluoroscopy," *Med. Phys.* **11**, 172-179 (1984).

²⁵J. A. Seibert, O. Nalcioglu, and W. Roeck, "Removal of image intensifier veiling glare by mathematical deconvolution techniques," *Med. Phys.* **12**, 281-288 (1985).

²⁶J. A. Seibert and J. M. Boone, "X-ray scatter removal by deconvolution," *Med. Phys.* **15**, 567-575 (1988).

DAMD17-98-18176, Final Report - August 2001

Computer Simulation of Breast Cancer Screening

PI: John M. Boone, Ph.D.

Appendix E:

JM Boone, KK Lindfors, VN Cooper III and JA Seibert, "Scatter/primary in mammography: comprehensive results", Medical Physics 27: 2408-2416 (2000)

Scatter/primary in mammography: Comprehensive results

John M. Boone,^{a)} Karen K. Lindfors, Virgil N. Cooper III, and J. Anthony Seibert
Department of Radiology, University of California, Davis, Sacramento, California 95817

(Received 10 March 2000; accepted for publication 7 August 2000)

Monte Carlo procedures using the SIERRA code (validated in a companion article) were used to investigate the scatter properties in mammography. The scatter to primary ratio (SPR) was used for quantifying scatter levels as a function of beam spectrum, position in the field, air gap, breast thickness, tissue composition, and the area of the field of view (FOV). The geometry of slot scan mammography was also simulated, and SPR values were calculated as a function of slot width. The influence of large air gaps (to 30 cm) was also studied in the context of magnification mammography. X-ray energy and tissue composition from 100% adipose to 100% glandular demonstrated little effect on the SPR. Air gaps over a range from 0 to 30 mm showed only slight effects. The SPR increased with increased breast thickness and with larger fields of view. Measurements from 82 mammograms provided estimates of the range of compressed breast thickness (median: 5.2 cm, 95% range: 2.4 cm to 7.9 cm) and projected breast area onto the film (left craniocaudal view, median: 146 cm², 95% range: 58 cm² to 298 cm²). SPR values for semicircular breast shapes, Mo/Mo spectra, and a 15 mm air gap were parametrized as a function of breast thickness and (semicircular) breast diameter. With the coefficients $a = -2.35452817439093$, $b = 22.3960980055927$, and $c = 8.85064260299289$, the equation $SPR = [a + b \times (\text{diameter in cm})^{(-1.5)} + c \times (\text{thickness in cm})^{(-0.5)}]^{-1}$ produces SPR data from 2 to 8 cm and from 3 to 30 cm breast diameters with an average error of about 1%. © 2000 American Association of Physicists in Medicine. [S0094-2405(00)02610-9]

Key words: scatter, mammography, breast imaging, Monte Carlo, computer simulation

I. INTRODUCTION

The scatter to primary ratio (SPR) in mammography applications has been studied by several investigators.¹⁻⁶ However, a comprehensive analysis of scattering properties covering a wide range of mammographically pertinent parameters has not been reported. In a companion paper,⁷ the SIERRA (simple investigational environment for radiology research applications) Monte Carlo routines were compared with physically-measured and Monte Carlo-derived SPR values with good results. In this investigation, the validated SIERRA Monte Carlo routines were used to compute the SPR under a wide variety of parameters relevant to mammography. Scatter conditions were evaluated for conventional x-ray mammography beams, and for substantially higher energy x-ray beams that may be used for digital mammography or dual energy mammography applications. The scatter properties of slot-scan geometry systems and of magnification mammography were also investigated.

Our purpose in this investigation was to quantify the presence of scattered radiation in mammography, in the absence of anti-scatter grids. Investigations by others^{8,9} have evaluated the role that grids play in the reduction of scatter and in the improvement of contrast in screen-film mammography. The role of grids is currently being reexamined in the context of digital mammography,^{4,10} with unique considerations for this modality such as signal to noise ratio improvement and the potential of aliasing artifacts.

II. METHODS

A complete description of the methods used to evaluate the scatter to primary ratio is given in the companion paper.⁷ Here, a brief summary will be given for continuity. Monte Carlo simulation routines were used to evaluate the point spread function (PSF) of scattered radiation. Monoenergetic x-ray beams were normally incident upon the top surface of the scattering phantom, and the distribution of the energy deposition in an ideal detector under the phantom was tallied at 31 different distances (air gaps) from the exit surface of the phantom, from 0 to 30 mm in 1 mm increments. Monoenergetic x-ray beams ranging from 5 keV to 120 keV were evaluated, in 1 keV increments. For polyenergetic x-ray beams, the monoenergetic PSFs were appropriately weighted using polyenergetic x-ray spectra. The x-ray spectra were computed from previously described spectral models.^{11,12} Mathematical scattering phantoms with thicknesses ranging from 2 cm to 8 cm consisting of 0% glandular tissue (i.e., 100% adipose), 50% glandular, and 100% glandular tissues were investigated.

The monoenergetic scatter PSFs were computed as a function of the radial distance from the input x-ray path, ranging from 0 to 200 mm, in 1 mm intervals. This sampling was sufficient to compute the scatter distribution for up to a 40 cm diameter circular field of view, far larger than that experienced in clinical mammography. Once the PSF was computed for a specific set of conditions including the x-ray spectrum, air gap, phantom thickness, and tissue composition (glandular fraction), the scatter distribution was computed

over the field of view of interest by convolving the PSF with the shape and dimensions of the field of view. The technique is general and any shape of the x-ray beam distribution can be evaluated. However, in this investigation x-ray beam geometries including rectangular, circular, and semi-circular fields of view were studied. The mathematical details of the convolution were presented in the companion paper. They are straightforward and their application should be intuitive to those familiar with convolution techniques.

One aspect of this investigation focused on quantifying the SPR in magnification mammography. To do this, the SIERRA Monte Carlo code was modified to compute the SPR at air gaps from 0 to 30 cm (instead of mm as mentioned above). The large air gaps led to poor photon collection efficiency and therefore larger numbers (10^8) of input photons were tracked per x-ray energy. Despite this, the extremely low scattered photon collection efficiency near the center of the annular ring collection geometry (where the area of each annulus was smaller) led to unacceptable noise levels in the PSFs. At these larger air gaps (>5 cm), the shape of the PSFs was found to be nearly exponential (with r^2 averaging 0.989 in a log-linear regression fit). Accordingly, to estimate the PSF at smaller radii r (<40 mm), the PSF from $r = 40$ mm to $r = 180$ mm was fit using log-linear regression and the fit coefficients were used to extrapolate the data to the $r = 1$ mm to $r = 40$ mm region of the PSF. This was only done for air gaps ≥ 20 cm.

It should be noted that the PSFs used in this investigation were produced using mathematical phantoms of infinite lateral extent, analogous to the situation where the x-ray beam is collimated to well within the physical edges of the scattering medium. However, in mammography, the physical edges of the breast reside well within the x-ray field. These differences were studied in the companion article, and found to have little influence in the calculated SPR. The typical influence of this difference in the geometry was seen to be a few percent, and only influenced SPR values within about 2 mm of the edge of the breast. This effect was considered negligible for most purposes.

In an effort to reduce the number of permutations of parameters being investigated, a small study was performed on 82 serial patients undergoing screen-film mammography at our institution. It was our original assumption that thicker compressed breasts corresponded to larger breast areas on the film, and thus the field of view and thicknesses would be correlated. The compressed breast thickness was tallied, and the width of the breast silhouette at the chest wall, and the chest wall-to-nipple distance were measured with a ruler and recorded as well. Virtually no correlation ($r^2 = 0.02$) between breast area and compressed breast thickness was found, surprisingly. Nevertheless, useful estimates of breast thicknesses and area distributions were obtained and results are provided in the appendix.

Most of the data presented were evaluated for parameters which are typically used in clinical mammography (screen-film and digital). For example, a 15 mm air gap was used in most comparisons because this is close to that used on most mammography systems. The parameters of beam spectrum

and breast thickness were correlated in most circumstances to reflect realistic techniques used in our mammography clinic. The technique chart (kV versus thickness and glandular fraction) was developed scientifically by exposing different thicknesses (2, 4, 6, and 8 cm) of breast phantoms (adipose, glandular and BR12, Computerized Imaging Reference Systems, Inc., Norfolk, VA) in a clinical screen-film mammography system (Lorad Mark IV, Trex Medical, Danbury, CT) using phototiming in the "autotime" mode (where only exposure time is automatically modulated). Exposures over the widest possible range of kVs (given tube loading and back-up timer constraints) with both molybdenum anode/molybdenum filter (Mo/Mo) and molybdenum anode/rhodium filter (Mo/Rh) spectra were made at each breast phantom thickness and composition. The kV corresponding to an exposure time of 2 seconds (200 mAs on the 100 mA system used) was selected as an optimum trade-off between good subject contrast (low kVp) and reduced potential for motion artifact (short exposure times). For the 50% glandular tissue composition used predominantly in this study, the kVps for a breast thickness of 2, 3, 4, 5, 6, 7, and 8 cm were 24, 24, 24, 25, 28, 30 and 32 kVp, respectively. Clinically, the Mo/Rh combination was used for the 8 cm breast at 32 kVp, however, a Mo/Mo combination was used for all thicknesses for consistency. Based on our computations, this had a negligible effect on the reported SPR results.

The SPR depends on the spatial location where it is measured. Single-value SPR values reported below were measured at the center of the field of view, unless indicated otherwise. Most of the previously reported data are for circular fields of view, as the inherent symmetry of the circle makes it an easy choice as a phantom shape. Circular phantoms have had historical significance in the physical assessment of scattered radiation in mammography.^{1,5} Nevertheless, the breast is nearly semi-circular. In this study, the scatter properties for both semi-circular and circular phantom shapes were assessed and a conversion between the two shapes was devised.

III. RESULTS

A. Scatter dependence on x-ray energy

Figure 1(a) illustrates the SPR as a function of kVp for Mo/Mo and rhodium anode/rhodium filter (Rh/Rh) x-ray spectra from 22 to 40 kVp. There is little x-ray spectral dependence on the SPR. For example, differences between the SPR at 40 kVp and 22 kVp are 1.0% for the 2 cm breast and 7.0% for the 4 cm breast (Mo/Mo spectra). A 12.7% difference was observed for the 6 cm breast and a 2.0% difference was observed for the 8 cm breast. Figure 1(b) illustrates the SPR as a function of the tungsten anode/aluminum filter (W/A1) spectra from 30 kVp to 120 kVp. These data were studied for those interested in dual energy mammography or the potential of using higher energy beams in digital mammography. A slight increase in the SPR was observed for the 6 and 8 cm breast thicknesses in going from 30 kVp to 45 kVp. However a slight decrease of the SPR with the kVp was observed at higher kVps. The magnitude of the differences

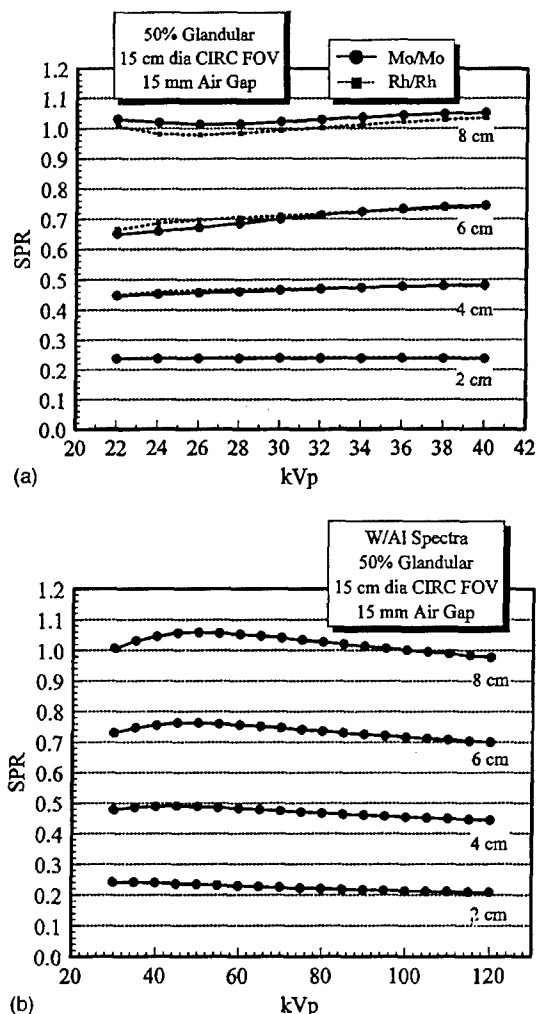


FIG. 1. (a) The scatter to primary ratio for 4 different breast thicknesses is shown as a function of kVp over the mammographic energy range. The data for both Mo/Mo and Rh/Rh x-ray spectra are illustrated. (b) The scatter to primary ratio is illustrated as a function of kVp over the much broader diagnostic energy range. Tungsten anode (W/AI) spectra were used.

between the 120 kVp and 30 kVp SPRs were 13.8%, 7.3%, 4.1%, and 2.9% for the 2, 4, 6, and 8 cm results, respectively, where the SPRs at 120 kVp were lower than those at 30 kVp.

B. Scatter dependence on position in field

The SPR is not a constant value for a given breast but it fluctuates significantly over the field of view (FOV). The geometry of a craniocaudal projection illustrated in Fig. 2(a) was used to study the positional dependence of the SPR. Figure 2(b) illustrates profiles of SPR data through the phantom for a 2 cm and 4 cm breast thickness. The dotted line corresponds to the profile *a*, as illustrated in Fig. 2(a). Figure 2(c) illustrates profiles for the 6 and 8 cm breast thicknesses. Appropriate kVps were used for each breast thickness, as indicated in the figures. The profiles were symmetric about the centerline of the breast, and therefore only half of each profile for each breast thickness was plotted. Not surpris-

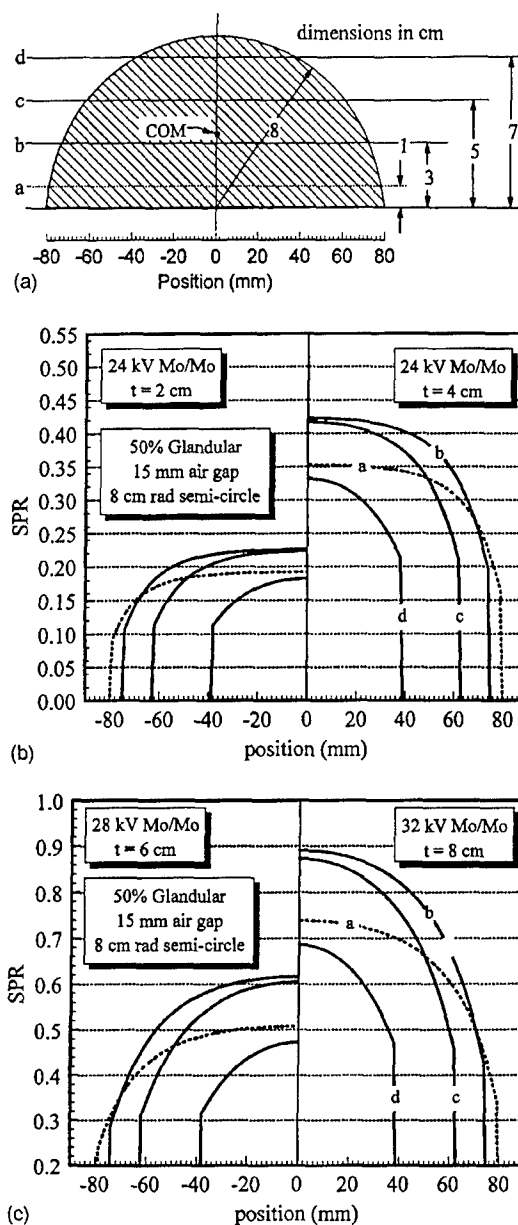


FIG. 2. (a) The geometry of the breast in a craniocaudal view is illustrated. The 4 horizontal lines running through the breast labeled *a*, *b*, *c* and *d*, correspond to the locations of the data plotted in (b) and (c). The center of mass (COM) for a semi-circle is also indicated. (b) The scatter to primary ratio is illustrated as a function of position for a 2 cm breast (left pane) and for a 4 cm breast (right pane). Each line on the right pane is labeled corresponding to the horizontal positions indicated in (a). (c) The scatter to primary ratio is shown as a function of field position for a 6 cm breast (left pane) and for an 8 cm breast (right pane).

ingly, the SPR is highest towards the center of the field and tapers off towards the edges of the field. The SPR was set to zero outside the FOV. The variation of the SPR across the FOV is dramatic. For example, for the 4 cm breast the SPR at the edge of the FOV is ~ 0.20 , but it increases to ~ 0.42 near the center of the field.

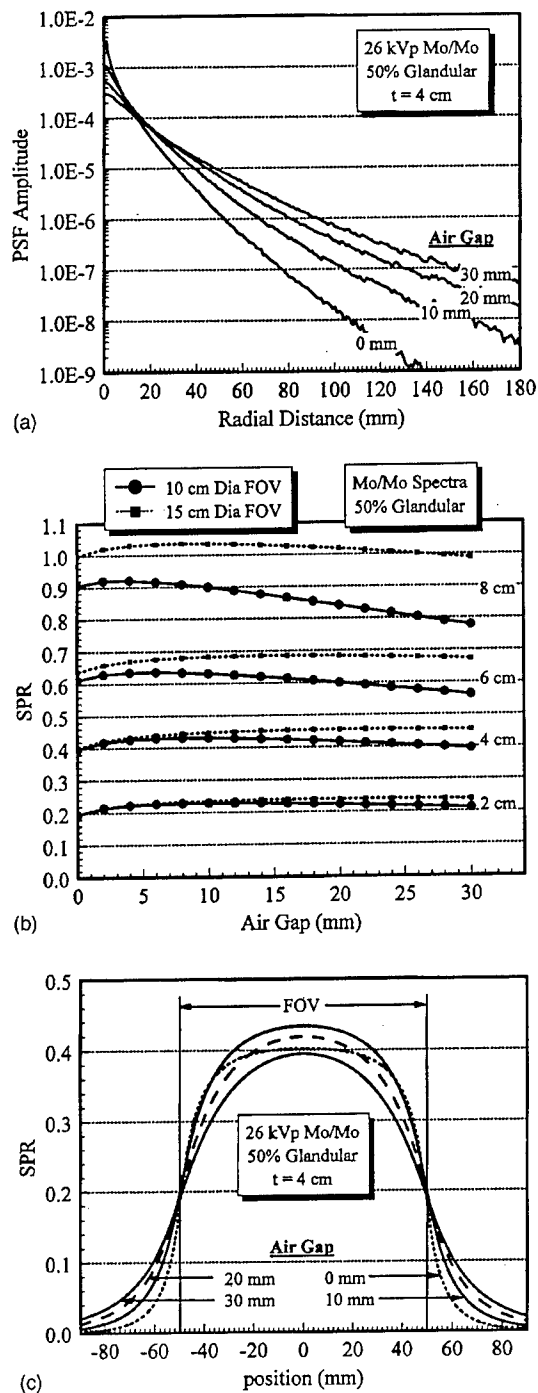


FIG. 3. (a) The point spread function amplitude (normalized such that the primary amplitude is equal to unity) is illustrated as a function of radial distance for PSFs corresponding to 4 different air gaps (as indicated). (b) The scatter to primary ratio is plotted as a function of the air gap for 4 different breast thicknesses. Data are plotted for two different circular fields of view. The kVps used were 24, 24, 28, and 32 for the 2, 4, 6, and 8 cm breast thicknesses. (c) The scatter profile across a 10 cm diameter circular field of view is illustrated for 4 different air gaps. The primary component inside the field of view is unity, and this value was used outside the field of view as well (where actually $\text{SPR} \rightarrow \infty$).

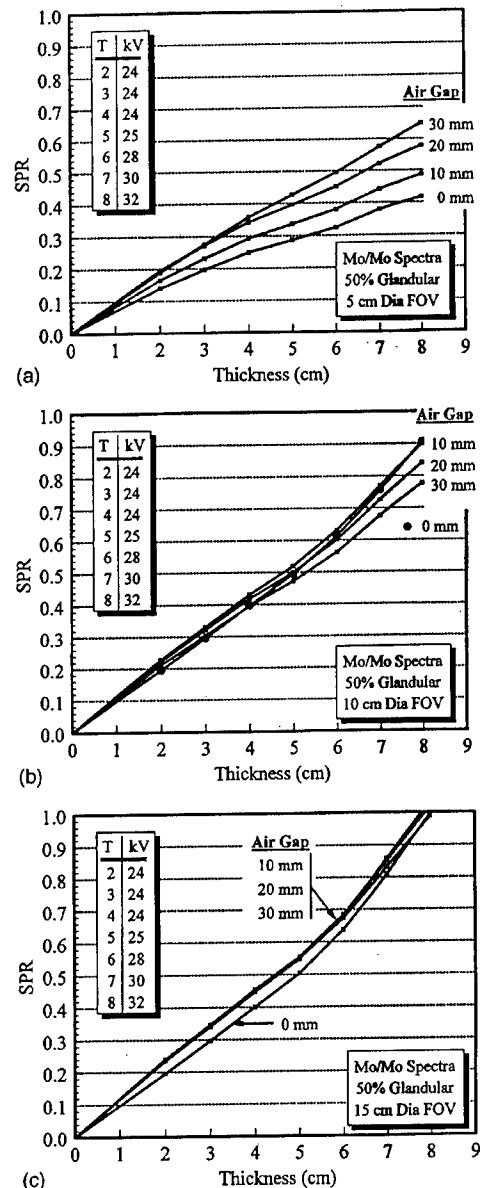


FIG. 4. (a) The scatter to primary ratio is illustrated as a function of thickness for 4 different air gaps (as indicated). The kVp increased with increasing breast thickness as indicated in the inset. These data are for a 5 cm diameter circular field of view. (b) The SPR versus breast thickness is illustrated for a 10 cm diameter circular field of view. (c) The SPR is illustrated as a function of breast thickness for a 15 cm diameter circular field of view.

C. Scatter dependence on air gap

The air gap distance in clinical mammography systems is approximately 1.5 cm, but this varies slightly depending on the manufacturer. Components of the system that contribute to the air gap include the cassette tunnel support, the anti-scatter grid, and its Bucky mechanism. Point spread functions (PSFs) of scattered radiation for a standard clinical x-ray beam (26 kVp Mo/Mo) for a 4 cm thick 50% glandular breast are shown in Fig. 3(a). Four PSFs are illustrated, at 0, 10, 20, and 30 mm air gaps. The 0 mm air gap PSF demon-

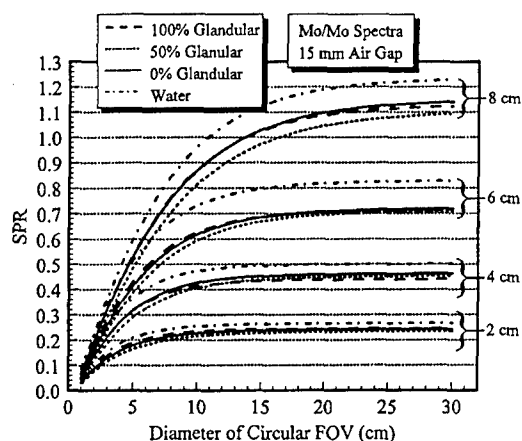


FIG. 5. The scatter to primary ratio is plotted as a function of the diameter of the circular field of view for four different breast thicknesses. The data for 4 different tissue compositions are illustrated for each breast thickness. The kVps were 24, 24, 28, and 32 kVp, for the 2, 4, 6, and 8 cm breast thicknesses, respectively.

strates the highest frequency attributes (most rapid fall-off with distance), and the PSFs tend to become lower frequency (more gradual fall-off) with an increasing air gap distance. The SPR is shown plotted as a function of air gap in Fig. 3(b), for four breast thicknesses and two common fields of view. For the larger FOV (15 cm diameter circle), the SPR demonstrates little variation with air gap over the range from 0 mm to 30 mm. For the smaller FOV (10 cm diameter circle), more variation is seen as the SPR falls off with increasing air gaps for the two larger breast thicknesses. In the limit of a very small FOV, one would expect near inverse square law fall-off, and thus it is consistent to observe increased air gap dependent SPR fall-off at smaller FOVs. The spatial distribution of the SPR across a circular FOV with a 10 cm diameter is shown in Fig. 3(c) for four different air gaps. As seen in the data shown in Fig. 3(b) as well, towards the center of the FOV the SPR initially increases for small air gaps. This is because scatter from the exit surface of the

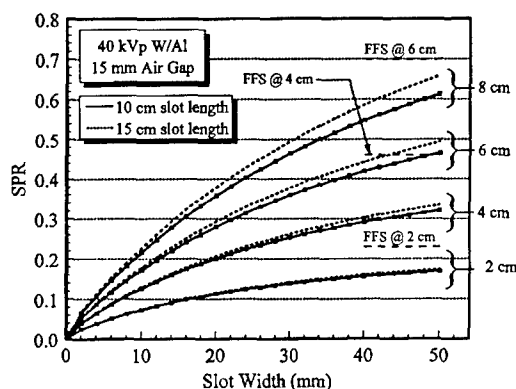


FIG. 6. The scatter to primary ratio is illustrated as a function of slot width for 4 different breast thicknesses. Data for both 10 cm and 15 cm slot lengths are shown. The full field SPR (FFS) is illustrated for the 2, 4, and 6 cm breast thicknesses as horizontal dashed lines.

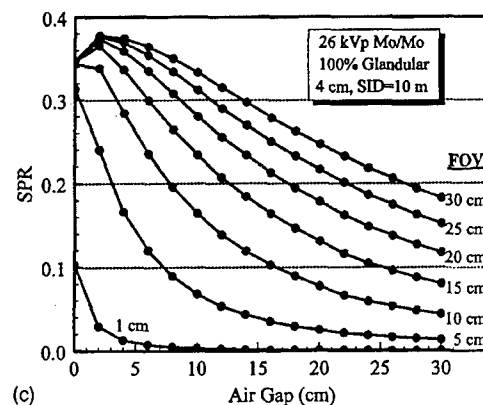
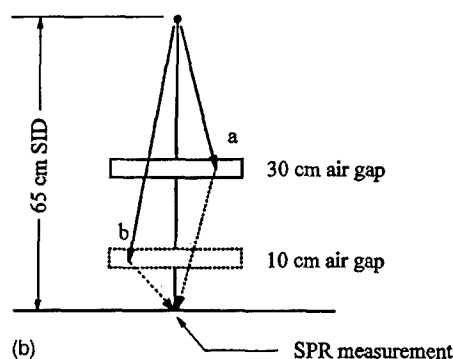
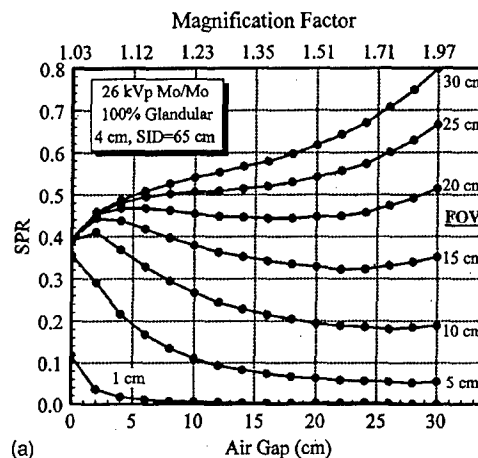


FIG. 7. (a) The scatter to primary ratio as a function of air gaps corresponding to magnification views is illustrated for a 4 cm breast thickness. The SPR for 7 different FOVs is shown. The magnification factors, calculated at mid-breast, corresponding to the air gaps and the 65 cm SID are illustrated at the top of the figure. The counterintuitive increase in the SPR with an increasing air gap is discussed in the text. (b) The geometry of the magnification mammography calculations is illustrated. (c) The SID was set to 10 meters, reducing the influence of the inverse square law in increasing the primary fluence incident upon the phantom. By reducing inverse square law effects to a negligible level (4%), the SPR is seen to fall off with increasing air gap as expected.

breast adjacent to the center of the FOV contributes to the SPR at the center. As the air gap gets larger, more of the scatter is capable of escaping the area directly under the breast and hence the SPR then decreases.

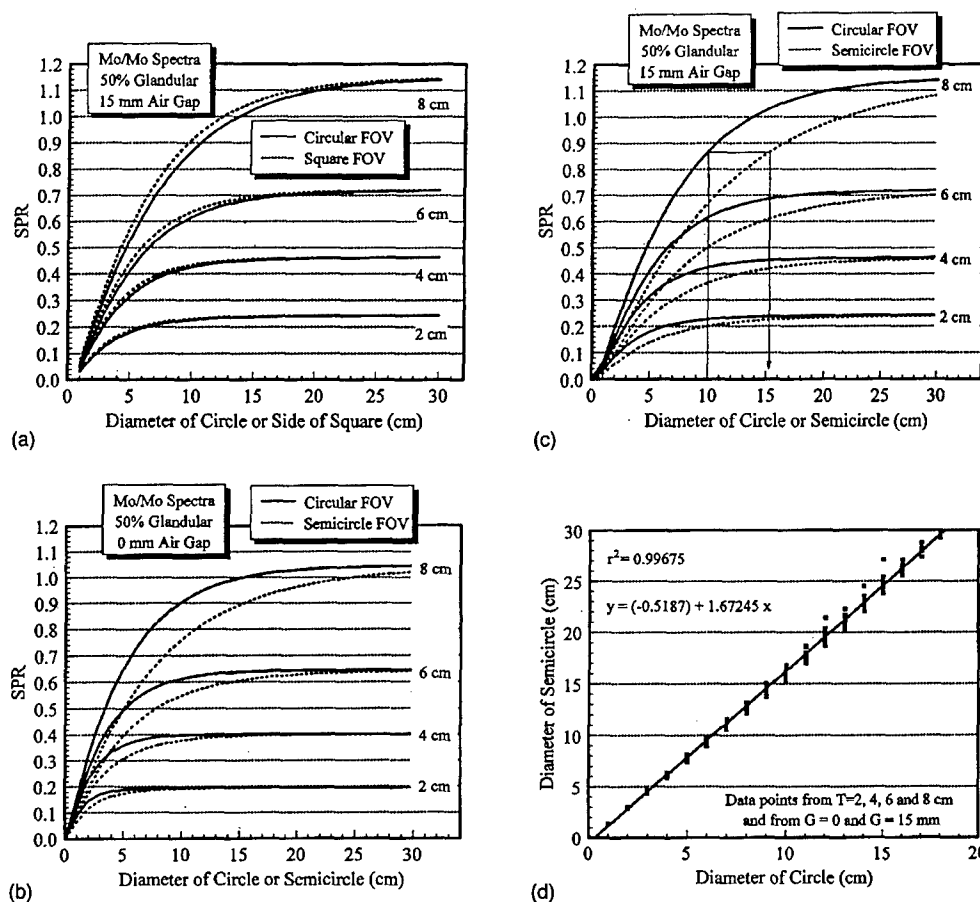


FIG. 8. (a) The scatter to primary ratio (calculated at the center of the field of view) is illustrated as a function of the diameter of a circular field of view (solid lines) or of the side length of a square field of view (dotted lines) for 4 different breast thicknesses. (b) The scatter to primary ratio is shown for circular and semicircular FOVs. The SPRs for the circular FOVs were calculated at the center of the circle. For the semi-circle, the SPRs were computed at the center of mass which coincides with the peak SPR in the FOV. These data are for a 0 mm air gap. (c) The SPR as a function of the diameter of circular and semicircular FOVs is shown for an air gap of 15 mm. A transform relating the diameters of circular FOVs to the diameter of a semi-circular FOV with the same SPR is illustrated as the vertical lines. For an 8 cm breast and a circular diameter of 10 cm, the line is read up to the circular SPR curve, reflected horizontally to the semi-circular SPR curve, and the line is then reflected downward to read the corresponding diameter. (d) The transform relating equivalent diameters (those that result in identical SPRs) between circular and semi-circular FOVs was computed and the data points illustrate these data. The linear fit to the data is shown.

D. Scatter dependence on breast thickness and area

The SPR as a function of breast thickness is well known to be nearly linear,⁵ and Fig. 4 illustrates this trend as well. Figures 4(a), 4(b), and 4(c) demonstrate the SPR versus thickness for three circular FOVs of diameters 5, 10, and 15 cm. For the 10 mm air gap data, the linear regression coefficients (r^2) are 0.986, 0.996, and 0.988 for the 5, 10, and 15 cm diameter FOVs, with respective slopes of 0.070, 0.110, and 0.126 cm^{-1} . As before, the kVp of the x-ray beam was increased with breast thickness as typically done in clinical situations.

Of the parameters which influence the SPR in mammography, the FOV and breast thickness demonstrated the greatest influence on the SPR values. Figure 5 shows the SPR as a function of the diameter of the circular FOV for four different breast thicknesses. In addition, at each thickness and FOV, SPRs are illustrated for three different glandular tissue ratios: (0%, 50%, and 100%), and water. Very similar results

were obtained for the three tissue compositions over the entire range of thicknesses and FOVs. For example, the coefficient of variation (σ/μ) calculated amongst the three tissue compositions (0%, 50%, and 100% glandular tissue), averaged over all FOVs was 4.0% for the 2 cm breast thickness, 5.3% for 4 cm, 4.7% for 6 cm, and 0.8% for the 8 cm breast thickness. The SPRs associated with water are noticeably higher than for breast tissue. The SPRs for water were analyzed using linear regression against the mean SPR for the three breast tissue types, and the slopes (and standard deviations of the slopes) of these analyses were 1.05 (0.01), 1.03 (0.02), 1.10 (0.01), and 1.07 (0.00) for the 2, 4, 6, and 8 cm data, respectively. With the exception of the 4 cm data, the SPR of water was larger than that of the mean breast tissue with statistical significance at the $p < 0.05$ level, with differences of 5%, 3%, 10%, and 7% observed for the 2, 4, 6, and 8 cm breast thicknesses.

Barnes devised a scanning multiple slit assembly^{13,14}

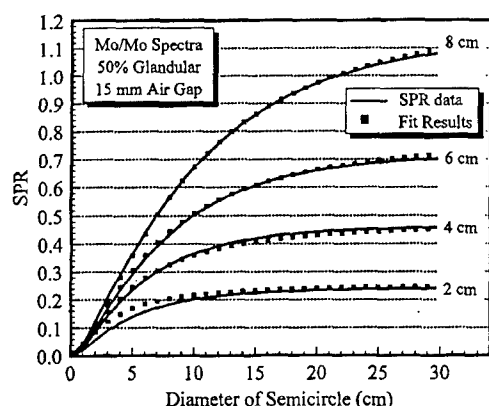


FIG. 9. This plot shows the SPRs for a semi-circular field and 15 mm air gap. The Monte Carlo calculated data (solid lines) and the computer fit data (symbols) are illustrated. The equation and coefficients are given in the text.

(SMSA) for reducing the SPR in mammography some years ago, and currently a digital mammography system¹⁵ derived from Yaffe's original design concept¹⁶ also makes use of a slot scat geometry. The SPR was integrated along the narrow dimension of a slot-scan aperture, since the scatter reaching a point on each pixel of the image is integrated along the direction of motion of the scanning slot. The SPR is shown as a function of the slot width in Fig. 6, for four different breast thicknesses and for two different slot lengths. The SPRs were determined at the center of the long axis of the slot. Compared to the SPRs for a circular field with a 15 cm diameter, the scatter reduction factors (ratio of SPRs) for a 2 mm slot width are 9.7, 11.7, 13.3, and 14.5 for breast thicknesses of 2, 4, 6, and 8 cm, respectively. For a 10 mm slot width, the scatter reduction factors drop to 3.1, 3.7, 4.0, and 4.4 for the same respective thicknesses. At 20 mm, these respective factors become 2.0, 2.3, 2.5, and 2.6.

E. Scatter dependence in magnification mammography

Magnification mammography is used frequently, and at most institutions no grid is used. The SPRs for a 4 cm breast and with a 26 kVp Mo/Mo spectrum and a fixed 65 cm source to image distance (SID) are shown as a function of the air gap in Fig. 7(a). For typical breast fields (15 cm diameter and lower), the SPRs fall-off with air gap distance. There is less fall-off with the larger breast areas. Surprisingly, the simulations also predict an actual increase in the SPR with an increasing air gap distance for very large area breasts. Breasts with areas larger than a 20 cm diameter (314 cm²) are quite rare (see the Appendix). Nevertheless, the larger diameters (25 and 30 cm) are included in Fig. 7(a) for completeness. For a relatively short SID, positioning the phantom from a 10 cm air gap to a 30 cm air gap increases the SPR by almost 50%. Why would the SPR increase as the air gap gets larger? The explanation is illustrated in Fig. 7(b). Changing the position of the phantom from a 10 cm air gap (where the mid-breast magnification factor is 1.2) to a 30 cm air gap (magnification=2.0) under fixed kV and mAs con-

ditions does not change the amount of primary radiation striking the center of the detector. However, positioning the phantom from the 10 cm air gap to the 30 cm air gap increases the intensity of primary radiation striking the surface of the phantom by a factor of 2.7 due to the inverse square law. Since the scatter fluence scales with the incident primary fluence to the phantom (in the absence of divergence effects), the amount of scattered radiation is also ~ 2.7 times greater. Even though solid angle effects reduce the amount of scatter reaching the SPR measurement site, these are more than compensated for (in the case of the larger diameter phantoms) by the increase in the number of scattered photons. Hence, the SPR increases with increasing air gap. To further clarify this observation, the calculations were repeated using a 10 meter SID [Fig. 7(c)]. With this much larger SID, the increase in the primary fluence striking the surface of the phantom in moving from the 10 cm to 30 cm air gap was only a factor of 1.04; however the solid angle-dependence of scatter collection efficiency was nearly identical to that for the 65 cm SID. The SPRs in Fig. 7(c), after an initial rise, fall off with air gap as expected.

F. Scatter dependence on shape of field of view

The shape of a real breast is rarely circular or square. However, these shapes lend themselves to easier measurement and have been used in the literature for characterizing the SPR. For a comparison between circular and square FOVs, [Fig. 8(a)] illustrates the SPR versus thickness as a function of both the diameter of a circular FOV and as a function of the side length of a square FOV. At smaller field sizes, the SPRs for the square FOVs are slightly higher than for circular FOVs, reflecting the 21% increase in area of a square versus a circle (when the side length of the square equals the diameter of the circle). At larger FOVs, the regions which define the difference between the circle and the square are sufficiently far away from the center where the SPRs were calculated that the SPR is no longer influenced.

For a phantom shape with no concavities (virtually all real breast silhouettes), it can be shown that the highest SPR for a monotonically decreasing PSF occurs at or near the two dimensional center of mass of the breast shape. The center of mass (COM) for circular and square phantoms are at their centers, where the center of mass for a semicircle occurs along the bilateral center line a distance $4r/3\pi$ from the centroid (r =radius) of the semi-circle [see "COM" in Fig. 2(a)]. The SPRs were calculated at the center of mass for both circles and semi-circles and these values are plotted in Fig. 8(b) (0 mm air gap) and 8(c) (15 mm air gap). Of course, the SPR at the center of mass for a semi-circle of radius r will be less than for a circle of radius r , since the area is halved, and this is appreciated in Figs. 8(b) and 8(c). To allow a conversion from circular diameters to semi-circular diameters, the diameter of a semi-circle corresponding to the diameter of a circle at equal SPR levels was computed from the data in Figs. 8(b) and 8(c). These results are illustrated in Fig. 8(d). The data at both air gaps (0 and 15

mm) and all four phantom thicknesses fell generally along a line described by

$$D_{\text{semi-circle}} = (-0.518) + 1.672 D_{\text{circle}},$$

where D_{circle} is the diameter of the circle and $D_{\text{semi-circle}}$ is the diameter of the semi-circle. This calibration can be used to convert the diameter reported for SPR results using circular fields to an equivalent diameter for semi-circular fields. The equation can be rearranged and used for the inverse corrections as well. This equation was produced using data spanning air gaps from 0 to 15 mm and phantom thicknesses from 2 to 8 cm. It should be robust over the mammography energy range and for different phantom compositions, given the observations presented previously with respect to these parameters.

Given that there is little energy dependence of the SPR and that most clinical mammography systems use air gaps in the vicinity of 1.5 cm, the SPR data as a function of thickness and field diameter were parametrized. The SPR was computed at the center of mass for a semi-circular breast shape for diameters ranging from 1 cm to 30 cm, and for breast thicknesses from 2 cm to 8 cm with 1 cm increments. The data calculated using Monte Carlo techniques are shown in Fig. 9 as the solid lines (the data for odd thicknesses were not shown for clarity). These data were fitted to a polynomial using commercially available software (TableCurve 3D, Jandel Scientific, Corte Madera, CA). For simplicity, the computer fit using only three coefficients ($r^2 = 0.998$, 210 points used in fit) was used. The fit data are shown as the square symbols in Fig. 9. The fit equation was

$$\text{SPR} = [a + b \times (\text{dia})^{-1.5} + c \times (\text{thickness})^{-0.5}]^{-1},$$

where $a = -2.35452817439093$, $b = 22.3960980055927$, $c = 8.85064260299289$, and where the units of dia and of thickness are centimeters. Using the fit equation given above, the average error from the Monte Carlo SPRs was -3.1% ($\sigma = 10.5\%$), where negative errors are due to the fit value being lower than the measured value. For breast diameters 3 cm and greater, the average error was -1.3% ($\sigma = 4.8\%$) and the median difference was -0.2% with a 95% range from -13.8% to 3.0% . This equation is valid for all diameters (not just integers) between 3 cm and 30 cm and all thicknesses from 2 cm to 8 cm.

The results of this investigation indicate that the scatter properties remain essentially constant over the practical range of x-ray beam energies used in diagnostic mammography. Indeed, only a slight change in the SPR is observed at beam energies ranging all the way up to 120 kVp. Over the air gaps associated with standard (nonmagnification) mammography, the SPR was found to be relatively independent of the breast tissue composition. For tissue composition in the range from 0% to 100% glandular, the SPR is also relatively constant. Using water as a breast phantom material does however produce higher SPRs. The SPR is highly dependent upon where in the field it is measured, and the maximum SPR generally occurs at the center of mass for typical compressed breast shapes. The SPR increases approximately

linearly with breast thicknesses, and asymptotic behavior is observed when the SPR is plotted as a function of the FOV diameter.

For the average semicircular breast area of 157 cm^2 (with an effective semi-circular diameter of 10 cm corresponding to the SPR levels of a 6.3 cm diameter circular field), the SPRs for a 15 mm air gap and appropriate thickness-dependent kVps were 0.20, 0.36, 0.49, and 0.64, for the 2, 4, 6, and 8 cm breast thicknesses, respectively.

ACKNOWLEDGMENTS

This investigation was funded in part by grants from the California Breast Cancer Research Program (1RB 0192), the Department of Defense Breast Cancer Research Program (DAMD17-98-1-8176), and the National Cancer Institute (R21 CA82077).

APPENDIX: TYPICAL BREAST AREAS

A mammographer (KKL) tallied the compressed breast thickness for a small sample of 82 consecutive left cranio-caudal mammograms. In addition, the width of the breast at the edge of the film corresponding to the chest wall was measured with a ruler, and the distance from the edge of the film at the chest wall to the nipple was measured as well. A histogram of the distribution of breast thicknesses from this sample is illustrated in Fig. 10. The mean compressed breast thickness was 5.2 cm ($\sigma = 1.3$ cm). The median thickness was 5.2 cm, and the range from 5% to 95% encompassed breast thicknesses from 2.8 cm to 7.1 cm. Half of the women had compressed breast thicknesses between 4.3 cm and 6.2 cm.

The measurements made on the mammograms were used to calculate the area of the breast on the image, assuming an ellipsoid. If the width at the chest wall is given by A , and the chest wall to nipple dimension is B , then the area was calculated as $\frac{1}{4}\pi AB$. Figure 11 illustrates a histogram of the areas of the 82 breast images measured. The mean area was 157.3 cm^2 which corresponds to a semi-circular diameter of 10 cm and a circular diameter [from Fig. 8(d)] of 6.2 cm. The median breast area was 145.7 cm^2 . Half of the breasts spanned

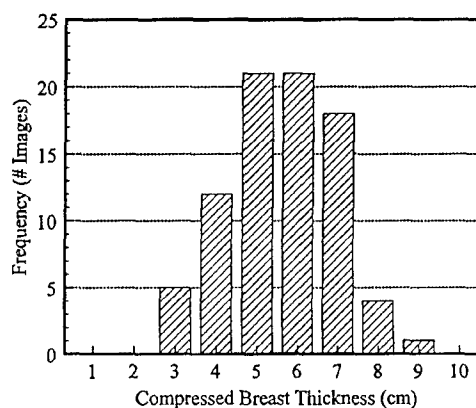


FIG. 10. The compressed breast thickness was read from 82 consecutive mammograms and the frequency distribution is illustrated. The median breast thickness was 5.2 cm.

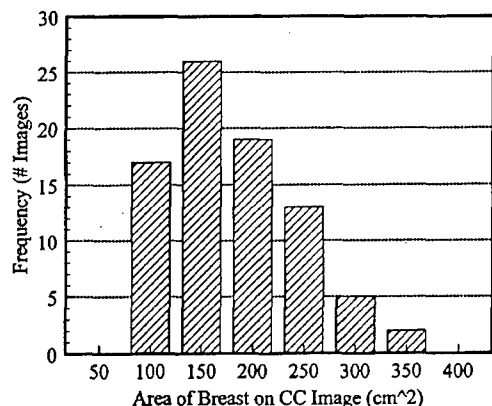


FIG. 11. The horizontal and vertical dimensions of the breast shadow were measured on 82 mammograms, and using the assumption of an ellipsoidal shape, the area of the breast in these CC mammograms was computed. This plot illustrates a histogram of the 82 breast areas. The median breast area was 145.7 cm².

areas from 108.7 cm² to 198.1 cm², corresponding to semi-circular diameters ranging from 8.3 cm to 11.2 cm. Converting these values to equivalent circular FOVs [from Fig. 8(d)] results in a range of circular diameters from 5.3 cm to 7.0 cm. The breast area at the 5th percentile was 76.5 cm², and at the 95th percentile the area was 263.8 cm².

^{a)}Corresponding address: John M. Boone, Ph.D., Department of Radiology, UC Davis Medical Center, 4701 X Street, Research Imaging Center, Sacramento, California 95817. Telephone: (916) 734-3158 Fax: (916) 734-0316; electronic mail: jmboone@ucdavis.edu

- ¹G. T. Barnes and I. A. Brezovich, "The intensity of scattered radiation in mammography," *Radiology* **126**, 243-247 (1978).
- ²G. T. Barnes, "Contrast and scatter in x-ray imaging," *Radiographics* **11**, 307-323 (1991).
- ³D. R. Dance and G. J. Day, "The computation of scatter in mammography by Monte Carlo methods," *Phys. Med. Biol.* **29**, 237-247 (1984).
- ⁴R. Fahrig, J. G. Mainprize, N. Robert, A. Rogers, and M. J. Yaffe, "Performance of glass fiber antiscatter devices at mammographic energies," *Med. Phys.* **21**, 1277-1282 (1994).
- ⁵S. L. Fritz, C. H. Chang, and W. H. Livingston, "Scatter/primary ratios for x-ray spectra modified to enhance iodine contrast in screen-film mammography," *Med. Phys.* **10**, 866-870 (1983).
- ⁶Z. Jing, W. Huda, and J. K. Walker, "Scattered radiation in scanning slot mammography," *Med. Phys.* **25**, 1111-1117 (1998).
- ⁷J. M. Boone and V. N. Cooper III, "Scatter/primary in Mammography: Monte Carlo validation," *Med. Phys.* **27**, 1818-1831 (2000).
- ⁸D. R. Dance, J. Persliden, and G. A. Carlsson, "Calculation of dose and contrast for two mammographic grids," *Phys. Med. Biol.* **37**, 235-248 (1992).
- ⁹P. S. Rezentes, A. de Almeida, and G. T. Barnes, "Mammography grid performance," *Radiology* **210**, 227-232 (1999).
- ¹⁰U. Neitzel, "Grids or air gaps for scatter reduction in digital radiography: a model calculation," *Med. Phys.* **19**, 475-481 (1992).
- ¹¹J. M. Boone and J. A. Seibert, "An accurate method for computer-generating tungsten anode x-ray spectra from 30 kV to 140 kV," *Med. Phys.* **24**, 1661-1670 (1997).
- ¹²J. M. Boone, T. R. Fewell, and R. J. Jennings, "Molybdenum, rhodium, and tungsten anode spectral models using interpolating polynomials with application to mammography," *Med. Phys.* **24**, 1863-1874 (1997).
- ¹³G. T. Barnes, X. Wu, and A. J. Wagner, "Scanning slit mammography," *Med. Prog. Technol.* **19**, 7-12 (1993).
- ¹⁴M. V. Yester, G. T. Barnes, and M. A. King, "Experimental measurements of the scatter reduction obtained in mammography with a scanning multiple slit assembly," *Med. Phys.* **8**, 158-162 (1981).
- ¹⁵M. M. Tesic, M. F. Piccaro, and B. Munier, "Full field digital mammography scanner," *Eur. J. Radiol.* **31**, 2-17 (1999).
- ¹⁶M. J. Yaffe, "Direct digital mammography using a scanned-slot CCD imaging system," *Med. Prog. Technol.* **19**, 13-21 (1993).

DAMD17-98-18176, Final Report - August 2001

Computer Simulation of Breast Cancer Screening

PI: John M. Boone, Ph.D.

Appendix F:

(2000) VN Cooper, JM Boone, and JA Seibert, "A lesion detectability simulation method for digital x-ray imaging", Medical Physics 27;66-74
(2000)

A lesion detectability simulation method for digital x-ray imaging^{a)}

V. N. Cooper III, J. M. Boone, and J. A. Seibert

Department of Radiology, University of California Davis, 4701 X Street, Sacramento, California 95831

(Received 16 February 1999; accepted for publication 22 October 1999)

A simulation method is described in this work that aids in quantifying the upper limits of lesion detectability as a function of lesion size, lesion contrast, pixel size, and x-ray exposure for digital x-ray imaging systems. The method entails random lesion placement with subsequent simulated imaging on idealized x-ray detectors with no additive noise and 100% quantum detective efficiency. Lesions of different size and thickness were simulated. Mean (expectation) lesion signal-to-noise ratios (LSNRs) were calculated and receiver operating characteristic (ROC) curves were constructed based on LSNR ensembles. Mean (expectation) values of the areas under the ROC curves were calculated for lesions of varying size on pixel arrays of varying size at different exposures. Analyses were performed across several parameters, including lesion size, pixel size, and exposure levels representative of various areas of radiography. As expected, lesion detectability increased with lesion size, contrast, pixel size, and exposure. The model suggests that lesion detectability is strongly dependent on the relative alignment (phase) of the lesion with the pixel matrix for lesions on the order of the pixel size. © 2000 American Association of Physicists in Medicine. [S0094-2405(00)01801-0]

Key words: simulations, digital radiography, lesion detectability, signal-to-noise ratio (SNR), receiver operating characteristic curve (ROC)

I. INTRODUCTION

Since the infancy of digital x-ray imaging, there has been much interest in pixel size requirements for adequate detection of lesions. Observational and experimental studies on lesion detectability as a function of pixel size abound in the literature.¹⁻⁹ Typically, these studies involve human detection of a specific type of lesion from images acquired with different pixel sizes. These studies then utilize some form of receiver operating characteristic curve (ROC)¹⁰ analysis to demonstrate lesion detectability as a function of pixel size. The data in the literature are somewhat limited, however, concerning theoretical studies¹¹ that describe the mechanism of lesion detectability as a function of pixel size.

This paper demonstrates a simple simulation model that may be used to gain insight into the maximum possible lesion detectability as a function of several variables, in particular pixel size. The mean lesion signal-to-noise ratio (LSNR), integrated over the entire lesion, was calculated as a function of lesion size, lesion transmission, x-ray exposure level, and pixel size. Standardized receiver operating characteristic (ROC) curves were constructed for lesion-present and lesion-absent LSNRs. The areas under the generated ROC curves, the A_z 's, corresponded to the detectability of the lesions in their entirety and were used as the measures of lesion detectability.

II. METHODS

A. Phase-dependent signal

It is well understood that discrete detectors inherently are shift-variant. As a consequence of this shift-variant nature,

the position of the lesion with respect to the pixel matrix can have a significant impact on lesion detectability. Lesion signals at discrete phases of the pixel array were calculated for an ideal digital stationary^{12,13} detection system employing varying pixel sizes with 100% active area. The system was modeled with no additive noise, 100% quantum detection efficiency, with an ideal point spread function (i.e., δ -function), and under scatter-free conditions. The number of quanta incident on a pixel is large in diagnostic radiology, and for large values of N , the Gaussian distribution is a good approximation to the Poisson distribution.¹⁵ Thus the Gaussian distribution with the standard deviation, σ , equal to the square root of the mean, μ , was used to simulate x-ray exposure to the detector. A Gaussian random number generator (GRNG) was used.¹⁴⁻¹⁶

Square lesions differing in size, composition, and thickness were considered. The lesions were assumed to be superimposed on homogeneous background tissue (i.e., see Fig. 1). The lesion under consideration was assumed to have the upper left-hand corner of its x-ray shadow fall on a reference pixel with pixel phase determined randomly with a uniform probability density function (PDF) for both detector plane (x and y) dimensions. The outputs of a uniform random number generator (URNG), on the interval $\{0,1\}$ were multiplied by the linear pixel dimensions and these values were used to define the translational phases, Ω_x and Ω_y (Fig. 2). This physically corresponded to the upper left-hand corner of the lesion having an equally likely chance of occurring at any location in the reference pixel. The locations of the other three corners of the lesion were determined by its dimensions.

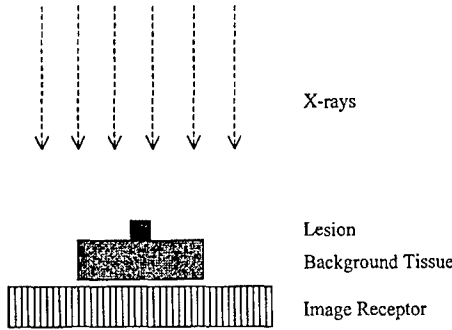


FIG. 1. The basic x-ray imaging geometry.

Following the placement of the lesion, x-ray exposure using a 50-keV monoenergetic beam was simulated and the total quanta at each pixel location were tallied. This was done for both lesion pixels and background pixels. The 50-keV monoenergetic beam is effectively equivalent to an 80-kVp beam with 2-mm Al filtration passing through 20 cm of tissue.¹⁷ The exposure-dependent total number of quanta captured by the pixels corresponding to the lesion shadow, $Q(X)_L$, were summed over the total number of lesion pixels, M_L

$$Q(X)_L = X \times \sum_{m=1}^{M_L} q_m, \quad (1)$$

where X is the radiation exposure expressed in mR. q_m is the number of quanta per mR captured by the m th pixel corresponding to the lesion shadow and is expressed as

$$q_m = q(\phi a^2, \sigma)_m \times (t f_m + (1 - f_m)), \quad (2)$$

where

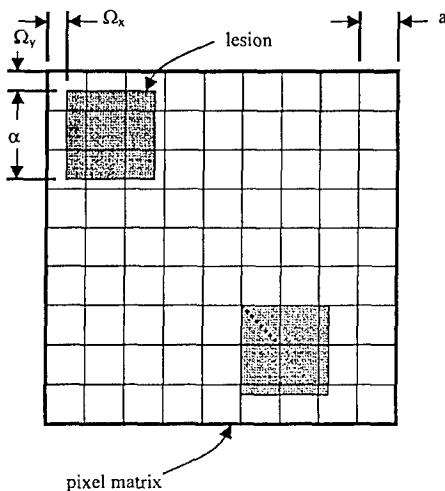


FIG. 2. A square lesion of side length α is shifted Ω_x and Ω_y from the origin of a square pixel of side length a . In the lower right corner is a lesion starting in-phase with a pixel of the array. The dots represent calculation points for demonstrating the shift-dependent nature of the LSNR. For the expectation LSNR, the phase was randomly selected and LSNR calculated multiple times effectively averaging over the entire pixel.

$$\sigma = \sqrt{\phi a^2} \quad (3)$$

and where ϕ is the x-ray photon fluence per unit exposure at 50 keV ($260\,718\text{ mm}^{-2}\text{ mR}^{-1}$);¹⁷ a^2 is the pixel area (a is the length of the pixel sides); ϕa^2 is the mean number of x-ray photons incident on that pixel per unit exposure; and σ is the Poisson noise associated with that number. $q(\phi a^2, \sigma)_m$ is the m th pixel realization of the unit-exposure x-ray quanta. The transmission associated with the lesion is given by t , and the fraction of the m th pixel covered by the lesion is represented by f_m .

Likewise, the background quanta, q_b , were summed over the total number of background pixels, M_B , to yield the total number of exposure dependent background quanta, Q_B :

$$Q(X)_B = X \times \sum_{b=1}^{M_B} q_b. \quad (4)$$

In general, M_B was significantly larger than M_L (typically by a factor of 100). Physically, this represents visualization and detection of a relatively small lesion in a relatively large background.

Q_L was divided by M_L to yield the mean lesion signal per pixel, $N(X)_L$,

$$N(X)_L = \frac{Q(X)_L}{M_L} \quad (5)$$

and likewise for the mean background signal per pixel, $N(X)_B$,

$$N(X)_B = \frac{Q(X)_B}{M_B}. \quad (6)$$

B. Lesion SNR (LSNR)

The mean lesion signal per pixel, $N(X)_L$, was subtracted from the mean background signal per pixel, $N(X)_B$,

$$N(X)'_L = N(X)_B - N(X)_L, \quad (7)$$

where $N(X)'_L$ is the background-corrected lesion signal. This signal, $N(X)'_L$, described on a per pixel basis, is summed over all M_L pixels corresponding to the lesion shadow. Physically, this represents the integration of signal over the entire lesion. The total lesion signal, $S(X)_L$, is given by:

$$S(X) = M_L \times N(X)'_L. \quad (8)$$

The variance in the integrated signal is physically represented as image noise and was quantified using standard error propagation techniques¹⁸ for Eqs. (7) and (8), and was given as:

$$\sigma(X)^2 = M_L^2 \times (\sigma(X)^2_{N(X)_L} + \sigma(X)^2_{N(X)_B}), \quad (9)$$

where $\sigma(X)_{N(X)_B}$ is the background noise per pixel, and $\sigma(X)_{N(X)_L}$ is the lesion noise per pixel. The background noise per pixel was calculated as the standard deviation of the background pixel quanta and was found not to depend on M_B , which is consistent with the ergodicity^{12,13} principle

TABLE I. Lesion size, pixel size, and exposure parameter values.

Lesion size (μm)	Pixel size (μm)	Exposure (mR)
25	25	0.0010
50	50	0.0025
75	75	0.0050
100	100	0.0075
150	150	0.010
200	200	0.025
250	250	0.050
300	300	0.075
350	400	0.10
400	500	0.25
450		0.50
500		0.75
600		1.0
700		2.5
800		5.0
900		7.5
1000		10
1250		25
1500		50
2000		

often invoked in noise quantification in x-ray imaging. The lesion variance per pixel, $\sigma(X)_{N(X)_L}^2$, was calculated as

$$\sigma(X)_{N(X)_L}^2 = \frac{\sum_{m=1}^{M_L} (q_m - N(X)_B \times [f_m t + (1 - f_m)])^2}{(M_L - 1)}, \quad (10)$$

where the numerator is the summed variance in the x-ray quanta corrected for partial pixel coverage by the lesion. Lesion SNR (LSNR) was then calculated as

$$\text{LSNR} = \frac{S(X)}{\sigma(X)}. \quad (11)$$

C. $\langle \text{LSNR} \rangle$

Random lesion placement and subsequent SNR calculation were performed 100 times to yield an ensemble of LSNRs. The expectation (mean) lesion SNR, $\langle \text{LSNR} \rangle$, was calculated as the mean of the lesion SNRs in the ensemble:

$$\langle \text{LSNR} \rangle = \frac{1}{K} \sum_{k=1}^K \text{LSNR}_k, \quad (12)$$

where LSNR_k is the k th realization of LSNR and K is the number of realizations in the ensemble.

D. $\langle A_Z \rangle$

Ensembles of 100 LSNRs were computed both for the cases of lesion present and lesion absent. The lesion absent ensemble was constructed by setting transmission, t , equal to 1.0. Both ensemble LSNR arrays were ordered and ROC analysis was performed. The area under the ROC curve, A_Z , was calculated via Reimann trapezoidal integration.¹⁶ A_Z was calculated ten different times, each time from different LSNR data to yield an expectation (mean) value, $\langle A_Z \rangle$, and an error estimate

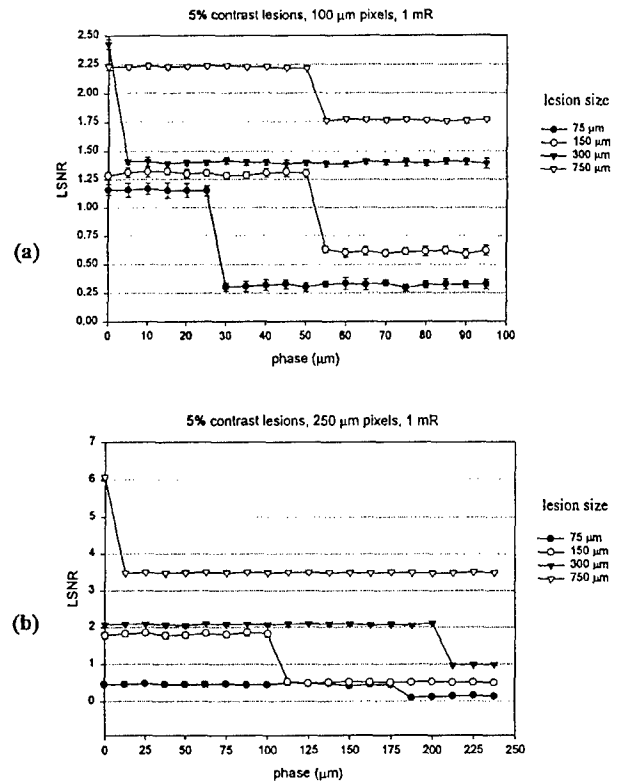


FIG. 3. The resulting shift-dependent (x and y simultaneous shifts) LSNR for a 95% transmitting lesion (constant) with (a) 1-mR exposure incident on an array with 100- μm pixels and (b) 1-mR exposure on 250- μm pixels. The error bars represent $\pm \sigma$.

$$\langle A_Z \rangle = \frac{1}{K} \sum_{k=1}^K (A_Z)_k, \quad (13)$$

where $(A_Z)_k$ is the k th realization in a K -length ensemble of A_Z 's. $\langle A_Z \rangle$ was used as the ultimate measure of lesion detectability.

E. Parameter values

$\langle A_Z \rangle$ and $\langle \text{LSNR} \rangle$ were calculated for several different combinations of lesion size, pixel size, and exposure level. Table I gives the values of all three parameters that were used in this study. Every permutation of the three parameters was simulated.

III. RESULTS

A. Phase-dependent SNR

To demonstrate the effects of pixel phase on LSNR, lesions of varying sizes were placed at discrete phases with $\Omega_x = \Omega_y = \Omega_{xy}$. LSNR as a function of pixel phase was calculated 100 times at each phase and the results were averaged to yield a mean LSNR at a given phase. This process was repeated ten different times at each phase to yield the mean LSNRs with smaller uncertainty (i.e., the mean of the sample means). Figure 2 illustrates the discrete phases used for this demonstration. Figure 3(a) shows the phase-dependent LSNR of 75-, 150-, 300-, and 750- μm lesions

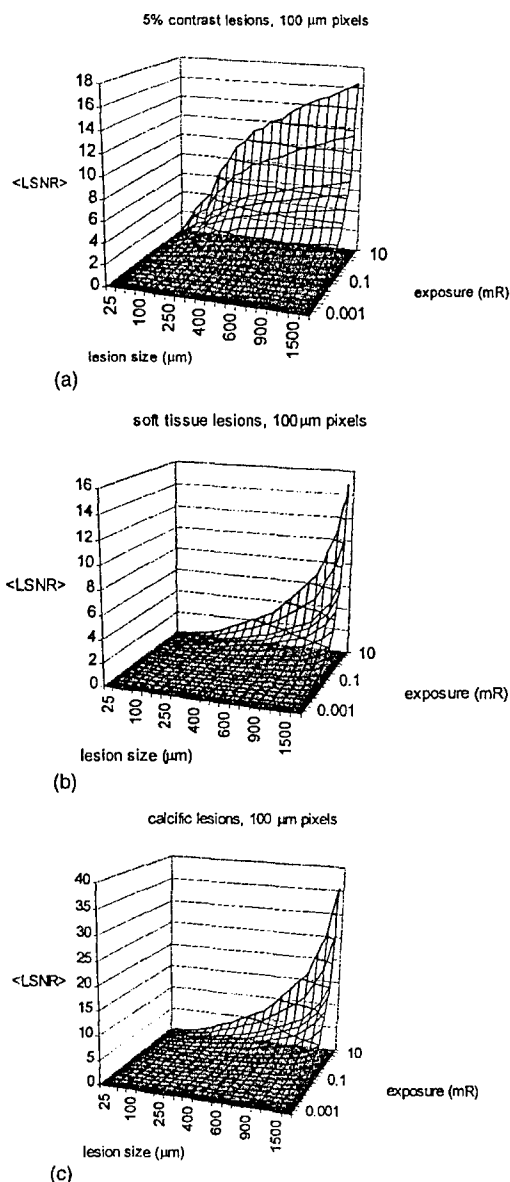


FIG. 4. <LSNR> for (a) 5% constant contrast lesions and 100-μm pixels, (b) cubic soft-tissue lesions and 100-μm pixels, and (c) cubic calcific lesions and 100-μm pixels.

with constant 5% contrast (95% transmission), 100-μm pixels, and 1-mR exposure. As the lesion size increased beyond the pixel size, the phase effects on the LSNR decreased. Notice that the 75-μm lesion, starting in-phase, had constant LSNR until the 25-μm shift value. The SNR plummeted at this point as the lesion was shifted into four different pixels with each pixel having lowered signal and greater coefficients of variation (relative noise). Physically, in these partially covered pixels, this represents a degradation of contrast and hence signal, due to a partial area effect, similar to the degradation of contrast due to the partial volume effect in computed tomography.

The 150-μm lesion had constant SNR until $\Omega_{xy} = 50 \mu\text{m}$, after which it covered nine pixels instead of four.

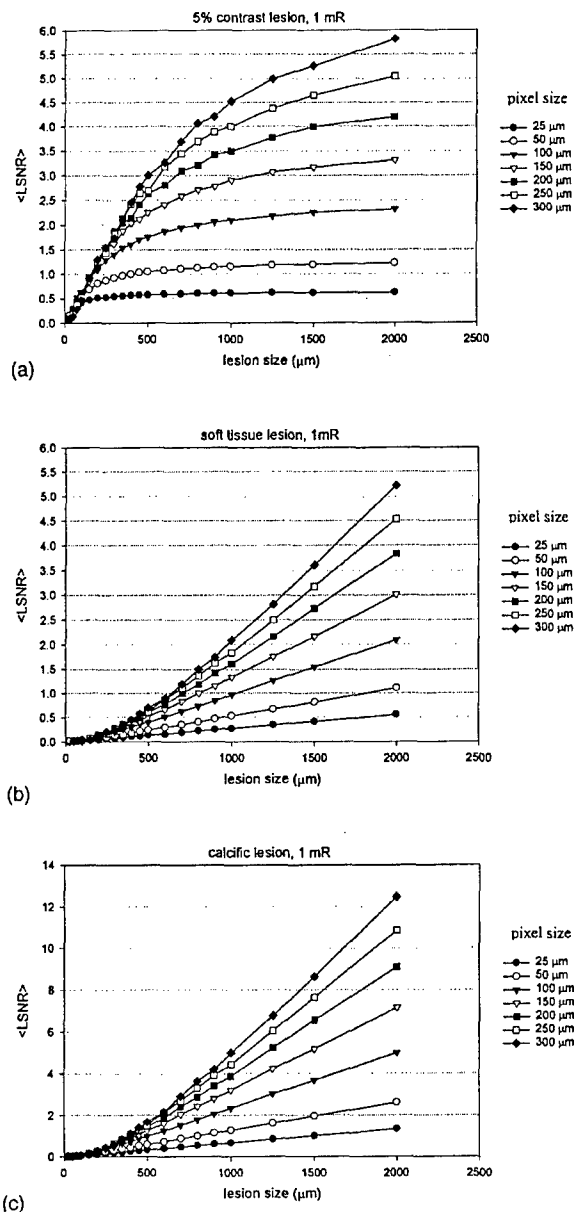


FIG. 5. <LSNR> at 1 mR for different pixel sizes for (a) 5% contrast lesions, (b) cubic soft tissue lesions, and (c) cubic calcific lesions.

The 750-μm lesion had a less-pronounced LSNR drop at $\Omega_{xy} = 50 \mu\text{m}$. The smaller drop was due to the fact that this large lesion had a greater proportion of pixels that were entirely covered by the lesion, somewhat mitigating the variational effects of edge pixels. Figure 3(b) shows the shift-dependent LSNR of 75-, 150-, 300-, and 750-μm lesions with constant 5% contrast, 1 mR, and 250-μm pixels. Similar phase-related behavior is exhibited. The effects of the large pixel size are discussed in Sec. IV.

B. <LSNR>

<LSNR> was calculated for various pixel sizes, lesion sizes, and exposures with 100 realizations of LSNR com-

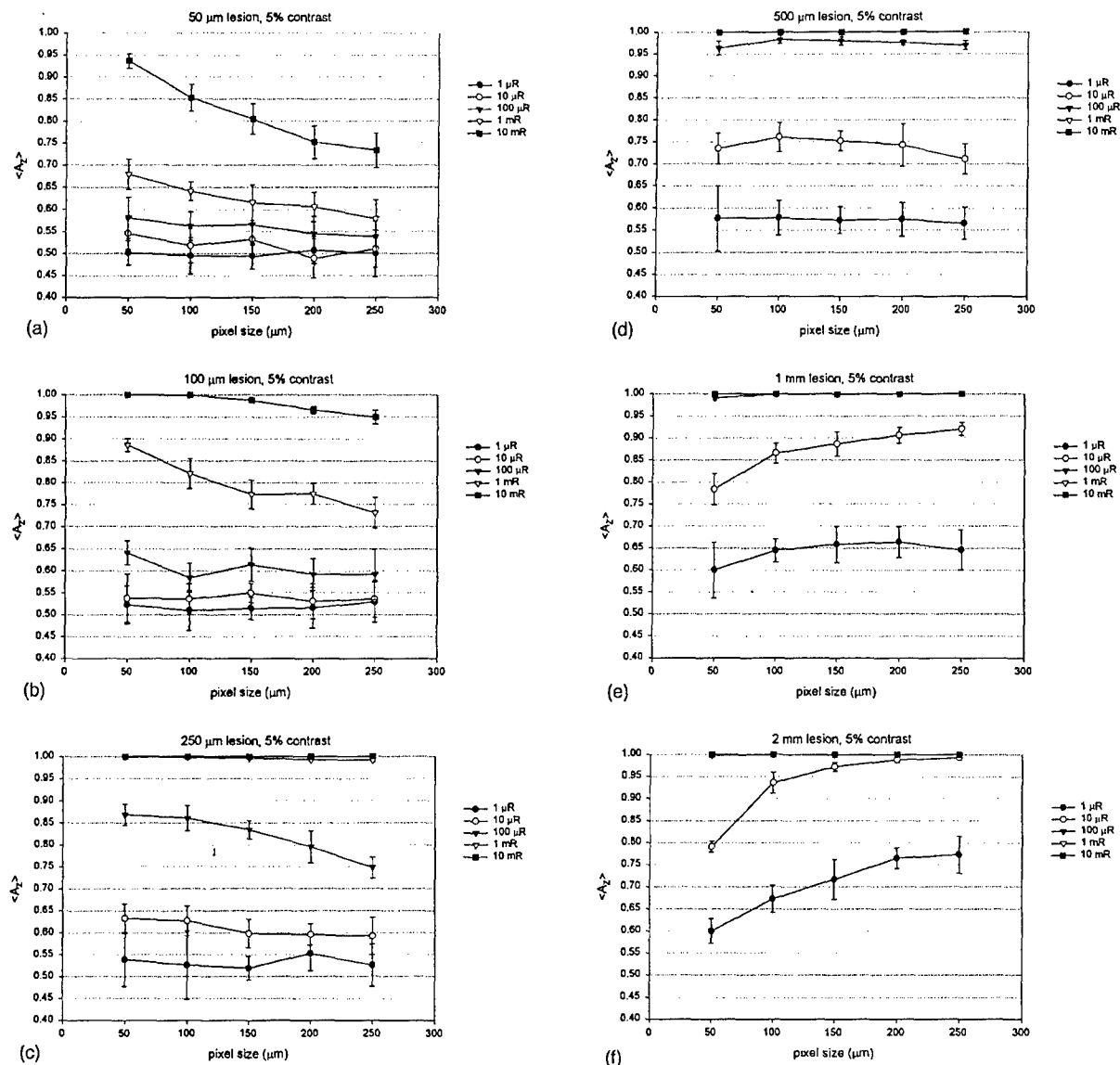


FIG. 6. 5% constant contrast lesion detectability, $\langle A_Z \rangle$, for (a) 50- μm lesions, (b) 100- μm lesions, (c) 250- μm lesions, (d) 500- μm lesions, (e) 1-mm lesions, and (f) 2-mm lesions. The error bars represent $\pm \sigma$. Note: In parts (d), (e), and (f), the data are obscured with $\langle A_Z \rangle$ equal to 1.0 at all pixel sizes for the highest exposures.

puted for each combination of pixel size, lesion size, and exposure. Both constant contrast (transmission) lesions and cubic lesions (thickness=length=width) were considered. Transmission was given by $e^{-\mu\alpha}$ for the cubic lesions where α is the thickness and μ is the linear attenuation coefficient at 50 keV and is equal to 0.57 cm^{-1} for bone and 0.23 cm^{-1} for soft tissue.¹⁹ Figure 4(a) shows the surface plot of $\langle \text{LSNR} \rangle$ of a lesion with constant 5% contrast for 100- μm pixels. Figure 4(b) shows the surface plot of $\langle \text{LSNR} \rangle$ for cubic soft tissue lesions for 100- μm pixels. Figure 4(c) shows the surface plot of $\langle \text{LSNR} \rangle$ for cubic calcific lesions for 100- μm pixels. Figure 5(a), (b), and (c) illustrates $\langle \text{LSNR} \rangle$ at 1 mR as a function of lesion size for a series of

pixel sizes, for 5% contrast lesions, soft tissue lesions, and calcific lesions, respectively. Error bars were not included in these figures for clarity.

C. $\langle A_Z \rangle$

$\langle A_Z \rangle$ was calculated from an ensemble of 10 A_Z realizations each based on 100 realizations each of lesion and no-lesion LSNRs. Figure 6(a)–(f) shows $\langle A_Z \rangle$ for 5% contrast lesions; Fig. 7(a)–(f) shows $\langle A_Z \rangle$ for cubic soft tissue lesions, and Fig. 8(a)–(f) shows $\langle A_Z \rangle$ for cubic calcific lesions. To clarify the interesting behavior of $\langle A_Z \rangle$ for lesion sizes on the order of pixel sizes, $\langle \text{LSNR} \rangle$ data at different exposures

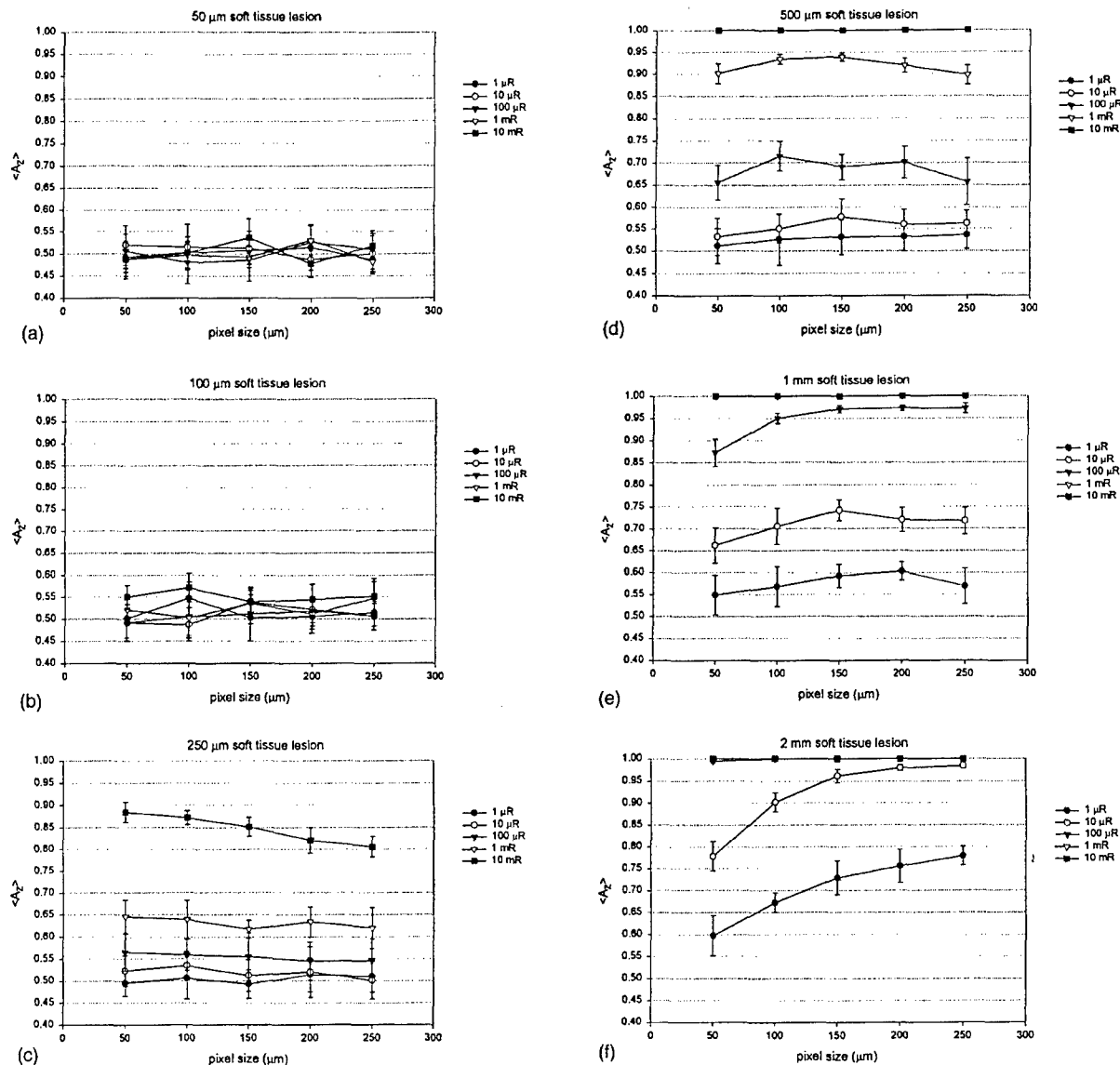


FIG. 7. Soft tissue lesion detectability, $\langle A_Z \rangle$, for (a) 50- μm cubic lesions, (b) 100- μm cubic lesions, (c) 250- μm cubic lesions, (d) 500- μm cubic lesions, (e) 1-mm cubic lesions, and (f) 2-mm cubic lesions. The error bars represent $\pm\sigma$. Note: In parts (e) and (f), the data are obscured with $\langle A_Z \rangle$ equal to 1.0 at all pixel sizes for the highest exposures.

for given lesion sizes with 5% contrast were replotted against pixel size. Figure 9(a)–(g) shows $\langle \text{LSNR} \rangle$ for 5% contrast lesions.

IV. DISCUSSION

A probabilistic model was presented whereby lesion SNR was calculated as a function of phase, lesion size, exposure, and pixel size. ROC methodology was utilized to quantify lesion detectability. As expected, lesion detectability mostly increased with increasing exposure, lesion size, and pixel size as a consequence of increased x-ray quanta involved in image formation. However, due to phase effects, there were some departures from expected behavior.

How a lesion aligns with the pixel matrix is a purely random phenomenon; however, detectability is strongly in-

fluenced by this pixel phase parameter as seen in Fig. 3. Consequently, the phase parameter can cause decreases in the $\langle \text{LSNR} \rangle$ due to the partial area effect (i.e., a degradation of contrast and hence, signal). Thus the error bars in the graphs of $\langle \text{LSNR} \rangle$ [Fig. 9(a)–(g)] are not entirely a function of x-ray quantum statistics, but include phase variability from partially covered pixels as well. The extent of this variability is strongly dependent on lesion size relative to pixel size. For large lesions covering many pixels, the abundance of pixels entirely covered by the lesion somewhat mitigates this phase effect. Conversely, for lesions covering a few pixels, the partially covered pixels make up a larger fraction of the total number of lesion pixels, hence, there is more LSNR variability, and $\langle A_Z \rangle$ is reduced accordingly. Consider Figs. 6(c) and 9(c) and 9(g). A 5% contrast 250- μm lesion imaged

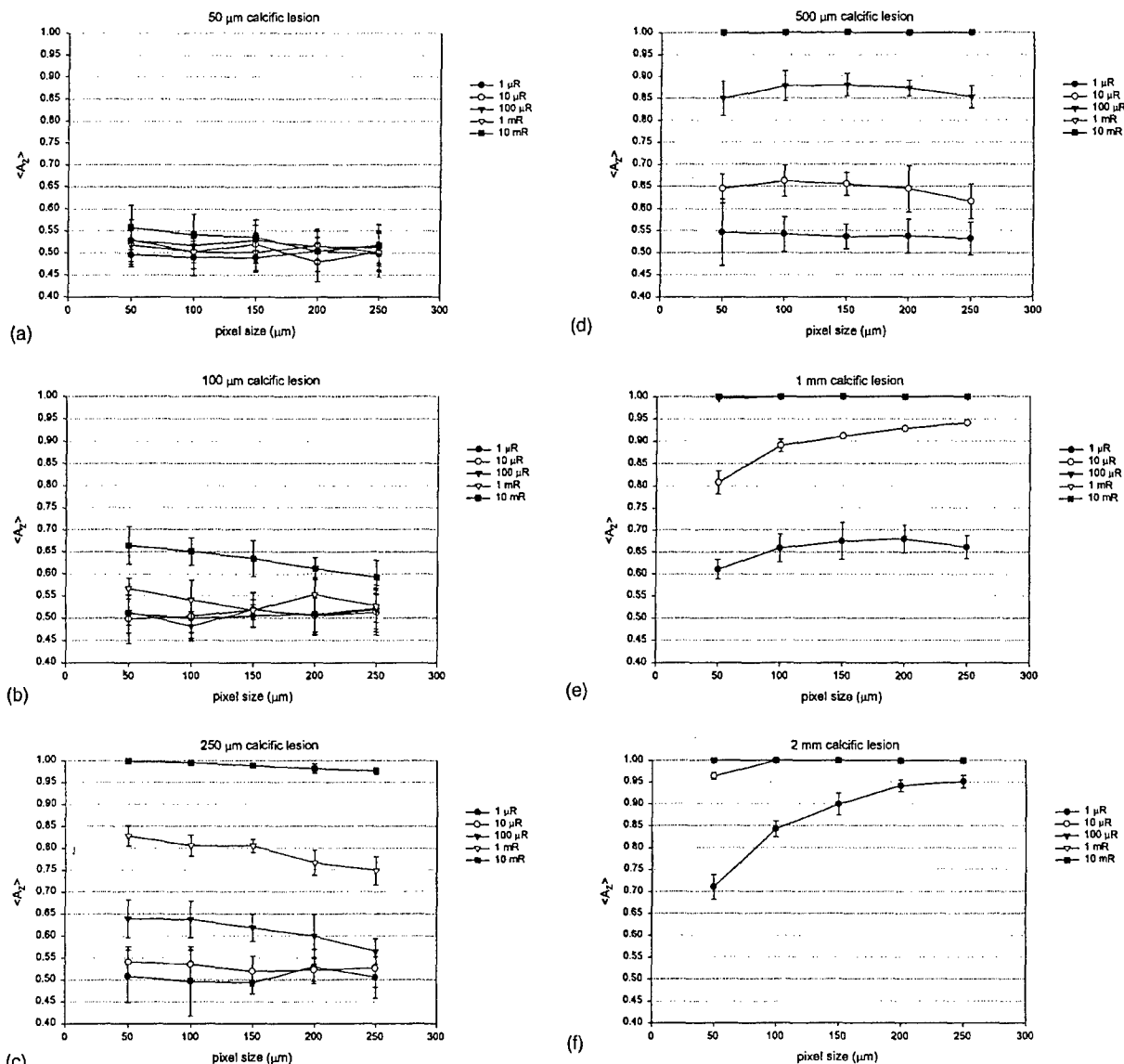


FIG. 8. Calcific lesion detectability, $\langle A_Z \rangle$, for (a) 50-μm cubic lesions, (b) 100-μm cubic lesions, (c) 250-μm cubic lesions, (d) 500-μm cubic lesions, (e) 1-mm cubic lesions, and (f) 2-mm cubic lesions. The error bars represent $\pm\sigma$. Note: In parts (d), (e), and (f), the data are obscured with $\langle A_Z \rangle$ equal to 1.0 at all pixel sizes for the highest exposures.

at 100 μR shows small error bars at 50-μm pixel size and progressively larger ones as pixel size is increased. For the 50-μm pixel size, the 250-μm lesion involves at least 25 pixels, and the majority of those pixels are inner or totally covered pixels. This large number of inner pixels mitigates the effects that the edge pixels have on the LSNR variability. On the other hand, the larger pixel sizes image the lesion with fewer pixels. Thus these edge pixels play larger roles in determining LSNR variability. Hence, the variability increases with pixel size, due to phase effects. Since $\langle A_Z \rangle$ is based on these LSNR realizations, and these LSNR realizations are not very different from the no-lesion case of zero SNR plus or minus some standard deviation, the LSNR variability plays a crucial role in determining $\langle A_Z \rangle$. The increasing LSNR variability at increasing pixel sizes yields decreasing

lesion detectability. In Fig. 9(c), that same 5% contrast 250-μm lesion imaged at 10 mR yields even larger variability as witnessed by the size of the error bars, yet $\langle A_Z \rangle$ remains at 1 when pixel size is increased. In this case, the LSNR variability increases compared to the 100-μR data due to the increased number of quanta used in the 10-mR data. The higher photon fluence magnifies the variability due to phase or edge pixel effects in an absolute sense. However, this higher fluence reduces this variability relative to the mean LSNR, $\langle \text{LSNR} \rangle$, by proportionately elevating $\langle \text{LSNR} \rangle$ more. That is, variability increases with increasing exposure in an absolute sense, but variability decreases in a relative sense to the mean signal. So, variability alone does not determine $\langle A_Z \rangle$; variability relative to the mean LSNR, $\langle \text{LSNR} \rangle$, must be considered. In this case, although the in-

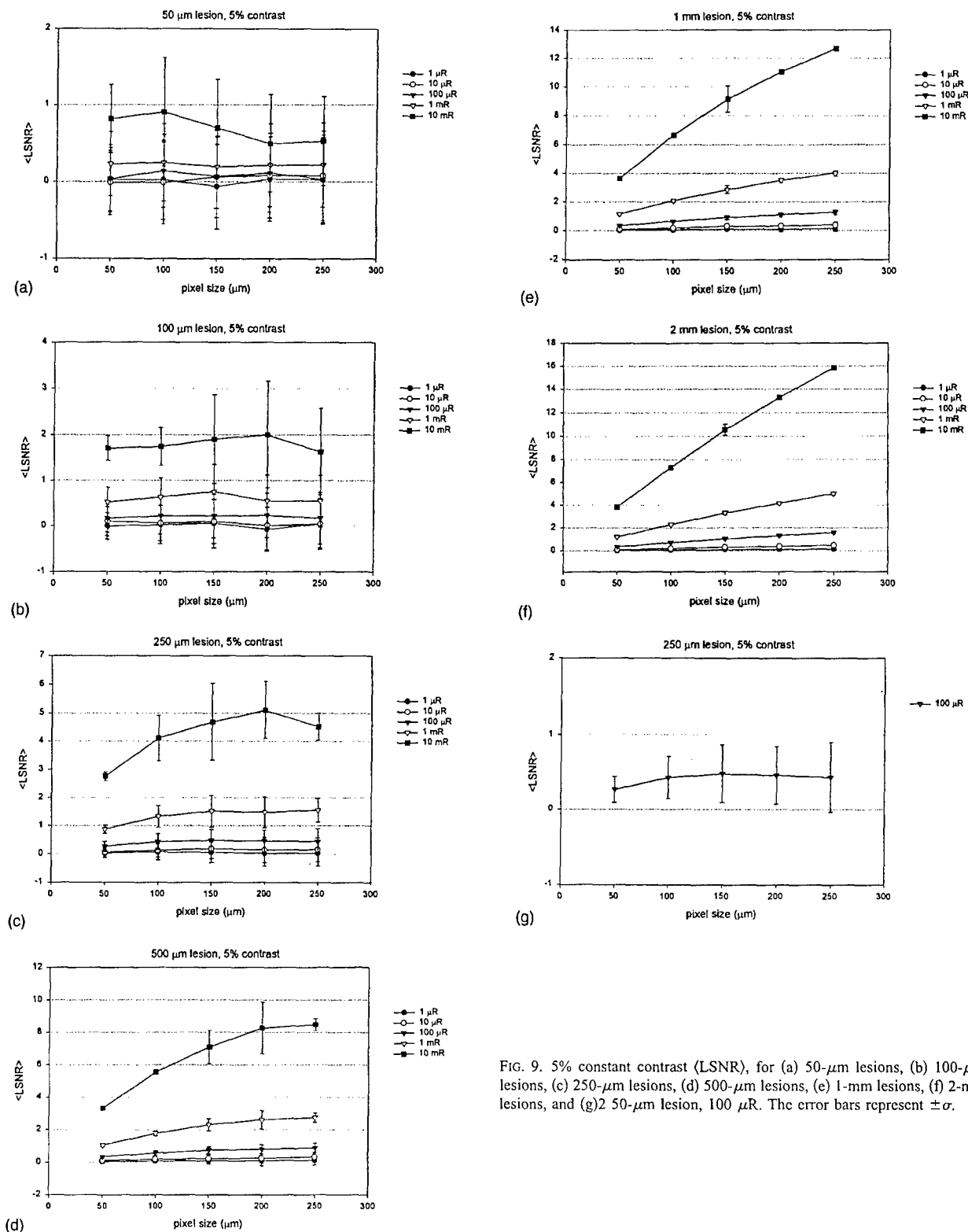


FIG. 9. 5% constant contrast ($\langle \text{LSNR} \rangle$), for (a) 50- μm lesions, (b) 100- μm lesions, (c) 250- μm lesions, (d) 500- μm lesions, (e) 1-mm lesions, (f) 2-mm lesions, and (g) 250- μm lesion, 100 μR . The error bars represent $\pm\sigma$.

creased quanta of the 10-mR image yielded increased LSNR variability, the LSNR estimates are elevated due to the increased quanta, and are far above the no-lesion case of zero SNR plus or minus some standard deviation for every stud-

ied pixel size. Hence, $\langle A_z \rangle$ remains at 1 for each studied pixel size. Consider Figs. 6(f) and 9(f) and the 2-mm lesions. $\langle \text{LSNR} \rangle$ increases as expected with increasing pixel size and has little variability. The very low LSNR variability in this

case is due to the fact that the 2-mm lesion is much larger than the pixel sizes. Hence, there are numerous fully covered pixels to mitigate the variational effects of edge pixels. Since the larger pixels collect more quanta per pixel, lesion detectability increases with increasing pixel size.

In this work, both fixed contrast and cubic lesions were considered. Although, the fixed contrast scenario aids in separating the effects of lesion contrast and areal coverage on lesion detectability, in reality, as lesions increase in area, they generally increase in thickness. Hence, the cubic lesion scenario is physically more appealing. The effects of increasing contrast with increasing lesion areal dimension may be inferred by comparing Figs. 6–8. Lesion detectability is shown to rapidly increase in the case of calcific lesions where contrast rapidly increased (Fig. 8). Although less pronounced, the same behavior was exhibited by the soft tissue lesion detectability (Fig. 7).

The preceding discussion is based on an ideal detector under ideal conditions. As such, this work represents the upper limits in lesion detectability. However, there are some potential modifications that may be made to the methodology for a more clinically representative simulation. Monte Carlo techniques in the study of scatter and dose distribution abound in the literature. While in this simulation study, the quanta incident on a pixel were studied in aggregate, it is not inconceivable to study the quanta, one photon at a time and trace the individual photon histories through scattering in the tissue and deposition of energy in the detector. This would allow study of lesion detectability in the presence of degraded contrast and hence, signal, due to photon scattering. In addition, electronic (additive) noise may be incorporated by way of a separate random number generator that simulates the dark electronic signal distribution.

ACKNOWLEDGMENTS

This work was supported in part by grants from the U.S. Department of Defense Breast Cancer Research Program (DAMD17-94-4424 and DAMD17-98-8176), the California Breast Cancer Research Program (1RB-0912 and 2RB-0071), and the National Cancer Institute (R21-CA82077). The first author is grateful to Dr. Claire Pellot-Barakat, for useful discussions on the topics of image noise and general image science, and Ms. Renee Rees for useful discussions of probabilistic models.

^aThis work was supported by the U.S. Department of Defense Breast Cancer Research Program (DAMD17-94-4424 and DAMD17-98-8176), the

California Breast Cancer Research Program (1RE-0912 and 2RB-0071) and the National Cancer Institute (R21-CA82077).

- ¹H. P. Chan, C. J. Vyborny, H. MacMahon, C. E. Metz, K. Doi, and E. A. Sickles, "Digital mammography. ROC studies of the effects of pixel size and unsharp-mask filtering on the detection of subtle microcalcifications," *Invest. Radiol.* **22**, 581–589 (1987).
- ²H. P. Chan, L. T. Niklason, D. M. Ikeda, K. L. Lam, and D. D. Adler, "Digitization requirements in mammography: Effects on computer-aided detection of microcalcifications," *Med. Phys.* **21**, 1203–1211 (1994).
- ³J. Ikezoe, S. Kido, N. Takeuchi, H. Kondoh, J. Arisawa, and T. Kozuka, "Image quality of digital chest radiography: evaluation of subtle interstitial lung abnormalities (preliminary study)," *Comput. Methods Programs Biomed.* **43**, 107–114 (1994).
- ⁴J. Ikezoe, N. Kohno, S. Kido, N. Takeuchi, T. Johkoh, J. Arisawa, and T. Kozuka, "Interpretation of subtle interstitial chest abnormalities: Conventional radiography versus high-resolution storage-phosphor radiography—A preliminary study," *J. Digit. Imaging* **8**, 31–36 (1995).
- ⁵A. Jonsson, S. Laurin, G. Karner, K. Herrlin, P. Hochbergs, K. Jonsson, O. Rudling, S. Sandstrom, M. Sloth, G. Svahn, and H. Pettersson, "Spatial resolution requirements in digital radiography of scaphoid fractures. An ROC analysis," *Acta Radiol.* **37**, 555–560 (1996).
- ⁶H. MacMahon, C. J. Vyborny, C. E. Metz, K. Doi, V. Sabeti, and S. L. Solomon, "Digital radiography of subtle pulmonary abnormalities: A ROC study of the effect of pixel size on observer performance," *Radiology* **158**, 21–26 (1986).
- ⁷M. D. Murphey, "Digital skeletal radiography: Spatial resolution requirements for detection of subperiosteal resorption," *AJR, Am. J. Roentgenol.* **152**, 541–546 (1989).
- ⁸M. D. Murphey, J. M. Bramble, L. T. Cook, N. L. Martin, and S. J. Dwyer, "Nondisplaced fractures: spatial resolution requirements for detection with digital skeletal imaging," *Radiology* **174**, 865–870 (1990).
- ⁹M. K. Shrout, J. Weaver, B. J. Potter, and C. F. Hildebolt, "Spatial resolution and angular alignment tolerance in radiometric analysis of alveolar bone change," *J. Periodontol.* **67**, 41–45 (1996).
- ¹⁰C. E. Metz, "ROC methodology in radiologic imaging," *Invest. Radiol.* **21**, 720–733 (1986).
- ¹¹M. L. Giger and K. Doi, "Investigation of basic imaging properties in digital radiography. 3. Effect of pixel size on SNR and threshold contrast," *Med. Phys.* **12**, 201–208 (1985).
- ¹²J. C. Dainty and R. Shaw, *Image Science* (Academic, London, 1974).
- ¹³M. J. Yaffe and R. M. Nishikawa, "X-ray imaging concepts: Noise, SNR and DQE," in *Specification, Acceptance Testing and Quality Control of Diagnostic X-ray Imaging Equipment*, edited by J. A. Seibert, G. T. Barnes, and R. G. Gould (American Institute of Physics, Woodbury, NY, 1994), pp. 109–144.
- ¹⁴R. L. Morin, *Monte Carlo Simulation in the Radiological Sciences* (CRC Press, Boca Raton, FL, 1988), pp. 14–52.
- ¹⁵G. E. P. Box and M. E. Muller, "A note on the generation of random normal deviates," *Ann. Math. Stat.* **29**, 610–611 (1958).
- ¹⁶W. H. Press, S. A. Teukolsky, W. T. Vetterling, and B. P. Flannery, *Numerical Recipes in C: The Art of Scientific Computing*, 2nd ed. (Cambridge University Press, New York, 1992).
- ¹⁷J. M. Boone, "Spectral modeling and compilation of quantum fluence in radiography and mammography," *Proc. SPIE* **3336**, 592–601 (1998).
- ¹⁸P. R. Bevington and D. K. Robinson, *Data Reduction and Error Analysis for the Physical Sciences*, 2nd ed. (McGraw-Hill, New York, 1983).
- ¹⁹H. E. Johns and J. R. Cunningham, *The Physics of Radiology*, 4th ed. (Charles C. Thomas, Springfield, IL, 1983).

DAMD17-98-18176, Final Report - August 2001

Computer Simulation of Breast Cancer Screening

PI: John M. Boone, Ph.D.

Appendix G:

JM Boone, "Glandular breast dose for monoenergetic and high-energy x-ray beams: Monte Carlo assessment", Radiology 213, .23-37 (1999)

Medical Physics

John M. Boone, PhD

Index terms:

Breast radiography, radiation dose,
00.47, 0.99

Breast radiography, technology, 00.12
Breast radiography, utilization, 00.99
Physics

Radiology 1999; 213:23-37

Abbreviations:

D_{gN} = normalized glandular dose

HVL = half-value layer

$f(E)$ = fractional energy absorption

Mo-Mo = molybdenum

anode-molybdenum filter

Mo-Rh = molybdenum

anode-rhodium filter

Rh-Rh = rhodium anode-rhodium
filter

W-Ag = tungsten anode-silver filter

W-Pd = tungsten anode-palladium
filter

W-Rh = tungsten anode-rhodium
filter

¹ From the Department of Radiology,
University of California, Davis, Medical
Center, 4701 X St, Radiology Research
Laboratories, Sacramento, CA 95817.
Received August 26, 1998; revision
requested October 23; final revision
received January 14, 1999; accepted
March 26. Supported in part by grants
from the United States Army Breast
Cancer Research Program (DAMD17-
94-J-4424 and DAMD17-98-1-8176),
the California Breast Cancer Research
Program (0192), and the National
Cancer Institute (R21 CA 82077). Ad-
dress reprint requests to the author
(e-mail: jmb Boone@ucdavis.edu).

© RSNA, 1999

See also the editorial by Kimme-Smith
(pp 7-10) in this issue.

Author contribution:

Guarantor of integrity of entire study,
J.M.B.

Glandular Breast Dose for Monoenergetic and High-Energy X-ray Beams: Monte Carlo Assessment¹

PURPOSE: To extend the utility of normalized glandular dose (D_{gN}) calculations to higher x-ray energies (up to 120 keV) and to provide the tools for investigators to calculate D_{gN} values for arbitrary mammographic and x-ray spectra.

MATERIALS AND METHODS: Validated Monte Carlo methods were used to assess D_{gN} values. One million x-ray photons (1-120 keV, in 1-keV increments) were input to a semicircular breast geometry of thicknesses from 2 to 12 cm and breast compositions from 0% to 100% glandular. D_{gN} values for monoenergetic (1-120 keV) x-ray beams, polyenergetic (40-120 kV, tungsten anode) x-ray spectra, and polyenergetic mammographic spectra were computed. Skin thicknesses of 4-5 mm were used.

RESULTS: The calculated D_{gN} values were in agreement within approximately 1%-6% with previously published data, depending on breast composition. D_{gN} tables were constructed for a variety of x-ray tube anode-filter combinations, including molybdenum anode-molybdenum filter, molybdenum anode-rhodium filter, rhodium anode-rhodium filter, tungsten anode-rhodium filter, tungsten anode-palladium filter, and tungsten anode-silver filter. D_{gN} values also were graphed for monoenergetic beams to 120 keV and for general diagnostic x-ray beams to 120 kV.

CONCLUSION: The tables and graphs may be useful for optimizing mammographic procedures. The higher energy data may be useful for investigations of the potential of dual-energy mammography or for calculation of dose in general diagnostic or computed tomographic procedures.

The assessment of radiation dose to the breast during mammography has been of interest to many investigators (1-19). Over the years, the normalized glandular dose (D_{gN}) has come to serve as the benchmark parameter, useful for calculating the glandular dose in clinical mammography. The D_{gN} values are essentially the roentgen-to-rad conversion values, calculated for the "at-risk" glandular component of the breast. Recent efforts to calculate D_{gN} tables for the mammography community have primarily been focused on clinically relevant spectra (4,5,7) with molybdenum anode-molybdenum filter (Mo-Mo), molybdenum anode-rhodium filter (Mo-Rh), or rhodium anode-rhodium filter (Rh-Rh) combinations in the 20-35-kV range.

In this work, D_{gN} tables were computed for much thicker breasts than for those in previous reports, with values reported here for breast thicknesses from 2 to 12 cm in 1-cm increments. While the typical compressed breast thickness in the United States is approximately 4.2 cm, there are many women with a compressed breast thickness that ranges to 12 cm or thicker. The tables provided in this article may be useful for these patients.

The motivation to extend D_{gN} tables to encompass higher energy levels was based on an interest in dual-energy mammography, where the optimal high-energy beam is likely to be very high (>100 keV), well beyond current clinical mammographic x-ray beam energies. In

addition, with the recent introduction of full-field digital mammography systems into the clinical environment, it is likely that slightly higher energy x-ray beams may become useful in some instances. This study was intended to extend the utility of D_{gN} calculations to higher x-ray energies (up to 120 keV) and to provide the tools for investigators to calculate D_{gN} values for arbitrary x-ray spectra, including monoenergetic x-ray beams (for example, produced by synchrotron sources [20], free-electron lasers [21], or other exotic x-ray sources). To this end, tables of D_{gN} values have been provided for the x-ray tube anode-filter combinations of Mo-Mo, Mo-Rh, Rh-Rh, tungsten anode-rhodium filter (W-Rh), tungsten anode-palladium filter (W-Pd), and tungsten anode-silver filter (W-Ag). Graphical data also are provided to demonstrate D_{gN} values for monoenergetic and polyenergetic x-ray beams.

MATERIALS AND METHODS

Details of the Monte Carlo Study

Monte Carlo procedures were used to compute the glandular dose to the breast. Although I have developed independent computer code for Monte Carlo studies (22,23), the TART97 Monte Carlo code was purchased from the Radiation Safety Information Computational Center, Oak Ridge National Laboratory (Oak Ridge, Tenn) for use in this study. The TART97 code was developed primarily at Lawrence Livermore National Laboratory (24) in Livermore, Calif, and is a thoroughly verified and mature Monte Carlo program. A full description of the TART97 Monte Carlo program is available in the literature (24); however, a brief description is appropriate here.

In a Monte Carlo simulation, each of the millions of photons traced in computations undergoes absorption or scattering, depending on the outcome of a random number generator. The probabilities of the multiple scattering calculations are weighted by the probability of that event at each x-ray energy studied. The TART97 Monte Carlo routine uses multiple scattering calculations, follows the history of all photons, and includes the photoelectric, Raleigh, and Compton scatter interaction mechanisms in the energy region reported. All photons were followed until they either left the volume of interest, were completely absorbed, or reached an arbitrarily small energy level (0.10 keV).

Monoenergetic x-ray photons at 1-keV intervals were input into a mathematic phantom in each of the simulation runs. Each photon run made use of 1 million photons at each monoenergetic energy level, and these data were used to construct monoenergetic D_{gN} tables in a procedure described later in this article. The lowest energy simulated was 1 keV, and the highest was 120 keV. For the polyenergetic spectra reported, weighted sums of the monoenergetic D_{gN} data were computed. The x-ray spectra used for this study were generated by using mathematic spectral models described previously (25,26). The x-ray attenuation coefficients for the filters also were reported previously (27).

Geometry and Composition Issues

The geometry simulated in this study is shown in Figure 1. Instead of a D-shaped semicircular breast shape, as others (4,5) have used, a cylindric breast shape was simulated (Fig 1a). The cone-shaped radiation field emitted from the source was collimated to irradiate half of the breast (a semicircle). The semicircular field geometry was particularly simple to simulate with the TART97 code and was efficient to run. The semicircle of breast tissue that was not in the radiation field was intended to simulate the presence of the torso of the patient (the chest wall). For their geometries, Wu et al (4) and Dance (5) assumed a D-shaped breast (no chest wall). The presence of tissue outside of the radiation field may have a minor influence in terms of backscatter, and this is of particular concern in this study due to the much higher x-ray energies studied here. While the nonirradiated semicircle is not the exact geometry of the chest wall, it was thought that the presence of some tissue behind the breast was slightly more representative of the geometry encountered in mammography, rather than no tissue outside of the radiation field.

Various breast compositions were studied, from 0% glandular-100% adipose to 100% glandular-0% adipose, by mass. D_{gN} values were computed for the proportion of glandular tissue mass to total breast tissue mass. For concise reference henceforward, the breast composition is referred to in terms of the glandular percentage alone. The compositional data from Hammerstein et al (28) were used. X-ray coefficients for compound (multi-elemental) substances such as breast tissue were prorated on the basis of the weight fraction of the element; however,

in substances where the density changed with the composition, the calculation of proportions is a little more complicated, and the techniques described in the following paragraphs were used.

For a tissue containing a weight fraction f_g of glandular tissue (and, correspondingly, a weight fraction of $1 - f_g$ for adipose tissue), it can be shown that the glandular volume fraction v_g is given by

$$v_g = \left[\frac{(1 - f_g) \rho_g}{f_g \rho_a} + 1 \right]^{-1}, \quad (1)$$

where ρ_g is the density of 100% glandular tissue ($\rho_g = 1.04$ g/cm³, from Hammerstein et al [28]) and ρ_a is the density of 100% adipose tissue ($\rho_a = 0.93$ g/cm³). Let the total volume be set to unit volume (1 cm³) for simplicity, such that $v_g + v_a = 1$ cm³, and the compound density is

$$\rho_{\text{compound}} = \rho_g v_g + \rho_a v_a. \quad (2)$$

The mass m of each component in the unit volume is simply $m_g = \rho_g v_g$ and $m_a = \rho_a v_a$, where the "g" subscripts refer to glandular tissue and the "a" subscripts refer to adipose tissue. For completeness, the elemental compositions and densities for a variety of glandular fractions are given in the Appendix. By using the above procedure, the linear attenuation coefficients for 0%, 50%, and 100% glandular tissues were compared with those reported by Hammerstein et al (28). These data are shown in Figure 2.

The breast tissue (glandular and adipose compound) is enclosed in a layer of skin, as illustrated in Figure 1. The skin thickness was varied in this study. For comparison with the results of Dance (5), a skin thickness of 5 mm was used. For comparison with the results of Wu et al (4), a skin thickness of 4 mm was used. For a single geometry and breast composition, the influence of skin thickness from 2 to 6 mm was studied. The density and elemental composition of skin, taken from Hammerstein et al (28), are reported in the Appendix.

Conversion of Monte Carlo Results to D_{gN} Values

For a given breast composition, photon energy, and geometry, the output produced by the TART97 Monte Carlo package that was of interest in this study was the energy deposited (normalized per input photon) in the breast tissue compartment (Fig 1). The average energy to the breast tissue compartment, per incident x-ray photon to the breast, was normalized by means of the energy of the incident photons (all Monte

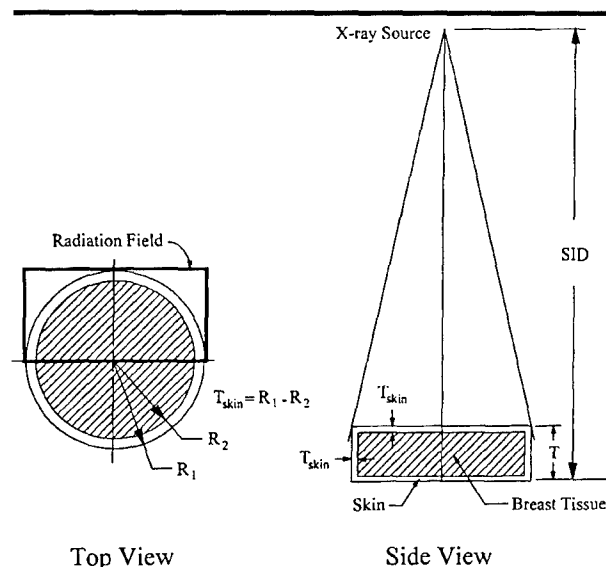


Figure 1. Diagram shows the geometry used for the Monte Carlo simulations. R_1 = radius of breast (including skin layer) in millimeters, R_2 = radius of breast (excluding skin layer) in millimeters, SID = source-to-image distance, T = breast thickness, T_{skin} = skin thickness in millimeters.

Carlo runs used monoenergetic spectra), such that the fractional energy absorption, $f(E)$, was calculated as follows:

$$f(E) = \frac{\text{energy absorbed per incident photon}}{\text{photon energy}} \quad (3)$$

The value of E is expressed in kiloelectron volts, and the x-ray photon spectra $\Phi(E)$ is normalized to the number of photons corresponding to 1 R (0.258 mC/kg) (for the entire spectrum). This type of normalization is typical (26) for investigators working with x-ray spectra. D_{gN} values were calculated by using

$$D_{gN} = \sum_{E=E_{min}}^{E_{max}} f(E) \times E(1.6021 \times 10^{-8}) \Phi(E) G \frac{\text{area}}{\text{mass}}, \quad (4)$$

where the value of $f(E)$ was defined in Equation (3), the constant corrects for various unit conversions, G is defined later in Equation (6), area is the surface area at the top of the breast (in the entrance plane) exposed to x-rays, and mass is that of the purely glandular portion of the breast tissue. Let f_g be the glandular fraction, by weight, of the breast tissue. For example, $f_g = 1.0$ for a 100% glandular breast, and $f_g = 0.5$ for a 50%

glandular breast. For a semicircular breast tissue compartment of radius R_2 (Fig 1), a breast density ρ , a compressed breast thickness T , and a skin layer thickness T_{skin} , the mass term in Equation 4 is given by

$$\text{mass} = f_g \frac{1}{2} \pi R_2^2 (T - 2T_{skin}) \rho. \quad (5)$$

The G term in Equation (4) corrects the normalized dose calculation specifically to the glandular component of the breast tissue (D_{gN}) in a heterogeneous tissue matrix. Values for breasts with a 0% glandular fraction are computed by extrapolation from D_{gN} calculations of glandular fractions in the 2%–5% range:

$$G = \frac{f_g \left(\frac{\mu_{en}}{\rho} \right)_g}{\left[f_g \left(\frac{\mu_{en}}{\rho} \right)_g + (1 - f_g) \left(\frac{\mu_{en}}{\rho} \right)_a \right]}, \quad (6)$$

where the mass energy absorption coefficients (μ_{en}/ρ) are specified with an "a" subscript for adipose tissue and with a "g" subscript for glandular tissue. D_{gN} and G were derived from first principles and by consulting previous publications (4,5). Units for D_{gN} (Eq [4]) were derived as follows: D_{gN} is expressed in millirad per roentgen, $f(E)$ has no unit, E is expressed in kiloelectron

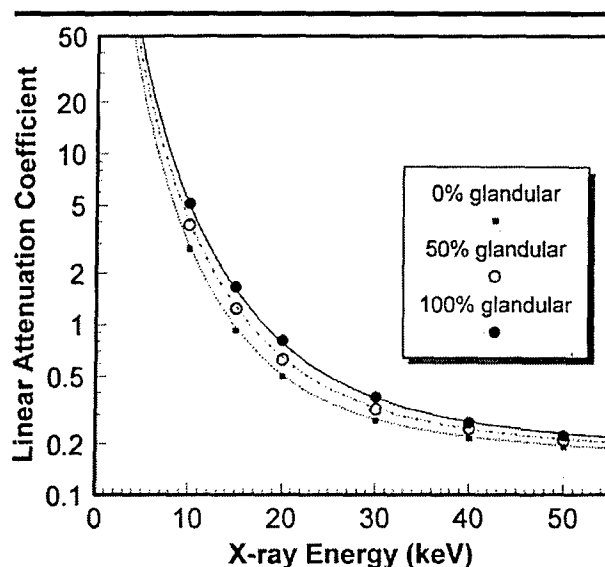


Figure 2. Graph shows comparison of the linear attenuation coefficients computed in the present study with those reported by Hammerstein et al (28) for 0%, 50%, and 100% glandular tissue. The data from Hammerstein et al are shown as the symbols, and the coefficients used in the present study are shown as lines. Excellent agreement in terms of attenuation coefficients was observed over the energy range compared.

volts per photon, $\Phi(E)$ is expressed as photons per square millimeter per roentgen, G has no unit, area is in square millimeters, and mass is in grams. The constant 1.6021×10^{-8} was derived as follows:

$$\begin{aligned} & (1.6021 \times 10^{-8}) \frac{(\text{mrad g})}{(\text{keV})} \\ &= (1.6021 \times 10^{-9}) \frac{\text{ergs}}{\text{keV}} \\ &\times \frac{1000 \text{ mrad}}{\text{Rad}} \times \frac{\text{g rad}}{100 \text{ ergs}}. \quad (7) \end{aligned}$$

RESULTS

Monte Carlo Results for $f(E)$ Values

The Monte Carlo results for 0% and 100% glandular breasts are illustrated in Figure 3. If the breast tissue were not encapsulated in a layer of skin, these curves would be pseudoexponential, $f(E)$ being unity at very low energy levels and decreasing almost exponentially with increasing energy level. However, x-ray photons of the lowest energy are unable to penetrate the relatively thin skin layer to contribute a fraction of their energy to the breast tissues; rather, the energy is deposited in the skin layer. The value of $f(E)$ is, therefore, substantially dampened

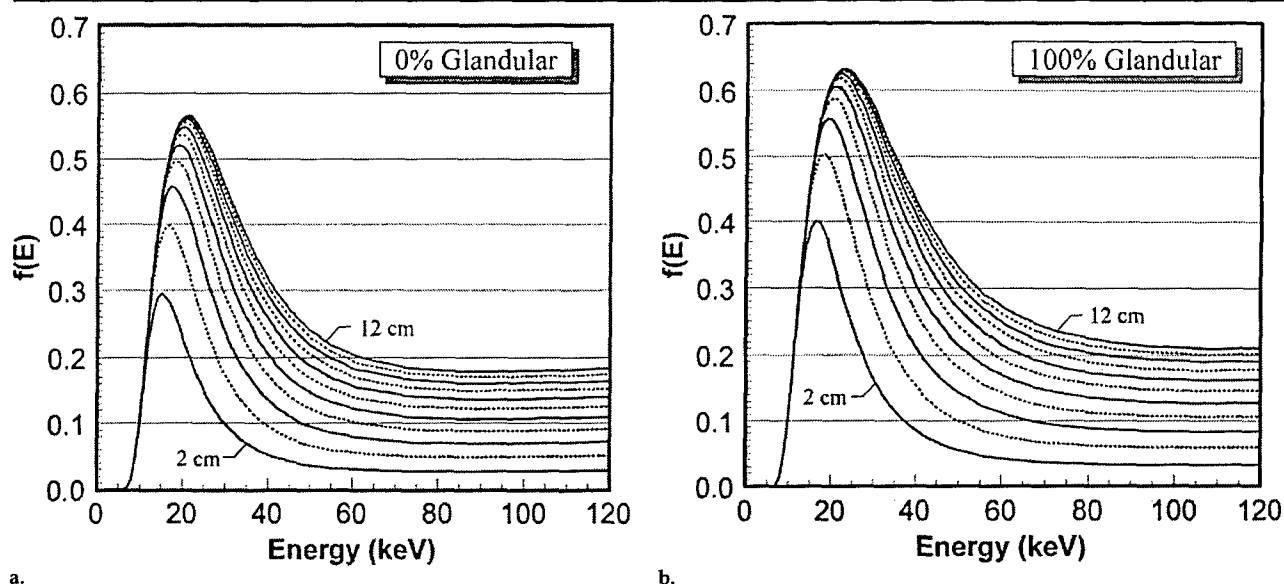


Figure 3. Graphs show $f(E)$ as a function of incident x-ray energy for (a) 0% glandular tissue and (b) 100% glandular tissue. The curves are shown for 11 tissue thicknesses ranging from 2 to 12 cm in 1-cm increments. The bottom curve represents the data for the 2-cm-thick breast; intermediate curves are not marked for clarity, but are in order from 3 to 11 cm. Dotted lines = curves for odd-numbered tissue thicknesses (3, 5, 7, 9, and 11 cm), solid lines = curves for even-numbered thicknesses (2, 4, 6, 8, 10, and 12 cm).

at the low energy levels because of the effect of skin filtration. As the glandular fraction increases, the $f(E)$ value of the incident x-rays increases slightly, as would be expected due to the changing composition and increasing density.

It is suspected that subject contrast will be near the maximum when imaging at the kiloelectron voltage corresponding to the peak $f(E)$ value for each breast thickness and composition. If one plots the data illustrated in Figure 3 differently, one can see the nonlinear effects of breast thickness on $f(E)$ (Fig 4). In Figure 4, the absorption of 10-keV photons was constant across breast thicknesses, which suggested that the absorption dynamics of these low-energy photons occurred in the first 2 cm of tissue. At higher incident photon energy levels, the $f(E)$ value increased with increasing breast thickness, as would be expected.

Figure 5 demonstrates yet a different perspective on these data: The $f(E)$ value is shown as a function of glandular fraction for different incident photon energy levels in a 4-cm-thick breast. Monte Carlo runs were performed with several intermediate glandular fractions (0%, 20%, 40%, 50%, 60%, 80%, and 100%) for the data shown in Figure 5. The curves shown in Figure 4— $f(E)$ versus breast thickness—are nonlinear, whereas the curves in Figure 5— $f(E)$ versus glandular fraction—are linear. This observation suggests that lin-

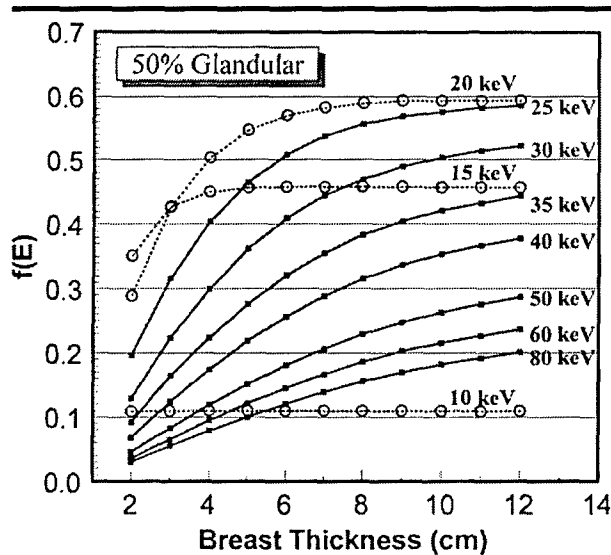


Figure 4. Graph shows data for a 50% glandular breast, with $f(E)$ as a function of breast thickness. The $f(E)$ value is almost constant as a function of breast thicknesses. The fact that the 10-keV photon absorption fraction is nonzero implies that 10-keV photons penetrate the skin layer, but the constant behavior as a function of breast thicknesses implies that the absorption kinetics take place principally in the first 2 cm of the breast. Higher energy photons show increased penetration of the skin layer ($f(E)$ values are higher for the 2-cm breast thickness) and also demonstrate that increased tissue absorption occurs with thicker breasts, as would be expected. Different symbols (■ and ○) and solid and dotted lines do not represent differences in data but were used for ease of reading.

ear interpolation between glandular fraction data, for the $f(E)$ values, was reasonable and preferable in comparison with

interpolation between breast thicknesses. As a result, only 0% glandular (100% adipose) and 100% glandular results need

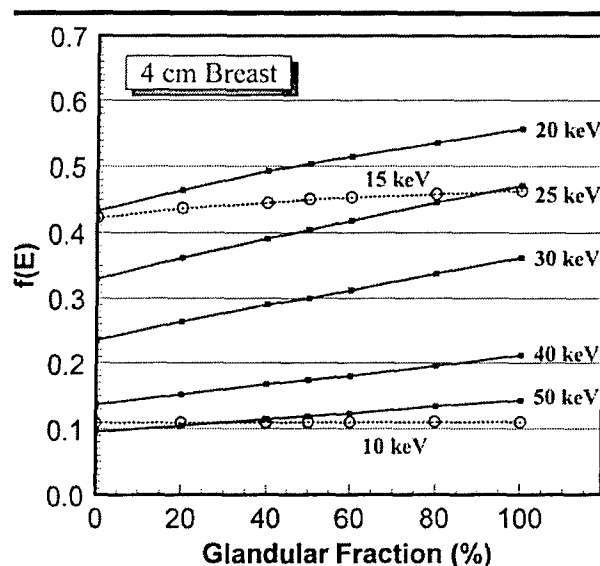


Figure 5. Graph shows $f(E)$ as a function of glandular fraction for various x-ray energies and a 4-cm breast thickness. The $f(E)$ curve is a nearly linear function of glandular fraction, as evidenced by the linearity of the curves. Different symbols (\blacksquare and \circ) and solid and dotted lines do not represent differences in data but were used for ease of reading.

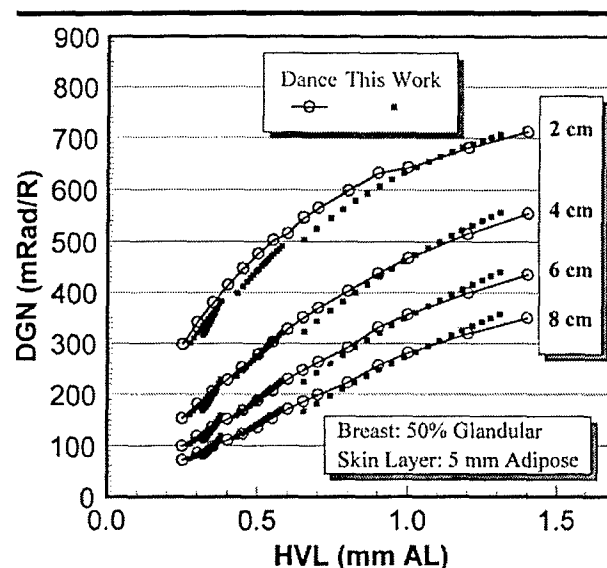


Figure 6. Graph shows D_{gN} values computed by Dance (5) (\circ) in comparison with those computed in the present study (\blacksquare) for breast thicknesses of 2, 4, 6, and 8 cm. Dance reported D_{gN} values as a function of the HVL of the x-ray beam, and that approach was adopted here as well. A good qualitative comparison is shown.

to be reported because other proportions can easily be calculated.

Comparison with D_{gN} Values in the Literature

The D_{gN} values computed in the present study were compared with the results of Dance (5), as illustrated in Figure 6. Dance presented conversion factors in different units (mean glandular dose per incident air kerma, $\text{mGy} \cdot \text{mGy}^{-1}$), which were recomputed to the units of millirad per roentgen for this comparison. The skin thickness was set to 5 mm, and a 50% glandular breast was modeled, consistent with Dance's method. Four breast thicknesses, 2, 4, 6, and 8 cm, were studied for this comparison. When the different Monte Carlo routines, and particularly the different x-ray spectra, used to produce these data are considered, the qualitative agreement seen in Figure 6 between Dance's data and the data from this study is good. The 4-cm-thickness data were subjected to quantitative comparison. Because the half-value layers (HVLs) corresponding to both data sets differed on a point-by-point basis, direct comparisons between the data sets were not possible. Therefore, both data sets were computer fit by using commercially available software (TABLECURVE 3.0; Jandel Scientific, Corta Madera, Calif), with excellent precision (4-cm-thickness data from Dance: $r^2 = 0.9999$; 4-cm-thickness

data from present study: $r^2 = 0.9975$), and comparison was then made between the computer-fit D_{gN} values (between data sets) over the HVL range of 0.25-mm aluminum to 1.3-mm aluminum. The 4-cm-thickness data from the present study were found to differ from those of Dance, on average, by -1.12% (SD, 2.66). In terms of absolute D_{gN} values, the difference was -3.34 mrad/R (SD, 10.6).

The data of Wu et al (4) are the most commonly used D_{gN} values in the United States. The D_{gN} values reported in the present study were calculated at exactly the same HVLs as those of Wu et al; thus, a direct comparison was possible. These comparative data are shown in Figure 7. D_{gN} values calculated at three breast thicknesses (4, 6, and 8 cm) and at seven kilovoltages (23–35 kV in increments of 2 kV) are shown for each breast composition. The D_{gN} values observed in this study were consistent with, but slightly lower than, those of Wu et al for a 0% glandular breast but were seen to be in excellent agreement with the values of Wu et al for 50% and 100% glandular breast compositions. The slight qualitative differences (5%–7%) in the data for a 0% glandular breast may be a consequence of different extrapolation techniques for a 0% glandular breast. The spectra computed for this study were hardened by adding an acrylic plastic sheet, such that the HVLs exactly matched those reported by Wu et al. While the kilovoltages and HVLs were identical, the D_{gN}

values calculated in the present study did make use of a different spectral model (25) than that (29) used by Wu et al, and this may explain the slight differences between the D_{gN} values derived in the present study and those derived in the study by Wu et al.

For the 0% glandular data, the mean differences (and SDs) averaged over the seven spectra (23, 25, 27, 29, 31, 33, and 35 kV) were -5.5% (SD, 1.3), -6.3% (SD, 1.7), and -6.8% (SD, 1.5) for the 4-, 6-, and 8-cm breast thicknesses, respectively. For the 50% glandular breast, the mean differences were -1.5% (SD, 1.4), -1.9% (SD, 1.5), and -2.3% (SD, 1.6) for the 4-, 6-, and 8-cm breast thicknesses, respectively. For the 100% glandular breast, the mean differences were 0.6% (SD, 1.5), 1.0% (SD, 1.4), and 1.1% (SD, 1.7) for the 4-, 6-, and 8-cm breast thicknesses, respectively.

Influence of Skin Thickness

The calculation of glandular dose for a patient has many uncertainties associated with it, and estimation of cancer risk on the basis of the glandular dose has even more uncertainties. The uncertainties in calculating glandular dose include uncertainties not only in the tabulated D_{gN} values but also practical uncertainties in assessing the thickness of the breast, the breast composition, the precise milliampere-second value used, the differences between the actual mammographic

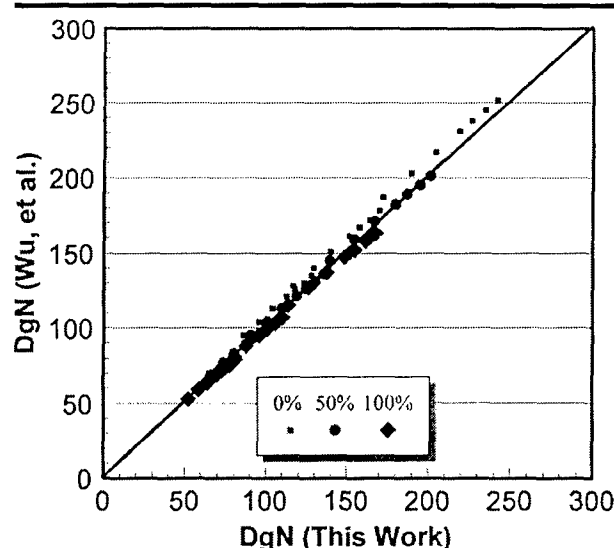


Figure 7. Graph shows D_{gN} values reported by Wu et al (4) along the y axis in comparison with D_{gN} values from the present study (along the x axis). Individual points represent the data obtained with an energy range of 23–35 kV (in 2-kV increments). The D_{gN} values reported here, averaged over all energy levels and breast thicknesses, differed from those of Wu et al by -6.2% for the 0% glandular breast, -1.9% for the 50% glandular breast, and $+0.9\%$ for the 100% glandular breast.

geometry and that used in Monte Carlo simulations, and so on.

Figure 3 illustrates that the highest $f(E)$ of incident x-ray photons occurred in the energy region from about 15 to 25 keV, where the $f(E)$ curves peaked. Not coincidentally, this is the energy region where the vast majority of the x-ray photons in conventional x-ray spectra (eg, Mo-Mo combination at 26 kVp) exist. The fact that there was high absorption in the breast in this energy region also suggests that photons in this energy range are useful for the production of high-contrast images. As mentioned earlier, the left edges of the peaks of the $f(E)$ curves seen in Figure 3 are a consequence of the absorption of incident x-rays by the skin layer. The steep slope of the left edges of the $f(E)$ peaks suggests that a small difference in the assumption of skin thickness may have a large influence on the overall accuracy of the dose calculation.

To examine this in the case of the typical breast, Monte Carlo simulations were performed by using different skin thicknesses. Figure 8 illustrates the calculated D_{gN} values for a 50% glandular, 4-cm-thick breast. Averaged over the different x-ray spectra (23–35 kV), the change in D_{gN} values (relative to a 4-mm skin thickness) that resulted from different skin thicknesses was 15.2% (SD, 2.1) for a 2-mm-thick skin layer, 7.1% (SD, 0.9) for a 3-mm-thick skin layer, -6.4% (SD,

0.7) for a 5-mm-thick skin layer, and -11.8% (SD, 1.3) for a 6-mm-thick skin layer.

The observation that skin thickness has a large influence on the D_{gN} value is not surprising given the shape of the absorption curves (Fig 3). The purpose of presenting these data is to demonstrate that, among the uncertainties involved in dose calculations, it is likely that the slight differences ($<6\%$) in tabulated D_{gN} values produced by different investigators are small, as compared with the large errors that can occur in making the wrong assumptions or generalizations about an individual patient's breast characteristics.

Monocenergetic Beams

Figure 9 illustrates the monoenergetic D_{gN} values expressed in millirad per 10^6 photons per energy interval. Although the general shapes of these curves are similar to those of the $f(E)$ curves in Figure 3, the influence of tissue thickness is inverted. D_{gN} values for the same x-ray energy and breast composition increased with decreasing breast thickness, because there is less self shielding in the thinner breast.

Although the D_{gN} values are high for thinner breasts, the entrance exposure during a mammogram is markedly lower in thin breasts; therefore, thin breasts typically receive substantially lower glandular doses than do thicker breasts. An alternate label

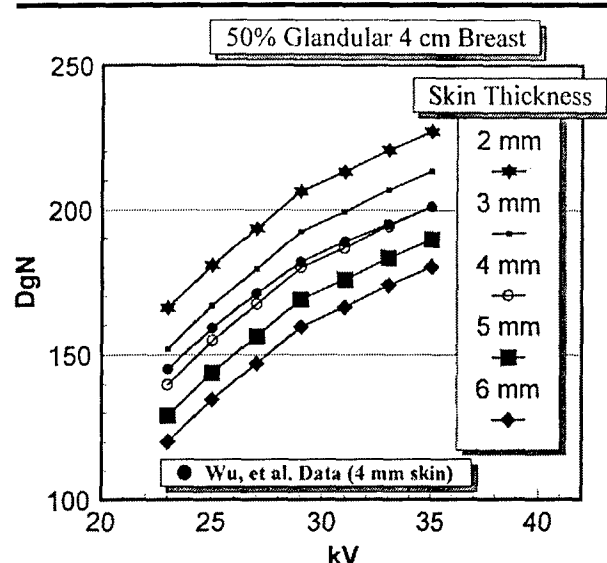


Figure 8. Graph illustrates the influence of skin thickness on the D_{gN} value. In comparison with the 4-mm skin thickness data from the study by Wu et al (4) (\bullet), the D_{gN} values increased, on average, by 7% for a 3-mm skin thickness and by 15% for a 2-mm skin thickness. The D_{gN} values decreased by 6% for a 5-mm skin thickness and by 12% for a 6-mm skin thickness. These simulations used a Mo-Mo spectrum.

for the y axis in Figure 9 would be $D_{gN} \times 10^{-6}$ per photon, or $D_{gN}(E)$. Therefore, by multiplying the data in Figure 9 by 10^{-6} and then integrating the product of an incident x-ray spectrum ($\Phi(E)$) and the appropriate curve in Figure 9 ($D_{gN}(E)$), the D_{gN} value for an arbitrary spectrum can be calculated as shown below:

$$D_{gN} = \sum_{E=E_{min}}^{E_{max}} D_{gN}(E) \times 10^{-6} \times \Phi(E), \quad (8)$$

where it is understood that the total number of photons in $\Phi(E)$ in Equation (8) is normalized to 1 R (0.258 mC/kg). The curves shown in Figure 9 coupled with the formula given in Equation (8) are most useful when one is dealing with an arbitrary x-ray spectrum, which is typically computed in units of photons per square millimeter per energy interval.

Photons at different energy levels contribute differently to exposure in air, owing to the energy dependence of the mass energy attenuation coefficient of air. As a consequence, D_{gN} values expressed in the traditional units of millirad per roentgen (vs x-ray energy) (Fig 10) have a different shape than those of the D_{gN} per photon curves in Figure 9. Figure 10 illustrates the millirad per roentgen D_{gN} values for 0% (Fig 10a) and 100% (Fig 10b) glandular tissue. Figure 10 is directly useful if one is interested in the D_{gN} value for a monoenergetic beam.

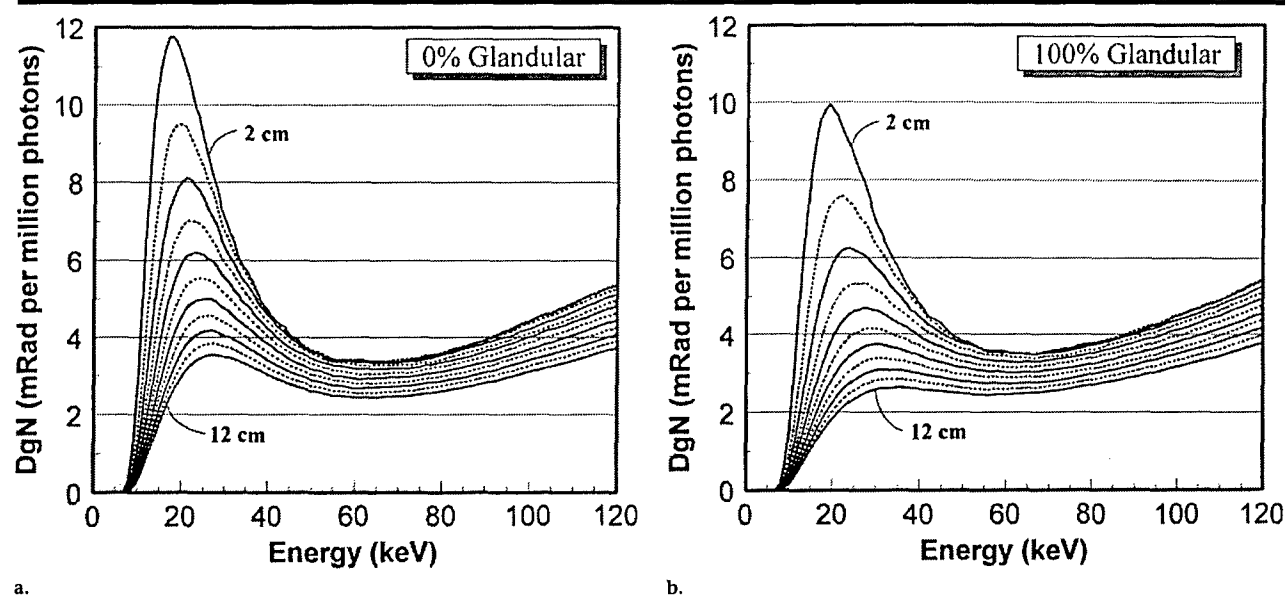


Figure 9. Graphs show D_{gN} values normalized per entrant photon instead of per roentgen (as is more typical) for (a) 0% glandular breasts and (b) 100% glandular breasts. Curves are shown for breast thicknesses ranging from 2 to 12 cm in 1-cm increments. The D_{gN} values shown here are higher for thin breasts and lower for thicker breasts, which is the reverse of the trend seen for $f(E)$ in Figure 3. This graph illustrates that, on a per photon basis, photons in the energy region between approximately 12 and 30 keV contribute the most to the D_{gN} value. This is the energy region where most conventional mammographic x-ray spectra are centered.

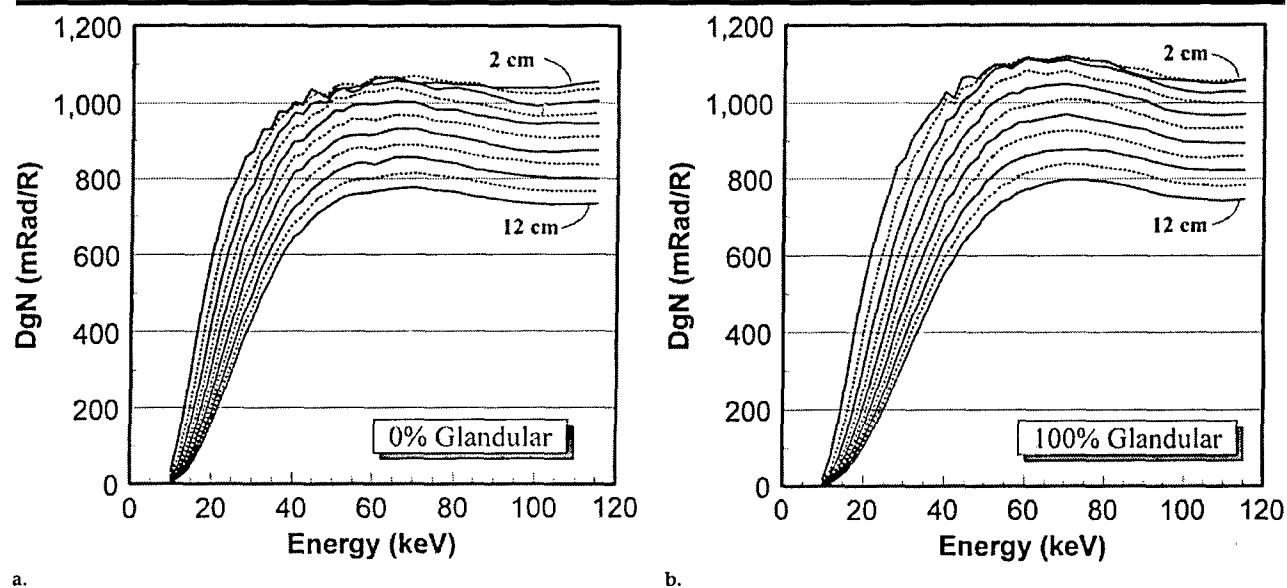


Figure 10. Graphs show D_{gN} values for monoenergetic x-ray energies for (a) 0% glandular breasts and (b) 100% glandular breasts. Breast thickness ranged from 2 to 12 cm in 2-cm increments. The D_{gN} values shown in these graphs are plotted in the conventional unit of millirad per roentgen, as opposed to millirad per photon as in Figure 9. The curves in this graph can be read directly when assessing D_{gN} for monoenergetic beams.

energetic beam of 1-R (0.258-mC/kg) incident exposure to the breast.

Mammographic Spectra

Tables 1–12 show the D_{gN} values for several conventional and unconventional

mammographic spectra. Tables 1, 3, 5, 7, 9, and 11 give D_{gN} values for the 0% glandular breast; Tables 2, 4, 6, 8, 10, and 12 give these values for the 100% glandular breast. For other glandular fractions, D_{gN} values may be linearly interpolated from the 0% and 100% glandular tables.

The data in Tables 1–12 were computed from simulations in which a 4-mm skin thickness was used. X-ray spectra were computed by using previously reported techniques (25). Tables 1–6 present D_{gN} values for conventional mammographic spectra, including Mo-Mo, Mo-Rh, and

TABLE 1
 D_{gN} Values for Mo-Mo (30- μ m-thick) Anode-Filter Combination and a 0% Glandular Breast

Energy (kV)	HVL	Breast Thickness (cm)										
		2	3	4	5	6	7	8	9	10	11	12
20	0.220	225	161	122	97	80	68	59	52	46	42	38
21	0.238	249	182	140	112	93	79	68	60	54	48	44
22	0.254	269	199	154	125	103	88	76	67	60	54	49
23	0.269	286	213	166	135	112	96	83	73	65	59	54
24	0.283	300	226	177	144	120	102	89	79	70	63	58
25	0.295	313	237	187	152	127	109	94	83	74	67	61
26	0.307	325	247	195	160	134	114	99	88	78	71	65
27	0.318	335	256	203	167	140	119	104	92	82	74	68
28	0.328	344	265	211	173	145	124	108	96	86	77	70
29	0.338	353	273	218	179	151	129	112	99	89	80	73
30	0.347	361	280	224	185	155	133	116	103	92	83	76
31	0.356	369	287	230	190	160	137	120	106	95	86	78
32	0.364	375	293	235	195	164	141	124	109	98	89	81
33	0.372	382	299	241	200	169	145	127	113	101	91	83
34	0.379	388	304	245	204	173	149	130	115	104	94	86
35	0.386	393	309	250	208	176	152	133	118	106	96	88
36	0.392	398	314	254	212	180	155	136	121	109	98	90
37	0.398	403	318	258	216	183	158	139	124	111	101	92
38	0.403	407	322	262	219	186	161	142	126	113	103	94
39	0.409	411	326	266	222	189	164	144	128	115	105	96
40	0.413	415	330	269	225	192	166	146	130	117	106	97

Note.— D_{gN} values are expressed in millirad per roentgen. To convert to SI units ($mGy \cdot mGy^{-1}$), multiply by 873^{-1} .

TABLE 2
 D_{gN} Values for Mo-Mo (30- μ m-thick) Anode-Filter Combination and a 100% Glandular Breast

Energy (kV)	HVL	Breast Thickness (cm)										
		2	3	4	5	6	7	8	9	10	11	12
20	0.220	169	108	78	60	49	41	35	31	28	25	23
21	0.238	191	125	90	70	57	48	41	36	32	29	26
22	0.254	209	138	101	78	64	54	46	41	36	33	30
23	0.269	224	150	110	85	70	59	50	44	39	36	32
24	0.283	237	160	117	92	75	63	54	48	42	38	35
25	0.295	249	169	125	97	79	67	58	51	45	41	37
26	0.307	259	177	131	103	84	71	61	54	48	43	39
27	0.318	269	184	137	107	88	74	64	56	50	45	41
28	0.328	278	191	142	112	92	77	67	59	52	47	43
29	0.338	286	198	148	116	95	80	70	61	54	49	45
30	0.347	293	204	153	121	99	84	72	63	57	51	46
31	0.356	300	210	157	124	102	86	75	66	59	53	48
32	0.364	307	215	162	128	105	89	77	68	61	55	50
33	0.372	313	220	166	132	109	92	80	70	63	57	51
34	0.379	318	225	170	135	112	95	82	72	65	58	53
35	0.386	324	229	174	139	115	97	84	74	66	60	55
36	0.392	328	233	178	142	117	100	87	76	68	62	56
37	0.398	333	237	181	145	120	102	89	78	70	63	58
38	0.403	337	241	184	148	122	104	91	80	72	65	59
39	0.409	341	244	187	150	125	106	93	82	73	66	60
40	0.413	344	248	190	153	127	108	94	84	75	68	62

Note.— D_{gN} values are expressed in millirad per roentgen. To convert to SI units ($mGy \cdot mGy^{-1}$), multiply by 873^{-1} .

Rh-Rh combinations. Tables 7-12 present D_{gN} values for unconventional mammographic spectra that are being considered as substitutes for use in women with thicker breasts and for digital mammography systems; these include W-Rh, W-Pd, and W-Ag combinations. Because of the strong L-characteristic x-ray emission of the tungsten anode around 12 keV, a

50- μ m thickness of filter material is needed to effectively eliminate these x-rays from the entrance beam.

Tables 1-12 allow interpolation across energy level (by using the HVL), thickness, and glandular fraction of the breast composition. For example, consider the case of a 4.2-cm-thick breast composed of 30% glandular and 70% adipose tissue

imaged at 26 kV with a Mo-Rh x-ray spectrum and an HVL of 0.37 mm aluminum: From Table 3 (0% glandular, Mo-Rh), the D_{gN} value at 4.2 cm and an HVL of 0.37 is interpolated from the four data points corresponding to 4- and 5-cm-thick breasts at HVLs of 0.363 mm aluminum (at 26 kV) and 0.375 mm aluminum (at 27 kV). In this case, $D_{gN} = [236(0.8) +$

TABLE 3
 D_{gN} Values for Mo-Rh (25- μ m-thick) Anode-Filter Combination and a 0% Glandular Breast

Energy (kV)	HVL	Breast Thickness (cm)										
		2	3	4	5	6	7	8	9	10	11	12
20	0.241	247	178	136	109	90	76	66	58	51	46	42
21	0.265	276	204	158	128	106	90	78	69	62	55	51
22	0.288	303	228	179	146	121	103	90	79	71	64	58
23	0.310	326	249	197	162	135	116	101	89	80	72	65
24	0.331	346	267	213	175	147	126	110	97	87	79	72
25	0.348	362	281	225	186	157	135	118	104	93	84	77
26	0.363	374	293	236	195	165	141	124	109	98	89	81
27	0.375	385	302	244	202	171	147	129	114	102	92	84
28	0.387	394	310	251	209	177	152	133	118	105	95	87
29	0.397	402	317	257	214	181	156	137	121	109	98	90
30	0.406	409	324	263	219	186	160	140	124	112	101	92
31	0.415	415	329	268	224	190	164	143	127	114	103	94
32	0.422	420	335	273	228	194	167	146	130	117	106	96
33	0.429	425	339	277	232	197	170	149	133	119	108	98
34	0.436	430	344	281	235	200	173	152	135	121	110	100
35	0.442	434	348	285	239	203	176	154	137	123	112	102
36	0.447	438	351	288	242	206	178	157	139	125	114	104
37	0.453	442	355	291	245	209	181	159	142	127	115	105
38	0.457	445	358	294	247	211	183	161	143	129	117	107
39	0.462	448	361	297	250	214	185	163	145	131	119	108
40	0.466	451	364	299	252	216	187	165	147	132	120	110

Note.— D_{gN} values are expressed in millirad per roentgen. To convert to SI units ($mGy \cdot mGy^{-1}$), multiply by 873^{-1} .

TABLE 4
 D_{gN} Values for Mo-Rh (25- μ m-thick) Anode-Filter Combination and a 100% Glandular Breast

Energy (kV)	HVL	Breast Thickness (cm)										
		2	3	4	5	6	7	8	9	10	11	12
20	0.241	187	121	87	67	54	46	39	35	31	28	25
21	0.265	215	142	103	80	65	55	47	42	37	33	30
22	0.288	239	161	119	93	76	64	55	48	43	39	35
23	0.310	261	178	133	104	85	72	62	54	48	44	40
24	0.331	279	193	145	114	93	79	68	60	53	48	44
25	0.348	294	205	154	122	100	84	73	64	57	51	47
26	0.363	306	215	162	128	105	89	77	68	60	54	49
27	0.375	315	223	168	133	110	93	80	70	63	57	52
28	0.387	324	230	174	138	114	96	83	73	65	59	53
29	0.397	331	236	179	142	117	99	86	75	67	61	55
30	0.406	338	241	183	146	120	102	88	78	69	62	57
31	0.415	344	246	187	149	123	104	90	79	71	64	58
32	0.422	349	250	191	152	126	107	92	81	73	66	60
33	0.429	354	255	195	155	128	109	95	83	74	67	61
34	0.436	358	258	198	158	131	111	96	85	76	69	62
35	0.442	362	262	201	161	133	113	98	87	77	70	64
36	0.447	366	265	204	164	136	115	100	88	79	71	65
37	0.453	370	269	207	166	138	117	102	90	81	73	66
38	0.457	373	271	209	168	140	119	104	92	82	74	67
39	0.462	376	274	212	170	142	121	105	93	83	75	69
40	0.466	379	277	214	173	144	123	107	94	85	76	70

Note.— D_{gN} values are expressed in millirad per roentgen. To convert to SI units ($mGy \cdot mGy^{-1}$), multiply by 873^{-1} .

$195(0.2)] \times (0.417) + [244(0.8) + 202(0.2)] \times (0.583) = 232.35$ mrad/R. The values in parentheses are the interpolation weights, and the values in square brackets are the thickness-interpolation values. The corresponding calculation was used to compute the D_{gN} value for a 100% glandular breast by using the same interpolation coefficients and the D_{gN} val-

ues in Table 4, which yielded $D_{gN} = [162(0.8) + 128(0.2)] \times (0.417) + [168(0.8) + 133(0.2)] \times (0.583) = 158.43$ mrad/R. By interpolating these two values to the 30% glandular fraction of the example, the result is $D_{gN-30} = D_{gN-0}(0.7) + D_{gN-100}(0.3) = 232.35(0.7) + 158.43(0.3) = 210$ mrad/R, where D_{gN-30} , D_{gN-0} , and D_{gN-100} are the D_{gN} values for 30%,

0%, and 100% glandular breasts, respectively.

High-Energy Polyenergetic Beams

Figure 11 illustrates the D_{gN} values for polyenergetic x-ray beams in the general diagnostic energy region. Figure 11a shows results for the 0% glandular breast,

TABLE 5
 D_{gN} Values for Rh-Rh (25- μ m-thick) Anode-Filter Combination and a 0% Glandular Breast

Energy (kV)	HVL	Breast Thickness (cm)										
		2	3	4	5	6	7	8	9	10	11	12
20	0.245	252	182	140	112	93	79	68	60	53	48	44
21	0.265	278	206	160	130	108	92	80	70	63	57	52
22	0.278	293	219	171	139	116	99	86	76	68	61	56
23	0.294	311	236	187	153	128	110	95	84	75	68	62
24	0.312	330	254	203	167	141	121	105	93	83	75	69
25	0.329	348	270	218	180	152	131	114	101	91	82	75
26	0.345	363	285	231	192	163	140	123	109	97	88	80
27	0.361	377	299	243	203	172	149	130	116	104	94	86
28	0.376	390	311	254	213	181	157	137	122	110	99	91
29	0.391	402	322	264	222	189	164	144	128	115	104	95
30	0.405	412	332	274	231	197	171	150	134	120	109	99
31	0.418	422	342	283	239	204	177	156	139	125	113	103
32	0.431	431	351	291	246	211	183	161	144	129	117	107
33	0.443	440	359	299	253	217	189	167	148	133	121	111
34	0.454	447	367	306	259	223	194	171	153	137	125	114
35	0.465	455	374	312	265	229	199	176	157	141	128	117
36	0.476	461	380	318	271	234	204	180	161	145	131	120
37	0.486	467	386	324	276	238	208	184	164	148	135	123
38	0.495	473	392	329	281	243	212	188	168	151	138	126
39	0.504	479	397	335	286	247	216	192	171	154	140	129
40	0.513	484	402	339	290	251	220	195	174	157	143	131

Note.— D_{gN} values are expressed in millirad per roentgen. To convert to SI units ($mGy \cdot mGy^{-1}$), multiply by 873^{-1} .

TABLE 6
 D_{gN} Values for Rh-Rh (25- μ m-thick) Anode-Filter Combination and a 100% Glandular Breast

Energy (kV)	HVL	Breast Thickness (cm)										
		2	3	4	5	6	7	8	9	10	11	12
20	0.245	192	124	90	70	56	47	41	36	32	29	26
21	0.265	216	144	105	82	67	56	48	42	38	34	31
22	0.278	230	154	114	89	72	61	53	46	41	37	34
23	0.294	248	169	126	99	81	68	59	52	46	41	38
24	0.312	266	184	138	109	89	76	65	57	51	46	42
25	0.329	282	198	150	119	98	83	71	63	56	50	46
26	0.345	297	211	160	127	105	89	77	68	60	54	50
27	0.361	311	223	170	136	112	95	82	72	65	58	53
28	0.376	323	233	179	143	118	100	87	77	68	62	56
29	0.391	334	243	187	150	124	106	92	81	72	65	59
30	0.405	345	252	195	157	130	111	96	84	75	68	62
31	0.418	354	261	202	163	135	115	100	88	79	71	65
32	0.431	363	269	209	169	140	120	104	91	82	74	67
33	0.443	372	276	216	174	145	124	107	95	85	76	70
34	0.454	379	283	222	179	150	128	111	98	87	79	72
35	0.465	387	289	227	184	154	131	114	101	90	81	74
36	0.476	393	295	232	189	158	135	117	104	93	84	76
37	0.486	399	301	237	193	162	138	120	106	95	86	78
38	0.495	405	306	242	197	165	141	123	109	97	88	80
39	0.504	411	311	246	201	169	145	126	111	100	90	82
40	0.513	416	316	251	205	172	147	129	114	102	92	84

Note.— D_{gN} values are expressed in millirad per roentgen. To convert to SI units ($mGy \cdot mGy^{-1}$), multiply by 873^{-1} .

and Figure 11b shows results for the 100% glandular breast. The x-ray spectra used for these calculations were generated by using a spectral model developed by the author (26). General radiographic (tungsten anode) x-ray spectra were computed from 40 to 120 kV, with the assumption of a 5% kilovoltage ripple (approximating an inverter generator), and with 2.5 mm

of added aluminum filtration. The HVL ranged from 1.6 mm aluminum at 40 kV to 5.0 mm aluminum at 120 kV, with an approximately linear relationship ($r^2 = 0.998$) between HVL and kilovolt level, where $kV = 23.318 \times HVL - 0.237$. This relationship can be used to convert HVL values to the kilovolt values in Figure 11.

The D_{gN} values for these high-energy x-ray beams may be useful for calculating glandular breast dose in some general diagnostic radiographic studies (lateral views) or in computed tomographic studies, if certain assumptions are made. One of the higher energy beams may be useful as the high-energy component of a dual-energy mammography system.

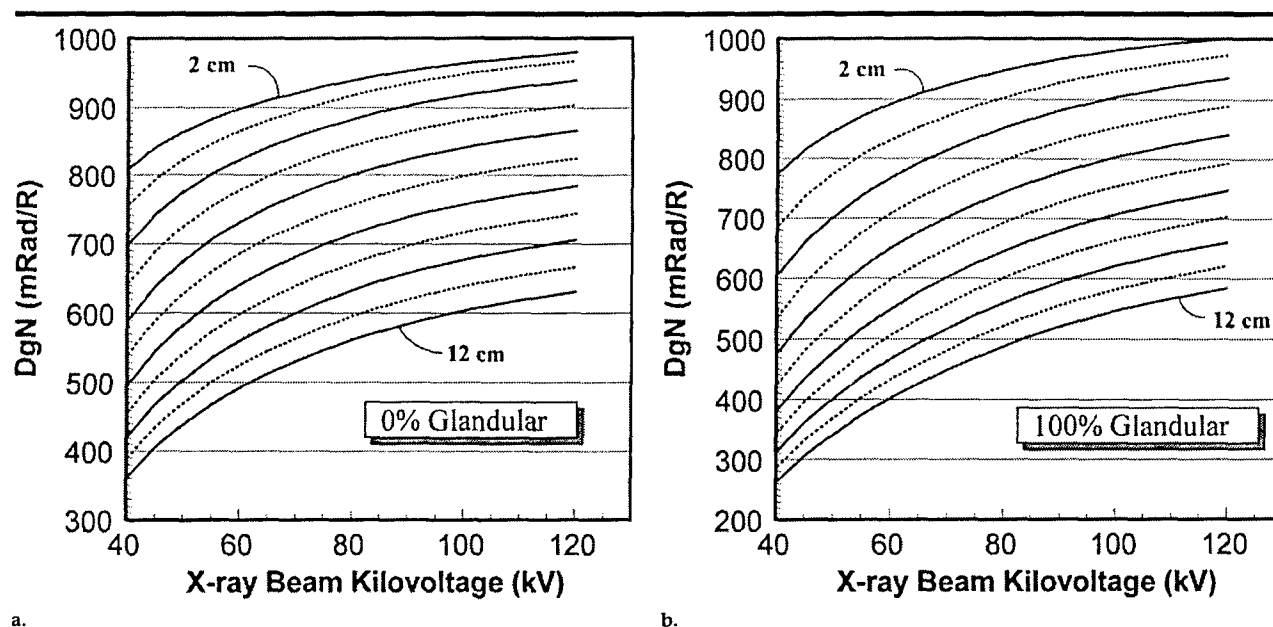


Figure 11. Graphs show D_{gN} values for conventional polyenergetic x-ray beams in which a tungsten anode and 2.5 mm of added aluminum filtration are used. D_{gN} values are shown for (a) 0% glandular breasts and (b) 100% glandular breasts.

TABLE 7
 D_{gN} Values for W-Rh (50- μ m-thick) Anode-Filter Combination and a 0% Glandular Breast

Energy (kV)	HVL	Breast Thickness (cm)										
		2	3	4	5	6	7	8	9	10	11	12
20	0.338	342	258	202	164	136	116	101	89	79	71	65
21	0.365	368	282	224	183	153	131	114	100	90	81	74
22	0.392	392	306	245	202	170	146	127	112	101	91	83
23	0.420	415	328	266	221	187	161	140	124	111	101	92
24	0.444	434	347	284	237	201	174	152	135	121	109	100
25	0.462	447	360	296	248	211	183	160	142	128	116	106
26	0.477	457	370	305	257	219	190	167	148	133	120	110
27	0.489	465	378	313	264	226	195	172	153	137	124	113
28	0.500	472	385	320	270	231	200	176	157	141	128	116
29	0.509	478	391	326	275	236	205	180	160	144	131	119
30	0.518	484	397	331	280	241	209	184	164	147	134	122
31	0.527	489	403	336	285	245	213	188	168	151	137	125
32	0.535	494	408	342	290	250	218	192	171	154	140	128
33	0.544	499	413	347	295	254	222	196	175	158	143	131
34	0.552	504	418	352	300	259	226	200	179	161	146	134
35	0.560	509	424	357	306	264	231	205	183	165	150	137
36	0.569	514	429	363	311	269	236	209	187	169	154	141
37	0.577	519	434	368	316	275	241	214	192	173	158	144
38	0.585	524	440	373	321	280	246	218	196	177	161	148
39	0.593	528	444	379	327	285	251	223	200	181	165	152
40	0.601	532	449	383	331	289	255	227	204	185	169	155

Note.— D_{gN} values are expressed in millirad per roentgen. To convert to SI units ($\text{mGy} \cdot \text{mGy}^{-1}$), multiply by 873^{-1} .

DISCUSSION

In this study, Monte Carlo techniques were used to calculate D_{gN} values. As validation of the procedures used here, D_{gN} values for conventional mammographic spectra were compared with the results of the seminal work of Dance (5)

and Wu et al (4). The comparison with Dance's results showed agreement within about 1%, and comparisons with the data of Wu et al showed agreement within a range of about 1%–6%, depending upon breast glandularity. The influence of skin thickness was evaluated (Fig 8), and it was seen that a difference of 1

mm in skin thickness (eg, 3-mm instead of 4-mm skin thickness) had an influence of approximately 7% on the D_{gN} values and that a difference of 2 mm (eg, 2-mm instead of 4-mm skin thickness) had an influence of 15%. As a consequence, the difference between the D_{gN} values of Wu et al and those in the present study is

TABLE 8
 D_{gN} Values for W-Rh (50- μ m-thick) Anode-Filter Combination and a 100% Glandular Breast

Energy (kV)	HVL	Breast Thickness (cm)										
		2	3	4	5	6	7	8	9	10	11	12
20	0.338	271	182	133	104	84	71	61	54	48	43	39
21	0.365	296	203	150	118	96	81	70	61	55	49	45
22	0.392	320	223	167	132	108	91	79	69	61	55	50
23	0.420	342	243	184	146	120	101	88	77	69	62	56
24	0.444	361	260	199	158	131	111	96	84	75	68	62
25	0.462	374	272	209	167	138	117	101	89	80	72	65
26	0.477	384	281	217	174	144	122	106	93	83	75	68
27	0.489	392	289	223	179	149	126	109	96	86	77	70
28	0.500	399	295	229	184	153	130	112	99	88	80	73
29	0.509	405	301	234	188	156	133	115	102	91	82	75
30	0.518	411	306	239	193	160	136	118	104	93	84	76
31	0.527	417	311	244	197	164	140	121	107	95	86	78
32	0.535	422	317	248	201	168	143	124	110	98	88	80
33	0.544	427	322	253	206	172	147	127	112	100	91	83
34	0.552	433	327	258	210	176	150	131	115	103	93	85
35	0.560	438	333	263	215	180	154	134	119	106	96	88
36	0.569	443	338	269	220	185	158	138	122	109	99	90
37	0.577	449	344	274	225	190	163	142	126	113	102	93
38	0.585	454	350	280	230	194	167	146	130	117	105	96
39	0.593	459	355	285	235	199	172	151	134	120	109	99
40	0.601	464	360	290	240	204	176	155	137	124	112	102

Note.— D_{gN} values are expressed in millirad per roentgen. To convert to SI units ($mGy \cdot mGy^{-1}$), multiply by 873^{-1} .

TABLE 9
 D_{gN} Values for W-Pd (50- μ m-thick) Anode-Filter Combination and a 0% Glandular Breast

Energy (kV)	HVL	Breast Thickness (cm)										
		2	3	4	5	6	7	8	9	10	11	12
20	0.341	345	260	204	166	138	117	102	90	80	72	66
21	0.369	371	285	226	185	155	132	115	102	91	82	75
22	0.396	396	309	247	204	172	147	128	114	102	92	84
23	0.424	418	331	268	223	189	162	142	126	113	102	93
24	0.452	439	352	288	241	205	177	155	138	124	112	102
25	0.478	458	371	306	258	220	191	167	149	134	121	110
26	0.497	471	384	319	270	231	200	176	157	141	128	117
27	0.514	482	395	329	279	239	208	183	163	147	133	121
28	0.527	490	403	337	286	246	214	189	168	151	137	125
29	0.539	497	410	344	293	252	219	193	173	155	141	129
30	0.550	503	417	350	298	257	224	198	177	159	144	132
31	0.560	509	423	356	304	262	229	202	181	163	148	135
32	0.570	514	428	362	309	267	233	206	184	166	151	138
33	0.579	520	434	367	314	272	238	211	188	170	154	141
34	0.588	525	439	372	319	277	242	215	192	173	158	144
35	0.597	530	444	378	325	282	247	219	196	177	161	148
36	0.606	534	449	383	330	287	252	223	200	181	165	151
37	0.615	539	455	388	335	292	257	228	205	185	169	155
38	0.624	543	460	393	340	297	261	233	209	189	172	158
39	0.632	548	464	398	345	301	266	237	213	193	176	161
40	0.640	552	469	403	350	306	270	241	217	197	179	165

Note.— D_{gN} values are expressed in millirad per roentgen. To convert to SI units ($mGy \cdot mGy^{-1}$), multiply by 873^{-1} .

smaller than typical differences in skin thickness.

Once the results of the present study had been verified against existing results for conventional x-ray spectra, the methods were used to extend D_{gN} Monte Carlo calculations to 120 keV. A series of tables for possible mammographic spectral candidates has been provided to allow direct

calculations of breast dose. Monoenergetic results also were computed and are presented in Figure 10. These data may be useful for computing the D_{gN} values for arbitrary x-ray spectra, including those that may be useful for dual-energy mammography in the high-energy region.

Mammography as a modality continues to mature, and, at present, there are

several digital mammography systems nearing the marketplace. Digital images allow the ability to retrospectively manipulate the displayed contrast. While it is impossible to recover subject contrast that is not recorded by the detector, it is thought that the ability to enhance displayed contrast retrospectively will be useful in improving image contrast in the

TABLE 10
 D_{gN} Values for W-Pd (50- μ m-thick) Anode-Filter Combination and a 100% Glandular Breast

Energy (kV)	HVL	Breast Thickness (cm)										
		2	3	4	5	6	7	8	9	10	11	12
20	0.341	274	184	135	105	85	72	62	54	48	44	40
21	0.369	299	205	152	119	97	82	70	62	55	50	45
22	0.396	323	225	169	133	109	92	79	70	62	56	51
23	0.424	345	245	186	147	121	102	89	78	69	63	57
24	0.452	366	265	203	162	133	113	98	86	77	69	63
25	0.478	385	282	218	175	145	123	106	94	84	75	69
26	0.497	398	294	229	184	153	130	113	99	89	80	73
27	0.514	409	304	237	191	159	135	117	104	92	83	76
28	0.527	417	312	244	197	164	140	121	107	96	86	79
29	0.539	424	319	250	203	169	144	125	110	98	89	81
30	0.550	431	325	256	208	173	148	128	113	101	91	83
31	0.560	437	331	261	212	177	151	132	116	104	94	85
32	0.570	442	336	266	217	181	155	135	119	106	96	87
33	0.579	448	342	271	221	185	159	138	122	109	98	90
34	0.588	453	347	276	226	189	162	141	125	112	101	92
35	0.597	459	353	281	231	194	166	145	128	115	104	95
36	0.606	464	358	286	235	198	170	149	132	118	107	97
37	0.615	469	364	292	241	203	175	153	135	121	110	100
38	0.624	474	369	297	245	208	179	157	139	125	113	103
39	0.632	479	374	302	250	212	183	161	143	128	116	106
40	0.640	483	379	307	255	217	187	164	146	131	119	109

Note.— D_{gN} values are expressed in millirad per roentgen. To convert to SI units ($mGy \cdot mGy^{-1}$), multiply by 873^{-1} .

TABLE 11
 D_{gN} Values for W-Ag (50- μ m-thick) Anode-Filter Combination and a 0% Glandular Breast

Energy (kV)	HVL	Breast Thickness (cm)										
		2	3	4	5	6	7	8	9	10	11	12
20	0.330	336	253	197	160	133	113	98	87	77	70	64
21	0.357	362	277	219	179	150	128	111	98	88	79	72
22	0.383	386	300	240	198	166	143	124	110	98	89	81
23	0.410	408	322	261	216	183	157	137	122	109	99	90
24	0.436	429	343	280	234	199	172	150	133	120	108	99
25	0.463	449	363	299	252	215	186	164	145	131	118	108
26	0.489	467	381	317	268	229	199	176	156	141	127	116
27	0.509	480	394	330	280	240	209	185	165	148	134	123
28	0.526	491	405	340	289	249	217	192	171	154	140	128
29	0.541	499	414	349	298	257	224	198	177	159	145	132
30	0.554	507	422	356	305	263	230	204	182	164	149	136
31	0.566	514	429	363	311	269	236	209	187	168	153	140
32	0.578	520	435	369	317	275	241	213	191	172	157	143
33	0.588	526	441	375	323	280	246	218	195	176	160	147
34	0.599	531	447	381	328	285	251	223	200	180	164	150
35	0.609	536	453	387	334	291	256	227	204	184	168	154
36	0.619	541	458	392	339	296	261	232	208	188	171	157
37	0.629	546	464	398	345	301	266	236	213	192	175	161
38	0.638	551	468	403	350	306	270	241	217	196	179	164
39	0.647	555	473	408	355	311	275	245	221	200	183	168
40	0.655	559	477	412	359	315	279	249	225	204	186	171

Note.— D_{gN} values are expressed in millirad per roentgen. To convert to SI units ($mGy \cdot mGy^{-1}$), multiply by 873^{-1} .

clinical setting. If this assumption proves to be true after experience, it is likely that some compromises in subject contrast may be appropriate under some circumstances. For example, in women with larger breasts, where dose levels are much higher, a shift to harder x-ray spectra may be effective, and this is one reason why tungsten anodes with higher-atomic-

number filtration are under investigation (and why the relevant D_{gN} values are reported here). At least one design under commercial investigation involves a scanning slot beam of x rays; such a design places high heat-loading demands on the x-ray tube. Tungsten is a remarkable anode material because of its high melting point, and this is another reason why

tungsten may become more common in some digital mammography systems. To be fully evaluated, new spectra with unconventional anode and filter materials will be studied for their influence on both image quality and patient dose. The D_{gN} values reported here may be useful toward that end.

It is likely that alternate spectra will

TABLE 12
 D_{gN} Values for W-Ag (50- μ m-thick) Anode-Filter Combination and a 100% Glandular Breast

Energy (kV)	HVL	Breast Thickness (cm)										
		2	3	4	5	6	7	8	9	10	11	12
20	0.330	266	178	130	101	82	69	60	52	47	42	38
21	0.357	291	198	147	115	94	79	68	60	53	48	44
22	0.383	314	218	163	129	105	89	77	67	60	54	49
23	0.410	336	238	180	143	117	99	86	75	67	61	55
24	0.436	357	257	196	157	129	109	95	83	74	67	61
25	0.463	377	276	213	171	141	120	104	92	82	74	67
26	0.489	395	292	228	184	153	130	113	99	89	80	73
27	0.509	408	305	239	193	161	137	119	105	94	85	77
28	0.526	419	315	248	201	168	143	125	110	98	89	81
29	0.541	428	324	255	208	174	148	129	114	102	92	84
30	0.554	436	331	262	214	179	153	133	117	105	95	86
31	0.566	443	338	268	219	184	157	137	121	108	98	89
32	0.578	449	344	274	224	188	161	141	124	111	100	91
33	0.588	455	350	280	230	193	166	144	128	114	103	94
34	0.599	461	356	285	235	197	170	148	131	117	106	96
35	0.609	467	362	291	240	202	174	152	134	120	109	99
36	0.619	472	368	296	245	207	178	156	138	123	112	102
37	0.629	478	373	302	250	211	182	160	141	127	115	105
38	0.638	483	379	307	255	216	187	163	145	130	118	108
39	0.647	488	384	312	259	220	191	167	149	133	121	110
40	0.655	492	388	316	264	225	195	171	152	137	124	113

Note.— D_{gN} values are expressed in millirad per roentgen. To convert to SI units ($mGy \cdot mGy^{-1}$), multiply by 873^{-1} .

continue to be studied to determine whether further optimization of the mammographic examination can be achieved, given various new technologic developments. Furthermore, there is a small group of women who have a compressed breast thickness exceeding 8 cm; in these cases, D_{gN} tables were not available, and, for such cases, x-ray spectra have not been optimized.

This study was intended to provide clinical medical physicists, as well as researchers, with the tools needed to calculate glandular breast dose for any arbitrary x-ray spectra in a simple but accurate manner. Efforts to computer fit these curves with adequate precision proved to be unsuccessful; therefore, the raw data in Figures 9 and 10 and in Tables 1–12 will be made available to all interested parties via e-mail request.

APPENDIX

The elemental compositions and densities of breasts with different glandular proportions and of skin are given in Table A1.

Acknowledgment: Dermott Cullen, PhD, of the Lawrence Livermore National Laboratory (Livermore, Calif) was most helpful in discussions concerning the use of the TART97 code, and his contribution to this study is gratefully acknowledged.

References

1. Kulkarni RN, Supe SJ. Radiation dose to the breast during mammography: a com-

TABLE A1
Weight Fractions of Elements and Total Tissue Density as a Function of Glandular Weight Fraction

Glandular Weight Fraction (%)	Total Tissue Density	Hydrogen	Carbon	Nitrogen	Oxygen	Phosphorus
0	0.9301	0.112	0.619	0.017	0.251	0.001
10	0.9399	0.111	0.576	0.019	0.294	0.001
20	0.9501	0.110	0.532	0.020	0.336	0.002
30	0.9605	0.109	0.488	0.022	0.379	0.002
40	0.9711	0.108	0.445	0.023	0.421	0.003
50	0.9819	0.107	0.401	0.025	0.464	0.003
60	0.9930	0.106	0.358	0.026	0.507	0.003
70	1.0044	0.105	0.315	0.028	0.549	0.004
80	1.0160	0.104	0.271	0.029	0.592	0.004
90	1.0278	0.103	0.227	0.030	0.634	0.005
100	1.0400	0.102	0.184	0.032	0.677	0.005
Skin	1.0900	0.098	0.178	0.050	0.667	0.007

Source.—Reference 28.

- prehensive, realistic Monte Carlo calculation. *Phys Med Biol* 1984; 29:1257–1264.
2. Doi K, Chan HP. Evaluation of absorbed dose in mammography: Monte Carlo simulation studies. *Radiology* 1980; 135:199–208.
3. Dance DR. The Monte Carlo calculation of integral radiation dose in xeromammography. *Phys Med Biol* 1980; 25:25–37.
4. Wu X, Barnes GT, Tucker DM. Spectral dependence of glandular tissue dose in screen-film mammography. *Radiology* 1991; 179:143–148.
5. Dance DR. Monte Carlo calculation of conversion factors for the estimation of mean glandular breast dose. *Phys Med Biol* 1990; 35:1211–1219.
6. Gingold EL, Wu X, Barnes GT. Contrast and dose with Mo-Mo, Mo-Rh, and Rh-Rh target-filter combinations in mammography. *Radiology* 1995; 195:639–644.
7. Wu X, Gingold EL, Barnes GT, Tucker DM. Normalized average glandular dose in molybdenum target-rhodium filter and rhodium target-rhodium filter mammography. *Radiology* 1994; 193:83–89.
8. Dance DR, Persliden J, Carlsson GA. Calculation of dose and contrast for two mammographic grids. *Phys Med Biol* 1992; 37:235–248.
9. Ng KH, Aus RJ, DeWerd LA, Vetter JR. Entrance skin exposure and mean glandular dose: effect of scatter and field gradient at mammography. *Radiology* 1997; 205:395–398.
10. Arfelli F, Bonvicini V, Bravin A, et al. A linear array silicon pixel detector: images

- of a mammographic test object and evaluation of delivered doses. *Phys Med Biol* 1997; 42:1565-1573.
11. Thilander-Klang AC, Ackerholm PH, Berlin IC, et al. Influence of anode-filter combinations on image quality and radiation dose in 965 women undergoing mammography. *Radiology* 1997; 203:348-354.
 12. Calicchia A, Gambaccini M, Indovina PL, Mazzei F, Pugliani L. Niobium/molybdenum K-edge filtration in mammography: contrast and dose evaluation. *Phys Med Biol* 1996; 41:1717-1726.
 13. Thiele DL, Craig AR. Mean glandular dose and the standard breast. *Australas Phys Eng Sci Med* 1996; 19:94-96.
 14. Gentry JR, DeWerd LA. TLD measurements of in vivo mammographic exposures and the calculated mean glandular dose across the United States. *Med Phys* 1996; 23:899-903.
 15. Monticciolo DL, Sprawls P, Kruse BD, Peterson JE. Optimization of radiation dose and image quality in mammography: a clinical evaluation of rhodium versus molybdenum. *South Med J* 1996; 89:391-394.
 16. Lee KH, Kandaiya S. Estimation of breast radiation dose in a mammographic system. *Appl Radiat Isot* 1996; 47:361-363.
 17. Faulkner K, Law J, Robson KJ. Assessment of mean glandular dose in mammography. *Br J Radiol* 1995; 68:877-881.
 18. Helvie MA, Chan HP, Adler DD, Boyd PG. Breast thickness in routine mammograms: effect on image quality and radiation dose. *AJR* 1994; 163:1371-1374.
 19. Boone JM, Shaber GS, Tecotzky M. Dual-energy mammography: a detector analysis. *Med Phys* 1990; 17:665-675.
 20. Burattini E, Cossu E, Di Maggio C, et al. Mammography with synchrotron radiation. *Radiology* 1995; 195:239-244.
 21. Tompkins PA, Abreu CC, Carroll FE, Xiao QF, MacDonald CA. Use of capillary optics as a beam intensifier for a Compton x-ray source. *Med Phys* 1994; 21:1777-1784.
 22. Boone JM, Seibert JA. Monte Carlo simulation of the scattered radiation distribution in diagnostic radiology. *Med Phys* 1988; 15:713-720.
 23. Boone JM, Seibert JA. Scattered energy deposition under shielding. *Invest Radiol* 1988; 23:627-631.
 24. Cullen DE. TART97 a coupled neutron-photon 3-D, combinatorial geometry Monte Carlo transport code. Livermore, Calif: Lawrence Livermore National Laboratory, 1997.
 25. Boone JM, Fewell TR, Jennings RJ. Molybdenum, rhodium, and tungsten anode spectral models using interpolating polynomials with application to mammography. *Med Phys* 1997; 24:1863-1874.
 26. Boone JM, Seibert JA. An accurate method for computer-generating tungsten anode x-ray spectra from 30 to 140 kV. *Med Phys* 1997; 24:1661-1670.
 27. Boone JM, Chavez AE. Comparison of x-ray cross sections for diagnostic and therapeutic medical physics. *Med Phys* 1996; 23:1997-2005.
 28. Hammerstein GR, Miller DW, White DR, Masterson ME, Woodard HQ, Laughlin JS. Absorbed radiation dose in mammography. *Radiology* 1979; 130:485-491.
 29. Tucker DM, Barnes GT, Wu XZ. Molybdenum target x-ray spectra: a semiempirical model. *Med Phys* 1991; 18:402-407.

DAMD17-98-18176, Final Report - August 2001

Computer Simulation of Breast Cancer Screening

PI: John M. Boone, Ph.D.

Appendix H:

JM Boone, TR Nelson, KK Lindfors, and JA Seibert, "Dedicated breast CT: Radiation dose and image quality evaluation", Radiology 2001 (*in press*)

DEDICATED BREAST CT: RADIATION DOSE AND IMAGE QUALITY EVALUATION

Presented at the 86th Annual Meeting of the Radiological Society of North America
Presentation #601, November 28, 2000 Radiology 217(P):2000;346

John M. Boone, Ph.D., *Thomas R. Nelson, Ph.D.,
Karen K. Lindfors, M.D., and J. Anthony Seibert, Ph.D.

Department of Radiology
University of California, Davis
*Department of Radiology
University of California, San Diego

KEYWORDS: Breast cancer, mammography, computed tomography, radiation dose, Monte Carlo, computer simulation, cadaver, screening

ABSTRACT

Purpose: The purpose of this investigation was to evaluate the feasibility of breast CT in terms of radiation dose and image quality. **Methods:** Validated Monte Carlo simulation techniques were used to estimate the average glandular dose. The mammograms of 82 women were analyzed for average compressed breast thickness and breast width near the chest wall, which allowed estimation of the corresponding breast diameters for breast CT. The calculated photon fluence at the detector for high quality abdominal CT (120 kVp, 300 mAs, 5 mm slice thickness) served as the benchmark for assessing the necessary mAs and corresponding dose for breast CT. Physical measurements of image noise were made using a 10 cm diameter Lucite cylinder imaged in a clinical CT scanner from 10 to 300 mAs for 80, 100, and 120 kVp. CT contrast for breast cancer was evaluated from published data, and contrast to noise (CNR) values were assessed as a function of breast dose. A cadaver breast was imaged in coronal section, approximating the acquisition geometry of a proposed breast CT scanner. **Results:** The average glandular dose (AGD) for 80 kVp breast CT was comparable to that of two-view mammography for 5 cm breasts (compressed breast thickness). For thicker breasts, breast CT dose was about one third less than two view mammography. Maximum dose in mammography assessed in 1 mm³ voxels was far higher (20 mGy) than for breast CT (5.4 mGy) for a typical 5 cm, 50% glandular breast. CT images for an 8 cm cadaver breast (AGD=6.3 mGy) were subjectively superior to a digital mammogram (AGD=10.1 mGy) of the same specimen. **Conclusions:** The potential of high signal to noise ratio images with low anatomical noise, obtainable at dose levels comparable with mammography, suggests that dedicated breast CT should be studied further for its potential in breast cancer screening and diagnosis.

INTRODUCTION

Mammography is used for breast cancer screening throughout the world, and the recent reduction in breast cancer mortality is largely attributed to earlier detection[1-3]. Despite this success, many investigators have proposed non x-ray screening approaches in the hopes of achieving even earlier breast cancer detection. Imaging technologies explored for breast cancer detection include scintimammography[4;5], positron emission tomography (PET)[6;7], magnetic resonance imaging (MRI) [8;9], optical imaging[10], microwave imaging[11], and ultrasound imaging[12]. Each approach has its advantages and disadvantages, but so far no other modality has been able to compete with mammography on the basis of detection performance, non-invasiveness, imaging time, and cost effectiveness. Consequently, many of these additional imaging tests are used in the clinical setting, after a screening mammogram or a clinical breast examination has revealed a possible abnormality.

Despite its utility, mammography is not without its limitations[13]. The most widely cited downfall of mammography relates to its reduction in sensitivity for women with dense breasts[14-16]. Imaging the dense breast with good sensitivity has taken on more importance as younger women are now screened routinely, as the use of hormone replacement therapy has expanded, and as genetic testing identifies younger women at high risk. Digital mammography systems[17;18] have been developed which have wider dynamic range than screen-film mammography, in part to address the increased challenges of imaging the dense breast. Results indicate that digital mammography may lead to important incremental improvement in cancer detection in the dense breast.

Computed tomography (CT) was studied in passing some years ago[19-22] for its utility in breast cancer screening, however CT has largely been dismissed from a practical role in breast cancer screening due to concerns about radiation dose and cost effectiveness. Most earlier studies used conventional CT scanner technology, where the images were acquired axially and thus the x-ray beam had to penetrate the thoracic cavity. Not only is a large amount of non-breast tissue exposed in this geometry, leading to significant dose inefficiency, but cardiac and respiratory motion have the potential to reduce image quality as well.

Despite the conventional wisdom that computed tomography would not be effective for breast cancer screening, it is nevertheless generally accepted that CT is far better than projection radiographic techniques in terms of contrast resolution, indeed by about a factor of ten[23]. When the complex normal anatomy (structured noise) of the dense breast is factored into the analysis of contrast resolution, the tomographic nature of CT provides the powerful ability of eliminating overlapping structures, which are problematic in conventional mammography.

The purpose of this investigation was to evaluate the feasibility of breast CT in terms of radiation dose and image quality. Whereas a host of other considerations such as diagnostic accuracy, cost, and interpretation time remain to be evaluated, dose and image quality are fundamental to the potential of dedicated breast CT. Thus, we believe our investigation represents a necessary first step in the assessment of the potential of breast CT.

METHODS

GEOMETRY

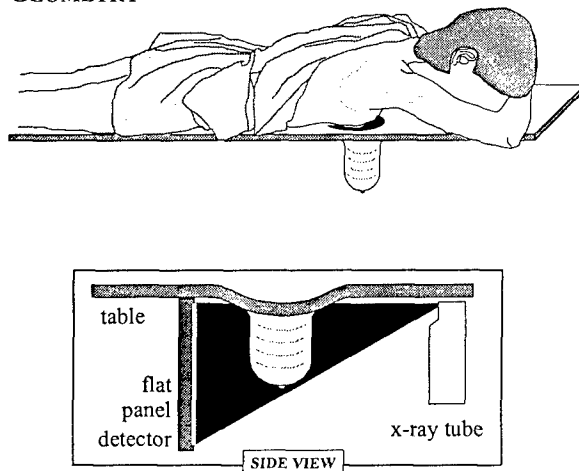


Figure 1: This figure shows the geometry of a CT scanner customized for breast imaging, where the breast would be imaged in the pendant position. The inset is a side view close up, which demonstrates that a swale in the table may allow imaging closer to the chest wall.

A plausible design for a CT scanner tailored specifically for breast cancer screening is shown in Figure 1. The scanner should avoid exposing tissues in the thoracic cavity, which necessitates that CT acquisition be performed in the coronal plane. Each breast would be scanned individually, with the women laying prone on a

table and the breast to be imaged hanging through a hole in the table, similar to the geometry of presently-available digital breast biopsy systems. With the breast hanging in the pendant position, the x-ray tube and detector arrays would rotate around the breast in the horizontal plane. In order to assure that breast tissues close to the chest wall and into the axilla are imaged, the x-ray tube and detectors would have to be positioned just below the bottom of the shielded table. The table surface surrounding the cut-out for the breast would be engineered with a swale to allow a portion of the chest wall to extend into the scanner field of view, to provide adequate coverage of the breast (see inset of Figure 1). While gentle pressure beyond gravity may be used to immobilize the breast and to pull breast tissue away from the chest wall, breast compression as is used in mammography would not be necessary.

The coronal acquisition geometry of the dedicated breast CT scanner will allow the reconstructed CT images to be sized to the dimensions of the breast. For example, for a 15 cm diameter field of view, a 512×512 CT image would have pixel dimensions of $\sim 300 \mu\text{m}$. There is a trade-off in CT between image noise and voxel volume, and there is probably little clinical motivation for acquiring slice thicknesses less than 1 mm when standard 2D viewing is used, since this would increase image noise and generate more images to interpret. Isotropic resolution (e.g. $300 \mu\text{m} \times 300 \mu\text{m} \times 300 \mu\text{m}$ voxels) may however be useful in concert with 3D viewing techniques, and could be achieved using cone beam techniques[24] with flat panel detectors[25;26]. For routine breast CT scanning, the slice thickness would likely be on the order of 1 to 2 mm.

The pendant breast would be approximately cylindrical in shape, with slight tapering in diameter anteriorly. The dimensions of the cylindrical breast were estimated based on assumptions illustrated in Figure 2. The breast dimensions of a small cohort of 82 women were evaluated in our breast clinic, based on measurements taken from the film images. Human use authority (exemption under category #4) was obtained for this activity. During normal mammographic interpretation, a mammographer (KKL) measured the width of the left breast image at the edge of the film corresponding to the width of the compressed breast near the chest wall, and recorded this dimension on a form. The compressed breast

thickness, which was printed onto the film, was also recorded.

Monte Carlo Simulations

Previously validated[27;28] Monte Carlo techniques were used to assess the radiation dose levels for dedicated breast CT. The SIERRA[27;28] (simple investigational environment for radiology research applications) code was modified to emulate the acquisition geometry of a dedicated breast CT scanner. The influence of the x-ray spectrum was explicitly evaluated as part of the simulation process. In order to estimate the appropriate amount of filtration for breast CT, x-ray spectral properties were measured on a commercial CT scanner at our institution (General Electric Lightspeed, Milwaukee, WI). With the CT gantry in the parked position (with assistance from service personnel), the half value layer (HVL) was determined using type 1100 aluminum and an ionization chamber (Keithley Triad, Cleveland, OH) for 80, 120, and 140 kVp. The output of the CT x-ray tube (air kerma per mAs @ isocenter) was also measured. Using a spectral model appropriate for CT[29], the amount of added Al filtration was varied mathematically until the modeled spectra matched both the HVL and output measurements of the commercial scanner. The filtered spectral model was then used for producing x-ray spectra from 30 to 140 kVp in the Monte Carlo simulations.

In CT, the dose for an axial CT slice at a given kVp is linearly related to the product of the x-ray beam current (mA) and acquisition time (s), commonly referred to as the mAs. Because the mAs is a part of the technique protocol on any CT scanner, the mAs was used in this study as a descriptor of x-ray beam quantity. The relationship between the output of the x-ray tube (mGy or mR) and photon fluence at the isocenter of the commercial CT scanner was determined as a function of the mAs at each kVp (JAS, JMB), using physical exposure measurements combined with spectral modeling techniques.

Radiation dose was computed using a cylindrical breast geometry with diameters ranging from 6 cm to 16 cm, which span the range of breast sizes which would likely be encountered clinically. Breast composition of 50% glandular and 50% adipose (a 50/50 breast) was simulated using the data of Hammerstein[30]. The isocenter is the position in space around which the x-ray tube and

detector arrays rotate, and was assumed to be coincident with the center of the breast cylinder. The x-ray source to isocenter distance was assumed to be 54 cm, similar to a clinical CT scanner at our institution. A fan beam of x-rays was incident on the right cylinder, with a 1 mm thick fan beam positioned orthogonal to the central axis of the cylinder. The x-ray source was rotated in the simulation 360° around the breast cylinder, in 3° increments for a total of 120 different source positions. For each simulated x-ray spectrum (i.e. kVp) and breast diameter, a total of 10^7 x-ray photons were tracked, and the energy deposition in a grid of $1\text{ cm} \times 1\text{ cm} \times 20\text{ cm}$ voxels was tallied. The mean and standard deviation in breast dose was computed from 10 Monte Carlo runs of 10^6 photons each, and these data were used to compute the coefficient of variation (the ratio of the standard deviation to the mean). For the evaluation of dose homogeneity, the dose distribution was measured using $1\text{ mm} \times 1\text{ mm} \times 20\text{ cm}$ voxels. The out-of-plane scattered radiation dose was tallied regardless of its distance from the collimated CT slice, along with the primary dose deposition. This acquisition geometry is equivalent to the measurement of the multiple slice average dose (MSAD), which the computed tomography dose index (CTDI) seeks to approximate[31]. The CTDI measurement is the standard measurement protocol used by the CT industry (by Federal statute) and by medical physicists (by convention) in the assessment of CT dose.

The energy deposition of ionizing radiation due to photoelectric interaction and Compton scattering events was tallied in each tissue voxel (JMB). Rayleigh interactions were also tracked but these do not result in energy deposition in the medium. The dose delivered in the medium under study was corrected to the glandular tissue dose using the energy dependent ratio of the mass energy attenuation coefficient of glandular tissue to that of the medium. This correction was performed on an interaction-by-interaction basis. The tallied energy (J) in each voxel was normalized by the mass of each voxel (kg) to determine the average glandular dose (Gy). The dose was then normalized to correspond to that delivered using 100 mAs, using the established relationship between photon fluence and mAs at each kVp. The resulting dose values are essentially CTDI determinations, in mGy per 100 mAs. Average glandular dose at other mAs settings could then easily be computed from these data.

To compute dose for a breast CT study, an estimate of the mAs necessary (at each kVp) for providing clinically useful images was required. Since the typical photon fluence levels at the CT detector (which largely determines the signal to noise ratio in the image) were unknown to us, we used the example of a typical CT technique that is known to produce CT images with high signal to noise ratio. A (non-helical) CT technique for abdominal CT of 120 kVp, 300 mAs, 5 mm slice thickness, and a 32 cm diameter cylindrical water-equivalent phantom was simulated. This technique was used in a computer simulation to determine the photon fluence striking the center of the CT detector array, integrated over a 360° rotation of the scanner. To maintain the same signal to noise ratio (SNR) in breast CT as in the abdominal CT benchmark, the same photon fluence should be incident on the detector arrays. A simulation was performed for cylinders of 50% glandular tissue composition of various diameters (6 to 16 cm). The mAs necessary to deliver the same photon fluence to the detector behind the breast for a 1 mm thick CT image was evaluated for x-ray spectra between 40 and 140 kVp.

The heterogeneity in dose for mammography and breast CT was evaluated (JMB) using 1 mm^3 voxels, and for mammography a rectangular cross-sectioned breast was simulated. The Monte Carlo techniques described previously were used to assess the dose distribution in CT, however in mammography the task is slightly more difficult due to the orthogonal compression used in two view mammography. To simplify this computation, mammographic exposure to a rectangular shaped breast (in coronal cross section) was simulated. The rectangular shape simplified the application of mathematical compression, as described below.

A 50% glandular 5 cm compressed breast thickness was used, and the median breast width determined from the breast size analyses was assumed for the width dimension. A 4 mm skin layer was also assumed[32]. Under compression, the cross section of the breast was modeled as a $5\text{ cm} \times 19.4\text{ cm}$ rectangle, and when uncompressed the breast cross section was warped using bilinear interpolation to a $9.85\text{ cm} \times 9.85\text{ cm}$ square, which is equal in area to the rectangle. Monte Carlo techniques were used to determine the dose deposition to the rectangular cross-sectioned breast, and the resulting Monte Carlo depth-dose curve was computer-fit using commercial software (Table Curve 2D, Jandel

Scientific, Corte Madera, CA). After breast exposure in one direction (e.g. craniocaudal) was performed, the rectangular breast was warped to a square, and then warped to a rectangle in the orthogonal direction (19.4 cm \times 5 cm) for a second (e.g. mediolateral oblique) exposure. For analysis of dose distribution, the breast was warped back to the square orientation. A 26 kVp molybdenum anode x-ray spectrum[33] filtered with 0.030 mm molybdenum and 3 mm Lucite (the compression paddle) was used. The entrance skin exposure used in this computation (17.5 mGy air kerma or 2000 mR) was determined by interpolation from technique data measured at our institution using 50% glandular phantoms. For dose comparisons, an 11 cm diameter breast (equal area) was simulated for exposure using the breast CT geometry as described above.

EXPERIMENTAL STUDIES

A 10 cm diameter Lucite cylinder, 10 cm in length, was fabricated for this project. The cylinder had two 12.7 mm diameter holes machined into it to accommodate a CT ionization pencil chamber, one at the center and one centered 19 mm from the edge of the cylinder. The cylinder was positioned at the isocenter of a commercial multislice CT scanner (GE Lightspeed, Milwaukee, WI) with a CT chamber (MDH 1015, 3 cc CT chamber, Monrovia, CA) placed in the center hole for measuring air kerma. At 80, 100, and 120 kVp, CT scans were made at a series of 14 exposure levels ranging from 10 mAs to 300 mAs. Images were acquired on the scanner using the detail reconstruction filter[34], with a 10 cm field of view, corresponding to pixel dimensions of 195 μ m \times 195 μ m. The slice thickness was 1.25 mm at isocenter of the scanner.

For each image acquired, three regions of interest (ROIs) were evaluated (JMB, JAS) using commercially available image analysis software (EFILM, University of Toronto). The root mean square (RMS) standard deviation (noise) in each of the ROIs was recorded, and the average noise value ($\sigma_{CT\#}$) of the three ROIs was computed for each image. The noise was fit as a function of mAs ($\sigma = a \text{ (mAs)}^b$) using commercially available software (Freelance 97, Lotus Corporation, Cambridge, MA), and these data allowed $\sigma_{CT\#}$ to be computed as a function of mAs or of dose for each kVp. These measurements of $\sigma_{CT\#}$ (noise) allowed the

denominator of the contrast to noise ratio to be evaluated as a function of kVp and mAs.

Johns and Yaffe[35] measured the linear attenuation coefficients for fibrous (glandular) tissue, fat from the breast (adipose tissue), and infiltrating ductal carcinoma (cancer), for monoenergetic x-rays ranging from 18 keV to 110 keV at 8 different energies. In addition to this attenuation coefficient data, the elemental composition of the three tissues (glandular, adipose, and cancer) were taken from Hammerstein[30], and mass attenuation coefficients were computed using the mixture rule[36] coupled with published attenuation coefficient data[37]. The mass attenuation coefficients of each of the tissue types were multiplied by the physical density (ρ) to compute the linear attenuation coefficient (LAC). The computer generated LACs for breast tissue[30;35] were used to computer-fit the measured LACs reported by Johns and Yaffe, using least squares techniques and letting the physical density and the relative glandular fraction vary as free parameters. Once the LAC versus monoenergetic x-ray energy was parameterized for each of the three tissue types, x-ray spectra[29] from 30 kVp to 140 kVp were used to weight the LAC, resulting in the effective LAC for each polyenergetic spectrum. This was done for adipose, glandular, and cancer tissues, as well as for water. Using the LACs for each tissue type and for water, the corresponding CT# was computed using the formula[23]:

$$CT\# = 1000 \frac{\mu_t - \mu_w}{\mu_w}$$

where the CT# (also called Hounsfield Unit) is for the tissue with LAC μ_t , and μ_w is the LAC of water.

Contrast to noise ratios (CNR) were computed using differences in CT# as contrast, and the noise measurements parameterized from experimental measurements as noise. The CNR values were converted to the signal to noise ratio (SNR) for different size objects using the well-known Rose relationship[38]:

$$SNR = CNR \times \sqrt{N}$$

where N is the number of pixels corresponding to the breast cancer lesion. For lesion diameter d

$$\text{and pixel dimension } \Delta, \quad N = \frac{\pi}{4} \left[\frac{d}{\Delta} \right]^2.$$

CADAVER BREAST IMAGING

A cadaver breast was acquired under proper authority at our institution. The breast was removed from the cadaver with the pectoralis major and minor attached, and was immediately fixed in 5% formalin. The pectoralis muscle with the accompanying skin flap was sutured onto stiff cardboard using plastic ties, in order to position the breast in a more natural position during CT scanning. The breast was placed in the head holder of a clinical multi-slice CT scanner (General Electric Corporation, Lightspeed, Milwaukee, WI), with the long axis of the cylinder of the breast parallel to the table motion. The breast was scanned at 80 kVp, with one acquisition taken at 50 mAs and without repositioning, another acquisition was acquired at 80 mAs. Non-helical images were acquired using a 1.25 mm slice thickness, and a 15.5 cm \times 15.5 cm field of view was reconstructed. This resulted in pixel dimensions of 303 μ m \times 303 μ m. Images were reconstructed using both standard and detail reconstruction filters.

The images were transferred to a imaging workstation for display and analysis. Software was written which loaded the CT images into a volume data set, and coronal, axial, and sagittal views were generated. The viewing software could average any number of adjacent images at any location in the volume, to create thicker slices.

For comparison images and dosimetry, the cadaver breast was placed under compression in a clinical mammography system and imaged using a prototype Fuji Computed Radiography (CR) system designed for digital mammography. The dedicated mammography imaging plate was read out using a clinical CR reader (Fuji CR 5000, Fuji Medical, Tokyo) with prototype software customized for digital mammography and used 100 μ m pixels. The compressed breast thickness averaged 8.0 cm in two placements in the compression device. The mammographic radiation dose to the breast was estimated using an 8 cm thick phantom designed to emulate a 50% glandular and 50% adipose breast (CIRS, Norfolk, VA). This phantom was imaged using the auto-kV/auto-filter mode on a MQSA certified clinical mammography system (Lorad

Mark IV). The system used a technique of 32 kVp, 226 mAs, with a molybdenum anode and rhodium filter. The relationship between mAs and air kerma entrance exposure to the breast was determined, and this value was used to calculate the entrance kerma to the breast. Published tables[32] were used to estimate the average glandular dose for the cadaver breast.

RESULTS AND DISCUSSION

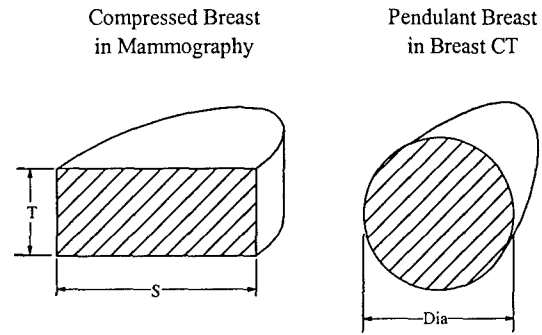


Figure 2: The geometry of the breast in mammography (top left) and in breast CT (top right) is illustrated. T is the thickness of the compressed breast, and S is the width of the breast at the edge of the mammogram. The area of the hatched region on both diagrams is the same. These shapes were used to convert compressed breast thickness (in mammography) to breast diameter (for CT).

BREAST MEASUREMENT RESULTS

The average breast width was 19.4 cm ($\sigma = 2.82$ cm), and was only poorly correlated with breast thickness ($r^2 = 0.159$). The magnification factor was not taken into consideration here, and so our estimates of the physical breast dimensions are slightly high (~5%). This will serve to error towards more conservative, higher dose estimates. The area of the approximately rectangular cross section of the breast in mammographic compression was assumed to be equivalent to the area of the cylindrical pendant breast (Figure 2), and the resulting diameter of the breasts were related to breast thickness T using:

$$\text{Diameter} = 2 \sqrt{\frac{19.4 \times T}{\pi}} = 4.97 \sqrt{T}$$

Monte Carlo Results

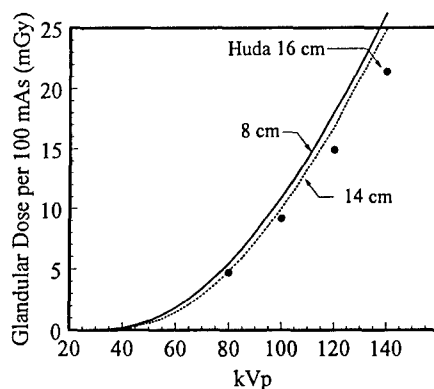


Figure 3: The average glandular dose per 100 mAs was determined using Monte Carlo techniques, and is shown as a function of kVp for different breast diameters (lines). Good correspondence is seen in comparison with the published data of Huda.

Figure 3 illustrates the mean glandular breast dose per 100 mAs as a function of kVp. The data in this figure include the inherent inefficiencies in x-ray production at lower kVps (in terms of air kerma per mAs), which are compounded by the fact that 8 mm of added aluminum filtration was used at all kVps. The glandular dose per 100 mAs, which is essentially a Monte Carlo determination of the CTDI values for breast CT, is not strongly dependent upon the diameter of the breast. Data for breast diameters of 8 cm and 14 cm are shown. Data for intermediate breast diameters were computed and fall between the two curves, but are not plotted in Figure 3 for clarity. The CTDI values reported by Huda[39] for a 16 cm head phantom are shown for comparison as the solid circles in Figure 3. Huda's values were converted from dose to Lucite to dose to glandular tissue, using the ratio of mass energy attenuation coefficients. There is excellent agreement with Huda's CTDI values considering that the x-ray beam filtration, f-factor, and diameter were slightly different.

Figure 4 illustrates the mAs necessary to achieve good image quality in breast CT as a function of kVp. The necessary mAs (at each kVp) was computed, matching the photon fluence at the CT detector array to that of a high dose clinical examination known to produce excellent image quality. Since these data were produced using computer simulation, no dose inefficiencies due to post patient collimation or multi-slice[40] detector/beam geometry were included in either the abdominal or breast CT

simulations. For the typical breast diameter of 10 to 12 cm, at 80 kVp the mAs required to produce a high quality breast CT image ranges from 72 to 110 mAs.

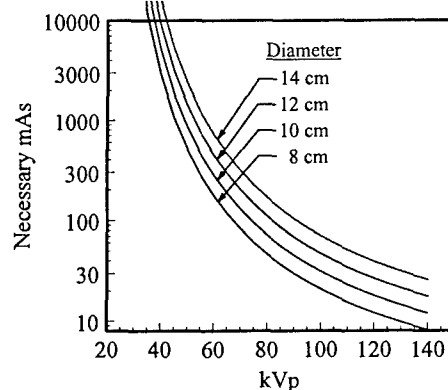


Figure 4: The mAs required to produce constant SNR images for 50% glandular/50% adipose breasts of various diameters is shown as a function of kVp. The mAs values shown produce the same photon fluence at the CT detector as a typical clinical CT examination where image quality is known to be excellent.

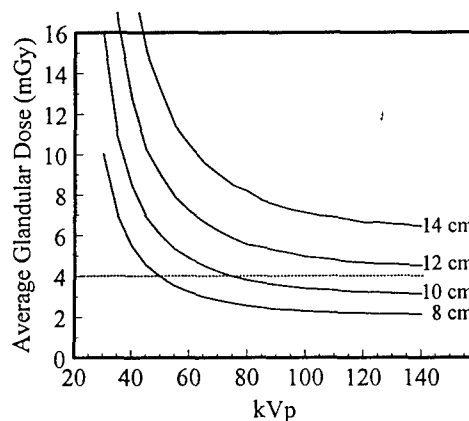


Figure 5: The average glandular dose is shown as a function of kVp, for 4 breast diameters. The data in this figure is the product of the data shown in Figures 3 and 4, with proper normalization. The typical dose for two view mammography for a 4 cm compressed breast (which corresponds to the 10 cm diameter breast in CT) is illustrated as the dashed line. CT dose is seen to be comparable to that of two view mammography.

Figure 5 shows the average glandular dose necessary to produce a 1 mm breast CT slice with good image quality. The data in Figure 5 are the product of the curves (at the same breast diameters) shown in Figures 3 and 4,

with proper normalization. Breast CT requires only one acquisition, whereas screening mammography performed in the United States makes use of two nearly orthogonal projections. Whereas the dose in breast CT at low kVps was extremely high, at 80 or 100 kVp the dose for breast CT is comparable to that of two-view mammography. For example, a 4.5 cm thick compressed breast may receive an average glandular dose in mammography of ~ 2.0 mGy per view, for a total of 4.0 mGy. The corresponding breast diameter is 10.5 cm, and at 80 kVp the average glandular dose for breast CT is also about 4.0 mGy. Figure 5 illustrates that women with larger breasts will experience larger doses in breast CT, and this assumes that the mAs is increased as the breast diameter increases in order to maintain constant image SNR. The automatic exposure control systems on mammography machines increase the entrance kerma for larger breasts as well, and therefore women with larger breasts experience larger x-ray doses in mammography. For both mammography and breast CT therefore, dose increases with breast size.

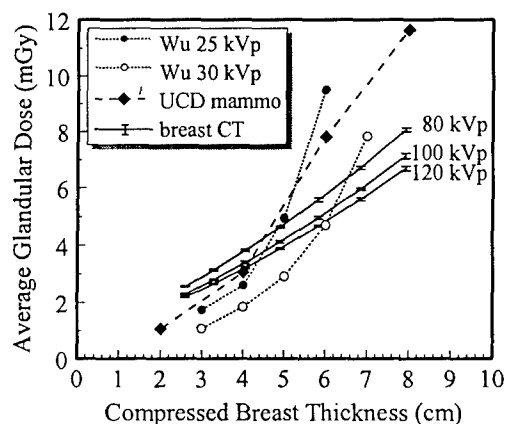


Figure 6: The average glandular dose is shown as a function of compressed breast thickness for two view mammography and breast CT. Dose computed by Wu et al[41] at 25 kVp and 30 kVp are shown for comparison. The "UCD mammo" data reflect realistic clinical mammography doses measured at our institution. Breast CT doses (shown with 95% confidence limits) are lower than two-view mammography for breasts larger than 5 cm, and are only slightly higher for smaller breasts.

Figure 6 shows a comparison of average glandular dose versus breast thickness between two-view mammography and breast CT. The curve marked "UCD mammo" illustrates doses

computed using clinical techniques appropriate for each breast thickness at our institution. The published values from Wu[41] for 25 kVp and 30 kVp mammography are also shown, and compare well with the UCD results when the differences in kVp are considered. The calculated breast CT doses are shown with 95% confidence intervals ($\pm 2\sigma$). For breasts greater than about 5 cm, breast CT at 80 kVp is seen to deliver less breast dose than mammography. The median breast thickness determined from the analysis of 82 women was 5.2 cm, and so about 50% of women have breasts larger than 5 cm. The dose benefit of breast CT increases for women with even thicker breasts, for example the breast CT dose at 80 kVp for a 6 cm thick, 50% glandular breast (5.8 mGy) was 26% less than that of two-view mammography (7.8 mGy). For a 8 cm thick breast, the CT dose (8.3 mGy) was 29% lower than mammography (11.6 mGy). Dose levels for CT at 100 and 120 kVp are even lower. The coefficient of variation of the breast CT doses (averaged across the breast diameters) were 0.44%, 0.51%, and 0.39%, for the 80 kVp, 100 kVp, and 120 kVp data, respectively.

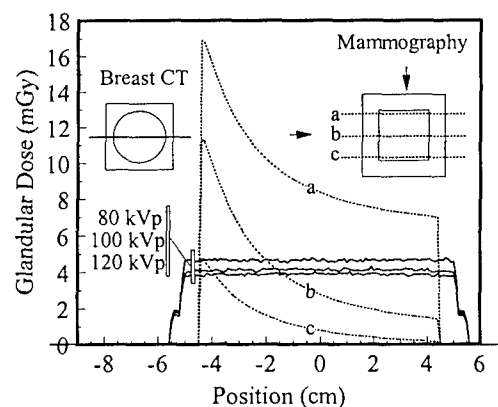


Figure 7: The distribution of glandular dose is shown as a function of position for both mammography and breast CT. The breast CT dose profiles demonstrate a virtually homogeneous distribution of dose to each voxel in the breast, and this is a consequence of the source rotating around the breast during CT acquisition. The combination of the nearly orthogonal CC and MLO views results in the markedly heterogeneous dose distribution in mammography. The dotted lines labeled a, b, and c on the graph correspond to the

The average glandular dose has become the standard metric for assessment of dose in mammography, however this parameter masks

the large spatial differences in radiation dose in the breast that occur in mammography. Monte Carlo techniques were used to evaluate the dose distribution in both breast CT and two-view mammography. The CT dose profiles shown in Figure 7 illustrate that dose to the breast during breast CT was very homogeneous. The 80 kVp breast CT doses were slightly higher than those at 100 and 120 kVp, which was expected since the mAs at 80 kVp was increased to maintain SNR. The dose distribution for mammography is also shown in Figure 7. The corner of the breast that was near the entrance x-ray beams for both the CC and MLO views received the highest dose, while the opposite corner received the lowest. While the average glandular dose for a 5 cm breast is very similar between breast CT and mammography, there is a huge amount of spatial variation in the dose received to the breast in mammography. Quantitative analysis of the dose histograms for two-view mammography indicated that 5% of the breast received an average of 14.2 mGy (1.4 rads), and 20% of the breast received a mean glandular dose greater than 10 mGy (1 rad). This is not surprising, given the low x-ray energies (and high attenuation) used in mammography.

EXPERIMENTAL RESULTS

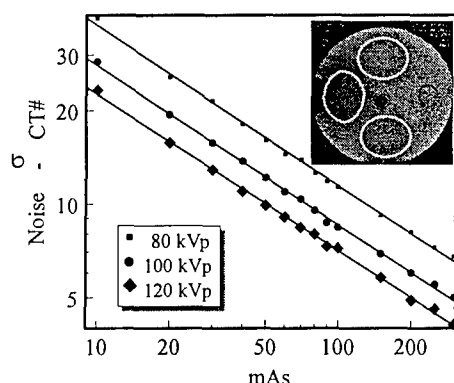


Figure 8: The standard deviation (noise) in the CT number of a 10-cm diameter Lucite cylinder are shown as a function of mAs for three kVps. The standard deviations were determined from 3 elliptical regions of interest on the CT images, as indicated on the inset. This graph is shown with logarithmic axes, and the slope of each best-fit line is $-1/2$, which is consistent with dose limited performance of the scanner. These data were used to characterize the noise in the image as a function of mAs and kVp.

CT image noise for a 10 cm Lucite phantom is illustrated in Figure 8. The inset shows a CT image of the phantom, and the position of the three region of interests that were used to compute the noise. The CT# noise ($\sigma_{CT\#}$) is greater at low mAs, as expected, and at the same mAs $\sigma_{CT\#}$ is higher for lower kVps, indicating a reduced number of x-ray photons reaching the detector at lower kVps. The power regression lines ($Y=aX^b$) using least squares criterion for fitting demonstrated excellent correlation to the measured data points, with r^2 values of 0.998, 0.998, and 0.999, for the 80 kVp, 100 kVp, and 120 kVp curves, respectively. The slopes of these log-log curves were determined to be essentially $-1/2$ (mean = -0.508, $\sigma = 0.0055$), which is consistent with quantum limited behavior of the CT scanner, where:

$$\sigma_{CT\#} = \frac{k}{\sqrt{mAs}}$$

and where k is a constant of proportionality. The data shown in Figure 8 allowed the parameterization of noise versus mAs and noise versus dose, which was useful for subsequent computation of CNR and SNR versus dose.

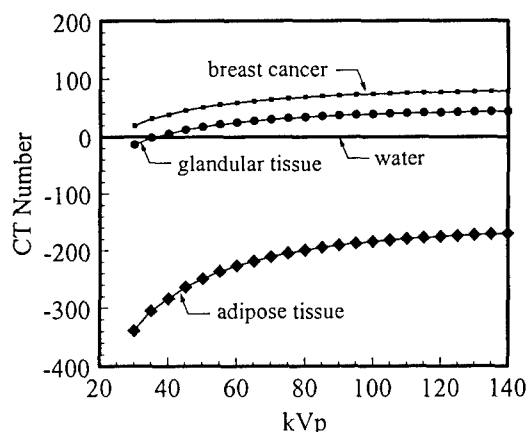


Figure 9
The CT numbers for breast cancer, glandular tissue, adipose tissue, and water are shown weighted for different kVp.

Relevant linear attenuation coefficients for polyenergetic CT spectra are illustrated as a function of kVp in Figure 9. The contrast of cancer on a CT image is the numerical difference between the CT number of cancer and that of the background tissue (adipose or glandular tissue).

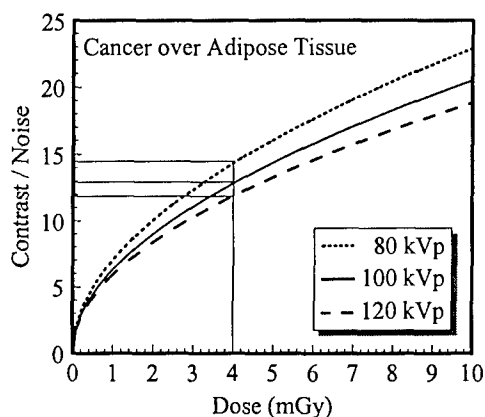


Figure 10: (A) The contrast to noise ratio of the breast cancer lesion against an adipose tissue background is shown as a function of dose for breast CT. At a dose of 4 mGy, the contrast to noise ratio is about 14 at 80 kVp.

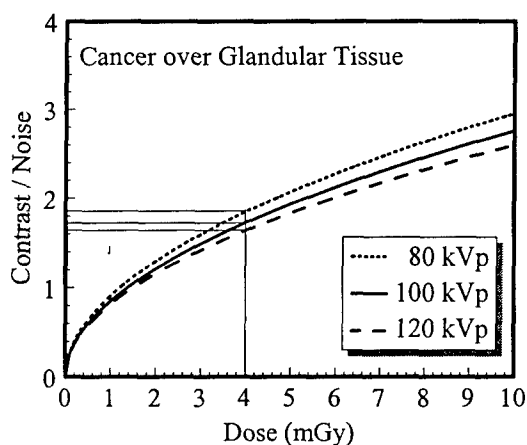


Figure 10: (B): The contrast to noise ratio is shown as a function of dose for breast cancer lesion against a glandular tissue background. At a dose of 4 mGy, the contrast to noise ratio (per pixel) is approximately 2.5.

The contrast to noise ratio (CNR) was calculated as a function of average glandular dose to the breast, for 80, 100, and 120 kVp, and is shown in Figure 10. The CNR for breast cancer against an adipose background is shown in Figure 10A, and the CNR for breast cancer against a glandular tissue background is shown in Figure 10B. At a dose of 4 mGy (i.e. two view mammography for a typical breast), the CNR at 80 kVp is 14.5 for cancer over adipose tissue (Figure 10A), and is 1.85 for cancer against a glandular tissue background (Figure 10B).

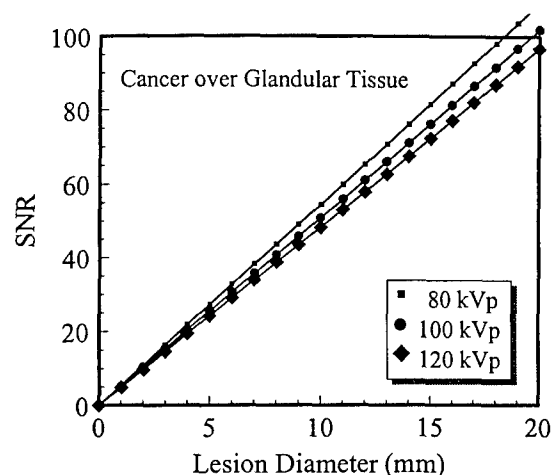


Figure 11: The SNR of a breast cancer lesion positioned in a glandular breast tissue background is shown as a function of lesion diameter. This data was calculated assuming $300 \mu\text{m} \times 300 \mu\text{m}$ pixels, a detail reconstruction filter, and an average glandular dose of 4 mGy delivered to a 10 cm diameter breast. The SNRs shown here confirm, based on the Rose criterion, that high SNR CT images can be acquired at clinically acceptable doses.

The SNR of breast lesions against a glandular tissue background was calculated from the CNR and pixel count per lesion, and is shown in Figure 11. This calculation assumes a homogeneous breast background, where the anatomical (structure) noise resulting from normal breast parenchyma was considered negligible. The actual SNR would be reduced due to the presence of anatomical noise.

CADAVER BREAST CT RESULTS

After scanning the breast at 50 mAs and 80 mAs, it was realized that this breast was larger than the median breast and a higher mAs should have been used. Since the 50 mAs and 80 mAs acquisitions were performed without repositioning, it was possible to simply add both image sets together, image by image, to synthesize CT images equivalent to 130 mAs acquisition at 80 kVp. Figure 12 illustrates a selection of four coronal CT images of the cadaver breast. The estimated average glandular dose from CT was 6.32 mGy for this relatively large breast. As the scan plane approached the posterior region of the cadaver breast specimen, dark regions on the image were visible which correspond to air pockets. These artifacts are clearly a consequence of using a cadaver breast, and would not be a factor in imaging live

women. The mammography dose for this 8 cm thick breast was estimated as 5.06 mGy for the CC view, and thus for standard two view mammography, the total average glandular dose would be 10.1 mGy. In comparison, the breast CT dose to this breast was estimated at 6.32 mGy. Therefore, the CT images shown in Figure 12 were acquired with 37% less mean glandular dose than routine two-view mammography.

A digital mammogram of the cadaver breast is illustrated in Figure 13A. The CT volume data set was used to generate a digital mammogram, albeit of low resolution, and this image is illustrated in Figure 13B. Other than the difference in spatial resolution and lack of compression in the CT data, the calculated projection image through the CT data set is

similar in overall appearance. For comparison, a breast CT image reformatted to the axial projection is shown in Figure 13C. The ductal structures that are clearly visible in Figure 13C are impossible to discern in the other two images. These images demonstrate the exceptional detail that tomographic images can provide of the breast. The CT images, when overlaid on each other to produce a projection image, suffer from the same tissue-overlay problems as the mammogram. This suggests that the problems frequently mentioned in the literature concerning mammography of dense breasts[14-16] are mainly due to the complicated overlapping structures, and are secondarily related to the mode of detection.

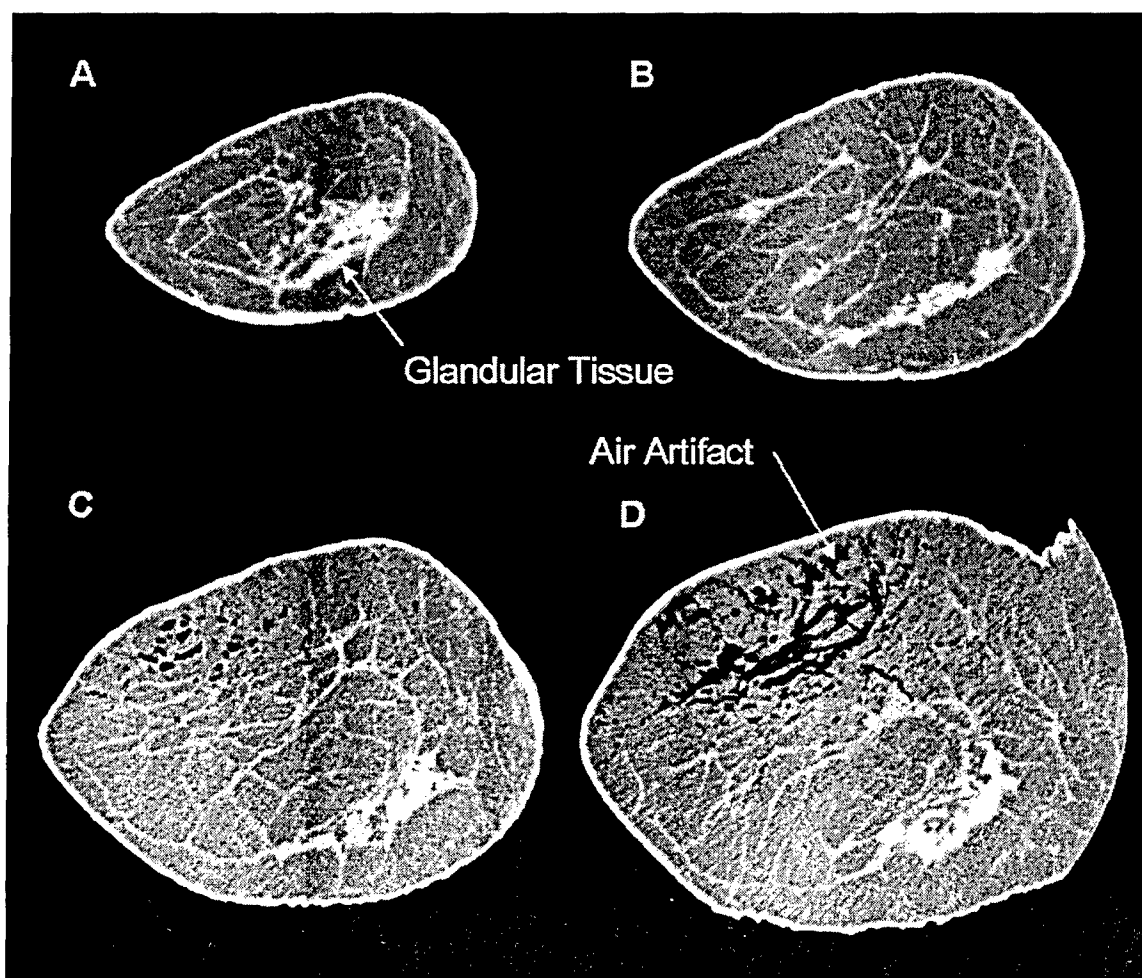


Figure 12: Four coronal CT images of a cadaver breast are shown. These images were acquired on a clinical CT scanner using 80 kVp and the equivalent of 130 mAs, with a slice thickness of 1.25 mm and pixel dimensions of $303 \mu\text{m} \times 303 \mu\text{m}$. The detail reconstruction filter was used. These images demonstrate far greater detail than that seen in mammograms. Air artifacts are a results of breast fixation and storage. Images A through D illustrate different coronal planes in the breast, from anterior (A) to posterior (D).

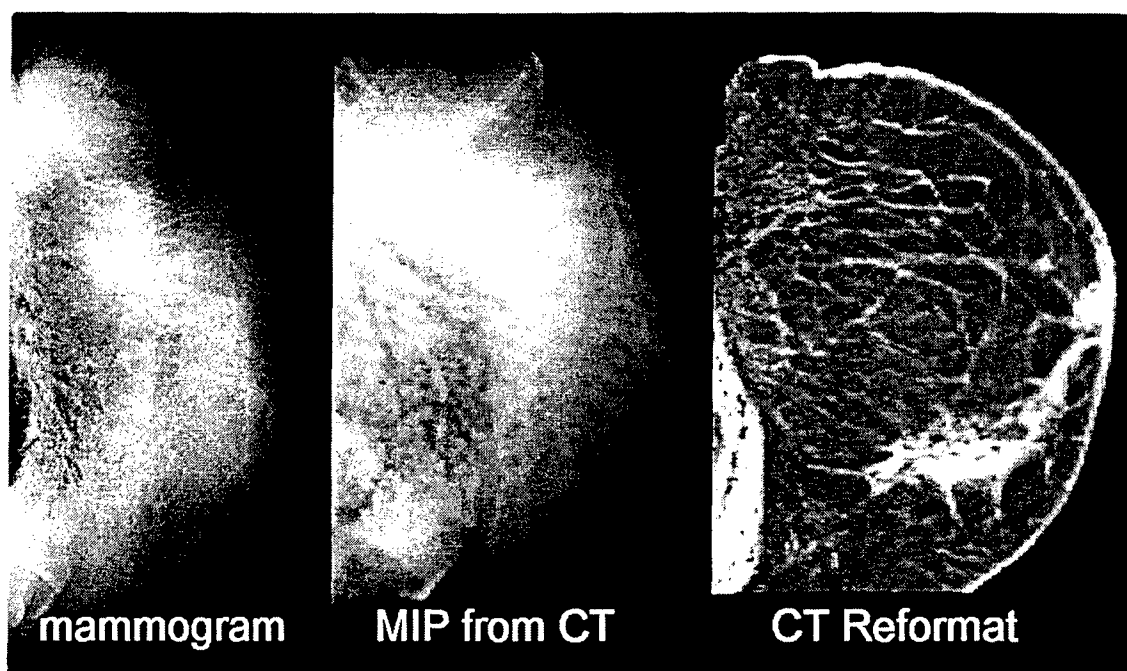


Figure 13: The cadaver breast was imaged using digital mammography (A), and the CT data set was used to compute a projection “mammogram” (B). The coronal CT slices were reformatted to the axial plane, and (C) is a mid-breast axial slice. In comparing these images, it is apparent that the depiction of detail in the breast is related less to the mode of detection than to the fact that overlaying tissue (as in images A and B) significantly obscures the visualization of anatomical structure (and probably breast cancer) in the breast. The fixation fluid produced a line artifact when the breast was compressed for mammography (arrow in Image A).

DISCUSSION

Radiation dose to the breast is a crucial issue in the context of breast CT feasibility. Figure 6 shows a comparison of breast CT dose versus the average glandular dose due to two view mammography, and breast CT demonstrates lower doses than mammography for breasts greater than 5 cm. While the data shown are experimental, the mammography doses are well established and the CT dose computations are completely consistent with published CTDI values. Compare the typical mammography setting of a 5 cm compressed breast with a 26 kVp Mo/Mo x-ray beam, with the corresponding 11 cm breast diameter and an 80 kVp x-ray beam as proposed for breast CT[33;37]. For 1000 input photons to the breast, 14 primary photons emerge in mammography, compared with 90 in breast CT (a 6.3-fold increase in photon penetration). In terms of energy fluence, for a spectrum with an entrant energy fluence of 1000 keV (integral of entire spectrum), 17 keV of primary radiation emerges

from the breast in mammography, compared with 96 keV in breast CT (a factor of 5.8 better x-ray energy penetration). CT is a high SNR imaging technique requiring relatively high photon fluence to the detectors, however the higher beam energy and commensurate increase in penetrability of the proposed breast CT spectrum more than compensates for this. The results of this research clearly demonstrates that high quality breast CT can be performed at dose levels that are equivalent to, or lower than, present day mammography.

The dose homogeneity in breast CT is far greater than in mammography. For nearly identical average glandular doses, the peak dose levels for an appreciable portion of the breast are far higher in mammography than the peak levels in breast CT. If radiation risk truly is a linear no-threshold phenomenon as assumed by regulatory bodies, then the risks between mammography and breast CT are equivalent. However, if radiation risk is non-linear as some radiobiological data suggests[42], then the radiation risk of breast CT would be lower than

that of mammography, due to the greater dose homogeneity.

In addition to the use of well-validated[27;28] Monte Carlo studies, experimental measurements were made of the noise properties in breast CT, and published data were used to evaluate the contrast properties of breast CT. Combining the contrast and noise data, the contrast to noise ratios and corresponding signal to noise ratios for small breast cancer lesions are impressive. The Rose Criterion states[43] that an object will be almost certainly be detected if the SNR exceeds 5, and using this criterion, lesions down to 2 or 3 mm in diameter may be easily detectable in breast CT. By comparison, the median lesion diameter detected using screen-film mammography has been reported to be between 11 mm and 16 mm[44-46]. These calculations are of course for the simple case where the background image behind the lesion is homogeneous, clearly not the case in most breast imaging. This is where the power of tomography comes to play: By reducing overlapping normal anatomy, the image background in breast CT (Figure 13) is far more homogeneous than in mammography, where overlapping breast parenchyma produces a very complicated normal breast background. The problem is worse for dense breasts. For an 11 cm diameter (median) breast and axially formatted slices, 1 mm thick CT slices would reduce the volume of underlying and overlying tissue by a factor of 110. While the amount of structured noise that the 109 out-of-plane slices contribute to the projection image (but not to the CT slice) depends upon the distribution of breast density, the combination of the improved SNR and the approximately ten-fold reduction in structured noise (~100 fold reduction in variance) suggest that the early breast cancer detection performance of breast CT may be impressive.

OTHER ISSUES

Digital tomosynthesis is a limited angle tomography technique that has been studied for use in breast screening[47;48]. While extremely promising, the potential of tomosynthesis in mammography has yet to be fully understood. It is likely that dedicated breast CT will result in significantly less structured noise than tomosynthesis, due to the much thinner tomographic slices that CT produces. Tomosynthesis will likely provide better spatial resolution but worse contrast resolution than CT, and less spatial resolution but better contrast

resolution for mammography in the dense breast. What the optimum tradeoff is between these parameters for clinical cancer detection remains to be studied.

Breast compression is a necessity in mammography, however, many women have substantial apprehension of compression, and hence of mammography[49-51]. Breast CT would not require compression, as it is not needed to produce high quality images, nor can traditional compression be used for advantage given the rotational acquisition requirements of CT. Since compression is not required in breast CT, it may be better tolerated than mammography by some women.

Microcalcifications are the sole basis for diagnosis in a significant minority (~19%) of breast cancers[52], and it remains to be seen how well breast cancers with microcalcifications can be detected using CT. It would be possible with flat panel cone beam acquisition techniques to produce high resolution images during the CT scan, which could provide better spatial resolution for microcalcification detection than the reconstructed CT images. The fundamental importance of microcalcification detection in cancer screening may be overestimated because this is what mammography happens to excel at. More research is warranted, but it is certainly possible that improvements in contrast resolution with slight compromises in spatial resolution may yield better overall cancer detection rates.

Rose's criterion[53] states that objects will be seen with high confidence when their SNR is greater than about 5. Figure 11 demonstrates that a 1 mm breast cancer lesion, laying against glandular tissue background, would have a SNR of about 5. When the added anatomical noise is included, it is likely that SNR levels will decrease and slightly larger lesions will be required to reach a SNR of 5 – the point where they would easily be detectable. If breast CT were to demonstrate with median detection of 5 mm lesions, for example, this would advance early detection by 0.93 years compared to 11 mm lesions (as in mammography), assuming a doubling time of 100 days[54]. Median detection of 3 mm lesions would result in a 1.5 year advantage in earlier detection. The potential for much earlier detection has important ramifications for reducing morbidity and mortality of breast cancer. For example, a 5 mm diameter lesion has just 9.4% of the cell count of an 11 mm lesion, and a 3 mm diameter lesion represents just 2% of the cells in an 11 mm tumor.

In summary, it has been a general perception for over two decades that breast CT would be radiation dose prohibitive for breast screening. In this investigation, the radiation dose resulting from a proposed breast CT scanner design was found to be comparable or less than the doses experienced in routine mammography. Analysis on phantom CT images also showed that the CNR and SNR of breast cancer would be high at reasonable dose levels. CT images of a cadaver specimen, acquired in the coronal plane at dose levels less than mammography, show promise by subjective inspection, however clinical studies are clearly needed to scientifically evaluate the potential of breast CT for breast cancer screening. In our opinion, the development of breast CT technology using modern detector systems is needed so that such studies can be initiated.

ACKNOWLEDGEMENTS

This research was supported in part by grants from the US Army Breast Cancer Research Program (DAMD17-98-1-8176) and from the National Cancer Institute (R21 CA82077).

REFERENCES

- (1) Tabar L, Chen HH, Fagerberg G, Duffy SW, Smith TC. Recent results from the Swedish Two-County Trial: the effects of age, histologic type, and mode of detection on the efficacy of breast cancer screening. *J Natl Cancer Inst Monogr* 1997;43-47.
- (2) Larsson LG, Andersson I, Bjurstam N, Fagerberg G, Frisell J, Tabar L, Nystrom L. Updated overview of the Swedish Randomized Trials on Breast Cancer Screening with Mammography: age group 40-49 at randomization. *J Natl Cancer Inst Monogr* 1997;57-61.
- (3) Larsson LG, Nystrom L, Wall S, Rutqvist L, Andersson I, Bjurstam N, Fagerberg G, Frisell J, Tabar L. The Swedish randomised mammography screening trials: analysis of their effect on the breast cancer related excess mortality. *J Med Screen* 1996; 3:129-132.
- (4) Kakuda JT, Stuntz ME, Vargas HI, Khalkhali I. Status of scintimammography and its relationship to other detection methods for breast cancer. *Cancer Biother Radiopharm* 1999; 14:435-442.
- (5) Yutani K, Shiba E, Kusuoka H, Tatsumi M, Uehara T, Taguchi T, Takai SI, Nishimura T. Comparison of FDG-PET with MIBI-SPECT in the detection of breast cancer and axillary lymph node metastasis. *J Comput Assist Tomogr* 2000; 24:274-280.
- (6) Rostom AY, Powe J, Kandil A, Ezzat A, Bakheet S, el Khwsky F, el Hussainy G, Sorbris R, Sjolint O. Positron emission tomography in breast cancer: a clinicopathological correlation of results. *Br J Radiol* 1999; 72:1064-1068.
- (7) Flanagan FL, Dehdashti F, Siegel BA. PET in breast cancer. *Semin Nucl Med* 1998; 28:290-302.
- (8) Coons TA. MRI's role in assessing and managing breast disease. *Radiol Technol* 1996; 67:311-336.
- (9) Morris EA, Schwartz LH, Dershaw DD, Van Zee KJ, Abramson AF, Liberman L. MR imaging of the breast in patients with occult primary breast carcinoma. *Radiology* 1997; 205:437-440.
- (10) Manoharan R, Shafer K, Perelman L, Wu J, Chen K, Deinum G, Fitzmaurice M, Myles J, Crowe J, Dasari RR, Feld MS. Raman spectroscopy and fluorescence photon migration for breast cancer diagnosis and imaging. *Photochem Photobiol* 1998; 67:15-22.
- (11) Hagness SC, Taflove A, Bridges JE. Two-dimensional FDTD analysis of a pulsed microwave confocal system for breast cancer detection: fixed-focus and antenna-array sensors. *IEEE Trans Biomed Eng* 1998; 45:1470-1479.
- (12) Jackson VP, Reynolds HE, Hawes DR. Sonography of the breast. *Semin Ultrasound CT MR* 1996; 17:460-475.
- (13) Bird RE, Wallace TW, Yankaskas BC. Analysis of cancers missed at screening mammography. *Radiology* 1992; 184:613-617.
- (14) Swann CA, Kopans DB, McCarthy KA, White G, Hall DA. Mammographic density and physical assessment of the breast. *AJR Am J Roentgenol* 1987; 148:525-526.
- (15) Jackson VP, Hendrick RE, Feig SA, Kopans DB. Imaging of the

- radiographically dense breast. *Radiology* 1993; 188:297-301.
- (16) Sabol JM, Soutar IC, Plewes DB. Mammographic scanning equalization radiography. *Med Phys* 1993; 20:1505-1515.
 - (17) Pisano ED, Parham CA. Digital mammography, sestamibi breast scintigraphy, and positron emission tomography breast imaging. *Radiol Clin North Am* 2000 ;38 (4):861 -9.
 - (18) Simonetti G, Cossu E, Montanaro M, Caschili C, Giuliani V. What's new in mammography. *Eur J Radiol* 1998; 27 Suppl 2:S234-S241.
 - (19) Chang CH, Sibala JL, Fritz SL, Dwyer SJ, Templeton AW. Specific value of computed tomographic breast scanner (CT/M) in diagnosis of breast diseases. *Radiology* 1979; 132:647-652.
 - (20) Gisvold JJ, Reese DF, Karsell PR. Computed tomographic mammography (CTM). *AJR Am J Roentgenol* 1979; 133:1143-1149.
 - (21) John V, Ewen K. CT scanning of the breast in problem cases. *Strahlenther Onkol* 1989; 165:657-662.
 - (22) Chang CH, Nesbit DE, Fisher DR, Fritz SL, Dwyer SJ, Templeton AW, Lin F, Jewell WR. Computed tomographic mammography using a conventional body scanner. *AJR Am J Roentgenol* 1982; 138:553-558.
 - (23) Bushberg JT, Seibert JA, Leidholdt EM, Boone JM. *The Essential Physics of Medical Imaging*. Baltimore: Williams and Wilkins, 1994.
 - (24) Siewerdsen JH, Jaffray DA. Cone-beam computed tomography with a flat-panel imager: effects of image lag. *Med Phys* 1999; 26:2635-2647.
 - (25) Antonuk LE, Jee KW, El Mohri Y, Maolinbay M, Nassif S, Rong X, Zhao Q, Siewerdsen JH, Street RA, Shah KS. Strategies to improve the signal and noise performance of active matrix, flat-panel imagers for diagnostic x-ray applications. *Med Phys* 2000; 27:289-306.
 - (26) Siewerdsen JH, Antonuk LE, El Mohri Y, Yorkston J, Huang W, Cunningham IA. Signal, noise power spectrum, and detective quantum efficiency of indirect-detection flat-panel imagers for diagnostic radiology. *Med Phys* 1998; 25:614-628.
 - (27) Boone JM, Buonocore MH, Cooper VN. Monte Carlo validation in diagnostic radiological imaging. *Medical Physics* 2000; 27: 1294-1304.
 - (28) Boone JM, Cooper VN. Scatter/Primary in Mammography: Monte Carlo validation. *Medical Physics* 2000; 27: 1818-1831.
 - (29) Boone JM, Seibert JA. An accurate method for computer-generating tungsten anode x-ray spectra from 30 kV to 140 kV. *Medical Physics* 1997; 24:1661-1670.
 - (30) Hammerstein GR, Miller DW, White DR, Masterson ME, Woodard HQ, Laughlin JS. Absorbed radiation dose in mammography. *Radiology* 1979; 130:485-491.
 - (31) Knox HH, Gagne RM. Alternative methods of obtaining the computed tomography dose index. *Health Phys* 1996; 71:219-224.
 - (32) Boone JM. Glandular breast dose for monoenergetic and high-energy x-ray beams: Monte Carlo assessment. *Radiology* 1999; 213:23-37.
 - (33) Boone JM, Fewell TR, Jennings RJ. Molybdenum, rhodium, and tungsten anode spectral models using interpolating 'polynomials with application to mammography. *Medical Physics* 1997; 24:1863-1874.
 - (34) Brooks RA, Di Chiro G. Theory of image reconstruction in computed tomography. *Radiology* 1975; 117:561-572.
 - (35) Johns PC, Yaffe MJ. X-ray characterisation of normal and neoplastic breast tissues. *Phys Med Biol* 1987; 32:675-695.
 - (36) Boone JM. X-ray production, interaction, and detection in diagnostic imaging. In: Beutel J, Kundel HL, Van Metter RL, editors. *Handbook of Medical Imaging*. Bellingham, WA: SPIE Press, 2000: 1-78.
 - (37) Boone JM, Chavez AE. Comparison of x-ray cross sections for diagnostic and therapeutic medical physics. *Med Phys* 1996; 23:1997-2005.
 - (38) Hasegawa BH. *The physics of medical x-ray imaging*. Madison, WI: Medical Physics Publishing Company, 1991.
 - (39) Huda W, Atherton JV, Ware DE, Cumming WA. An approach for the

- estimation of effective radiation dose at CT in. *Radiology* 1997; 203:417-422.
- (40) McCollough CH, Zink FE. Performance evaluation of a multi-slice CT system. *Med Phys* 1999; 26:2223-2230.
 - (41) Wu X. Breast dosimetry in screen film mammography. In: Barnes GT, Frey GD, editors. *Screen Film Mammography: Imaging considerations and medical physics responsibilities*. Madison, WI: Medical Physics Publishing, 1991: 159-175.
 - (42) Rossi HH. Radiation physics and radiobiology. *Health Phys* 1996; 70:828-831.
 - (43) Burgess AE. The Rose model, revisited. *J Opt Soc Am A Opt Image Sci Vis* 1999; 16:633-646.
 - (44) Curpen BN, Sickles EA, Solitto RA, Ominsky SH, Galvin HB, Frankel SD. The comparative value of mammographic screening for women 40-49 years old versus women 50-64 years old. *AJR Am J Roentgenol* 1995; 164:1099-1103.
 - (45) Arnesson LG, Vitak B, Manson JC, Fagerberg G, Smeds S. Diagnostic outcome of repeated mammography screening. *World J Surg* 1995; 19:372-377.
 - (46) Thurfjell E. Mammography screening methods and diagnostic results. *Acta Radiol Suppl* 1995; 395:1-22.
 - (47) Niklason LT, Christian BT, Niklason LE, Kopans DB, Castleberry DE, Opsahl-Ong BH, Landberg CE, Slanetz PJ, Giardino AA, Moore R, Albagli D, DeJule MC, Fitzgerald PF, Fobare DF, Giambattista BW, Kwasnick RF, Liu J, Lubowski SJ, Possin GE, Richotte JF, Wei CY, Wirth RF. Digital tomosynthesis in breast imaging. *Radiology* 1997; 205:399-406.
 - (48) Webber RL, Underhill HR, Freimanis RI. A controlled evaluation of tuned-aperture computed tomography applied to digital spot mammography. *J Digit Imaging* 2000; 13:90-97.
 - (49) Kashikar-Zuck S, Keefe FJ, Kornguth P, Beaupre P, Holzberg A, Delong D. Pain coping and the pain experience during mammography: a preliminary study. *Pain* 1997; 73:165-172.
 - (50) Aro AR, Absetz-Ylostalo P, Eerola T, Pamilo M, Lonnqvist J. Pain and discomfort during mammography. *Eur J Cancer* 1996; 32A:1674-1679.
 - (51) Kornguth PJ, Keefe FJ, Conaway MR. Pain during mammography: characteristics and relationship to demographic and medical variables. *Pain* 1996; 66:187-194.
 - (52) Tabar L. Radiology of the minimal breast cancer. *Radiology* 217(P), 54. 11-1-2000. (Abstract)
 - (53) Rose A. *Vision: Human and Electronic*. New York: Plenum Press, 1974.
 - (54) Spratt JS, Greenberg RA, Heuser LS. Geometry, growth rates, and duration of cancer and carcinoma in situ of the breast before detection by screening. *Cancer Res* 1986; 46:970-974.



DEPARTMENT OF THE ARMY
US ARMY MEDICAL RESEARCH AND MATERIEL COMMAND
504 SCOTT STREET
FORT DETRICK, MARYLAND 21702-5012

REPLY TO
ATTENTION OF:

MCMR-RMI-S (70-1y)

28 Aug 02

MEMORANDUM FOR Administrator, Defense Technical Information
Center (DTIC-OCA), 8725 John J. Kingman Road, Fort Belvoir,
VA 22060-6218


SUBJECT: Request Change in Distribution Statement

1. The U.S. Army Medical Research and Materiel Command has reexamined the need for the limitation assigned to technical reports written for this Command. Request the limited distribution statement for the enclosed accession numbers be changed to "Approved for public release; distribution unlimited." These reports should be released to the National Technical Information Service.

2. Point of contact for this request is Ms. Kristin Morrow at DSN 343-7327 or by e-mail at Kristin.Morrow@det.amedd.army.mil.

FOR THE COMMANDER:

Encl


PHYLIS M. RINEHART
Deputy Chief of Staff for
Information Management

ADB231838
ADB240253
ADB251610
ADB275099
ADB253637
ADB261538
ADB275186
ADB264648
ADB275102
ADB241899
ADB259033
ADB266113
ADB275663
ADB254489
ADB262700
ADB276708
ADB274345
ADB274844
ADB275154
ADB275535
ADB275101
ADB275451
ADB274597
ADB273871
ADB275145
ADB274505
ADB275851
ADB274459
ADB277942
ADB277404
ADB277494
ADB277536